V. 121, NO. 3
MAY 2024

ACI MATERIALS JOURNAL

A JOURNAL OF THE AMERICAN CONCRETE INSTITUTE

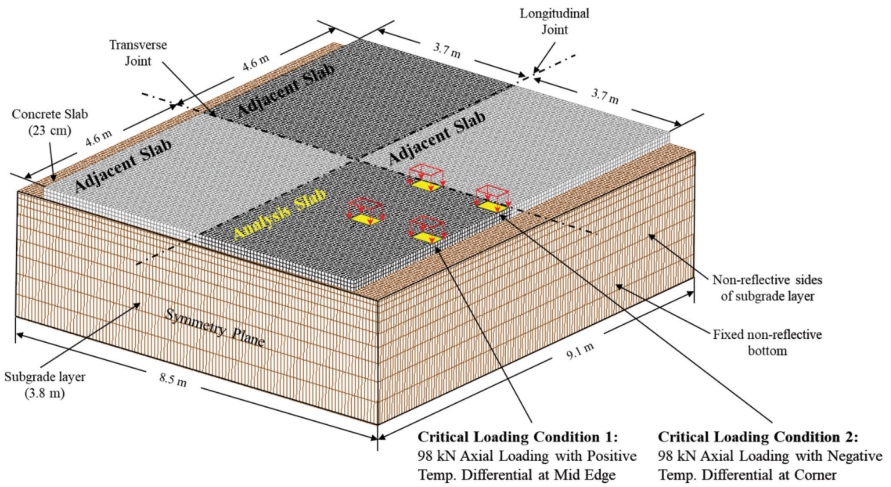

American Concrete Institute

CONTENTS

PRINTED WITH SOY INK

ACI MATERIALS JOURNAL

MAY 2024, V. 121, NO. 3

A JOURNAL OF THE AMERICAN CONCRETE INSTITUTE
AN INTERNATIONAL TECHNICAL SOCIETY

3 **Use of Metakaolin and Slag Geopolymer Adhesives for Fixing Tiles**, by Joseph Jean Assaad and Marianne Saba

17 **Study on Pore Characteristics of Microfoam Concrete Based on Different Mixing Ratios**, by C. Jin, N. Jiang, H. Li, C. Liu, A. Cao, J. Wang, and X. Wen

29 **Multi-Approaches to Improve Internally Cured Concrete for Rigid Pavement Application**, by Sangyoung Han, Thanachart Subgranon, Hung-Wen Chung, Kukjoo Kim, and Mang Tia

43 **Assessment of Approaches for Determining Time-Zero of Concrete**, by Liang Li

53 **Development and Characterization of Tension-Hardening Quarry Waste-Based Geopolymer Concrete**, by Zoi G. Ralli and Stavroula J. Pantazopoulou

69 **Contribution of Shrinkage-Reducing Admixture and Lightweight Sand to Moist-Curing Requirement for Fiber-Reinforced Ultra-High-Performance Concrete**, by Le Teng, Alfred Addai-Nimoh, and Kamal H. Khayat

81 **Curing of Concrete Specimens Containing Metakaolin, Zeolite, and Micro-/Nanobubble Water in Seawater**, by P. Mohsenzadeh Tochahi, G. Asadollahfardi, S. F. Saghravani, and N. Mohammadzadeh

91 **Three-Stage Testing Protocol to Recreate Thermomechanical Properties of Mass Concrete**, by A. S. Carey, G. B. Sisung, I. L. Howard, B. Songer, D. A. Scott, and J. Shannon

The *ACI Materials Journal* (ISSN 0889-325x) is published bimonthly by the American Concrete Institute. Publication office: 38800 Country Club Drive, Farmington Hills, MI 48331. Periodicals postage paid at Farmington, MI, and at additional mailing offices. Subscription rates: $199 per year, payable in advance. POSTMASTER: Send address changes to: *ACI Materials Journal*, 38800 Country Club Drive, Farmington Hills, MI 48331.

Canadian GST: R 1226213149.

Direct correspondence to 38800 Country Club Drive, Farmington Hills, MI 48331. Telephone: +1.248.848.3700.
Website: http://www.concrete.org.

MEETINGS

JUNE 2024

5-7—ConCreep12, Delft, the Netherlands, www.aanmelder.nl/129439

9-14—SCMT6 - Sustainable Construction Materials and Technologies Conference, Lyon, France, www.scmt-conferences.com/scmt6

12-14—DFI SuperPile '24: Piling Design & Construction Conference, San Francisco, CA, https://dfi-events.org/superpile24/index.html

19-21—Italian Concrete Conference 2024, Florence, Italy, https://www.cte-it.org/attivita-e-programmi/italian-concrete-conference_2022/

19-21—Net-Zero Future 2024, Oslo, Norway, https://netzfuture.com

23-26—12th ACI/RILEM International Conference on Cementitious Materials and Alternative Binders for Sustainable Concrete (ICCM 2024), Toulouse, France, https://www.iccm2024.com

23-26—UCA North American Tunneling Conference – NAT 2024, Nashville, TN, https://natconference.com

JUNE-JULY 2024

30-5—18th World Conference on Earthquake Engineering (WCEE2024), Milan, Italy, www.wcee2024.it

JULY 2024

8-11—NICOM8: Eighth International Symposium on Nanotechnology in Construction Materials, Catania, Italy, www.nicom.global

18-20—CFACON24 – Concrete Foundations Convention, Rio Grande, Puerto Rico, www.cfaconcretepros.org/events/details/?event=573fb936-0078-c608-9610-0b460fb96925

22-25—BEI-2024 – Bridge Engineering Institute Conference, Las Vegas, NV, www.beibridge.org

23—CIA Victoria Annual Engineering Trade Exhibition, Preston, VIC, Australia, https://concreteinstitute.com.au/professional-development/upcoming-events/cia-vic-annual-engineering-tradeexhibtition-309

AUGUST 2024

6-8—Concrete Show 2024, São Paulo, Brazil, www.concreteshow.com.br/en/home.html

21-23—2nd International Conference on Sustainable Development in Concrete Technology - ICSDCT 2024, Pune, India, https://sites.google.com/dypcoeakurdi.ac.in/icsdct2021

ACI CONCRETE CONVENTION: FUTURE DATES

2024—November 3-6, Philadelphia Marriott Downtown, Philadelphia, PA
2025—Mar. 30-Apr. 2, Sheraton Centre Toronto Hotel, Toronto, ON, Canada
2025—October 26-29, Hilton Baltimore & Baltimore Marriott Inner Harbor, Baltimore, MD
2026—Mar. 29-Apr. 1, Hyatt Regency O'Hare Chicago, Rosemont/Chicago, IL

For additional information, contact:
Event Services, ACI
38800 Country Club Drive
Farmington Hills, MI 48331
Telephone: +1.248.848.3795
email: conventions@concrete.org

ON FRONT COVER: 121-M25, p. 36, Fig. 6—Three-dimensional (3-D) finite element (FE) model for four test slabs and location of critical loading conditions with combined environmental and wheel loading.

Contributions to *ACI Materials Journal*

The *ACI Materials Journal* is an open forum on concrete technology and papers related to this field are always welcome. All material submitted for possible publication must meet the requirements of the "American Concrete Institute Publication Policy" and "Author Guidelines and Submission Procedures." Prospective authors should request a copy of the Policy and Guidelines from ACI or visit ACI's website at **www.concrete.org** prior to submitting contributions.

Papers reporting research must include a statement indicating the significance of the research.

The Institute reserves the right to return, without review, contributions not meeting the requirements of the Publication Policy.

All materials conforming to the Policy requirements will be reviewed for editorial quality and technical content, and every effort will be made to put all acceptable papers into the information channel. However, potentially good papers may be returned to authors when it is not possible to publish them in a reasonable time.

Discussion

All technical material appearing in the *ACI Materials Journal* may be discussed. If the discussion is received within four months of the paper's print publication, it will appear in the issue dated ten months from this journal's date. Discussion material received after specified dates will be considered individually for publication or private response. ACI Standards published in ACI Journals for public comment have discussion due dates printed with the Standard. Discussion should be complete and ready for publication, including finished, reproducible illustrations. Discussion must be confined to the scope of the paper and meet the ACI Publication Policy.

Follow the style of the current issue. Discussions should not exceed 1800-word equivalents (illustrations and tables count as 300 words each). References should be complete. Do not repeat references cited in original paper; cite them by original number. Numbering of additional references, figures, tables, and equations should follow sequentially from the original manuscript throughout the discussion. The discusser must indicate the month, year, volume number, issue number, authors' names, and manuscript number of the original manuscript. Closures responding to a single discussion should not exceed 1800-word equivalents in length, and to multiple discussions, approximately one half of the combined lengths of all discussions. Closures are published together with the discussions.

Discuss the paper, not some new or outside work on the same subject. Use references wherever possible instead of repeating available information.

Discussion offered for publication should offer some benefit to the general reader. Discussion which does not meet this requirement will be returned or referred to the author for private reply.

Send manuscripts to:
http://mc.manuscriptcentral.com/aci

Send discussions to:
Journals.manuscripts@concrete.org

ACI MATERIALS JOURNAL TECHNICAL PAPER

Title No. 121-M23

Use of Metakaolin and Slag Geopolymer Adhesives for Fixing Tiles

by Joseph Jean Assaad and Marianne Saba

This paper assesses the suitability of geopolymers (GPs) for use as adhesives for ceramic tile fixing, including their compliance to the relevant EN 12004 specification. Two series prepared with different percentages of metakaolin (MK), blast-furnace slag (BFS), and limestone materials activated by an alkaline NaOH/Na_2SiO_3 solution are investigated. Tested properties included the thixotropy, setting, compressive strength, open time, and adhesion bond strength under different exposure conditions (that is, dry, wet, heat, or freezing-and-thawing cycles). Compared to cement-based mortars containing adjusted proportions of cellulose and redispersible polymers, the GPs exhibited higher thixotropy, reflecting additional energy for spreading the material over the substrate, yet better maintenance of the alternating patterns of ripples and grooves at rest. The bond strengths tested under different exposure conditions were remarkably high for the MK-based GP, given the fine MK particle sizes that foster geopolymerization and cross-linking of solid bonds in the hardened structure. The BFS-based GP exhibited relatively lower bond strengths (compared to MK) due to coarser particles. Such results can be of interest to civil engineers and manufacturers of ready-to-use building materials that aim at reducing the portland cement footprint while assuring performance and sustainability of tiling applications.

Keywords: blast-furnace slag; bond strength; ceramic tiles; geopolymer; metakaolin; polymer-modified mortar; thixotropy.

INTRODUCTION

Cementitious-based tile adhesive mortars are widely used in the building industry. These are typically composed of portland cement, mineral fillers, and sand together with a combination of cellulose ether (CE) and redispersible polymer (RDP) powders.[1-3] The CE is incorporated to increase stickiness and air entrainment of freshly mixed mortars, which eases their spreading in thin layers onto horizontal and vertical substrates.[4,5] Water retention also improves with CE additions, allowing enough time for cement hydration, especially when the application is made on absorbing substrates.[5] A variety of CE polymers exists in the market such as hydroxyethyl cellulose (HEC), hydroxyethyl-methyl cellulose (HEMC), and hydroxypropyl-methyl cellulose (HPMC).[2,4,5] On the other hand, RDP is produced by spray-drying polyvinyl alcohol (PVA), ethylene-vinyl acetate (EVA), or other acrylic co-polymers containing latex emulsion.[6,7] The use of RDP favors film formations within the matrix and its interfacial boundaries, thus enhancing flexibility and tensile strengths of the hardened material.[6,8] Dimmig-Osburg et al.[9] and Su et al.[10] reported that part of such polymers is immediately adsorbed on cement grains after mixing for early film formation, while the other part is dispersed in the pore solution to undergo film formation through covalent latex bonds and chemical interactions during the drying period. Su et al.[10] found that RDP-modified thin-bed mortars are resistant to drying shrinkage, thus reducing the detachment problems between the tiles and substrates.

Numerous studies have been carried out to understand the mechanisms of polymer-modification and evolution of physical properties and strength of thin-bed mortars used as tile adhesives. Owing to the high surface/volume ratios, this kind of mortar often exhibits rapid evaporation and drying of the top surface, leading to reduced adhesion strength.[11-13] This phenomenon (known as open time) reflects the time interval during which the mortar remains "tacky" to the touch. Mansur et al.[2] and Su et al.[10] attributed the loss of tackiness to the water flux that transports the dissolved CE to the top mortar surface, where it concentrates with time to form a solid skin and reduce the wettability of ceramic tiles. Similar conclusions were drawn by Jenni et al.,[11] who revealed through optical microscopy that the enrichment of inorganic phases and carbonated hydration products increases with open time. The authors quantitatively represented the evolution of mortar properties after application, including the formation and cross-linking of polymer films, capillary forces, fractionation associated with water migration, and cement hydration. Petit and Wirquin[14] reported that skinning is important to assure proper bonding; however, too-thin skin permits excessive water evaporation and local decohesion problems, while too-thick skin increases dryness of top surface and reduces wettability.

The mortar-tile interfaces are vulnerable to stress concentration and formation of local flaws resulting from different weathering conditions encountered during the service life. EN 12004-1[15] distinguishes four exposure conditions (that is, dry, wet, heat, or freezing-and-thawing [F/T] cycles) for assessing the performance of the tile-mortar-substrate composite system. Wetzel[16] measured a substantial amount of capillary shrinkage resulting from water discharge driven by evaporation or absorption by the substrate. Such volume change leads to stress accumulation and debonding phenomena preferentially along the tile interfaces, or occasionally as vertical cracks within the mortar. Jenni et al.[3]

ACI Materials Journal, V. 121, No. 3, May 2024.

MS No. M-2022-379.R1, doi: 10.14359/51740702, received July 7, 2023, and reviewed under Institute publication policies.

showed that the adhesive strength might degrade due to wall effect and bleeding occurring along the tile interface. The incorporation of CE and RDP helps improving the mortar's homogeneity, which densifies the microstructural network along the tile interstices.[2,5,17] Nevertheless, such a network of cross-linked polymer films can be weakened in wet conditions due to dissolving and swelling phenomena, leading to reduced adhesion.[18,19] The multiple drying-and-wetting cycles may considerably increase interfacial stresses, causing the crystallization of secondary hydrates that provoke crack propagation and severely deteriorate adhesion strengths.[9,14,18]

Limited studies evaluated the suitability of alkali-activated materials, known as geopolymers (GPs), for use in tile adhesive applications. GPs are synthetized using aluminosilicate precursors such as metakaolin (MK), blast-furnace slag (BFS), fly ash, and silica fume that are activated using alkaline solutions.[20,21] The precipitated compounds create a rigid Si-O-Al bond network that hardens at ambient temperature and possesses comparable mechanical properties to those achieved with cementitious materials. Typical promising GP niche applications include soil grouting to resolve problems related to seepage and stability,[22] refractory materials exposed to elevated temperature and fire,[23] strengthening foam used as core infill for sandwich insulating panels,[24] underwater material with reduced washout loss for marine and hydraulic works,[25] and mortars used as masonry plasters and renders.[26] In this latter application, the MK-based GPs were particularly suitable to speed up the masonry construction operations and eliminate the hassle of water curing normally needed with cement-based plasters.[26]

Freshly mixed GPs exhibit considerably increased cohesiveness than cementitious materials, which can be attributed to the higher viscosity of the alkaline mixing solution.[22,27,28] This theoretically makes them suitable for tile adhesive applications whereby the mortar should be applied using a toothed trowel to create alternating patterns of ripples and grooves together with constant layer thickness. Favier et al.[28] reported that the viscosity of sodium hydroxide (NaOH) and sodium silicate (Na_2SiO_3) solutions is 10 to 100 times higher than water, leading to significant increase in rheological properties. The colloidal and inter-particle interactions between the aluminosilicate precursors are negligible, reflecting that the increase in rheology is mostly affected by the interstitial viscosity and hydrodynamic dissipation of the alkaline solution.[28] Palacios et al.[29] found that the increased yield stress and plastic viscosity are more accentuated when GPs are prepared with higher-molar NaOH solutions. Many scholars[22,30] showed that the use of high-range water-reducing admixtures (HRWRAs) is not efficient to improve the workability of GPs (that is, unlike the case of cementitious materials), making the dilution of alkaline solution using water the only efficient alternative to mitigate the increased mixture cohesiveness. Assaad and Saba[31] reported that a 10% water dilution reduced the plastic viscosity of MK-based GPs by approximately 25% (yet, at the expense of strength, which decreased by approximately 15%), leading to improved trowability of mortars during plastering works.

GPs require dry curing conditions for proper geopolymerization reactions, setting, and strength development,[20,21] making them potentially good interlayers for bonding the ceramic tiles to existing substrate in a relatively dry environment. Earlier studies showed that mixing water is not chemically bound during geopolymerization, and that elevated temperatures ranging from 40 to 80°C (104 to 176°F) could accelerate its loss and cause an increase in early strength, compared to companion specimens cured in ambient temperature.[23,32,33] Lemougna et al.[34] reported an approximate 85% drop in compressive strength for GPs immersed in water for 24 hours after demolding; the strength can, however, be partially or totally recovered if the specimens are oven-dried at 90°C overnight. Similar observations were made by Chen et al.,[35] who attributed the drop in strength to partial Si-O-Na bond dissolution in presence of water coupled with excessive presence of alkali ions in the pore solution. Curing in dry conditions and/or at elevated temperatures also reduces drying shrinkage because of faster water removal from the GP as well as enhanced cross-linking of the Si-O-Na bonds.[21,36,37] In contrast, specimens cured in humid conditions showed higher drying shrinkage and a porous microstructure.[31,36,38]

GPs exhibit superior durability and resistance to attack by hazardous materials such as chlorides, acids, and sulfates, which makes them suitable for tiling works subjected to those kinds of chemical spills.[21,30,38] Fernández-Jiménez and Puertas[39] reported that the weight loss of BFS-based GP specimens did not exceed 7% when submerged in 2% sulfuric acid, as compared to 35% for cementitious products. Bakharev et al.[40] noticed that the weight loss hovered at approximately 8% for MK-based GPs immersed in 5% hydrochloric acid. Unlike the calcium hydroxide that is released from cement hydration, the aluminosilicate-hydrate (A-S-H) gels formed during polymerization are stable and resistant to chemical reactions. Ariffin et al.[41] showed that the strength of cement-based mortars significantly dropped by 68% after 30 days of immersion in 2% sulfuric acid solution, while this was only 35% after 18 months for GP mixtures made of palm oil and powdered fuels.

This paper is part of a comprehensive study undertaken to assess the suitability of GPs for niche constructional applications—namely, mortars used as adhesives for ceramic tile installation. Two GP series prepared with different MK-to-limestone and BFS-to-limestone ratios are investigated. Tested properties included the thixotropy, setting time, compressive strength, open time, and adhesion strength determined under dry, wet, heat, or F/T cycles. Particular emphasis is placed on comparing the test responses to cement-based mortars containing different CE and RDP rates.

RESEARCH SIGNIFICANCE

Cementitious mortars intended for fixing ceramic tiles are normally produced in compliance to the EN 12004 standard specification.[15] Limited data exists in literature regarding the suitability of GPs for such applications, particularly the behavior of the composite substrate-adhesive-tile system to the different exposure conditions specified in EN 12004. The

Table 1—Chemical and physical properties for CEM, MK, BFS, and LF

	SiO_2, %	Al_2O_3, %	Fe_2O_3, %	CaO, %	MgO, %	SO_3, %
CEM	21.4	4.3	3.1	62.9	2.8	0.45
	C_3S = 43.7%; C_3A = 8.3%; loss on ignition = 1.87%; Na_2O_{eq} = 0.52%; free lime = 0.31%; K_2O = 0.76%; minor elements (such as TiO_2, ZnO, P_2O_5) = 1.59%; Blaine fineness = 335 m^2/kg; specific gravity = 3.14; characteristic 28-day compressive strength = 42.5 MPa					
MK	55	39	1.8	0.35	0.25	—
	Loss on ignition = 1%; fineness by Brunauer-Emmett-Teller (BET) method = 19,000 m^2/kg; Na_2O = 0.56%; TiO_2 = 0.95%; minor elements = 1.09%; specific gravity = 2.2					
BFS	32.82	11.85	1.17	40.53	8.39	1.4
	Loss on ignition = 0.2%; specific gravity = 2.94; K_2O = 0.92%; TiO_2 = 1.1%; MnO = 0.65%; minor elements = 0.97%; Blaine fineness = 410 m^2/kg					
LF	5.74	0.15	0.05	48.8	0.08	1.33
	Loss on ignition = 41.7%; Blaine fineness = 290 m^2/kg; K_2O = 0.18%; minor elements = 1.97%; specific gravity = 2.68					

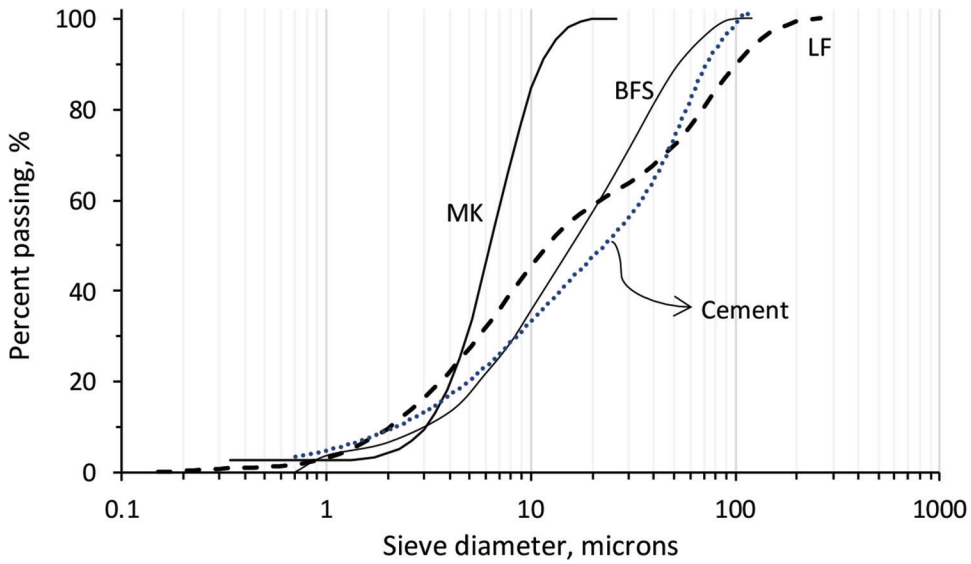

Fig. 1—Particle size distribution curves for cement, MK, BFS, and LF.

GP mixtures contained different MK, BFS, and limestone filler (LF) proportions. Such data can be of particular interest to engineers and ready-to-use building material manufacturers that aim at reducing the use of portland cement while assuring durability and sustainability of tiling applications.

EXPERIMENTAL INVESTIGATION

Materials

Portland cement (CEM) along with MK, BFS, and LF were used in this study. The CEM complies to ASTM C150 Type I: its Blaine fineness and characteristic 28-day compressive strength are 335 m^2/kg (164 ft^2/lb) and 42.5 MPa (6164 psi), respectively. Artificial MK obtained by calcining kaolinitic clay and rapidly water-cooled BFS obtained from the steel-making process were used. These aluminosilicate materials are ideal for producing GPs given their richness in SiO_2 and Al_2O_3 contents, as reflected in the chemical composition given in Table 1. The 28-day strength activity indexes for the MK and BFS were 93% and 84.3%, respectively, making them comply to ASTM C989/C989M.[42] The MK is remarkably finer than all other materials, as shown in the particle size distribution curves determined using a laser diffraction analyzer (Fig. 1). The LF had 290 m^2/kg (142 ft^2/lb) Blaine fineness and was used to improve the binder packing density and/or to replace part of the aluminosilicate materials during GP production.[26]

Continuously graded siliceous sand having 1.2 mm (0.05 in.) maximum grain size was used for producing the mortars. Its specific gravity, bulk density, and water absorption determined as per ASTM C128[43] were 2.66, 1490 kg/m^3 (91.8 lb/ft^3), and 0.55%, respectively. The materials finer than 75 µm determined as per ASTM C117[44] were equal to 0.12%.

The CEM-based mortars contained HEC and EVA-based RDP in powder forms. The HEC is a water-soluble polymer derived from polysaccharide carbohydrates in which the hydroxyethyl groups are attached to the anhydroglucose units by ether linkages; its bulk density and molecular weight are 450 g/L (0.99 lb/mole) and 736.7 g/mole (1.62 lb/mole), respectively. The EVA is an elastomeric polymer incorporated in tile adhesives to enhance the open time, flexibility, and bonding strengths[1,6]; its bulk density and molecular weight are 390 g/L (0.86 lb/mole) and 114.1 g/mole (0.25 lb/mole), respectively. Also, a polycarboxylate ether (PCE) powder HRWRA was used as water reducer in CEM-based mortars.

Table 2—Proportions, liquid demand, and alkali content of CEM and GP mortars

	CEM25	CEM30	CEM35	MK12.5	MK17.5	MK22.5	BFS12.5	BFS17.5	BFS22.5
Cement, %	25	30	35	—	—	—	—	—	—
MK, %	—	—	—	12.5	17.5	22.5	—	—	—
BFS, %	—	—	—	—	—	—	12.5	17.5	22.5
LF, %	5	5	5	12.5	7.5	2.5	12.5	7.5	2.5
Graded sand, %	69.35	63.7	58.15	75	75	75	75	75	75
HEC, % of cement	0.3	0.35	0.4	—	—	—	—	—	—
EVA, % of cement	0.2	0.8	1.2	—	—	—	—	—	—
PCE, % of cement	0.15	0.15	0.25	—	—	—	—	—	—
Water*, mL	175 to 195	195 to 215	220 to 240	—	—	—	—	—	—
w/*c*	0.74	0.68	0.66	—	—	—	—	—	—
Alkaline solution*, mL	—	—	—	330 to 340	365 to 375	410 to 420	310 to 320	325 to 335	335 to 345
Na_2O/SiO_2	—	—	—	0.30	0.27	0.25	0.35	0.32	0.29
Na_2O/Al_2O_3	—	—	—	1.72	1.30	1.14	5.25	3.96	3.15
H_2O/Na_2O	—	—	—	13.07	13.07	13.07	13.07	13.07	13.07
Si/Al	—	—	—	2.85	2.45	2.29	7.40	6.16	5.38
w/*s*	—	—	—	0.715	0.622	0.578	0.689	0.596	0.522
w/*MK* (or, *w*/*BFS*)	—	—	—	1.550	1.173	1.026	1.436	1.083	0.861

*Water and alkaline solutions are given per kg; 1 mL = 0.033 fl oz.

The alkaline activator for GP production comprised Na_2SiO_3 and NaOH solutions. The Na_2SiO_3 solution had a specific gravity of 1.39 and a SiO_2-to-Na_2O ratio of 1.86. The 10-Molar NaOH solution was prepared by mixing NaOH beads of 98% purity with tap water at least 24 hours prior to use; its specific gravity is 1.33. The Na_2SiO_3-to-NaOH ratio was set at 2.[21,26]

Decorative ceramic tiles complying to EN 14411 were used for assessing the bond strengths of CEM and GP mortars.[45] The tiles' backsides had a porous texture with a water absorption of 14 ± 3%; these were cut to 50 x 50 mm (1.96 x 1.96 in.) dimensions for testing. The chemical composition for the ceramic tiles including SiO_2, CaO, Al_2O_3, MgO, and Fe_2O_3 was 38.6%, 35.3%, 14.6%, 3.7%, and 4.1%, respectively.

Mortar proportions

Typically, cementitious mortars used as adhesives for tile fixing are manufactured to comply with the EN 12004 specification.[15] The standard stipulates that the bond strength measured after 20 minutes (that is, open time) should not drop below 0.5 MPa (72.5 psi). The products are classified in two acceptance criteria, including C1 outlining general requirements and C2 reflecting improved material characteristics. The C1 class requires a minimum of 0.5 MPa (72.5 psi) bond strength performed under different weathering conditions (that is, ambient temperature, water immersion, heat aging, and F/T cycles), while the strength should be higher than 1 MPa (145 psi) for adhesives complying to C2 class.[15]

Three CEM-based mortars are tested in this work (Table 2); the cement and admixture contents (that is, HEC, EVA, and PCE) were adjusted to secure different performance levels, as per EN 12004.[15] Hence, for example, the cement content increased from 25 to 30% for CEM25 and CEM30 mortars, respectively, and reached 35% for the higher-performance CEM35 mixture. The corresponding EVA content gradually increased from 0.2 to 0.8% and 1.2%, respectively. The LF content remained fixed at 5%, while the PCE dosage varied from 0.15 to 0.25%. The sand content was adjusted in all mortars to achieve a 100% mixture, by mass. Ordinary tap water was used when mixing the cement-based mortars.

The GP mixtures comprised three MK-based mortars and another three BFS-based mortars, as presented in Table 2. The aluminosilicate content and its dilution rate with the LF were predetermined following preliminary tests to achieve different performance levels.[25,26] Hence, the binder content (that is, aluminosilicate and LF) was set at 25% by total mass, while the sand was kept constant at 75%. The aluminosilicate gradually varied from relatively low to high concentration; for instance, the MK-LF ratios were 12.5% to 12.5% in the MK12.5 mixture, while this was 22.5% to 2.5% for the MK22.5 mixture. The same nomenclature and composition were used for the BFS-based mortars, while the same alkaline solution described earlier was used for batching.

Mortar mixing

All mortars were mixed using a laboratory mixer; the ambient temperature and relative humidity (RH) hovered at approximately 20 ± 3°C (68 ± 5.4°F) and 55 ± 5%, respectively. The amount of tap water (for CEM-based mortars) or alkaline solution (for GPs) was adjusted to meet the consistency commonly required for tile adhesives applied using toothed trowels, as will be discussed later. The resulting water-solid ratio (*w*/*s*), water-MK ratio (*w*/*MK*), and water-BFS ratio (*w*/*BFS*) are computed as follows

$$w/s = \frac{\text{Water in } Na_2SiO_3 \text{ and NaOH solutions}}{\text{Mass of MK (or BFS)} + \text{Solid content in } Na_2SiO_3 \text{ and NaOH}}$$

$$w/MK = \frac{\text{Water in } Na_2SiO_3 \text{ and NaOH solutions}}{\text{Mass of MK}}$$

$$w/BFS = \frac{\text{Water in } Na_2SiO_3 \text{ and NaOH solutions}}{\text{Mass of BFS}}$$

Table 2 summarizes the mortar compositions along with the resulting liquid demand and various alkali-activator ratios. The mixing procedure consisted of homogenizing the binder (CEM, MK, BFS, and LF) and sand, then adding the liquid solution at low speed (140 rpm) over 3 minutes. After a 30-second rest period, mixing was resumed for 3 additional minutes at medium speed (285 rpm).

Testing methods and procedures

Thixotropy measurements—Right after mixing, a four-bladed slotted vane connected to a rheometer was used to assess the thixotropic breakdown curves of fresh mortars. The testing protocol consisted of applying a given rotational speed and recording the decay in torque over time; two consecutive tests were performed at rotational speeds of 50 and 150 rpm. The material was kept for 30 seconds at rest before each test, and re-homogenized manually each time.

The vane used measured 24 mm (0.94 in.) height (H) and 12 mm (0.47 in.) diameter (D), while the slots height (h) and width (d) were 12 and 4 mm (0.47 and 0.16 in.), respectively. Earlier studies showed that the presence of slots helps reducing the plug flow, including the migration of particles away from the center to keep the impeller in contact with "new" material.[46,47] The vane was immersed in the mortar in a way to keep the top blade edges flush with the upper material surface, which can be relevant to reduce disruption of thixotropic materials (that is, such as those used in this work) and ensure uniform stress distribution along the blades.[46,47] The conversion of torque (T) measurements into shear stress (τ) was realized using the following expression[47]

$$T = \left[\left(\frac{\pi D^3}{2}\right)\left(\frac{1}{6} + \frac{H}{D}\right) + \left(\frac{\pi d^3}{2}\right)\left(\frac{1}{3} - \frac{Dh}{d^2}\right)\right]\tau$$

Setting time and compressive strength—The setting times were determined using the Gillmore apparatus, as per ASTM C266.[48] The compressive strength (f_c') was determined using 40 x 40 mm (1.57 x 1.57 in.) cubes, as per EN 196-1.[49] The specimens were demolded after 24 hours and stored in plastic bags at 20 ± 3°C (68 ± 5.4°F) until testing after 28 days. EN 12004 does not provide specific limitations for setting times and f_c' for tile adhesives; however, these were evaluated in this study to enable better performance comparison between cementitious and GP mortars.

Bond strengths to ceramic tiles—The bond between ceramic tiles and concrete substrates was realized under different conditions following the EN 1348 test method.[50] Initially, the unreinforced substrates were prepared by casting 28 MPa (4060 psi) concrete into different slabs having 300 x 300 mm (11.8 x 11.8 in.) surface area and 50 mm (1.96 in.) thickness. The top surfaces were roughened using steel-wire brush to remove the thin laitance layer, dirt, and free particles.

A toothed trowel having 6 x 6 mm (0.24 x 0.24 in.) notches was used to spread the freshly mixed mortars on the concrete substrates (Fig. 2). The trowel was held at an angle of approximately 60 degrees to the substrate and drawn across the slab in straight parallel lines. The tiles were applied on the adhesive mortar at distances not less than 100 mm (3.94 in.) apart, which were then loaded with a 2 kg (4.4 lb) mass for 30 seconds.[50] Five different types of bond strength tests were performed, as follows:

Initial bond strength ($\psi_{initial}$)—In this test, the tiles were applied right after the spreading of mortar, and the composite system was allowed to cure in room conditions where ambient temperature and RH were 20 ± 3°C (68 ± 5.4°F) and 55 ± 5%, respectively. After 28 days, the pull-head plates were glued using high-strength epoxy resin on the ceramic tiles, and tensile load applied perpendicular to the slab at uniform rate hovering 0.25 kN/s (56 lb/s). The bond strength was taken as the mean of four measurements and determined as the load to cause rupture divided by 2500 mm^2 (3.87 in.^{2}). Also, the fracture patterns including adhesive-type (that is, at the interface between mortar and substrate), cohesive-type (that is, failure in the ceramic tile itself), and substrate-type (that is, failure in the concrete substrate) were noted.[51] These are referred to as A, C, and S, respectively.

Open time (ψ_{OTime})—This test reflects the time interval during which the mortar can still secure adequate bond between the ceramic tiles and substrate, as per EN 1346.[52] Hence, the tiles are placed 7.5, 15, and 20 minutes after applying the mortar on the concrete substrates, and each loaded with a 2 kg (4.4 lb) mass for 30 seconds. As earlier, the composite system was cured in room conditions and bond strength measured after 28 days.

Bond after water immersion (ψ_{water})—After 7 days of room curing (that is, ambient temperature and RH were 20 ± 3°C [68 ± 5.4°F] and 55 ± 5%, respectively), the composite system was immersed in water for 21 days.[50] The bond strength tests were then realized as mentioned earlier.

Bond after heat aging (ψ_{heat})—After 14 days of room curing, the composite system is placed in air-circulating oven at 70 ± 3°C (158 ± 5.4°F) for 14 days.[50] The bond strengths are then determined.

Bond after F/T cycles ($\psi_{F/T}$)—After 7 days of room curing, the composite system was immersed in water for 21 days before carrying out a total of 25 F/T cycles. Each cycle consists of placing the test units in –15 ± 3°C (5 ± 5.4°F) freezer for 2 hours, then immersing in water at 20 ± 3°C (68 ± 5.4°F) for another 2 hours.[50] The bond tests were then realized as mentioned earlier.

RESULTS AND DISCUSSION

Liquid demand

The amount of liquid (that is, whether water or alkaline solution) required to achieve the alternating patterns of ripples and grooves for various tested mixtures is plotted in Fig. 3. In the case of cement-based mortars, CEM35

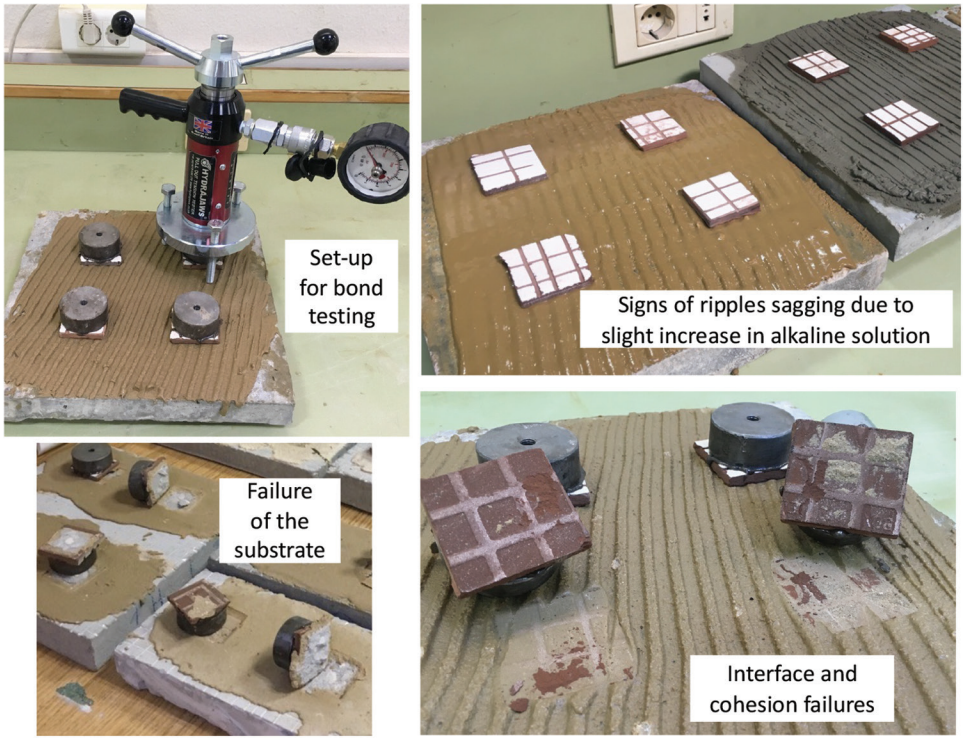

Fig. 2—Typical photos for bond strength testing.

required the highest water demand of 230 mL (7.77 fl oz), while this decreased to 205 and 185 mL (6.93 and 6.25 fl oz) for CEM30 and CEM25, respectively. This can naturally be attributed to two main reasons, including the increased cement content that necessitates higher water for proper lubrication as well as to the increased HEC/EVA concentration.[7,14] The presence of such polymers thickens the liquid phase through chain entanglements and develops attractive forces through hydrogen bonds, thus requiring additional water to achieve the desired consistency.[53,54]

The GPs required significantly higher demand for alkaline solutions (Fig. 3), as compared to the amount of water required for CEM-based mortars. Hence, the alkaline solution varied from 335 to 415 mL (11.32 to 14.03 fl oz) for MK-based GPs, and from 315 to 340 mL (10.65 to 11.5 fl oz) for BFS-based GPs. Similar observations were made by other scholars[20,22,26] who associated this behavior to the increased viscosity of the suspending alkaline solution (that is, NaOH and Na_2SiO_3), thus increasing the liquid demand for a given workability. Nevertheless, it is worth noting that the alkaline solution should be properly dosed within ±5 mL/kg (±0.077 fl oz/lb) (that is, within ±1.5% of total solution) during GP mixing to obtain the alternating patterns of ripples and grooves (Table 2). In fact, tests have shown that insufficient alkaline concentration would significantly increase the GP cohesiveness and require more energy for adequate spreading on the substrate, while in contrast, the proneness of ripples to sagging increases with an excess in the liquid concentration (as shown in Fig. 2). A wider range in water demand varying within ±10 mL/kg (±0.15 fl oz/lb) (that is, ±5% of total water) can be tolerated for CEM-based mortars, mostly due to the presence of HEC/EVA polymers that thicken the liquid phase and reduce its sensitivity to water variations.

The alkaline solution gradually increased when the MK concentration increased in the GP mortar. Hence, this varied from 335 to 370 and 415 mL (11.3 to 12.5 and 14.03 fl oz) for MK12.5, MK17.5, and MK22.5, respectively; the corresponding *w/s* varied from 0.715 to 0.622 and 0.578, respectively. This can be related to the increased MK fineness and plasticity of the aluminosilicate sheets, thus necessitating additional liquid to secure the targeted consistency.[31,32,35,36] For similar LF concentration, the demand in alkaline solution of BFS-based GPs remained comparatively lower than MK-based ones, which can be attributed to different fineness levels of the MK and BFS materials (Fig. 1). Hence, the liquid demand varied from 315 to 330 and 340 mL (10.65 to 11.15 and 11.5 fl oz) for BFS12.5, BFS17.5, and BFS22.5, respectively.

Thixotropic properties

Typical thixotropic breakdown curves for selected CEM and GP mixtures determined at 50 rpm are plotted in Fig. 4. All curves are characterized by a peak shear stress ($\tau_{initial}$) that represents the initial structural condition after the rest period, and thereafter stress decay with time towards equilibrium where the entanglements and attractive forces are reduced to a minimum value. The equilibrium stress (τ_{equil}) reflects the alignment and asymmetrical spatial distribution of particles in the direction of flow.[29,46,54]

Table 3 summarizes the $\tau_{initial}$ and τ_{equil} values determined at 50 and 150 rpm. The coefficient of variation (COV) determined on triplicate specimens for τ_{equil} responses varied within limited ranges from 7.6 to 11.5%, reflecting acceptable repeatability. The COV is computed as the ratio

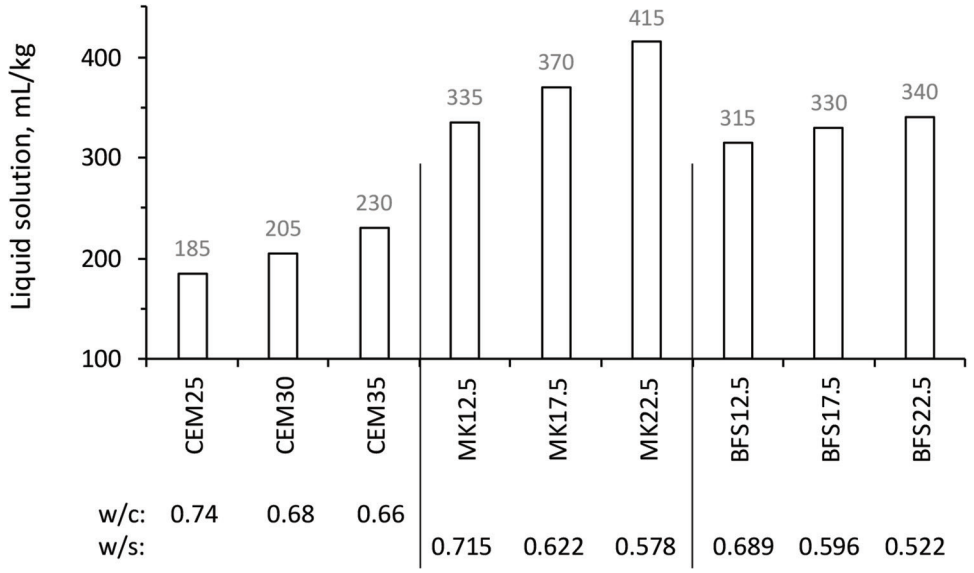

Fig. 3—Liquid demand for various CEM and GP mortars.

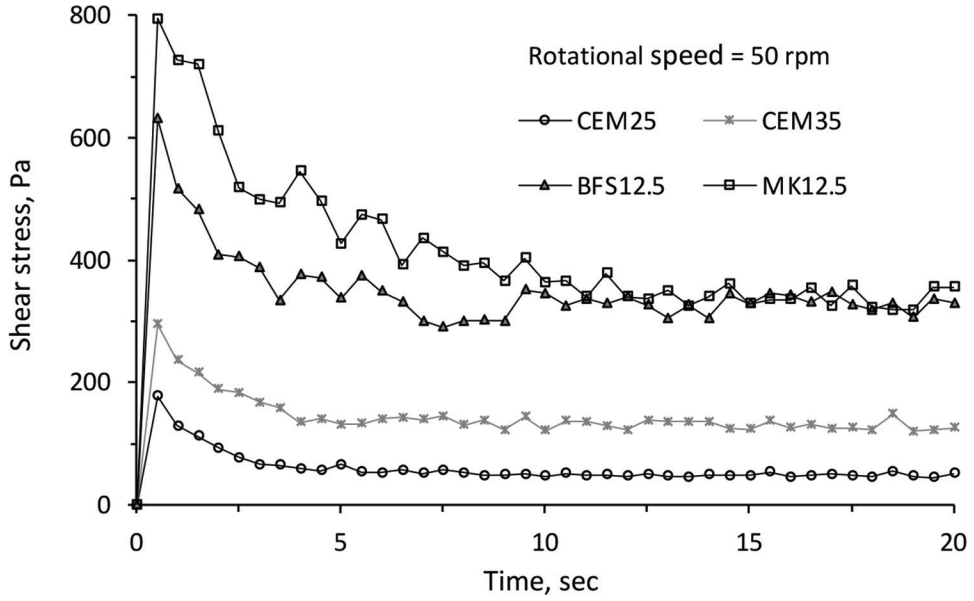

Fig. 4—Typical shear stress versus time decay for CEM and GP mortars.

between the standard deviation and mean responses, multiplied by 100. In contrast, the COV remarkably increased for $\tau_{initial}$ values to range between 10.7 and 20.2%. This can be attributed to the vane insertion process that alters the contact with the surrounding mortar, as well as the sensitivity of rheometer to detect the initial stresses required to breakdown the structure.[47]

Figure 5 illustrates the τ_{equil} values determined at 50 and 150 rpm. As normally expected, the CEM-based mortars incorporating increased HEC/EVA concentration required higher shear stresses at equilibrium, given the increased level of polymer entanglements and associations that aggravate the resistance to flow.[7,14,54] Hence, for example, τ_{equil} determined at 150 rpm increased from 259.4 to 453.7 Pa (0.037 to 0.066 psi) for CEM25 and CEM35, respectively. Because of higher viscosity of alkaline solution, the GPs exhibited higher thixotropic responses as evidenced by the increased $\tau_{initial}$ and τ_{equil} values (Table 3 and Fig. 5). Hence, for example, the τ_{equil} determined at 150 rpm reached 801.4 and 1091.6 Pa (0.12 to 0.16 psi) for MK12.5 and MK22.5, respectively, which represents an average varying from 1.8 to four times higher than the values recorded from CEM-based mortars. From a practical point of view, the increased thixotropy reflects additional energy for spreading the GP, which thereafter maintains its alternating shape after being left at rest (Fig. 2). This process, however, occurs smoothly as the position of the ripples can shift in any direction as the toothed trowel is run several times over the substrates.

The $\tau_{initial}$ and τ_{equil} for BFS-based GPs were relatively lower than the values determined using the MK-based ones (Table 3 and Fig. 5). For example, τ_{equil} determined at 150 rpm reached 640.5 and 975.4 Pa (0.093 and 0.14 psi) for BFS12.5 and BFS22.5, respectively, representing an average varying from 1.11- to 1.25-times higher than the values recorded from the CEM-based mortars. This can be attributed to two factors including the reduced liquid demand needed for the

Table 3—Thixotropy, f_c', and bond strengths for various CEM and GP mortars

	CEM25	CEM30	CEM35	MK12.5	MK17.5	MK22.5	BFS12.5	BFS17.5	BFS22.5
50 rpm: $\tau_{initial}$, Pa	177.83	240.7	294.6	794.2	592.81	1216.2	630.7	674.3	595.6
50 rpm: τ_{equil}, Pa	48.73	119	128.4	342.1	269.5	478.1	331.2	316.1	481.4
150 rpm: $\tau_{initial}$, Pa	633.5	1367.5	1221.2	2123.6	3180.4	5471.2	1914.9	1727.7	3835.8
150 rpm: τ_{equil}, Pa	259.2	439.1	453.7	801.4	748.4	1091.6	640.5	609.7	975.4
Unit weight, kg/m^3	1920	1925	1955	1890	1860	1875	1855	1900	1890
Set time, hr:min	7:20	10:40	16:30	8:40	8:50	7:40	n/a	10:35	9:45
f_c', MPa	17.7	23.4	20.2	23.6	35	44.1	18.5	27.3	32.8
$\psi_{initial}$, MPa (fracture)	0.77 (A)	0.92 (A)	1.56 (A/C)	2.37 (A)	3.08 (S)	3.11 (S)	1.02 (A)	1.33 (A)	2.1 (A/C)
7-minute ψ_{OTime}, MPa	0.68	1.1	1.5	2.1	2.48	2.83 (S)	0.84	1.3	1.77
15-minute ψ_{OTime}, MPa	0.52	0.95	1.23	1.83	1.4	2.88 (S)	0.92	1.06	1.6
20-minute ψ_{OTime}, MPa	0.35	0.42	1.09	0.8	0.96	1.84	0.6	0.77	1.33
ψ_{water}, MPa	0.33	0.55	0.74	1.7	2.64	3 (S)	0.63	1.02	1.44
ψ_{heat}, MPa	0.62	0.85	1.39	1.46	1.8	2.26	0.65	0.82	1.62
$\psi_{F/T}$, MPa	0.41	0.52	1.03	1.3	1.85	2.53	0.51	0.77	1.5

Note: 1 Pa = 0.00015 psi; 1 kg/m^3 = 0.062 lb/ft^3; 1 MPa = 145 psi.

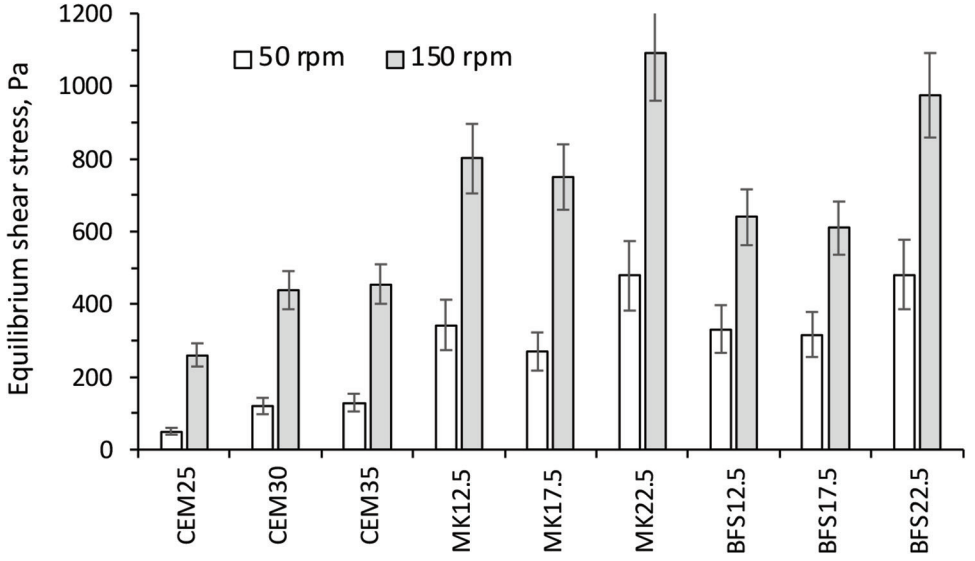

Fig. 5—Effect of mortar composition on τ_{equil} values determined at 50 and 150 rpm.

BFS-based GPs as well as the relatively coarser BFS particles that reduce internal friction within the matrix.[22,25]

The relationships between the shear stresses determined at 50 and 150 rpm are plotted in Fig. 6. Clearly, the stresses increased at higher rotational speeds due to increased dynamic forces generated during shearing.[54] The τ_{equil} values yielded a correlation coefficient (R^2) of 0.91, reflecting high interdependency on similar phenomena. The decrease in R^2 to 0.7 for $\tau_{initial}$ responses can be associated to rheological artifacts including slippage at early stages of vane rotation.[47]

Setting times and compressive strength

The setting times, f_c', and bond strengths determined under different exposure conditions are given in Table 3. As illustrated in Fig. 7, the setting times remarkably increased from 7:20 to 10:40 and 16:30 hr:min for CEM25, CEM30, and CEM35, respectively. The corresponding f_c' varied from 17.7 to 23.4 MPa (2567 to 3393 psi), and then dropped to 20.2 MPa (2929 psi) for CEM35 (although this latter mortar yielded the highest bond strengths, as will be discussed later). This can be directly attributed to the increased HEC/EVA polymers that alter the evolution of cement hydration including the formation of calcium-silicate-hydrate (C-S-H) compounds.[3,6] Petit and Wirquin[14] demonstrated that part of CE and RDP polymers is released into the interstitial solution, while the remainder is adsorbed onto the cement grains to delay the setting times.

The f_c' gradually increased for GPs containing higher MK or BFS concentration (that is, mixtures containing reduced LF content in the total binder). Hence, the f_c' varied from 23.6 to 35 and 44.1 MPa (33,422 to 5076 and 6396 psi) for MK12.5, MK17.5, and MK22.5, respectively. Knowing

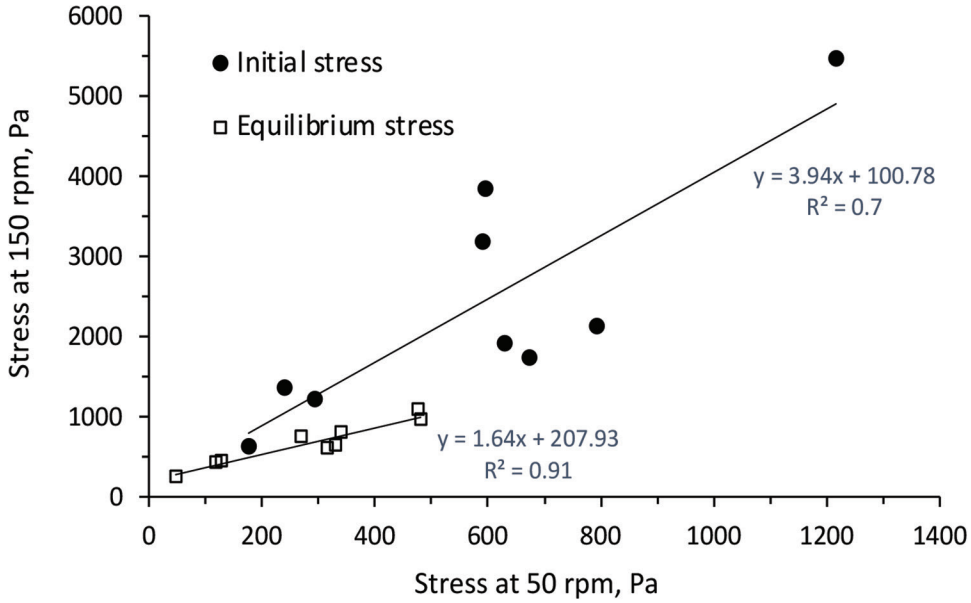

Fig. 6—Relationships between shear stresses determined at 50 and 150 rpm.

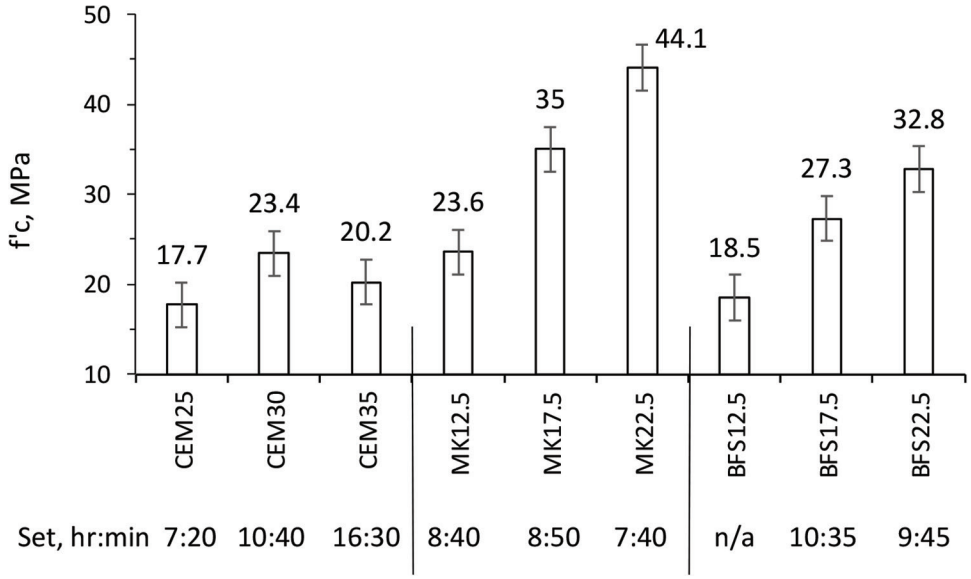

Fig. 7—Effect of CEM and GP mortars on f_c' *and setting times. (Note: 1 MPa = 145 psi.)*

the inert LF nature, the increased strength can naturally be related to a higher aluminosilicate precursor content in the mortar that promotes geopolymerization in presence of the alkaline solution.[20,21,36] Concurrently, the decrease in *w/s* from 0.715 to 0.631 and 0.574 for MK12.5, MK17.5, and MK22.5, respectively, can reduce the porosity and improve the denseness of the matrix.[34,35] At similar precursor content, the strength of BFS-based GPs was relatively lower than MK-based ones, which can be attributed to the coarser BFS particles (as shown in Fig. 1). Hence, the f_c' varied from 18.5 to 27.3 and 32.8 MPa (2683 to 3959 and 4757 psi) for BFS12.5, BFS17.5, and BFS22.5, respectively. The setting times for GPs varied within limited ranges (that is, from 7:40 to 10:35 hr:min), regardless of the binder type and concentration.

Initial and open-time bond strengths

CEM-based mortars—Figure 8 plots the bond strengths determined when the ceramic tiles are applied right after the mortar spreading (that is, $\psi_{initial}$) as well as after 7.5, 15, and 20 minutes (that is, ψ_{OTime}). As shown, the $\psi_{initial}$ gradually increased from 0.77 to 0.92 and 1.56 MPa (111.7 to 133.4 and 226.3 psi) for CEM25, CEM30, and CEM35, respectively. This can be attributed to two concomitant reasons related to the higher cement and EVA contents. The former component favors the formation of additional C-S-H binding compounds, while the presence of polymers enhances film formations through covalent latex bonds and chemical interactions along the tile-mortar interfaces.[2,5]

As expected, the ψ_{OTime} decreased over time because of the conjuncture of different phenomena such as water evaporation, skinning, and enrichment of inorganic phases along the interface that weaken the bond properties.[2,11,12] Hence, the

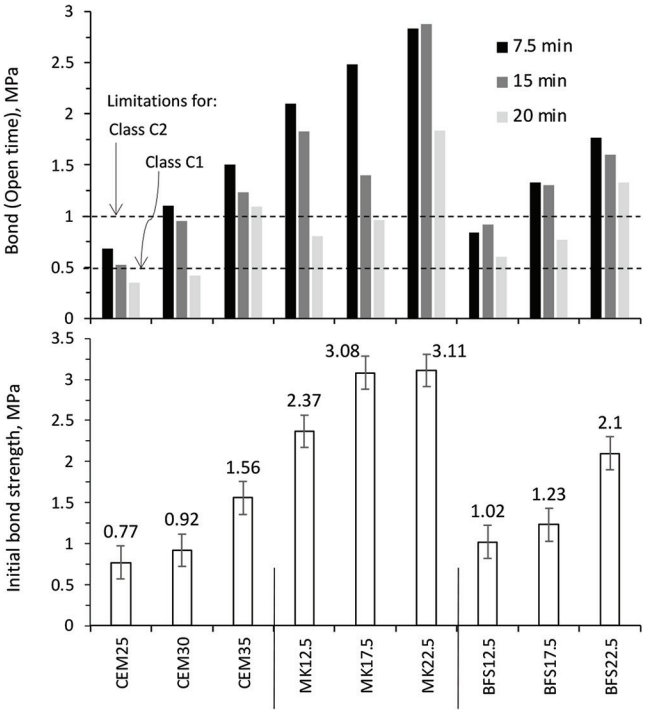

Fig. 8—Effect of mixture composition on ψ_{initial} and ψ_{OTime} responses. (Note: 1 MPa = 145 psi.)

ψ_{OTime} for CEM25 dropped to 0.52 and 0.35 MPa (75.4 and 50.7 psi) after 15 and 20 minutes, respectively, revealing its noncompliance to C1 class in EN 12004.[15] In contrast, the ψ_{OTime} remained higher than 1.0 MPa (145 psi) for CEM35, making it compliant to C2 class. In addition to increased cement content, the incorporation of 1.2% EVA in CEM35 played a major role for assuring proper bond strengths over time.[1,2]

GP mortars—The $\psi_{initial}$ significantly increased for MK-based GPs, reflecting the superior performance over the cement-based mortars (Fig. 8). Hence, $\psi_{initial}$ reached 2.37 MPa (343.7 psi) for MK12.5 and higher than 3 MPa (435.1 psi) (that is, substrate failure) for MK17.5 and MK22.5 mixtures. This can be associated to a combination of phenomena including greater affinity and assemblage of Si-O-Na ionic species resulting from the MK-based GP and ceramic tiles that are rich in silicate units.[36,55] Zhang et al.[37] reported that the dissolution of monomeric aluminate and silicate species generates higher contacts between the disaggregated interfaces, causing precipitation and formation of solid three-dimensional phases consisting of Si-O-Al-O bonds. Also, the fine MK particles may have penetrated the tiles open structure to reduce the wall effect and form dimers that foster geopolymerization particularly at the mortar-tile interfaces.[30,32]

A substrate-type failure occurred after 7.5 and 15 minutes for MK22.5, while ψ_{OTime} reached 1.84 MPa (266.8 psi) after 20 minutes (Table 3). This reflects the excellent adhesive properties achieved over time for this mortar, making it complying by a large extent to the requirements for C2 class (because EN 12004 specifies that ψ_{OTime} should be higher than 1 MPa [145 psi]). The bond gradually decreased over time for mixtures containing reduced MK concentration. Hence, ψ_{OTime} was 0.8 and 0.96 MPa (116 and 139.2 psi) for MK12.5 and MK17.5, respectively, after 20 minutes, making them comply with C1 class (because ψ_{OTime} is higher than 0.5 MPa [72.5 psi]). Compared to cement-based mortars, the superior GP performance can be attributed to the absence of the skinning phenomenon[2-4]; this was visually observed since the top GP surface was continuously replenished with the alkaline solution that prevents dryness and improves the wettability of ceramic tiles over time.

Because of increased BFS concentration in the binder, the $\psi_{initial}$ varied from 1.02 to 1.23 and 2.1 MPa (147.9 to 178.4 and 304.6 psi) for BFS12.5, BFS17.5, and BFS22.5, respectively (Fig. 8). Nevertheless, such strengths remained relatively lower than those obtained from the MK-based GPs, which as explained earlier, can be attributed to the coarse BFS particles that reduce polymerization and cross-linking of solid bonds in the hardened structure. As with the MK-based GPs, the ψ_{OTime} of BFS-based GPs gradually reduced over time (Fig. 8). The BFS22.5 containing the highest BFS content of 22.5% complied with C2 class, while the other BFS-based mortars complied with C1 class. It is to be noted that an acceptable relationship with R^2 of 0.67 exists between f_c' and $\psi_{initial}$ values for all tested mortars, as shown in Fig. 9.

Bond strengths after different exposure conditions

The bond strengths for CEM and GP mortars determined after water immersion, heat, and F/T cycles are illustrated in Fig. 10. This figure also plots the drop in bond normalized with respect to corresponding $\psi_{initial}$, as follows

$$\Delta(\psi_{water}),\ \% = \frac{\psi_{water} - \psi_{initial}}{\psi_{initial}} \times 100$$

$$\Delta(\psi_{heat}),\ \% = \frac{\psi_{heat} - \psi_{initial}}{\psi_{initial}} \times 100$$

$$\Delta(\psi_{F/T}),\ \% = \frac{\psi_{F/T} - \psi_{initial}}{\psi_{initial}} \times 100$$

Bond after water immersion—As shown in Fig. 10, the CEM-based mortars exhibited the highest drops in bond strength with $\Delta(\psi_{water})$ reaching –57%, –40.2%, and –52.6% for CEM25, CEM30, and CEM35, respectively. Such results concur with other scholars[6,14] who attributed this drop to solubility of the HEC/EVA polymer films upon continuous contact with water. Jenni et al.[3] reported that water can dissolve such films and damage the microstructure at the mortar-tile interfaces, leading to weaker adhesion. The ψ_{water} for CEM25 was 0.33 MPa (47.9 psi) (that is, below the C1 class requirement), while this was 0.74 MPa (107.3 psi) for CEM35.

Unlike CEM-based mortars, the retention of bond strengths remained very high for GPs subjected to water immersion. Hence, a substrate failure occurred for MK22.5, while ψ_{water} of 1.7 MPa (246.5 psi) was recorded for MK12.5 (that is, $\Delta(\psi_{water})$ of –28.3%), making them compliant to C2 class. This can be attributed to the applicable dry curing regime during the first 7 days after tile application (as

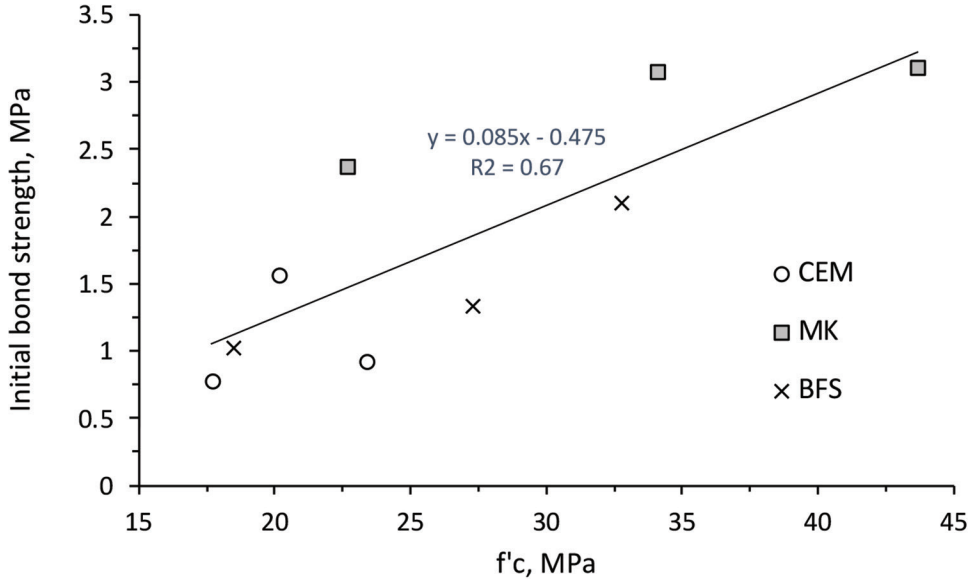

Fig. 9—Relationship between f_c' *and* $\psi_{initial}$ *for tested mortars. (Note: 1 MPa = 145 psi.)*

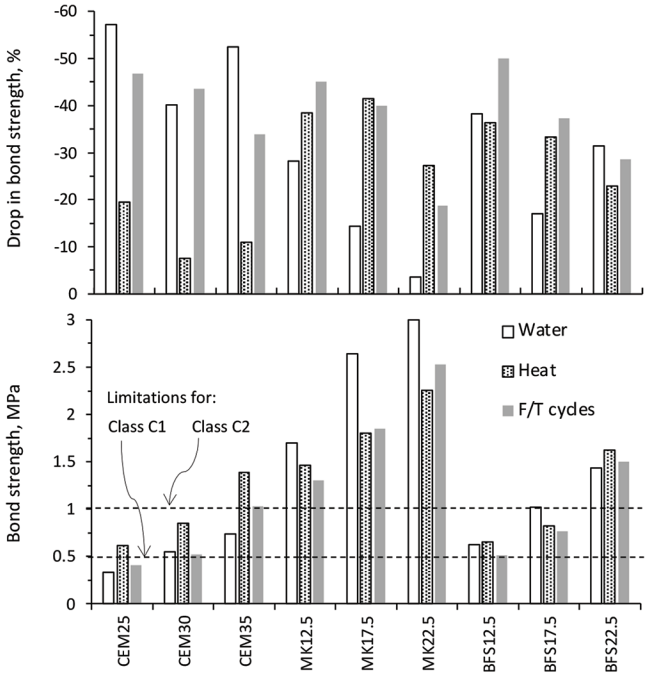

Fig. 10—Effect of mixture composition on bond strength determined under different exposure conditions. (Note: 1 MPa = 145 psi.)

per EN 12004), giving ample time for the GPs to acquire enough strength before being immersed in water for 21 days. According to Firdous and Stephan,[20] the polymerization including the reaction time during which no further heat is released is very limited in GP materials (that is, approximately 20 to 30 hours), mainly requiring dry conditions for fast evaporation of water. Djobo and Stephan[55] demonstrated by isothermal calorimetry that geopolymerization of volcanic ash is characterized by a single exothermic peak reached in less than 1 hour. This peak is associated with fast sorption of alkaline solution and dissolution of the aluminosilicate species, particularly at increased fineness and elevated temperatures. This physically reflects that GPs exhibit superior resistance to water immersion compared to CEM-based mortars, provided that the initial curing (that is, the first 7 days) is performed in dry conditions, as per EN 12004.

The ψ_{water} for BFS-based GPs followed the same trend as the MK-based ones, albeit the magnitude of bond was relatively lower (Fig. 10). Hence, ψ_{water} varied from 0.63 to 1.44 MPa (91.4 to 208.8 psi) for BFS12.5 and BFS22.5, respectively, revealing compliance to C1 and C2 classes, respectively.

Bond after heat—For certain cementitious applications, the elevated temperatures was found to promote diffusion of polymers within the mortar-tile interstices, leading to improved mechanical anchorage and bonding strengths.[14,16] This might explain the relatively low drop in ψ_{heat} that reached 0.62 and 0.85 MPa (89.9 and 123.3 psi) for CEM25 and CEM30 (that is, C1 class), and 1.39 MPa (201.6 psi) for CEM35 (that is, C2 class). The corresponding $\Delta(\psi_{heat})$ was –19.5%, –7.6%, and –10.9%, respectively (Fig. 10). Additionally, it is worth noting that the CEM-based mortars exhibit increased elasticity due to the presence of HEC/EVA polymers,[2,11,12] which could have played a beneficial role to prevent debonding at the interfaces and lead to increased strengths.

Compared to cement-based mortars, the GPs exhibited relatively higher levels of bond drop after heat aging; the $\Delta(\psi_{heat})$ ranged from –27 to –42% for MK-based mixtures, and from –23 to –36% for BFS-based ones (Fig. 10). In general, it is well established that complete geopolymerization reactions take place at elevated temperatures varying from 40 to 85°C (104 to 185°F) during the first few days after mixing, while the strength deteriorates if the specimens are kept at high temperature for longer elapsed times.[23,32] In this experimental program, the composite slabs are cured in reverse method (that is, room temperature during the first 14 days, then at 70°C [158°F] for another 14 days, as per EN 12004), which explains the drop in bond measurements. Heah et al.[56] concluded that the increase in temperature from

40 to 60, 80, and 100°C (104 to 140, 176, and 212°F) favored the strength gain after 1 to 3 days. However, the strength of specimens degrades when curing at elevated temperatures continued for longer periods of time because of thermolysis that weakens the cross-linking of Si-O-Al-O polymeric bonds.[56] Similar conclusions were made by Rovnaník[33] and Kani and Allahverdi[57] when testing GPs hydrothermally cured at different temperatures (that is, from 45 to 85°C [104 to 185°F]) over various time periods. Regardless of the binder type, the GP strength deteriorated at 28 days when the elevated temperature was applied at later curing ages, in comparison to specimens cured in ambient temperature.[33,57]

As shown in Fig. 10, the MK-based GPs exhibited remarkably higher ψ_{heat} values than BFS-based ones, given the increased MK fineness that fosters the development of strength.[31,36] Hence, ψ_{heat} varied from 1.46 to 1.8 and 2.26 MPa (211.7 to 261.1 and 327.8 psi) for MK12.5, MK17.5, and MK22.5, respectively, making them all comply to C2 class. The ψ_{heat} was respectively 0.65 and 0.82 MPa (94.3 and 118.9 psi) for BSF12.5 and BFS17.5 (that is, C1 class), while increased to 1.62 MPa (234.9 psi) for BFS22.5 (that is, C2 class).

Bond after F/T cycles—The drop in bond for cement-based mortars due to F/T cycles is comparatively similar to what is observed when the specimens are immersed in water. The $\psi_{F/T}$ for CEM25 was 0.41 MPa (59.4 psi) (that is, below C1 class), while this increased to 0.52 MPa (75.4 psi) for CEM30 (that is, complying to C1) and 1.16 MPa (168.2 psi) for CEM35 (that is, complying to C2). The corresponding $\Delta(\psi_{F/T})$ was –46.8%, –43.5%, and –34%, respectively (Fig. 10). This can mostly be attributed to dissolving of the HEC/EVA polymer films, given that the composite slabs are immersed in water for 21 days before carrying out the F/T cycles. As explained earlier, those films are water-soluble,[3,6,14] causing a decrease in bond strengths.

The $\psi_{F/T}$ followed a decreasing trend for GPs prepared with reduced MK or BFS concentration, albeit the rate of drop remained comparatively lower than that recorded for the CEM-based mortars. Hence, $\psi_{F/T}$ decreased from 2.53 to 1.85 and 1.3 MPa (366.9 to 268.3 and 188.5 psi) for MK22.5, MK17.5, and MK12.5, respectively. The corresponding $\Delta(\psi_{F/T})$ varied from –45.1% to –39.8% and –18.6%, respectively. Consistent with f_c' and previous bond strengths, the $\psi_{F/T}$ was slightly lower for BFS-based GPs, varying from 1.5 to 0.77 and 0.51 MPa (217.5 to 111.7 and 73.9 psi) for BFS22.5, BFS17.5, and BFS12.5, respectively (that is, the $\Delta(\psi_{F/T})$ is equal to –50% to –37.4% and –28.5%, respectively). It is worth noting that different factors are known to affect the resistance against F/T cycles for GP or cement-based materials.[58-61] For example, Lingyu et al.[38] reported that the frost resistance of MK-based GPs can be correlated to permeability, porosity, and critical pore diameter. Pilehvar et al.[59] showed that common air-entrainers have poor compatibility in high-alkaline solutions, while the incorporation of BFS strengthens the tensile strength and improves the frost resistance.

CONCLUSIONS

This paper is part of a comprehensive work undertaken to assess the potential uses of geopolymer (GP) materials in the building industry. The executed testing program demonstrated the feasibility of metakaolin (MK) and blast-furnace slag (BFS)-based GPs for fixing ceramic tiles in compliance to EN 12004 standard specification. Based on foregoing, the following conclusions can be warranted:

1. Because of increased viscosity of alkaline solution, the MK and BFS-based GPs required about twice higher liquid demand than portland cement (CEM)-based mortars. The alkaline solution should not vary by more than ±3% during batching, for proper maintain of ripples and grooves after spreading using a toothed trowel.

2. The GPs exhibited higher thixotropic responses than CEM-based mortars, reflecting additional energy for spreading, yet better maintain of the alternating patterns at rest. The shear stresses recorded for BFS-based GPs are lower than those determined using the MK-based ones, given the reduced demand for alkaline solution and coarser BFS particles.

3. The compressive strength f_c' gradually increased for GPs containing higher MK or BFS concentration, reaching 44.1 and 32.8 MPa (6395 and 4756 psi) for MK22.5 and BFS22.5, respectively. Their setting times varied within limited ranges (that is, from 7:40 to 10:35 hr:min), regardless of the binder type and concentration.

4. The MK-based GPs exhibited significantly higher $\psi_{initial}$ and ψ_{OTime} responses, as compared to CEM-based mortars. This was attributed to greater assemblage of ionic species as well as finer MK particles that foster the formation of solid bonds. The GP upper surface is continuously replenished with alkaline liquid solution, thus increasing ψ_{OTime} through improved wettability of ceramic tiles.

5. The BFS-based GPs exhibited relatively lower $\psi_{initial}$ and ψ_{OTime} responses, as compared to MK-based ones. This was attributed to the coarser BFS particles that reduce cross-linking of solid bonds in the hardened structure.

6. Unlike CEM-based mortars, the bond strengths of MK and BFS-based GPs did not remarkably curtail due to water immersion. This was related to the dry curing regime applied during the first 7 days after tile application, thus giving enough time for the GP to acquire strength.

7. Compared to CEM-based mortars, the GPs exhibited relatively higher levels of bond drop after heat aging. The $\Delta(\psi_{heat})$ ranged from –27% to –42% for MK-based mixtures, and from –23% to –36% for BFS-based ones.

8. The maintain of bond strength for MK and BFS-based GPs against freezing-and-thawing (F/T) cycles was better than CEM-based mortars. The drop in bond recorded for the cement-based mortars was associated to dissolving of the HEC/EVA polymer films after water immersion for 21 days.

CONFLICT OF INTEREST

The authors declare that there is no conflict of interest regarding the publication of this paper.

AUTHOR BIOS

Joseph Jean Assaad *is a Professor of civil engineering. He received his PhD from the University of Sherbrooke, Sherbrooke, QC, Canada. His research interests include grinding aids for clinker, rheology, admixtures for specialty concrete, formwork pressure, repair, and durability.*

ACI member **Marianne Saba** *is an Assistant Professor of civil engineering at the University of Balamand, Balamand, Lebanon. She received her PhD in chemistry from Lille University, Lille, France. Her research interests include water quality, solid waste treatment, and geopolymers for sustainable development.*

ACKNOWLEDGMENTS

The authors wish to acknowledge the support provided by the laboratory personnel of the Civil and Environmental Engineering Department in the University of Balamand, Al-Koura, Lebanon. The CEM, BFS, and LF were supplied by Cimenterie Nationale, Liban; the MK was supplied by AGS Mineraux, France; and the Na_2SiO_3 was supplied by Sigma-Aldrich.

REFERENCES

1. Assaad, J. J., "Development of Polymer-Modified Cement for Adhesive and Repair Applications," *Construction and Building Materials*, V. 163, 2018, pp. 139-148. doi: 10.1016/j.conbuildmat.2017.12.103

2. Mansur, A. A. P.; Santos, D. B.; and Mansur, H. S., "A Microstructural Approach to Adherence Mechanism of Poly(Vinyl Alcohol) Modified Cement Systems to Ceramic Tiles," *Cement and Concrete Research*, V. 37, No. 2, 2007, pp. 270-282. doi: 10.1016/j.cemconres.2006.11.011

3. Jenni, A.; Holzer, L.; Zurbriggen, R.; and Herwegh, M., "Influence of Polymers on Microstructure and Adhesive Strength of Cementitious Tile Adhesive Mortars," *Cement and Concrete Research*, V. 35, No. 1, 2005, pp. 35-50. doi: 10.1016/j.cemconres.2004.06.039

4. Salman, M. N.; Ma, G.; Ijaz, N.; and Wang, L., "Importance and Potential of Cellulosic Materials and Derivatives in Extrusion-Based 3D Concrete Printing (3DCP): Prospects and Challenges," *Construction and Building Materials*, V. 291, 2021, p. 123281. doi: 10.1016/j.conbuildmat.2021.123281

5. Wan, Q.; Wang, Z.; Huang, T.; and Wang, R., "Water Retention Mechanism of Cellulose Ethers in Calcium Sulfoaluminate Cement-Based Materials," *Construction and Building Materials*, V. 301, 2021, p. 124118. doi: 10.1016/j.conbuildmat.2021.124118

6. Betioli, A. M.; Filho, J. H.; Cincotto, M. A.; Gleize, P. J. P.; and Pileggi, R. G., "Chemical Interaction Between EVA and Portland Cement Hydration at Early-Age," *Construction and Building Materials*, V. 23, No. 11, 2009, pp. 3332-3336. doi: 10.1016/j.conbuildmat.2009.06.033

7. Assaad, J. J., "Feasibility of Specialty Cement Possessing Improved Bond Properties," *Advances in Cement Research*, V. 29, No. 7, 2017, pp. 302-312. doi: 10.1680/jadcr.17.00031

8. Zampini, D.; Shah, S. P.; and Jennings, H. M., "Early Age Microstructure of the Paste–Aggregate Interface and its Evolution," *Journal of Materials Research*, V. 13, No. 7, 1998, pp. 1888-1898. doi: 10.1557/JMR.1998.0268

9. Dimmig-Osburg, A.; Pietsch, I.; and Pietsch, J., "Polymer Additives and Their Influence on the Cement Microstructure in the Early Stages of Hardening," *ZKG International*, V. 59, 2006, pp. 72-83.

10. Su, Z.; Sujata, K.; Bijen, J. M. J. M.; Jennings, H. M.; and Fraaij, A. L. A., "The Evolution of the Microstructure in Styrene Acrylate Polymer Modified Cement Pastes at the Early Stage of Cement Hydration," *Advanced Cement Based Materials*, V. 3, No. 3-4, 1996, pp. 87-93. doi: 10.1016/S1065-7355(96)90041-3

11. Jenni, A.; Zurbriggen, R.; Holzer, L.; and Herwegh, M., "Changes in Microstructures and Physical Properties of Polymer-Modified Mortars During Wet Storage," *Cement and Concrete Research*, V. 36, No. 1, 2006, pp. 79-90. doi: 10.1016/j.cemconres.2005.06.001

12. Jenni, A.; Herwegh, M.; Zurbriggen, R.; Aberle, T.; and Holzer, L., "Quantitative Microstructure Analysis of Polymer-Modified Mortars," *Journal of Microscopy*, V. 212, No. 2, 2003, pp. 186-196. doi: 10.1046/j.1365-2818.2003.01230.x

13. Slowik, V.; Schmidt, M.; and Fritzsch, R., "Capillary Pressure in Fresh Cement-Based Materials and Identification of the Air Entry Value," *Cement and Concrete Composites*, V. 30, No. 7, 2008, pp. 557-565. doi: 10.1016/j.cemconcomp.2008.03.002

14. Petit, J. Y., and Wirquin, E., "Evaluation of Various Cellulose Ethers Performance in Ceramic Tile Adhesive Mortars," *International Journal of Adhesion and Adhesives*, V. 40, 2013, pp. 202-209. doi: 10.1016/j.ijadhadh.2012.09.007

15. EN 12004-1:2017, "Adhesives for Ceramic Tiles – Part 1: Requirements, Assessment and Verification of Constancy of Performance, Classification and Marking," European Committee for Standardization, Brussels, Belgium, 2017.

16. Wetzel, A., "Mechanisms of Shrinkage and Adhesion Failure of Tile Adhesive Mortars," PhD thesis, University of Bern, Bern, Switzerland, 2010.

17. Silva, D. A.; Roman, H. R.; and Gleize, P. J. P., "Evidences of Chemical Interaction between EVA and Hydrating Portland Cement," *Cement and Concrete Research*, V. 32, No. 9, 2002, pp. 1383-1390. doi: 10.1016/S0008-8846(02)00805-0

18. Yiu, C. Y.; Ho, D. C. W.; and Lo, S. M., "Weathering Effects on External Wall Tiling Systems," *Construction and Building Materials*, V. 21, No. 3, 2007, pp. 594-600. doi: 10.1016/j.conbuildmat.2005.11.002

19. Bonapasta, F.; Buda, F.; Colombet, P.; and Guerrini, G., "Cross-Linking of Poly(Vinyl Alcohol) Chains by Ca Ions in Macro-Defect-Free Cements," *Chemistry of Materials*, V. 14, No. 3, 2002, pp. 1016-1022. doi: 10.1021/cm010573q

20. Firdous, R., and Stephan, D., "Natural Pozzolan Based Geopolymers: A Review on Mechanical, Microstructural and Durability Characteristics," *Construction and Building Materials*, V. 190, 2018, pp. 1251-1263. doi: 10.1016/j.conbuildmat.2018.09.191

21. Mustafa Al Bakri, A. M.; Kamarudin, H.; Bnhussain, M.; Rafiza, A. R.; and Zarina, Y., "Effect of Na_2SiO_3/NaOH Ratios and NaOH Molarities on Compressive Strength of Fly-Ash-Based Geopolymer," *ACI Materials Journal*, V. 109, No. 5, Sept.-Oct. 2012, pp. 503-508.

22. Laskar, A. I., and Bhattacharjee, R., "Rheology of Fly-Ash-Based Geopolymer Concrete," *ACI Materials Journal*, V. 108, No. 5, Sept.-Oct. 2011, pp. 536-542. doi: 10.14359/51683263

23. Kong, D. L.; Sanjayan, J. G.; and Sagoe-Crentsil, K., "Comparative Performance of Geopolymers Made with Metakaolin and Fly Ash after Exposure to Elevated Temperatures," *Cement and Concrete Research*, V. 37, No. 12, 2007, pp. 1583-1589. doi: 10.1016/j.cemconres.2007.08.021

24. Mohd Ali, A. Z.; Sanjayan, J.; and Guerrieri, M., "Performance of Geopolymer High Strength Concrete Wall Panels and Cylinders When Exposed to a Hydrocarbon Fire," *Construction and Building Materials*, V. 137, 2017, pp. 195-207. doi: 10.1016/j.conbuildmat.2017.01.099

25. Hwalla, J.; Saba, M.; and Assaad, J. J., "Suitability of Metakaolin-Based Geopolymers for Underwater Applications," *Materials and Structures*, V. 53, No. 119, 2020, pp. 1-14. doi: 10.1617/s11527-020-01546-0

26. Saba, M., and Assaad, J. J., "Effect of Recycled Fine Aggregates on Performance of Geopolymer Masonry Mortars," *Construction and Building Materials*, V. 279, 2021, p. 122461. doi: 10.1016/j.conbuildmat.2021.122461

27. Palomo, A.; Banfill, P. F. G.; Fernández-Jiménez, A.; and Swift, D. S., "Properties of Alkali-Activated Fly Ashes Determined from Rheological Measurements," *Advances in Cement Research*, V. 17, No. 4, 2015, pp. 143-151. doi: 10.1680/adcr.2005.17.4.143

28. Favier, A.; Hot, J.; Habert, G.; Roussel, N.; and de Lacaillerie, J. B. E., "Flow Properties of MK-Based Geopolymer Pastes. A Comparative Study with Standard Portland Cement Pastes," *Soft Matter*, V. 10, No. 8, 2014, pp. 1134-1141. doi: 10.1039/c3sm51889b

29. Palacios, M.; Banfill, P. F. G.; and Puertas, F., "Rheology and Setting of Alkali-Activated Slag Pastes and Mortars: Effect of Organic Admixture," *ACI Materials Journal*, V. 105, No. 2, Mar.-Apr. 2008, pp. 140-148.

30. Rashad, A. M., "A Comprehensive Overview About the Influence of Different Admixtures and Additives on the Properties of Alkali-Activated Fly Ash," *Materials & Design*, V. 53, 2014, pp. 1005-1025. doi: 10.1016/j.matdes.2013.07.074

31. Assaad, J. J., and Saba, M., "Suitability of Metakaolin-Based Geopolymers for Masonry Lastering," *ACI Materials Journal*, V. 117, No. 6, Nov. 2020, pp. 269-279. doi: 10.14359/51725991

32. Alonso, S., and Palomo, A., "Alkaline Activation of Metakaolin and Calcium Hydroxide Mixtures: Influence of Temperature, Activator Concentration and Solids Ratio," *Materials Letters*, V. 47, No. 1-2, 2001, pp. 55-62. doi: 10.1016/S0167-577X(00)00212-3

33. Rovnaník, P., "Effect of Curing Temperature on the Development of Hard Structure of Metakaolin-Based Geopolymer," *Construction and Building Materials*, V. 24, No. 7, 2010, pp. 1176-1183. doi: 10.1016/j.conbuildmat.2009.12.023

34. Lemougna, P. N.; MacKenzie, K. J. D.; and Melo, U. C., "Synthesis and Thermal Properties of Inorganic Polymers (Geopolymers) for Structural and Refractory Applications from Volcanic Ash," *Ceramics International*, V. 37, No. 8, 2011, pp. 3011-3018. doi: 10.1016/j.ceramint.2011.05.002

35. Chen, L.; Wang, Z.; Wang, Y.; and Feng, J., "Preparation and Properties of Alkali Activated Metakaolin-Based Geopolymer," *Materials (Basel)*, V. 9, No. 767, 2016, pp. 1-12. doi: 10.3390/ma9090767

36. Rakhimova, N. R., and Rakhimov, R. Z., "Reaction Products, Structure and Properties of Alkali-Activated Metakaolin Cements Incorporated with Supplementary Materials – A Review," *Journal of Materials Research and Technology*, V. 8, No. 1, 2019, pp. 1522-1531. doi: 10.1016/j.jmrt.2018.07.006

37. Zhang, Y. S.; Sun, W.; and Li, J. Z., "Hydration Process of Interfacial Transition in Potassium Polysialate (K-PSDS) Geopolymer Concrete," *Magazine of Concrete Research*, V. 57, No. 1, 2005, pp. 33-38. doi: 10.1680/macr.2005.57.1.33

38. Lingyu, T.; Dongpo, H.; Jianing, Z.; and Hongguang, W., "Durability of Geopolymers and Geopolymer Concretes: A Review," *Reviews on Advanced Materials Science*, V. 60, No. 1, 2021, pp. 1-14. doi: 10.1515/rams-2021-0002

39. Fernández-Jiménez, A., and Puertas, F., "The Alkali-Silica Reaction in Alkali-Activated Granulated Slag Mortars with Reactive Aggregate," *Cement and Concrete Research*, V. 32, No. 7, 2002, pp. 1019-1024. doi: 10.1016/S0008-8846(01)00745-1

40. Bakharev, T.; Sanjayan, J. G.; and Cheng, Y. B., "Resistance of Alkali-Activated Slag Concrete to Acid Attack," *Cement and Concrete Research*, V. 33, No. 10, 2003, pp. 1607-1611. doi: 10.1016/S0008-8846(03)00125-X

41. Ariffin, M. A. M.; Bhutta, M. A. R.; Hussin, M. W.; Mohd Tahir, M.; and Aziah, N., "Sulfuric Acid Resistance of Blended Ash Geopolymer Concrete," *Construction and Building Materials*, V. 43, 2013, pp. 80-86. doi: 10.1016/j.conbuildmat.2013.01.018

42. ASTM C989/C989M-18, "Standard Specification for Slag Cement for Use in Concrete and Mortars," ASTM International, West Conshohocken, PA, 2018.

43. ASTM C128-15, "Standard Test Method for Relative Density (Specific Gravity) and Absorption of Fine Aggregate," ASTM International, West Conshohocken, PA, 2015.

44. ASTM C117-17, "Standard Test Method for Materials Finer than 75-µm (No. 200) Sieve in Mineral Aggregates by Washing," ASTM International, West Conshohocken, PA, 2017.

45. EN 14411, "Carreaux céramiques - Définitions, classification, caractéristiques, évaluation et vérification de la constance de performance et marquage," European Committee for Standardization, Brussels, Belgium, 2016.

46. El Sakka, F.; Assaad, J. J.; Hamzeh, F.; and Nakhoul, C., "Thixotropy and Interfacial Bond Strengths of Polymer-Modified Printed Mortars," *Materials and Structures*, V. 52, No. 79, 2019, p. 79. doi: 10.1617/s11527-019-1356-7

47. Assaad, J.; Harb, J.; and Maalouf, Y., "Effect of Vane Configuration on Yield Stress Measurements of Cement Pastes," *Journal of Non-Newtonian Fluid Mechanics*, V. 230, 2016, pp. 31-42. doi: 10.1016/j.jnnfm.2016.01.002

48. ASTM C266-99, "Standard Test Method for Time of Setting of Hydraulic-Cement Paste by Gillmore Needles," ASTM International, West Conshohocken, PA, 1999.

49. EN 196-1, "Méthodes d'essais des ciments - Partie 1: détermination des résistances," European Committee for Standardization, Brussels, Belgium, 2016.

50. EN 1348, "Adhesives for Tiles — Determination of Tensile Adhesion Strength for Cementitious Adhesives," European Committee for Standardization, Brussels, Belgium, 2017.

51. Assaad, J. J.; Gerges, N.; Khayat, K. H.; Lattouf, N.; and Mansour, J., "Assessment of Bond Strength of Underwater Polymer-Modified Concrete," *ACI Materials Journal*, V. 116, No. 6, Nov. 2019, pp. 169-178. doi: 10.14359/51716982

52. EN 1346, "Adhesives for Tiles — Determination of Open Time," European Committee for Standardization, Brussels, Belgium, 2017.

53. Liu, J.; Wang, K.; Zhang, Q.; Han, F.; Sha, F.; and Liu, J., "Influence of Superplasticizer Dosage on the Viscosity of Cement Paste with Low Water-Binder Ratio," *Construction and Building Materials*, V. 149, 2017, pp. 359-366. doi: 10.1016/j.conbuildmat.2017.05.145

54. Khayat, K. H., and Assaad, J., "Use of Thixotropy-Enhancing Agent to Reduce Formwork Pressure Exerted by Self-Consolidating Concrete," *ACI Materials Journal*, V. 105, No. 1, Jan.-Feb. 2008, pp. 88-96. doi: 10.14359/19211

55. Djobo, J. N. Y., and Stephan, D., "Understanding the Binder Chemistry, Microstructure, and Physical Properties of Volcanic Ash Phosphate Geopolymer Binder," *Journal of the American Ceramic Society*, V. 105, No. 5, 2022, pp. 3226-3237. doi: 10.1111/jace.18333

56. Heah, C. Y.; Kamarudin, H.; Al Bakri, A. M. M.; Binhussain, M.; Luqman, M.; and Nizar, I. K., "Effect of Curing Profile on Kaolin-Based Geopolymers," *Physics Procedia*, V. 22, 2011, pp. 305-311. doi: 10.1016/j.phpro.2011.11.048

57. Kani, E. N., and Allahverdi, A., "Effects of Curing Time and Temperature on Strength Development of Inorganic Polymeric Binder Based on Natural Pozzolan," *Journal of Materials Science*, V. 44, No. 12, 2009, pp. 3088-3097. doi: 10.1007/s10853-009-3411-1

58. Aygörmez, Y.; Canpolat, O.; Al-Mashhadani, M. M.; and Uysal, M., "Elevated Temperature, Freezing-Thawing and Wetting-Drying Effects on Polypropylene Fiber Reinforced Metakaolin Based Geopolymer Composites," *Construction and Building Materials*, V. 235, 2020, p. 117502. doi: 10.1016/j.conbuildmat.2019.117502

59. Pilehvar, S.; Szczotok, A. M.; Rodriguez, J. F.; Valentini, L.; Lanzon, M.; Pamies, R.; and Kjoniksen, A.-L., "Effect of Freeze-Thaw Cycles on the Mechanical Behavior of Geopolymer Concrete and Portland Cement Concrete Containing Micro-Encapsulated Phase Change Materials," *Construction and Building Materials*, V. 200, 2019, pp. 94-103. doi: 10.1016/j.conbuildmat.2018.12.057

60. Shamsa, M. H.; Al-Shathr, B. S.; and Al-Attar, T. S., "Performance of Geopolymer Concrete Exposed to Freezing and Thawing Cycles," *Engineering and Technology Journal,* V. 37 Part A, No. 3, 2018, pp. 78-84. 10.30684/etj.37.3A.1

61. Assaad, J. J.; Hamzeh, F.; and Hamad, B., "Qualitative Assessment of Interfacial Bonding in 3D Printing Concrete Exposed to Frost Attack," *Case Studies in Construction Materials*, V. 13, 2020, p. e00357. doi: 10.1016/j.cscm.2020.e00357

ACI MATERIALS JOURNAL TECHNICAL PAPER

Title No. 121-M24

Study on Pore Characteristics of Microfoam Concrete Based on Different Mixing Ratios

by C. Jin, N. Jiang, H. Li, C. Liu, A. Cao, J. Wang, and X. Wen

The use of construction waste to prepare recycled micro powder can improve the use of construction waste resources and effectively reduce carbon emissions. In this paper, researchers used waste concrete processing micro powder to prepare foam concrete (FC) and quantitatively characterized the performance and pore structure of FC by scanning electron microscopy (SEM), pore and fissure image recognition and analysis system (PCAS), and mechanical property testing methods with different mixing ratios of micro powder. The results showed that the effect of single mixing of micro powder or fly ash is better than the composite mixing test, and the optimal proportion of compressive strength of single mixing of micro powder is higher than that of single mixing of fly ash. The optimum mixing ratio is 6:4 between cement and micro powder, and the best effect is achieved when the micro powder mixing amount is 40%. Single or double mixing can fill the pores between the foam and strengthen the performance of the substrate. The tests of single-mixed or compound-mixed micro powder showed that the fractal dimension decreased with the increase of porosity; when the fractal dimension of the specimen increased, the average shape factor became smaller, the compressive strength decreased, and the water absorption rate increased.

Keywords: fractal dimension; porosity; recycled micro powder.

INTRODUCTION

Foam concrete (FC) is a porous, ultra-light material made of calcium (cement and lime) and silica materials (quartz sand, granulated blast-furnace slag, fly ash, shale, and so on) mixed with an appropriate amount of aerating agent through batching, mixing, placing, aerating, and maintenance.[1] The density of FC is light, between 400 and 1800 kg/m^3, and has excellent properties such as fireproofing, heat insulation, and sound insulation.[2] In practice, the quality of hardened FC is generally not high and has low strength, water absorption, and shrinkage. The strength of FC is an important indicator that affects its use.[1] The typical strength values for FC with densities between 800 and 1600 kg/m^3 range from 1 to 10 MPa.[3] FC produced within this range should only be used for general purposes such as gap fillers. At a minimum strength of 25 MPa, FC has the potential to be used as a structural material.[4,5]

Huang et al.[6] found that the compressive strength of FC decreases as an exponential function of density. Visagie and Kearsly[7] found that higher density did not affect the cavity distribution, which may be related to a more uniform distribution of cavities at higher densities. Nambiar and Ramamurthy[8] found an inverse relationship between the dry density of FC and its porosity. Pang and Wang,[9] Zhang et al.,[10] and Hilal et al.[11] investigated the effect of density class (600, 1000, and 1400 kg/m^3) on the pore morphology of FC and found that the average equivalent pore size and the shape factor of the FC increased gradually with the decrease of density class. Fang et al.[12] carried out an in-depth investigation on FC, focused on exploring the problems related to compressive strength, and found that adding certain fly ash, which is used to replace some of the cement in it, can weaken its compressive strength. The compressive strength and pore structure parameters were combined, and the relationship was clearly expressed as functional. The specific relationship is expressed as $f_c = f_c'(1 - \Sigma\varepsilon_i^{0.35}\varphi_i)$, which provides many scholars with new ideas and directions about the relationship between the pore structure parameters and mechanical properties of FC.

The research on FC with waste micro powder focuses on controlling material proportions and pore structure, and using waste micro powder to prepare FC can solve environmental pollution and resource consumption problems and promote sustainable development and green building.

RESEARCH SIGNIFICANCE

As society continues to develop, the disposal of waste concrete has become an important environmental issue in China. If waste concrete is landfilled directly without any treatment, not only will it occupy a large amount of land area, but certain components in the waste concrete will make it a potential source of pollution. Therefore, the use of recycled microfoam concrete[13] can effectively deal with the landfill problem of waste concrete and reduce the amount and cost of cement used in FC by replacing some of the cement with micro powder. Moreover, fly ash mixed into concrete plays a role in regulating the distribution of cement particles, making them more uniformly distributed and preventing the cohesion of cement particles.[14] In this paper, different mixing ratios of micro powder and fly ash were used to replace part of the cement to study the performance of FC. It effectively reduces costs by saving natural resources, bringing good economic benefits, and protecting the ecological environment. It is an effective way to recycle waste concrete.

ACI Materials Journal, V. 121, No. 3, May 2024.

MS No. M-2022-380.R7, doi: 10.14359/51740703, received February 13, 2024, and reviewed under Institute publication policies.

EXPERIMENT OVERVIEW

Materials

Test raw materials—In this study, quantitative analysis of cement, fly ash, and micro powder was performed using X-ray fluorescence (XRF), and qualitative analysis was performed using X-ray diffraction (XRD).

Cement—PO 42.5 ordinary silicate cement produced by a plant in Qinghai Province was selected, and its basic properties are shown in Table 1. The cement was analyzed by XRD, and its main mineral composition results are shown in Fig. 1.

Recycled micro powder—Using laboratory waste concrete components, the powder was milled with a ball mill for 45 minutes and then filtered through a 200-mesh sieve; powder with a particle size of less than 0.075 mm was required for this experiment. The recycled micro powder of waste concrete was analyzed using XRD, and the results of its main mineral composition are shown in Table 1 and Fig. 2.

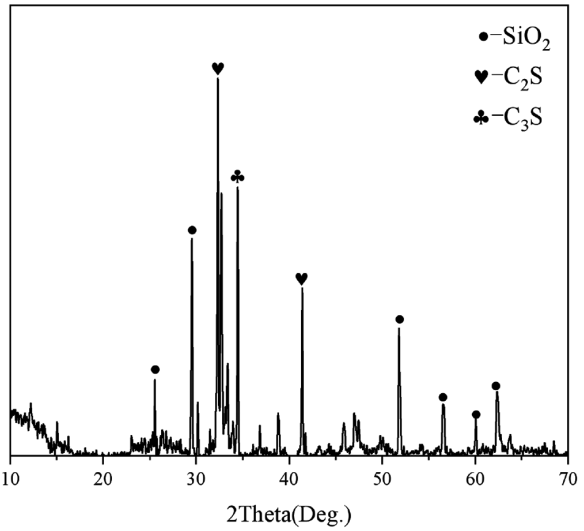

Fig. 1—XRD diagram of cement.

Based on the data in Table 1, it can be seen that recycled micro powder contains a certain amount of SiO_2 and $CaCO_3$, which are also some of the main chemical components of cement and possess a certain degree of activity. Therefore, recycled micro powder has the potential to be used as a mineral mixture to replace part of the cement. By looking at Fig. 2, it can be seen that recycled micro powder is mainly composed of aggregate rock minerals such as quartz, calcite, and dolomite. The particle morphology of the recycled micro powder shows irregular characteristics. Summarizing the information in Table 1 and Fig. 2, it can be concluded that recycled micro powder may have a high potential for application in cement production. Recycled micro powder contains chemical compositions similar to those of cement, and its particle morphology is suitable for use as part of mineral mixtures. Therefore, recycled micro powder can be considered an alternative material to improve resource use and environmental friendliness in cement production.

Fly ash—The composition of the Class F fly ash, selected from a factory in Shandong Province, is shown in Table 1. The microscopic morphology is shown in Fig. 3. According to Fig. 3, most fly ash particles are spherical, and the surface is smooth and dense, outside of which are irregular particles.

Foaming agents—The foaming agent is an important component of FC. Performance testing of foaming agents was performed according to JC/T 2199-2013.[15] The physical properties of the plant protein-type foaming agent are shown in Table 2.

Specimens

Activity test—The activity index is a ratio obtained by comparing the compressive strength of cementitious sands

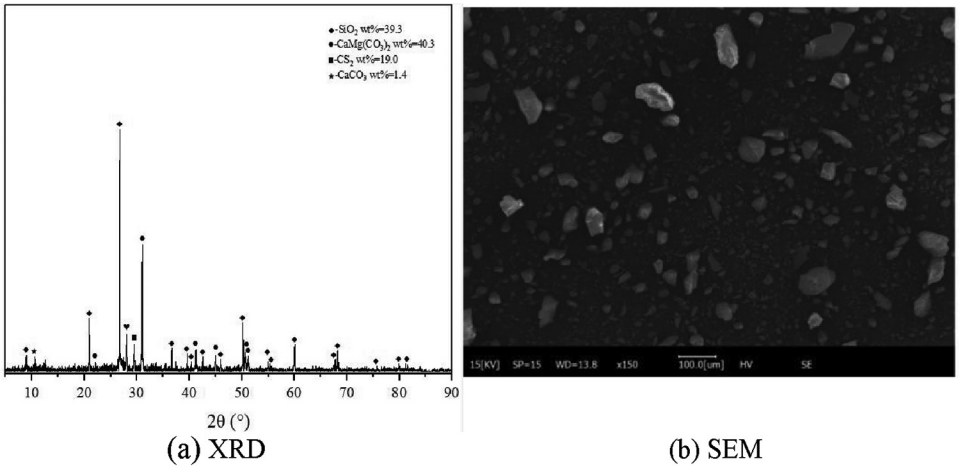

Fig. 2—XRD and SEM images of recyled micro powder.

Table 1—Main chemical composition of cementitious materials (XRF), %

Raw materials	SiO_2	Al_2O_3	Fe_2O_3	CaO	K_2O	SO_3	MgO	Loss
Cement	19.80	7.67	2.66	40.40	0.95	2.31	2.06	24.15
Recycled micro powder	38.9	8.00	4.42	38.20	1.62	1.14	5.89	1.83
Fly ash	53.97	31.15	4.16	4.01	2.04	0.73	1.01	2.93

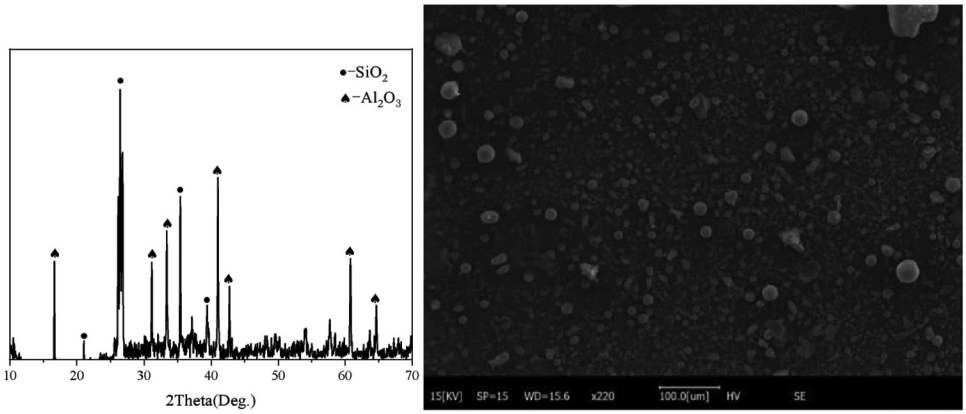

(a) XRD (b) SEM

Fig. 3—XRD and SEM images of fly ash.

Table 2—Physical properties of vegetable protein-based foaming agents

Serial number	Projects	Standard	Results	Judgment
1	Settling distance of a standard bubble column at 1 h/mm	≤5	2	Qualified
2	Leaching volume/mL of a standard bubble column left to stand for 1 hour	≤25	22	Qualified
3	Bubble population density, kg/m^3	48 ~ 52	48	Qualified
4	Foaming times	–15 ~ 30	21	Qualified

Table 3—Cement paste mixing ratios for different admixtures

Serial number	Type	Cement, g	Recycled powder, g	Fly ash, g	Water, g
1	Recycled powder	70	30	0	45
2	Fly ash	70	0	30	45
3	Void	100	0	0	45

mixed with a certain proportion of mineral admixtures with that of cementitious sands of the same age without mineral admixtures. This index can more accurately assess the activity of mineral admixtures in cement concrete and is a simple, easy, and widely used measurement method. This paper proposes the activity index method to conduct a pilot study on recycled micro powder with a substitution ratio of 30% to investigate its activity performance after being used as an admixture. The test is proposed to be conducted according to the requirements of GB/T 17671-2021.[16] The recycled micro powder and fly ash are individually blended, replacing 30% of cement, and their activity indexes are determined at different ages. The specimens used in the test are 100 x 100 x 100 mm cubes. The ratio design is shown in Table 3.

The activity index of each admixture was calculated according to the activity index in Eq. (1), and the results are shown in Table 4.

$$A = R_1/R_2 \times 100 \quad (1)$$

In the formula, A is activity index (%); R_1 is compressive strength of the standard specimen with admixture after a certain age (MPa); and R_2 is compressive strength (MPa) of the blank standard sand mastic specimen at the same age.

According to the test results, the compressive strength of the cement paste mixed with recycled micro powder was 61.0% at 7 days with respect to the compressive strength at 28 days, whereas the compressive strength of the cementitious sand mixed with fly ash was 59.7% at 7 days with respect to the compressive strength at 28 days. In comparison, the compressive strength of cement paste without admixture was 62.1% at 7 days with respect to 28 days. It can be seen that the addition of recycled micro powder and fly ash produced some attenuating effect on the early strength of the cement paste, which is related to the relatively low activity of recycled micro powder and fly ash and the limitation of the rate of their hydration reaction. In addition, using fly ash as a reference, it can be assumed that recycled micro powder is active.

The main components of recycled micro powder are incompletely hydrated cement particles and $Ca(OH)_2$. During the hydration process, they produce calcium carbonate silicate and calcium carbonate aluminate, respectively, which are subsequently further hydrated to produce calcim-silicate-hydrate (C-S-H) gels. Because the regenerated micro powder is obtained by ball-mill grinding, its particle size is small and its specific surface area is large. Therefore, in the early hydration reaction, the reaction rate of regenerated micro powder is faster than that of fly ash. Regenerated micro powder will consume $Ca(OH)_2$ produced by cement hydration faster in the early stage, promote the hydration reaction of cement, and generate more C-S-H gels faster. Therefore, in terms of early activity, recycled micro powder is slightly better than fly ash.

However, in terms of late strength growth, fly ash grows faster than recycled micro powder. This suggests that fly ash has a better volcanic ash effect (that is, secondary hydration) and is superior to recycled micro powder in terms of

Table 4—Activity indexes of each admixture at different ages

Serial number	Type	Dopant, %	Compressive strength, MPa		7-day activity index, %	28-day activity index, %
			7 days	28 days		
1	Recycled powder	30	24.50	40.15	69.41	70.69
2	Fly ash	30	25.65	43.00	72.66	75.70
3	Void	0	35.30	56.80	100.00	100.00

Table 5—Micro powder cement single-mixing test

Group number	Category	Cement, %	Recycled micro powder, %	Water, %	Foam, %
1	C100	100	0	45	3
2	C90R10	90	10	45	3
3	C80R20	80	20	45	3
4	C70R30	70	30	45	3
5	C60R40	60	40	45	3

Table 6—Fly ash cement single-mixing test

Group number	Category	Cement, %	Fly ash, %	Water, %	Foam, %
1	C100	100	0	45	3
6	C90F10	90	10	45	3
7	C80F20	80	20	45	3
8	C70F30	70	30	45	3
9	C60F40	60	40	45	3

Table 7—Fly ash and micro powder cement compound test

Group number	Category	Cement, %	Fly ash, %	Recycled micro powder, %	Water, %	Foam, %
1	C100	100	0	0	45	3
10	C70F10R20	70	10	20	45	3
11	C70F15R15	70	15	15	45	3
12	C70F20R10	70	20	10	45	3
13	C60F10R30	60	10	30	45	3
14	C60F20R20	60	20	20	45	3

late-stage activity. Taken together, the two activities are similar and not significantly different. In addition, the magnitude of activity of recycled micro powder mainly depends on the content of unhydrated cementitious materials.[17]

Dry density—In this study, the dry density of FC was set to 800 kg/m^3. According to Chinese standard JG/T 266-2011,[18] the dry density of Grade A08 FC is between 750 and 850 kg/m^3, and the coefficient of thermal conductivity should be no higher than 0.21 W/(m·K). The specimen used for the test is a cylinder with a diameter of 50 mm and a height of 100 mm.

Water absorption—The water absorption of the FC describes the degree of water absorption.

Water absorption test specimens should be made in accordance with the provisions of Chinese standard JG/T 266-2011. Prior to testing, place three specimens into the electric blast-drying oven. Ensure that the specimens are maintained at a temperature of 60 ± 5°C during the drying process. Following two intervals of 4 hours each, assess the specimens for a difference in mass less than 1 g, indicating the achievement of constant mass. Once the specimens have cooled to room temperature, transfer them to a constant-temperature bath set to 20 ± 5°C. Subsequently, add water to a level equivalent to one-third of the height of the specimens and maintain this condition for 24 hours. Repeat this step twice, increasing the water level to match the height of the specimens on each occasion. Finally, increase the water level to two-thirds of the specimen height and allow for an additional 24 hours. Then, pour water over the specimens to a depth exceeding 30 mm and maintain for a further 24 hours. Remove the specimens from the water and proceed with testing using the immersed specimens.

Remove the specimen from the water, wipe off the surface water with a damp cloth, and immediately weigh the mass of each piece (mg), accurate to 1 g. The specimen used for the test is a cylinder with a diameter of 50 mm and a height of 100 mm.

The rate of water absorption is calculated according to Eq. (2)

$$W_R = (m_g - m_0)/m_0 \quad (2)$$

In the formula, W_R is water absorption (%) calculated to the nearest 0.1; m_0 is the mass of the specimen after drying (g); and m_g is the mass of the specimen after water absorption (g).

The water absorption of the group of specimens is the average value of the water absorption of three specimens and is accurate to 0.1%.

Single-factor tests

Individual test with cement micro powder—In Tables 5 to 7, "C" is cement, "R" is recycled micro powder, and "F" is fly ash. For example, "C90R10" means that the cement and recycled micro powder are 90% and 10% of the total powder, respectively, and the dosing amounts in the experimental ratio are mass dosing.

Table 8—Dry density and water absorption of FC with different mixing ratios

Name	Dry density, kg/m^3	Water absorption, %
C100	762	55.2
C90R10	1002.8	58
C80R20	878	69.5
C70R30	868.8	64.1
C60R40	1096.1	48.4
C90F10	1004.8	38.6
C80F20	983.2	44.4
C70F30	980.1	56.8
C60F40	702.2	62.8
C70F10R20	982	58.1
C70F15R15	828	74.5
C70F20R10	851.5	56.1
C60F10R30	911.6	61.2
C60F20R20	1212.7	37.4

In this group of experiments, the amount of micro powder was used as the variable; all other factors were kept constant, and the specific amount of mixture is shown in Table 5.

Individual test of cement fly ash—In this group of tests, the amount of fly ash was used as the variable, and all other factors were kept constant. The specific amount per mixture is shown in Table 6.

Cement, fly ash, and micro powder compound test

Given a fixed quantity of cement, adjustments are made to the proportions of micro powder and fly ash, while all other variables remain constant. The specific amount of admixture is shown in Table 7.

EXPERIMENTAL RESULTS

Dry density

According to the data in Table 8, the dry density of pure cement FC is 762.00 kg/m^3, which is 4.75% lower than the standard value, and the coefficient of thermal conductivity is lower than 0.21 W/(m·K), which is in line with the permissible error in Chinese standard JGJ/T 341-2014.[19]

Water absorption

According to the data in Table 8, the water absorption of FC at different ratios is much higher than the porosity. The reason is that during the mixing and blending process of foam and slurry, part of the foam undergoes a defoaming phenomenon, leading to more through and non-closed holes in the FC. These pores can improve the water absorption performance of FC. However, when calculating the porosity, it is more important to consider the volume of closed pores and small pores. Therefore, the water absorption of FC is much higher than the porosity.

Table 9—Compressive strength of micro powder cement single-mixing test

Group number	Category	Age			
		3 days, MPa	7 days, MPa	14 days, MPa	28 days, MPa
1	C100	2.096	2.854	3.108	3.121
2	C90R10	1.609	2.512	2.880	3.336
3	C80R20	2.518	2.931	3.978	4.366
4	C70R30	2.194	4.348	5.068	5.580
5	C60R40	3.418	5.396	5.970	6.721

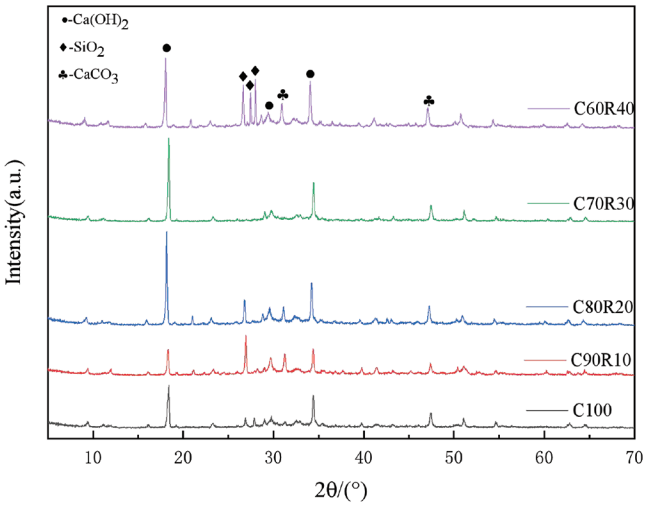

Fig. 4—XRD pattern of micro powder cement at 28 days.

Compressive strength of single-admixture test with cement micro powder

According to Table 9 and Fig. 4, the compressive strength of recycled micro powder FC increases with age. At the 28th day, hydration was basically completed. The compressive strength peaked at 6.721 MPa when the micro powder admixture was 40%, which was 2.15 times higher than the compressive strength of pure cement FC.

XRD composition analysis of recycled micro powder FC with different mixing ratios reveals that when the micro powder content is increased to 10%, its $Ca(OH)_2$ content is significantly higher than that of pure cement FC. When the micro powder content reaches 30%, the $Ca(OH)_2$ content reaches the maximum value and gradually decreases. This is because the recycled micro powder and hydration products have a volcanic ash reaction to produce C-S-H gel, and the recycled micro powder replaces part of the cement, which reduces the original hydration product $Ca(OH)_2$. In addition, the content of SiO_2 and $CaCO_3$ increases with the increase of micro powder mixing amount. When the dosage of micro powder reaches 40%, the content of SiO_2 and $CaCO_3$ reaches the maximum value; SiO_2 can significantly improve the compressive properties of concrete, while $CaCO_3$ can play a good filling role in concrete.

The porosity of recycled micro powder FC increases gradually with the gradual increase of micro powder admixture. However, in the laboratory, micro powder was tested at a 50% dosage, and the results dropped so much that subsequent tests

Table 10—Compressive strength of fly ash cement single-mixing tests

Group number	Category	Age			
		3 days, MPa	7 days, MPa	14 days, MPa	28 days, MPa
1	C100	2.096	2.854	3.108	3.121
6	C90F10	1.814	2.888	4.262	4.785
7	C80F20	2.015	2.133	3.722	4.447
8	C70F30	1.489	1.921	2.841	4.166
9	C60F40	1.353	1.683	2.639	3.649

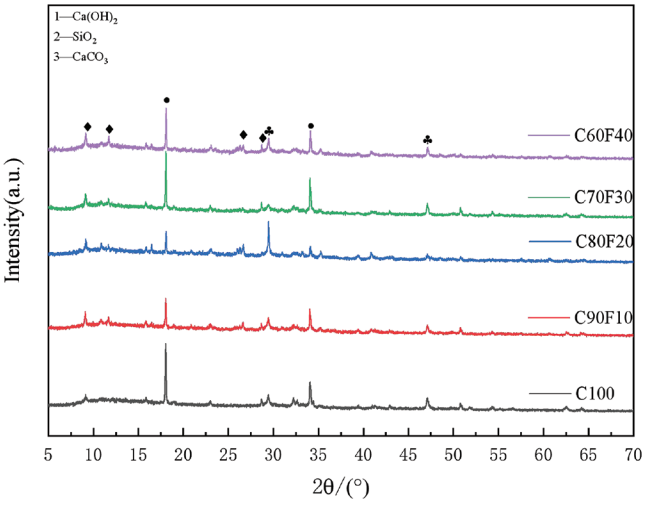

Fig. 5—XRD pattern of fly ash cement at 28 days.

could not be carried out, so micronutrient dosages between 40 and 50% are optimal. Therefore, moderate addition of micro powder helps reduce FC's porosity and improve its compressive strength.

Compressive strength of single-admixture test of fly ash cement

According to Table 10 and Fig. 5, at the 28th day, the compressive strength of the FC decreased continuously with the increase of fly ash content, but it was still higher than that of pure cement FC. This is because some of the fly ash particles are larger than the pores of the FC and cannot fill them well; at the same time, the fly ash fails to fill the connecting holes and large pores in the FC, resulting in smaller defects. Therefore, the increase of fly ash decreases the compressive strength.

According to the XRD composition analysis of the fly ash FC, when the fly ash content is 10%, the content of $Ca(OH)_2$ is the highest, but the content of SiO_2 and $CaCO_3$ is the lowest; when the fly ash content is 30%, the content of $Ca(OH)_2$ is the lowest, and the content of SiO_2 and $CaCO_3$ is the highest. This is because the SiO_2 in fly ash and the hydration product $Ca(OH)_2$ undergo volcanic ash reaction to form a C-S-H gel, which reduces the content of $Ca(OH)_2$. The unreacted portion of SiO_2 significantly improves the compressive properties of the FC, while $CaCO_3$ effectively fills the pores in the FC.

Table 11—Compressive strength of fly ash and micro powder cement compound tests

Group number	Category	Age			
		3 days, MPa	7 days, MPa	14 days, MPa	28 days, MPa
10	C70F10R20	1.086	1.526	1.923	2.885
11	C70F15R15	0.7718	1.406	1.786	2.597
12	C70F20R10	0.9022	1.538	1.693	2.050
13	C60F10R30	0.5967	1.122	1.519	2.123
14	C60F20R20	0.5283	0.8055	1.058	1.630

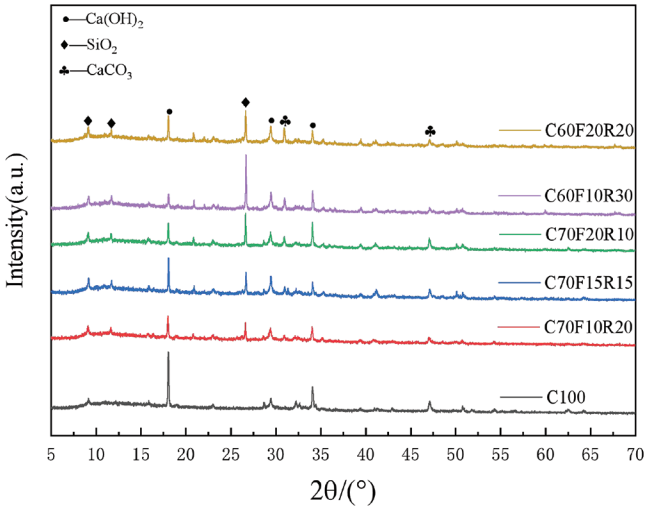

Fig. 6—XRD pattern of fly ash and micro powder cement at 28 days.

It was shown that the porosity of fly ash FC increased with the increase of fly ash admixture. The porosity reached a maximum value of 30.89% when the fly ash admixture reached 40%. However, the porosity is still 11.5% lower than pure cement FC. Therefore, the admixture of fly ash can fill the pores in pure cement FC and solve the problem of high porosity of FC, thus improving its compressive strength.

Although the strength of FC with 30% fly ash admixture was lower than that of specimens with 10% fly ash admixture, the optimum ratio of fly ash alone was 7:3, taking into account the hydration products.

Compressive strength of cement, fly ash, and micro powder compound test

According to the data in Table 11 and Fig. 6, the compressive strength of C70F10R20 was 11.1% higher than that of C70F15R15 and 40.7% higher than that of C70F20R10 with a controlled cement dosage of 70%. In addition, the contents of SiO_2 and $CaCO_3$ reached the highest in C70F20R10, and $Ca(OH)_2$ did in C70F15R15. Therefore, at a controlled cement dosage of 70%, the best results were obtained with 15% micro powder and 15% fly ash.

In addition, the SiO_2 and $CaCO_3$ contents of C60F10R30 were significantly higher than that of C60F20R20 at a controlled cement admixture of 60%, and the compressive strength values of C60F10R30 were greater than that

of C60F20R20, which confirms that the SiO_2 and $CaCO_3$ contents help to improve the compressive strength of concrete.

At different composite mixing ratios, cement, fly ash, and micro powder ratios from 7:1:2 to 6:2:2, the porosity of the FC increased gradually with the increase in fly ash. The porosity reached a maximum value of 22.15% when the ratio of cement, fly ash, and micro powder was 7:2:1.

Therefore, the optimum mixing ratio of cement and micro powder is 6:4 when micro powder is mixed alone; the optimum mixing ratio of cement and fly ash is 7:3 when fly ash is mixed alone; and the optimum mixing ratio of cement, micro powder, and fly ash is 7:1.5:1.5 when micro powder and fly ash are mixed.

To summarize, the effect of a single mixing of micro powder or fly ash was significantly better than the results of the composite mixing test, and the optimum ratio compressive strength of a single mixing of micro powder was higher than that of a single mixing of fly ash. Therefore, the authors chose the optimum mixing ratio of 6:4 for the tested cement and micro powder, and the best results were obtained when the micro powder mixing amount was 40%.

MICROSCOPIC ANALYSIS OF FC WITH DIFFERENT RATIOS

FC, with its complex internal structure and uneven distribution of pores with different sizes and shapes, needs to be analyzed from the macro- to microlevel, which helps to improve the design and application of FC and to understand the interactions of different components in FC and their effects on the material properties. Fractal geometry is an effective tool for explaining irregularities and disorder in nature, and its fractal dimension can quantitatively describe the complexity of the spatial distribution of pores in a material. The complexity of pore distribution is related to its fractal dimension; the larger the fractal dimension is, the more complex the spatial distribution is, and the stronger the ability of micropores to occupy the space.[20]

The scanning electron microscope (SEM) images were analyzed using the pore and fissure image recognition and analysis system (PCAS). The images were parameterized based on binarization, with the pore throat set to 2 pixels and the minimum pore set to 50 pixels, resulting in the final images. The final images are shown in Fig. 7 to 20 for the imaging of FC with different proportions, where Fig. (a) is the original image of the SEM of the FC, and Fig. (b) is the image after binarization by the PCAS software. Figure (c) is the imaging result, where the different colors were used to distinguish the different pore sizes. (Note: A full-color PDF of this paper can be found at www.concrete.org.)

Based on the PCAS images for pore analysis, the relevant parameters for different samples are shown in Table 12. The shape factor (F_s) reflects the roughness of the pore edges,

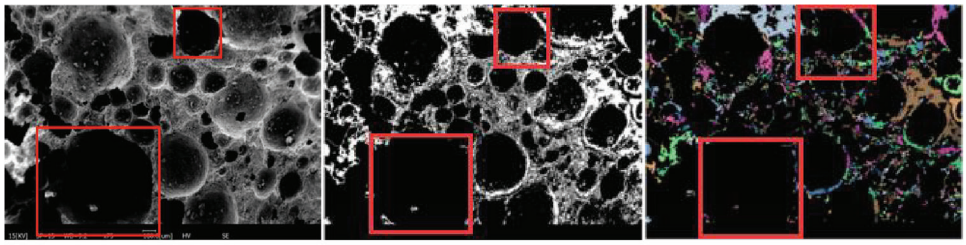

Fig. 7—Raw SEM and PCAS processed images of C100.

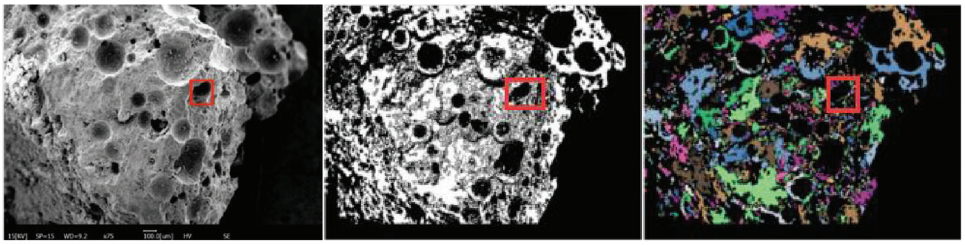

Fig. 8—Raw SEM and PCAS processed images of C90R10.

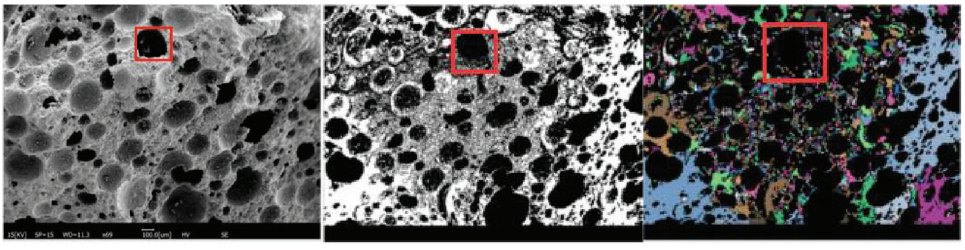

Fig. 9—Raw SEM and PCAS processed images of C80R20.

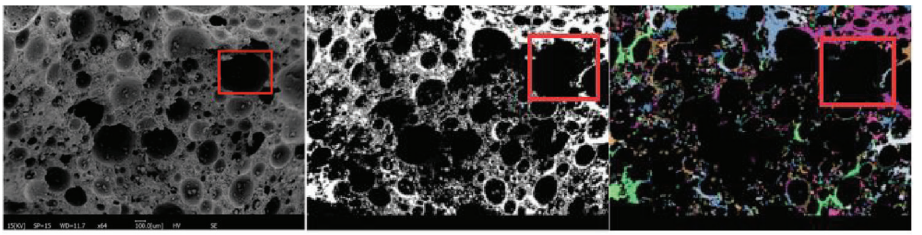

Fig. 10—Raw SEM and PCAS processed images of C70R30.

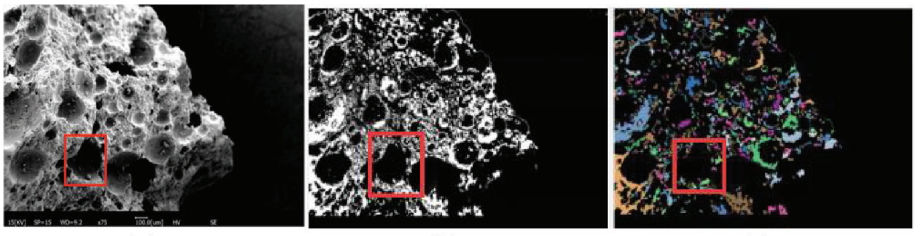

Fig. 11—Raw SEM and PCAS processed images of C60R40.

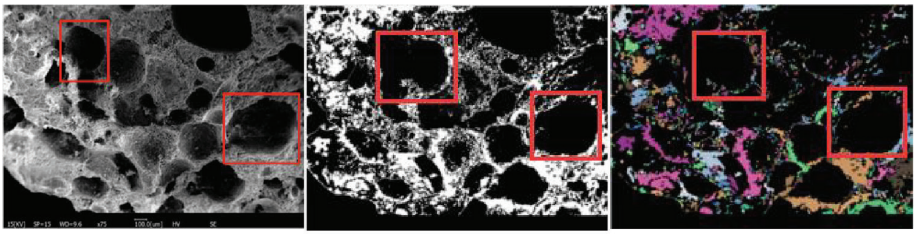

Fig. 12—Raw SEM and PCAS processed images of C90F10.

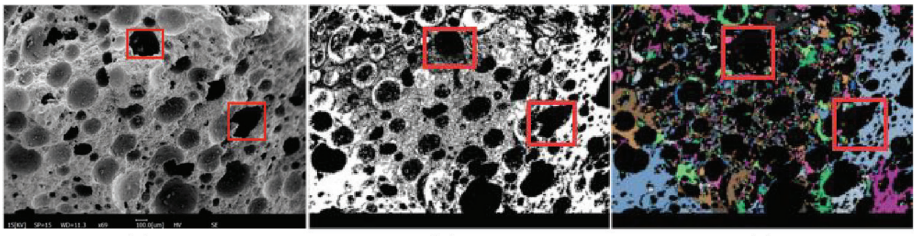

Fig. 13—Raw SEM and PCAS processed images of C80F20.

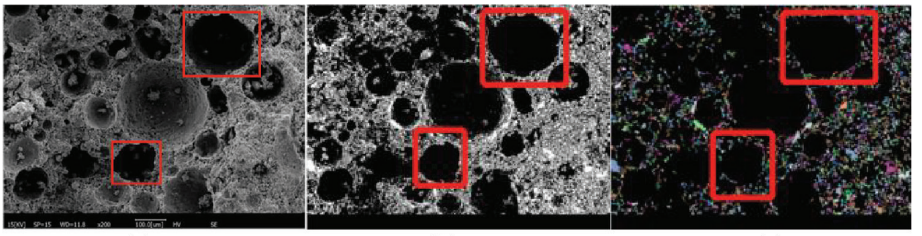

Fig. 14—Raw SEM and PCAS processed images of C70F30.

with a maximum value of 1. The smaller the value of the shape factor is, the rougher the pore edges are, and the corresponding structure is more complex. The probability entropy (H) is used to quantify the directionality of the pore space, and the value of probability entropy ranges from 0 to 1. The larger the value is, the more undirected the pore space development is. The fractal dimension (D_f) is used to characterize the degree of parameter variation within a certain range—that is, the non-homogeneity of the data.[21]

The results showed that the porosity of FC was influenced by the micro powder and fly ash admixture. When micro powder was added alone, the porosity of FC gradually became larger

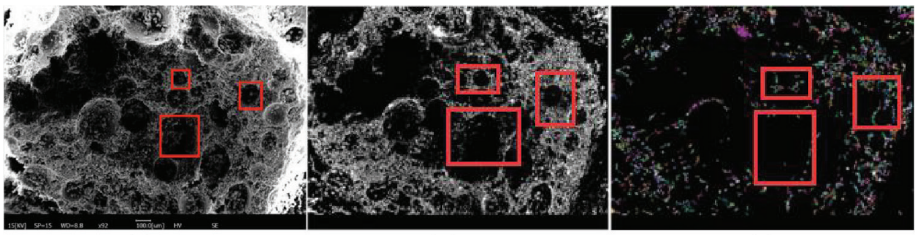

Fig. 15—Raw SEM and PCAS processed images of C60F40.

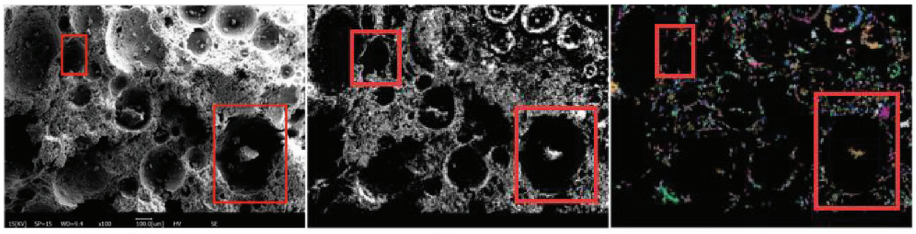

Fig. 16—Raw SEM and PCAS processed images of C70F10R20.

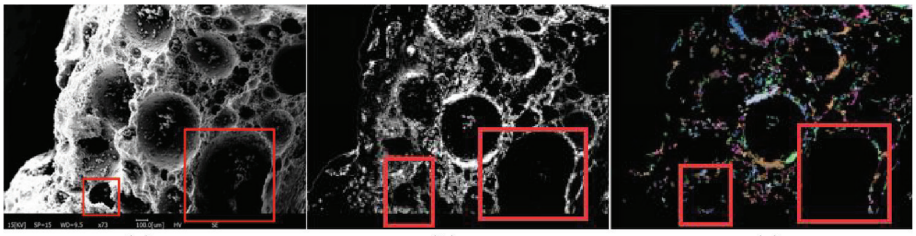

Fig. 17—Raw SEM and PCAS processed images of C70F15R15.

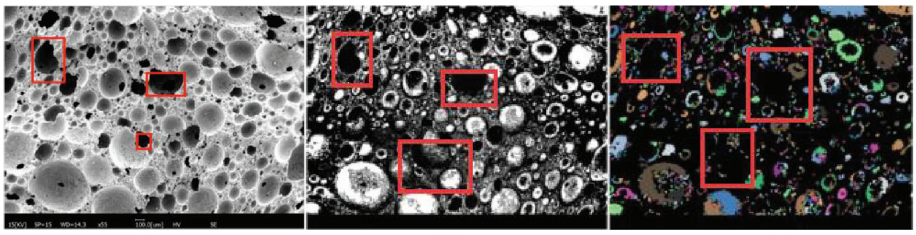

Fig. 18—Raw SEM and PCAS processed images of C70F20R10.

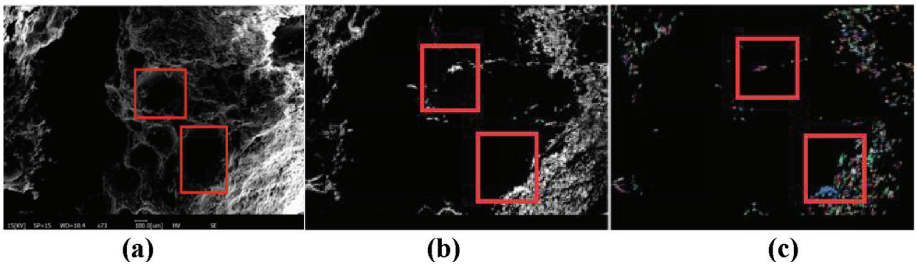

Fig. 19—Raw SEM images and PCAS processed images of C60F10R30.

and less connected with the increase of micro powder content. When the micro powder content reached 40%, the porosity of FC reached the highest value. A similar effect was produced by fly ash, where the lower the fly ash admixture resulted in smaller pores at a fixed cement dosage. The composite use of fly ash and micro powder can make the overall structure more stable, as shown in Table 12. The analysis results show that in the preparation of FC, attention should be paid to the selection of materials and mixing ratios to obtain the ideal pore structure and, in turn, achieve better performance indexes.

According to Table 12, in the case of a single admixture of micro powder, as the proportion of micro powder gradually

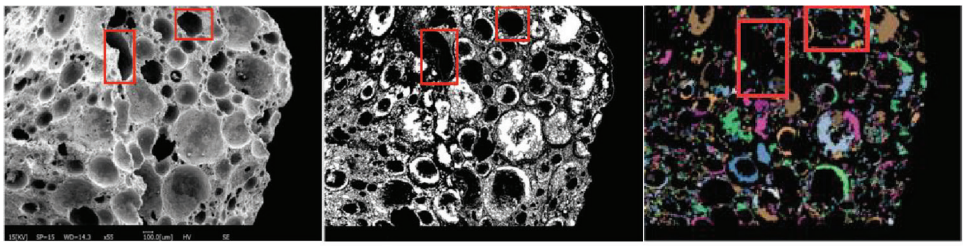

Fig. 20—Raw SEM images and PCAS processed images of C60F20R20.

Table 12—Basic information for testing FC at different blending ratios

Name	Number of individual pores	Average area/pixel, mm^2	Average circumference/pixel, mm	Probabilistic entropy (J/K)	Average shape factor F_s	Fractal dimension D_f	Porosity, %
C100	1414	303.41	86.32	0.9874	0.3617	1.2502	34.91
C90R10	1106	332.07	92.77	0.9904	0.4099	1.2753	29.89
C80R20	1031	238.42	82.57	0.9847	0.3797	1.2835	20
C70R30	956	219.97	82.68	0.9945	0.3641	1.2554	17.11
C60R40	764	246.42	85.21	0.993	0.4035	1.2703	15.32
C90F10	846	329.25	91.2	0.9811	0.4117	1.2608	8.75
C80F20	1031	238.42	82.57	0.9847	0.3797	1.2835	17.1
C70F30	1964	105.9	64.99	0.9919	0.342	1.3583	22.67
C60F40	1037	103.73	75.33	0.9926	0.2786	1.648	30.89
C70F10R20	476	106.66	68.18	0.9538	0.3269	1.4521	9.03
C70F15R15	798	139.81	73.96	0.9854	0.3438	1.3417	9.08
C70F20R10	1306	199.69	82.16	0.9904	0.3341	1.2263	21.22
C60F10R30	994	117.66	73.32	0.9935	0.3016	1.3438	9.52
C60F20R20	1172	232.2	82.9	0.9917	0.3562	1.171	22.15

becomes larger before reaching the saturation state of micro powder, the porosity of the concrete prepared after addition also gradually increases when the content of micro powder reaches 10%. The porosity at this time reaches a peak of 29.89%; after that, with the increase of micro powder content, the porosity of the specimens continuously decreases, and when the content of micro powder is 40%, the porosity of the FC reaches its lowest, which is 15.32%. Therefore, the appropriate amount of added micro powder can reduce the porosity of FC. The same applies to the analysis of the situation when fly ash is added alone. It can be found that, similar to the situation when micro powder is added alone, the porosity is 34.91% when no fly ash is added. As the fly ash content rises, the number of pores in the prepared FC also increases, so the porosity rises. When the content of fly ash reaches 40%, it reaches the peak of porosity of 30.89%, while the porosity is only 8.75% when adding fly ash with 10% admixture. It can be seen that the effect of filling pores with fly ash is not as ideal as micro powder.

Under the compound condition, the porosity of the FC gradually increased when the cement, fly ash, and micro powder were paired from 7:1:2 to 7:2:1. When the fly ash content accounted for 20% and micro powder accounted for 10%, the porosity reached a maximum of 22.15%, and when the cement content was further reduced, the rise in fly ash content caused the porosity to drop steeply from the original peak point to 9.52%.

In summary, the greater the porosity of FC, the lower the compressive strength.

According to Table 12, the fractal dimension is not only related to the average shape factor but also has a certain functional relationship with the compressive strength and water absorption rate. Whether single or compound, the larger the fractal dimension index of the specimen, the smaller the average shape factor and the lower the compressive strength. On the contrary, when the water absorption of the specimen is higher, the corresponding fractal dimension index will increase accordingly. Besides, using pure cement as the control standard, it was found that the porosity of the prepared FC decreased from 29.89 to 20% when the amount of micro powder was mixed from 10 to 20%—that is, the porosity was relatively reduced when the micro powder content increased. At this time, both fractal size and porosity showed a corresponding relationship: when the porosity increased, the fractal size relatively decreased, and vice versa—when the porosity increased, the fractal size decreased. When fly ash was added as admixture alone, the situation was almost the same as that of micro fine single admixture. With the increase of fly ash content, the porosity gradually increases; when the fractal size shows a relative decrease, the fractal size and porosity maintain a

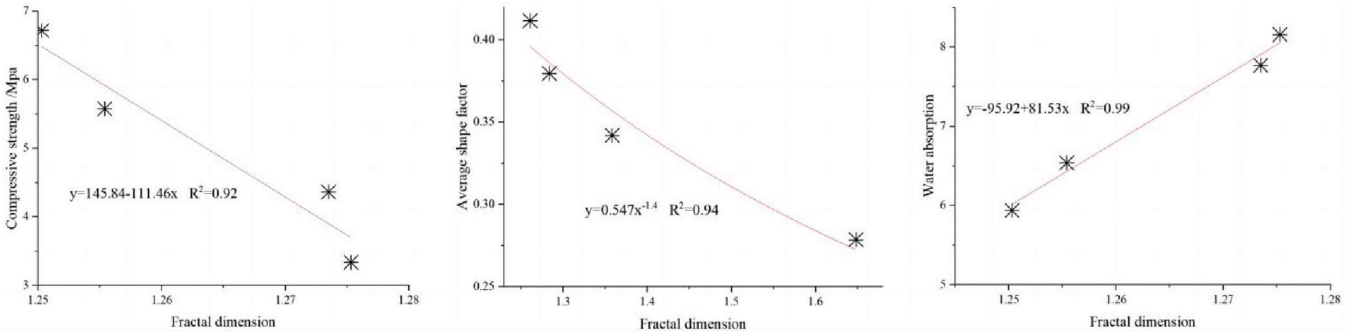

Fig. 21—Relationship between fractal dimension and compressive strength and durability index (as example of single-mixed micro powder).

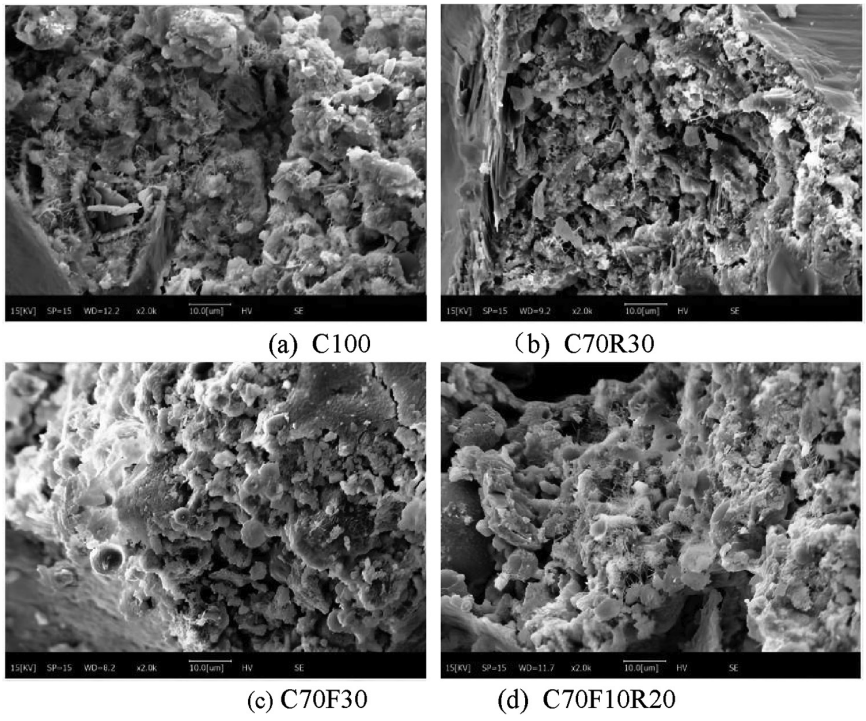

Fig. 22—Microscopic morphology of FC.

complementary relationship: the porosity decreases, then the fractal size increases.

When micro powder is compounded with concrete at the same time, no matter if the cement content is 60 or 70%, under the same cement mixture, the change of fly ash and micro powder content ratio does not affect the change law of fractal size and porosity: if the fractal size decreases, then porosity increases; if the fractal size increases, then porosity decreases.

In summary, in the process of preparing FC, when the pore range is certain, the fractal size decreases with the increase of porosity; and when the pore is certain, the fractal size determines the pore range: a small fractal size means the pore distribution range is narrow, and the pores are more concentrated, which is almost consistent with the results of Wei et al. [22] on fractal size.

In the case of a single mixture of micro powder, the fitted curve of fractal dimension as a function of compressive strength, water absorption, porosity, and average shape factor is shown in Fig. 21.

Combining the microscopic scan analysis with the previous study, Fig. 22 shows the microscopic morphology of the monomeric and complex blends of micro powder and fly ash, respectively, with 70% cement as the reference. It can be seen that the pure cement specimens mainly produce hydration products such as hexagonal lamellar, fibrous C-S-H gels, and needle-like calcium vanadium. These hydration products lap each other and form a stable microstructure. In contrast, in the specimens mixed with 30% recycled micro powder and fly ash, and 15% micro powder mixing 15% fly ash, the filling effect of micro powder and fly ash help to improve the performance of the cementitious material. Some of the micro powder also has the effect of supplementing the inter-foam voids, but due to the reduction of cement dosage in the composite cementitious system, it can be seen from the SEM images that the microstructure becomes loosened with the increase of fly ash. In the pure cement state, the pore number and pore size of the sample are large, while the pore size is in the normal range. Meanwhile, the porosity and compressive strength of the sample were maintained at

the average level. As the micro powder increases to 30%, the corresponding porosity decreases, leading to a denser FC and an increase in compressive strength. Similarly, when the fly ash content reaches 30%, the number of pores surpasses that of the 10% fly ash FC mixture, resulting in a 0.5% increase in porosity and a corresponding decrease in compressive strength. However, compared to the pure cement state, the concrete's compressive strength still demonstrates improvement. When micro powder and fly ash are combined in a 1:1 ratio, the pores become larger, leading to a decrease in compressive strength throughout the process compared to the pure cement state.

CONCLUSIONS

During the preparation of foam concrete (FC), attention should be paid to the selection of materials and mixing ratios to obtain an ideal pore structure and, consequently, better performance indexes.

The test results show that:

1. The single addition of micro powder and fly ash are significantly better than the results of the compound addition. The compressive strength value of the best ratio of the single addition of micro powder is higher than the best ratio of the single addition of fly ash. Therefore, the best results are achieved when the amount of micro powder is between 40 and 50%.

2. It can be found that the fractal dimension decreases with the increase of porosity through the tests of single- or compound-mixed micro powder. Meanwhile, when the fractal dimension of the specimen increases, the average shape factor becomes smaller and the compressive strength decreases, while the water absorption increases accordingly.

AUTHOR BIOS

Changhui Jin *is a Master's Student in the School of Civil Engineering, Qinghai University, Qinghai, China. Her research interests include new construction materials.*

Ningshan Jiang *is an Associate Professor at Qinghai University, where he received his BS, MS, and PhD. His research interests include construction materials and permafrost engineering.*

Hui Li *is a Professor-Level Senior Engineer at Qinghai University. He received his MS from Hubei University of Technology, Wuhan, China, and his PhD from China University of Geosciences, Wuhan, China. His research interests include geotechnical engineering disaster prevention and mitigation and protection.*

Chengkui Liu *works at the Qinghai Research Institute of Building Materials Science. He received his master's degree from Qinghai University. His research interests include the durability of building materials.*

Aoxiang Cao *is an Undergraduate Student in the School of Civil Engineering at Qinghai University. His research interests include new construction materials.*

Jianing Wang *is a Master's Student in the School of Civil Engineering at Qinghai University. His research interests include new construction materials.*

Xiaochu Wen *is an Undergraduate Student in the School of Civil Engineering at Qinghai University. His research interests include new construction materials.*

ACKNOWLEDGMENTS

Financial support from the Qinghai Building and Materials Research Co., Ltd., and the Key Lab of Plateau Building and Eco-community in Qinghai, China, is gratefully acknowledged. The authors also wish to thank N. Jiang for fruitful discussions.

REFERENCES

1. Tingting, X.; Ningshan, J.; Lianxin, L.; Lin, G.; and Peng, W., "Study on the Effect of External Additives on the Strength and Dry Density of Foam Concrete," *Journal of Qinghai University*, V. 31, No. 6, 2013, pp. 19-23.

2. Othuman Mydin, M. A., and Wang, Y. C., "Structural Performance of Lightweight Steel-Foamed Concrete-Steel Composite Walling System under Compression," *Thin Wall Structures*, V. 49, No. 1, 2011, pp. 66-76. doi: 10.1016/j.tws.2010.08.007

3. British Cement Association, "Foam Concrete – Composition and Properties," Camberley, UK, 1994, 4 pp.

4. Dransfield, J. M., "Foam Concrete: Properties, Applications and Potential," *Foam Concrete: An Introduction to the Product and Its Properties, One Day Awareness Seminar*, University of Dundee, Dundee, UK, 2000, pp. 1-11.

5. Jones, M. R., and McCarthy, A., "Preliminary Views on the Potential of Foamed Concrete as a Structural Material," *Magazine of Concrete Research*, V. 57, No. 1, 2005, pp. 21-31. doi: 10.1680/macr.2005.57.1.21

6. Huang, H.; Gong, N.; Mu, C.; Zhou, H.; and Liu, W., "Dynamic Mechanical Properties and Constitutive Relationship of Foam Concrete," *Jianzhu Cailiao Xuebao*, V. 23, No. 2, 2020, pp. 466-472. (in Chinese)

7. Visagie, M., and Kearsly, E. P., "Properties of Foamed Concrete as Influenced by Air-Void Parameters," *Concrete Beton*, V. 101, 2002, pp. 8-14.

8. Nambiar, E. K. K., and Ramamurthy, K., "Air-Void Characterisation of Foam Concrete," *Cement and Concrete Research*, V. 37, No. 2, 2007, pp. 221-230. doi: 10.1016/j.cemconres.2006.10.009

9. Pang, C. M., and Wang, S., "Void Characterization and Effect on Properties of Foam Concrete," *Journal of Building Materials*, V. 20, No. 1, 2017, pp. 93-98. (in Chinese)

10. Zhang, X.; Wang, W.; Yang, D.; and Zhang, L., "Characteristic on Pore Structure of Foamed Concrete and Study Development of its Effecting Factors," *China Concrete and Cement Products*, No. 7, 2018, pp. 63-68. (in Chinese)

11. Hilal, A. A.; Thom, N. H.; and Dawson, A. R., "On Entrained Pore Size Distribution of Foamed Concrete," *Construction and Building Materials*, V. 75, 2015, pp. 227-233. doi: 10.1016/j.conbuildmat.2014.09.117

12. Fang, Y.; Wang, R.; Pang, E.; and Yue, Z., "Relationship Between Compressive Strength and Pore Structure of Cement-Fly Ash Foam Concrete," *Journal of Silicates*, V. 38, No. 4, 2010, pp. 621-626. (in Chinese)

13. Liu, M., "Research on the Performance of Recycled Powder Foam Concrete," dissertation, Yangzhou University, Yangzhou, China, 2021. (in Chinese)

14. Nan, H., "Application of Fly Ash Concrete and its Long-Term Significance," *Building Materials Technology and Application*, No. 4, 2010, pp. 23-24. (in Chinese)

15. JC/T 2199-2013, "Foam Agent for Foam Concrete," Standardization Administration of China, Beijing, China, 2013. (in Chinese)

16. GB/T 17671-2021, "Test Method for Strength of Cementitious Sand (ISO Method)," Standardization Administration of China, Beijing, China, 2021. (in Chinese)

17. Zhang, J., "Research on the Preparation and Performance of Recycled Micronized Foam Concrete," Qinghai University, Qinghai, China, 2020. (in Chinese)

18. JG/T 266-2011, "Foam Concrete," Standardization Administration of China, Beijing, China, 2011. (in Chinese)

19. JGJ/T 341-2014, "Technical Specification for Application of Foam Concrete," Standardization Administration of China, Beijing, China, 2014. (in Chinese)

20. Wang, Q., "Fractal Theory and its Application in Hydrology," *Shanxi Water Resources Science and Technology*, No. 3, 2003, pp. 21-23. (in Chinese)

21. Liu, P.; Liu, W.; and Xu, H., "Quantitative Evaluation of Dolomite Dissolution Pore Structure Based on SEM and PCAS," *Geological Hazards and Environmental Protection*, V. 34, No. 1, 2023, pp. 59-63. (in Chinese)

22. Wei, J.; Yu, Q.; Zeng, X.; and Bai, R., "Study on the Fractal Dimension of Pore Structure in Concrete," *Journal of South China University of Technology*, No. 2, 2007, pp. 121-124.

ACI MATERIALS JOURNAL TECHNICAL PAPER

Title No. 121-M25

Multi-Approaches to Improve Internally Cured Concrete for Rigid Pavement Application

by Sangyoung Han, Thanachart Subgranon, Hung-Wen Chung, Kukjoo Kim, and Mang Tia

A comprehensive laboratory testing program, field-testing program, numerical analysis, and life-cycle cost analysis were conducted to evaluate the beneficial effects of incorporating shrinkage-reducing admixture (SRA), polymeric microfibers (PMFs), and optimized aggregate gradation (OAG) into internally cured concrete (ICC) mixtures for rigid pavement applications. Results from the laboratory program indicate that all the ICC mixtures outperformed the standard concrete (SC) mixture. All the ICC mixtures showed a decrease in drying shrinkage compared to the SC mixture. Based on the laboratory program, three ICC mixtures and one SC mixture were selected for the full-scale test and subjected to a heavy vehicle simulator for accelerated fatigue testing. Extensive testing and analysis have shown that ICC mixtures incorporating SRA, PMFs, and OAG can be beneficially used in pavement applications to achieve increased pavement life.

Keywords: critical stress analysis; full-scale test slabs; internally cured concrete (ICC); optimized aggregate gradation (OAG); polymeric microfibers (PMFs); shrinkage-reducing admixture (SRA).

INTRODUCTION

High-strength concrete (HSC) and high-performance concrete (HPC) mixtures have gained popularity in recent years because of their potential long-term benefits in performance.[1] However, these types of concrete generally exhibit a substantial magnitude of autogenous shrinkage due to the lower water-cement ratio (*w*/*c*) and finer pore constitutions.[2,3] Additionally, for these modern concrete mixtures, the blended cement matrix incorporating fly ash, slag, and silica fume has been preferred over pure portland cement owing to their various benefits, such as improved integrity, enhanced sustainability, and reduced cost. Nevertheless, blended cementitious materials require additional curing water because the shrinkage accompanying the pozzolanic and hydraulic reactions of these cement replacements is substantial when compared with that of pure portland cement.[4,5] Given the characteristics of modern concrete mixtures, using modern concrete with insufficient hydrating water increases the potential risk of shrinkage cracking at an early age, which can cause structural deficiencies and instability.

In coping with the shrinkage cracking of modern concrete at early ages, the internal curing (IC) technique has been successfully introduced by the concept that water can be embedded in the concrete through water-filled components such as expanded lightweight aggregate (LWA), superabsorbent polymers, and cellulose fibers.[6,7] In particular, the use of saturated LWA as water-filled inclusion has been widely used in North America. LWA is a highly porous material that can be used as a replacement for natural coarse and/or fine aggregate.[8] When saturated, each LWA particle acts like a small reservoir inside the concrete, which will release water to the surrounding cement paste during its hydration stage. This mechanism helps to prevent the self-desiccation phenomenon and promote the hydration of the cement, thereby alleviating the degree of autogenous cracking.[9-12] Additionally, using LWA offers other improved properties, including increased workability,[13] higher ultimate strength,[14] reduced likelihood of thermal cracking,[15] improved freezing-and-thawing resistance,[16] and improved transport properties, such as reduced permeability, ion diffusion, and sorption.[14]

In addition to the aforementioned benefits in the aspects of plastic, hardened, and durable properties, using internally cured concrete (ICC) in the rigid pavement structure significantly helps reduce the moisture-related curling/wrapping magnitude and drying shrinkage, which decrease pavement serviceability.[17,18] High levels of curling deformations in pavements have been correlated to issues of rideability,[19] cracking,[20] and durability.[21] As a result, numerous studies have documented the widespread use of ICC in various types of pavements for mitigating the issues of curling/wrapping and drying shrinkage.[22]

The majority of the literature has focused on the beneficial effects of ICC on pavement structure, particularly in reducing curling magnitudes and drying shrinkage. However, these studies have been limited to identifying the effect of only one method of IC inclusion in the concrete mixture. In contrast, the current study considered both IC inclusion and design-enhanced techniques that are expected to maximize the benefits of the ICC mixture (referred to as the hybrid ICC mixture hereafter). The ICC mixtures were evaluated by incorporating the enhanced techniques, including a shrinkage-reducing admixture (SRA), polymeric microfibers (PMFs), and optimized aggregate gradation (OAG), and were compared to a concrete mixture without ICC. In this study, a laboratory testing program, a full-scale field-testing program, and a numerical analysis were performed to investigate and maximize the benefits of the hybrid ICC mixture in rigid pavement applications.

To identify the suitable concrete mixture for rigid pavement applications, a comprehensive testing program was carried out. This program included both laboratory and full-scale field-testing programs to evaluate the combined

ACI Materials Journal, V. 121, No. 3, May 2024.
MS No. M-2023-055.R1, doi: 10.14359/51740564, received October 18, 2023, and reviewed under Institute publication policies.

effects of incorporating SRA, PMFs, and OAG techniques in standard concrete (SC) and ICC. Based on the laboratory test results and evaluation, three ICC mixtures and one SC mixture were selected to be evaluated in full-size pavement test slabs, which were subjected to loading by a heavy vehicle simulator (HVS). Finally, finite element (FE) analysis was employed to assess the structural performance of these concrete mixtures for pavement applications.

EFFECT OF ENHANCED TECHNIQUES

Effect of shrinkage-reducing admixture on pavement applications

Numerous researchers have emphasized using SRAs in pavement structures to mitigate the risks of early-age and long-term shrinkage cracking.[23-25] When incorporated into concrete, SRAs have been shown to attenuate shrinkage resulting from drying or self-desiccation.[26,27] Consequently, for scenarios where pavement curling and drying shrinkage are anticipated challenges, incorporating SRAs into the concrete mixture is strongly advocated to alleviate these concerns. This study evaluated the characteristics of the ICC mixture with and without SRAs to better understand the combined effects of using LWA and SRA in concrete pavement.

Effect of fiber-reinforced concrete on pavement applications

According to the literature, the use of fiber-reinforced concrete (FRC) has been shown to have several benefits over SC. FRC has a higher ultimate strength and toughness, as well as reduced shrinkage cracking, improved permeability resistance, and delayed macrocracking.[28-30] These advantages come from the fibers' anchoring of the concrete materials, which favors cohesiveness, tensile strength, and permeability. Although FRC has some limitations in structural applications because the fibers are randomly positioned and not aligned with the main stress directions, its efficacy in pavement applications is notable, especially in its capacity to modulate crack width and postpone initial cracking.[31] Depending on the dosages of incorporated macro-synthetic fibers, one can adhere to these general guidelines: a low dosage ranging from 1.8 to 2.4 kg/m^3 (0.11 to 0.15 lb/ft^3) can augment crack control and toughness; a medium dosage of 2.4 to 4.2 kg/m^3 (0.15 to 0.26 lb/ft^3) can extend the spacing between the control joints; and a high dosage starting at 4.5 kg/m^3 (0.28 lb/ft^3) can significantly expand joint spacing, even prompting consideration for joint-free pavements akin to continuously reinforced concrete pavement (CRCP).[32,33]

In this study, the choice of fibers was carefully considered, and microfibers (diameter less than 0.022 mm [0.000867 in.]) were selected over macrofibers (0.5 mm [0.02 in.] diameter). Microfibers were proven not only to significantly improve ultimate strength and toughness far beyond that of macrofibers but also to have less impact on the workability of the fresh concrete.[28,34] The synthetic fiber used in this study was also attractive due to its good chemical stability, low density, and efficient mixing characteristics compared to metallic fibers.[35] As a result, a PMF was chosen for use in this study to evaluate ICC performance with or without PMFs.

Effect of optimized aggregate gradation on pavement applications

It is widely recognized that the nominal size, gradation, and proportions of aggregates are important factors affecting the plastic and hardened properties of the concrete.[36] The concept of the OAG is to constitute well-distributed aggregates by controlling the proportion of the different-sized aggregates, typically at least three different categorized aggregates.[37] The application of OAG in the concrete mixture design can enable the cement matrix to fill in the space between aggregates more homogeneously, which in turn can directly enhance both hydration and strength development. With this favorable phenomenon from designing concrete based on the OAG technique, a targeted compressive strength[38] and better workability[39] were effectively gained from OAG concrete even though less cementitious material was used than in SC. To identify the potential effects of the OAG technique on the ICC mixture as pavement application, the two following cement-paste contents were used: 100% and 90% of the paste quantity of the SC mixture.

This paper employed the modified OAG proposed by Lindquist et al.[37] This method was used to proportion the virgin coarse aggregate, virgin fine aggregate, and LWA components forming the concrete mixtures under evaluation. One of the key tools for assessing the mixture's properties is the coarseness factor chart, which plots the coarseness factor (CF) against the workability factor (WF).

$$\mathrm{CF} = Q \div (Q + I) \times 100 \quad (1)$$

where Q is the percent retained on 37.5 + 25.0 + 19.0 + 12.5 + 9.5 mm (1.48 + 0.98 + 0.75 + 0.49 + 0.37 in.); and I is the percent retained on 4.75 + 2.36 mm (0.19 + 0.09 in.). The WF of a concrete mixture can be calculated as follows

$$\mathrm{WF} = W \div (Q + I + W) \times 100 + CCF \quad (2)$$

where W is the percent retained on 1.18 + 0.6 + 0.3 + 0.15 + 0.075 mm (0.05 + 0.02 + 0.01 + 0.006 + 0.003 in.) + pan (sieve); and $CCF = 2.5 \times (C - 335) + 56$ (where C is the amount of cement in kg/m^3).

To determine the workability of a specific concrete mixture, both the CF and WF are plotted on this chart. Ideally, a concrete mixture with an OAG should fall within the workability box. This box's boundaries are delineated by the corner coordinates, as advised by the Montana Department of Transportation (MDT).[40] A mixture that plots within this box is considered favorable and will likely result in a workable concrete mixture that can be placed and finished easily and will have good long-term performance.

By adhering to the OAG procedure outlined by Lindquist et al.,[37] this study ascertained optimized proportions of coarse and fine aggregates in the different concrete mixtures containing LWA. Furthermore, MDT[40] designates the ideal target line in the percent retained chart (notably, the haystack gradation, a humped curve line based on an "8-18" band gradation of percent retained aggregate on each sieve).

RESEARCH SIGNIFICANCE

Although extensive research has been carried out on the effect of ICC on rigid pavements for enhancing serviceability and durability, no study has been done to evaluate the effects of other enhancing techniques on ICC. This study investigated the effects of using PMFs, OAG, and SRA on ICC by means of a laboratory testing program, full-scale pavement tests, and numerical analysis. The results from this study can be used to optimize the use of these enhanced techniques on ICC for rigid pavement applications.

EVALUATION OF CONCRETE MIXTURES IN LABORATORY PROGRAM

Concrete mixture design

The ICC mixtures were compared to the SC mixture for the construction of concrete pavement slabs with a *w*/*c* of 0.44. To investigate the ICC in terms of mechanical performance, the following different enhanced techniques were incorporated: PMF, OAG, and SRA. The designed volumetric proportions of these mixtures are shown in Fig. 1, and the detailed numerical mixture design is presented in Table 1. Table 2 presents the properties of the natural different-sized aggregates and LWA used. All used aggregates were

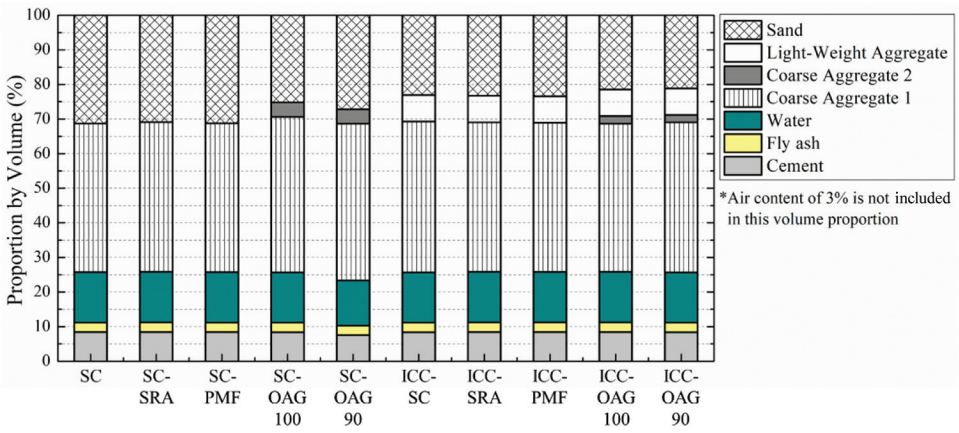

Fig. 1—Proportions of concrete mixture design by volume.

Table 1—Concrete mixture design for laboratory testing program

Selected concrete mixtures	SC (control)	SC-SRA	SC-PMF	SC-OAG 100	SC-OAG 90	ICC (control)	ICC-SRA	ICC-PMF	ICC-OAG 100	ICC-OAG 90
Cement, kg/m^3	256.3	256.3	256.3	256.3	230.8	256.3	256.3	256.3	256.3	230.8
Fly ash, kg/m^3	64.1	64.1	64.1	64.1	57.5	64.1	64.1	64.1	64.1	57.5
Water, kg/m^3	141.2	141.2	141.2	141.2	127.0	141.2	141.2	141.2	141.2	127.0
Coarse aggregate 1, kg/m^3	873.9	998.5	1003.2	1009.2	1020.4	1006.2	1002.0	1003.8	967.0	960.5
Coarse aggregate 2, kg/m^3	—	—	—	151.9	150.7	—	—	—	86.6	128.1
Lightweight aggregate, kg/m^3	—	—	—	—	—	113.9	113.9	113.9	113.9	106.2
Fine aggregate, kg/m^3	812.8	803.3	811.0	640.1	691.8	604.5	606.3	612.9	552.9	602.8
Air entrainer, mL/kg	0.02	0.09	0.09	0.06	0.08	0.00	0.12	0.15	0.12	0.08
Water reducer, mL/kg	3.0	3.0	3.1	2.9	2.9	2.9	2.9	2.9	2.9	3.1
High-range water reducer, mL/kg	3.5	3.6	3.1	1.1	2.7	2.2	1.9	2.2	1.9	3.7
Shrinkage-reducing admixture, mL/kg	—	12.8	—	—	—	—	12.8	—	—	—
Synthetic microfiber, kg/m^3	—	—	0.9	—	—	—	—	0.9	—	—

Note: 1 kg/m^3 = 0.062 lb/ft^3; 1 mL/kg = 0.015 fl. oz./lb.

Table 2—Specific gravity and water absorption of aggregates used

Four aggregates used	Coarse aggregate 1	Coarse aggregate 2	Fine aggregate	Lightweight aggregate
Bulk specific gravity (saturated surface-dry)	2.428	2.452	2.651	1.538
Bulk specific gravity (dry)	2.343	2.354	2.633	1.229
Apparent specific gravity (dry)	2.559	2.608	2.640	1.802
Water absorption, %	3.6	4.2	0.3	25.8
Aggregate type	Limestone	Limestone	Sand	Expanded clay
Aggregate source	Florida	Florida	Florida	Louisiana

tested for their physical and chemical properties and satisfied the requirements of ASTM C1761/C1761M.

Moreover, for the mixtures incorporating the OAG technique, the following cement-paste contents were used: 100% and 90% of the paste quantity of the SC mixture. To improve the optimized gradation, two different natural coarse aggregates were used. Coarse aggregate 1 had a nominal maximum size of 25.4 mm (1 in.), and coarse aggregate 2 had a nominal maximum size of 9.5 mm (0.37 in.). For the ICC mixtures, a part of the fine aggregate was replaced with the pre-wetted LWAs of expanded clay. The quantity of LWA used was an amount that supplied 3.2 kg (7 lb) of absorbed water per 45.4 kg (100 lb) of cement used. Figure 2 shows the gradation chart of the selected aggregates in this study. All batching, mixing, casting, and curing processes were performed in the conventional method.

Concrete mixture properties

From 10 concrete mixtures evaluated in the laboratory testing program, one SC and three ICC mixtures with the best potential performance were selected to be used in two separate full-scale test slabs. Two main attributes considered in making the selection were the workability of the fresh concrete and the properties of the hardened concrete. Table 3 presents the plastic properties of the 10 concrete mixtures compared to Florida Department of Transportation (FDOT) specifications from the laboratory testing program.[41] For the plastic properties, the slump, air content, temperature, and unit weight data were measured in accordance with ASTM standards: ASTM C143/C143M, ASTM C231/C231M, ASTM C1064/C1064M, and ASTM C138/C138M. In summary, all mixtures showed good performance in terms of plastic properties. All mixtures were judged as suitable for the rigid pavement applications based on FDOT specifications.

Three categories of properties of hardened concrete are critical to assessing the performance of rigid pavement applications in terms of strength, drying shrinkage, and permeability, indicated by rapid chloride penetration (RCP). For the strength properties, the compressive strength, modulus of rupture (MOR), and modulus of elasticity (MOE) data are shown in Fig. 3. All concrete mixtures have suitable strengths for pavement applications that meet the allowable requirement according to the AASHTO specification.[42] Note that all hardened properties were determined with an average value of three samples for each test.

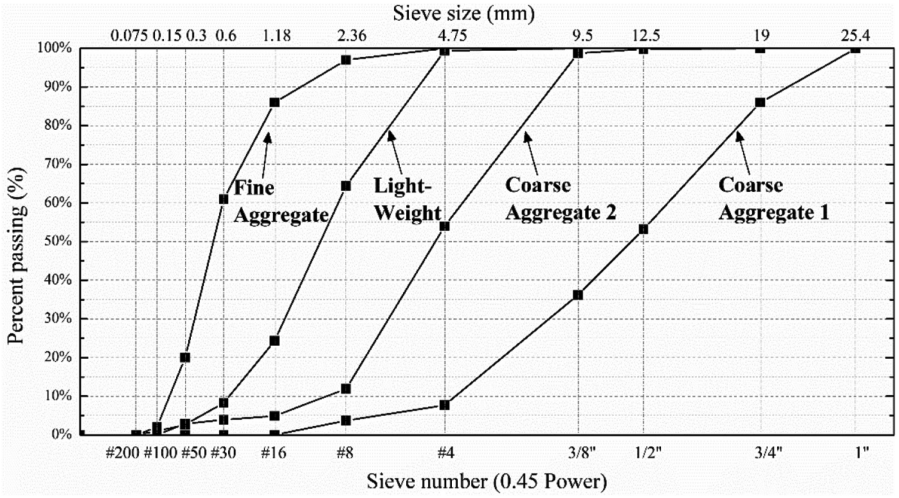

Fig. 2—Gradation of aggregates used in study.

Table 3—Concrete plastic properties

Concrete mixtures	Slump, cm	Air content, %	Temperature, °C	Unit weight, kg/m^3
SC (control)	12.7	4.7	22.8	2249
SC-SRA	6.35	3.3	23.9	2268
SC-PMF	11.4	4.6	23.3	2225
SC-OAG 100	4.5	2.1	23.9	2313
SC-OAG 90	7.6	3.6	24.7	2292
ICC (control)	5.7	2.7	24.1	2227
ICC-SRA	7.0	3.9	21.9	2204
ICC-PMF	3.0	2.6	23.3	2243
ICC-OAG 100	6.4	2.2	23.9	2249
ICC-OAG 90	7.6	3.5	23.9	2196
FDOT specification	2.5 to 12.7	1 to 6	20 to 30	—

Note: 1 cm = 0.39 in.; °F = (°C × 9/5) + 32; 1 kg/m^3 = 0.062 lb/ft^3.

More importantly, one of the key factors to evaluate structural performance is the ratio of the MOR over the MOE (*R*/*E*). For several published studies, MOR has been used as the independent indicator to evaluate the resistance of fatigue cracking; the risk of fatigue cracking decreases as MOR increases.[43] Meanwhile, a lower MOE yields lower residual stresses, closely correlated to the reduction of the potential cracking when the same loading is applied.[14,44] In general, the MOE of the concrete increases as the concrete strength, such as compressive strength and MOR, increases. A higher-strength concrete mixture is recommended, but higher stress is simultaneously involved in the concrete structure due to increased MOE. Therefore, the desirable concrete mixture has an appropriate combination of MOR and MOE, which can be expressed by a high ratio of *R*/*E*. In this study, *R*/*E* was used to evaluate the potential structural performance of the concrete mixtures from the laboratory program. Figure 3 also exhibits the *R*/*E* of all the mixtures. The ICC concrete mixtures show improvement in the *R*/*E*, especially the three mixtures of ICC-PMF, ICC-ACO 100, and ICC-ACO 90, which substantially increased the *R*/*E* compared to the non-ICC concrete mixtures.

Table 4 shows the results from the laboratory program of the coefficient of thermal expansion (CTE), drying

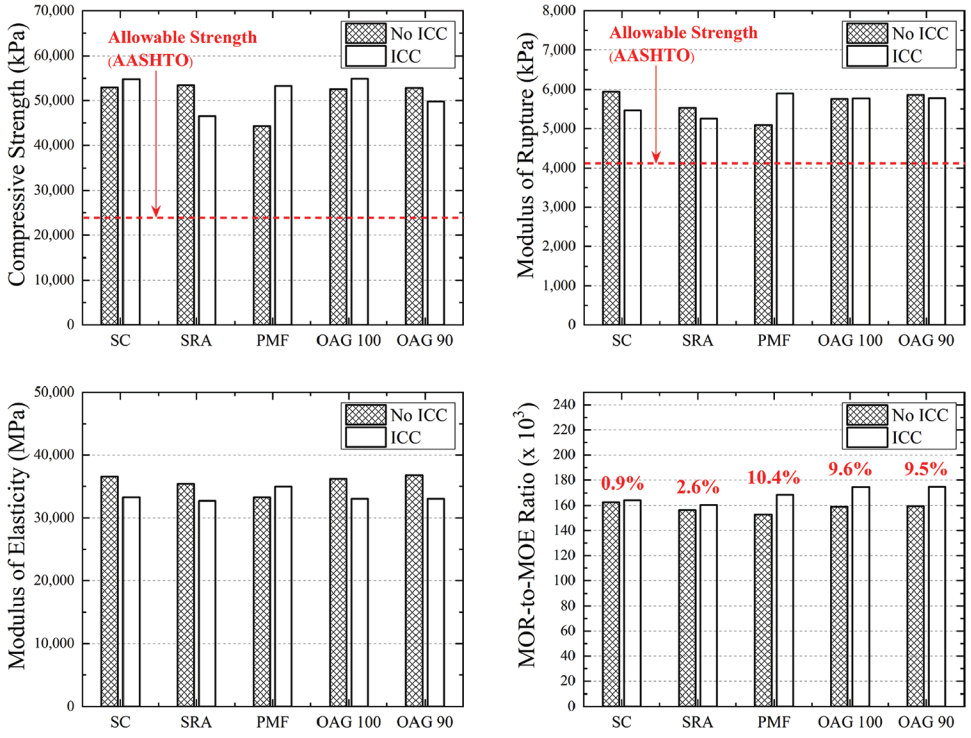

Fig. 3—Hardened concrete properties at 28 days from laboratory testing program: (top left) compressive strength of each concrete mixture; (top right) MOR of each concrete mixture; (bottom left) MOE of each concrete mixture; and (bottom right) key factor of R/E *for evaluation of each concrete mixture.*

Table 4—Concrete CTE, shrinkage, and permeability properties at 28 days

Concrete mixtures	CTE, με/°F		Surface resistivity, kΩ·cm		Rapid chloride permeability, coulombs	
	28 days	365 days	28 days	365 days	28 days	365 days
SC (control)	4.41	5.20	10.0	45.4	3579	710
SC-SRA	4.57	5.32	10.0	41.2	4166	729
SC-PMF	3.66	5.23	9.9	38.1	4131	771
SC-OAG 100	4.42	4.48	9.6	46.3	3820	758
SC-OAG 90	4.70	4.54	10.1	44.8	3769	768
ICC (control)	3.79	4.97	10.5	45.5	3902	662
ICC-SRA	4.21	5.22	11.1	49.1	3413	614
ICC-PMF	3.66	4.18	11.8	50.4	3354	586
ICC-OAG 100	3.56	4.19	11.1	49.7	3755	650
ICC-OAG 90	4.44	4.28	12.4	48.2	3339	542
AASHTO specification	—		Moderate: 10 Low: 20		Low: 2000 Very low: 20,000	

shrinkage, and permeability for the concrete mixtures at 28 days. The tests of CTE, drying shrinkage, surface resistivity, and RCP were conducted in accordance with standards such as AASHTO T 336, ASTM C157, FM 5-579, and ASTM C1202. Studies on the performance of concrete pavement recommended using lower CTE and shrinkage to reduce the thermal and built-in stresses.[45] Additionally, a reduced concrete permeability will prevent the penetration of water, gas, and ions into the hardened concrete, which may result in structure deficiencies pertaining to freezing and thawing, sulfate attack, and alkali-aggregate reaction.[46] All the concrete mixtures had a minimal length change both in contraction and expansion as well as acceptable permeability according to AASHTO specifications.[42]

One of the primary goals of using IC in the concrete mixture was to alleviate the possibility of cracking, which can be indirectly evaluated with the degree of drying shrinkage. To evaluate long-term performance, the length changes due to the effect of drying shrinkage were measured for 2 years in this laboratory program. Figure 4 shows the time-series drying shrinkage for the ICC mixtures compared to the control mixture of SC. It is noted that the hybrid ICC mixtures with SRA, PMFs, and OAG had considerably lower drying shrinkage than the SC mixture. This reduction can be largely attributed to the provision of IC water by the ICC, which inherently mitigates drying shrinkage.

Concrete mixture selection

The concrete mixtures from the laboratory program were evaluated to select the potential best mixtures for full-scale pavement slab evaluation. The desirable characteristics of concrete for pavement slabs, in terms of stress generation under loading, are high flexural strength, low MOE, and low CTE. Moreover, having low permeability and drying shrinkage is important for the long-term serviceability and durability of concrete pavement slabs.

All the hybrid ICC mixtures showed satisfied plastic and hardened properties for the rigid pavement applications. In particular, based on the *R*/*E* results from Fig. 3 (bottom right), the hybrid ICC mixtures show a great advantage for the potential fatigue resistance, which will be evaluated by both full-scale tests and numerical analysis. Thus, the hybrid ICC mixtures, such as ICC-SRA, ICC-PMF, and ICC-OAG 100, were selected to be evaluated in the full-scale field program. The test slab designation and their corresponding concrete mixtures are shown in Table 5.

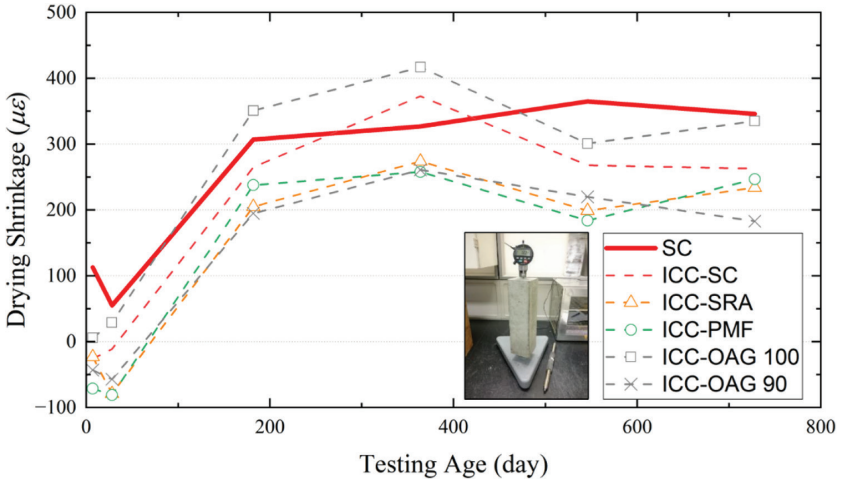

Fig. 4—Drying shrinkage of ICC mixtures for 2 years.

Table 5—Slab designation and corresponding selected concrete mixtures for evaluation

Selected concrete mixtures	SC without ICC	ICC-SRA	ICC-PMF	ICC-OAG 100
Cement, kg/m^3	256.3	256.3	256.3	256.3
Fly ash, kg/m^3	64.1	64.1	64.1	64.1
Water, kg/m^3	141.0	141.0	141.0	141.0
Coarse aggregate 1, kg/m^3	894.7	1617.9	1006.2	936.8
Coarse aggregate 2, kg/m^3	70.6	—	—	138.2
Lightweight aggregate, kg/m^3	—	168.5	113.7	113.7
Fine aggregate, kg/m^3	856.0	540.5	578.1	575.9
Air entrainer, mL/kg	—	—	1.3	0.2
Water reducer, mL/kg	2.9	2.9	3.3	2.9
High-range water reducer, mL/kg	4.9	2.7	3.3	2.5
Shrinkage-reducing admixture, mL/kg	—	2.9	—	—
Synthetic microfiber, kg/m^3	—	—	0.9	—

FULL-SCALE FIELD TEST PROGRAM

Description of test slabs

This study aims to examine the feasibility of rigid pavement using hybrid ICC mixtures by considering long-term performance metrics. Given the challenges faced by prior research in predicting long-term structural performance, the present investigation employs an accelerated testing approach using an HVS. This study investigates the viable application of rigid pavement with the hybrid ICC mixtures in terms of short- and long-term performance. The full-scale test slabs were constructed to monitor the structural behavior subjected to HVS loading. Each test slab was 3.6 x 4.6 m (11.8 x 15.1 ft) in size and 23 cm (9 in.) in thickness, which represents a typical jointed plain concrete pavement (JPCP) slab. These test slabs were constructed over an existing 5 cm (2 in.) thick asphalt layer, which acted as a leveling course and provided the firm and consistent foundation for the concrete slabs, supported by a 27 cm (11 in.) limerock base layer. The full-scale test slabs were constructed, and HVS loading was applied after 130 days to evaluate the accelerated fatigue performance and the verification of the developed FE model. Only the two test slabs of SC and ICC-PMF were evaluated with the HVS due to the limited schedule of the HVS used.

The concrete mixtures used in the test slabs were evaluated for their fresh concrete properties at the time of the placement of the concrete slabs. At the same time, the samples were made to evaluate the properties of hardened concrete. Table 6 shows the tested plastic and hardened properties of the concrete mixtures compared with the corresponding standards. The workability rating was good for all the mixtures with respect to ease of placement and finishing. The air contents of all the concrete mixtures were within the allowable FDOT specification (1 to 6%). For the hardened concrete, all reported properties of the hybrid ICC mixtures were similar to those of the SC mixture. The strength results were as expected because earlier studies have reported that neither the use of ICC nor less than a 1% volume fraction of FRC helps improve the strength properties directly.[47,48]

Instrumentation layout and installation

The test slabs were instrumented with fiber-optic sensors (FOS) to measure dynamic strains in the slabs. The embedded FOS gauges were placed at the mid-edge of the slab on the HVS wheel's path. For each gauge location, two FOS gauges were placed at a depth of 5 cm (2 in.) from the concrete surface and 5 cm from the bottom of the concrete layer in the longitudinal direction. Figure 5 presents the instrumentation layout for the test slabs with the loading locations of the falling weight deflectometer (FWD) and HVS. HVS loading was applied using a single wide tire with a contact pressure of 827 kPa (120 psi) and a load of 53 kN

Table 6—Plastic and hardened properties of concrete used in test slabs

Selected concrete mixtures	SC without ICC	ICC-SRA	ICC-PMF	ICC-OAG 100
Slump, cm	7.0	7.0	8.9	16.5
Air content, %	4.4%	2.7%	5.1%	1.3%
Unit weight, kg/m^3	2226.6	2210.6	2114.4	2210.6
Compressive strength, MPa	37.3	38.5	29.1	35.9
Modulus of elasticity, MPa	29,647	27,924	25,855	26,545
Modulus of rupture, kPa	5688	5792	4929	5206

Note: 1 MPa = 145 psi; 1 kPa = 0.145 psi.

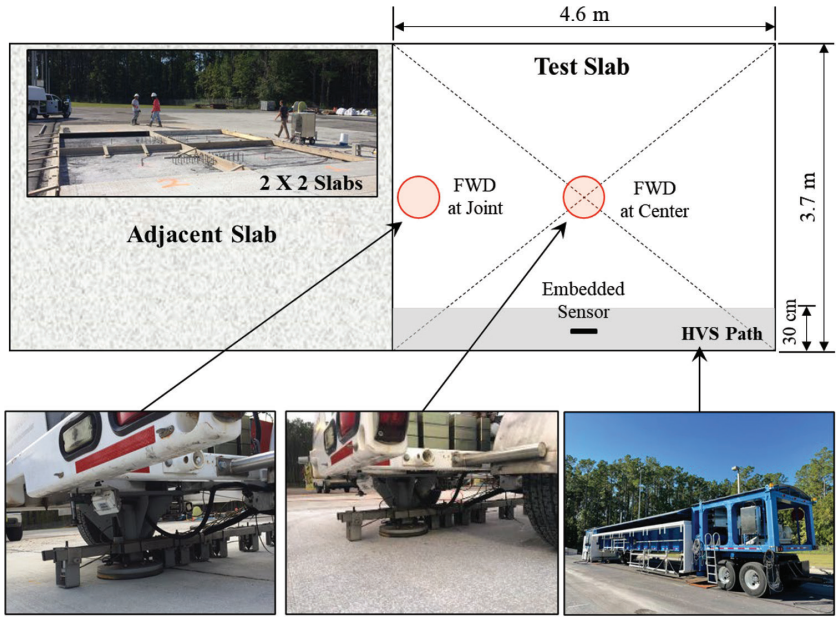

Fig. 5—Instrumentation design for FWD and HVS testing.

(12 kip), traveling at approximately 12 km/h (7 mph) in a single direction. During HVS testing, dynamic strain data from the tested slab were recorded at every 1-hour interval for 200 seconds to capture the dynamic strains caused by 20 HVS wheel passes.

NUMERICAL EVALUATION OF CRITICAL STRESS ANALYSIS

Validation of FE model

Figure 6 shows the three-dimensional (3-D) FE model developed for the critical stress analysis of the test slabs. The effects of temperature differential in the concrete slab were considered in the critical stress analysis. The concrete is characterized by its elastic modulus, Poisson's ratio, and CTE. The properties of the concrete used in the model were initially obtained from the measured properties of the sampled concrete. The effective elastic modulus of the subgrade and load transfer across the joint were obtained through the back-calculation method by matching the analytical to the measured FWD deflections.[49] Surface deflections in the concrete pavement caused by a 53 kN (12 kip) FWD were used to estimate the values of the effective elastic modulus of the subgrade and the stiffness of the springs for the load transfer at the joints. Figure 7 shows one of the examples of the matched deflection basins from the back-calculation process for estimating joint spring stiffness.

Verification of FE model

Using the filtered strain data, the behavior of longitudinal tensile strains caused by a 53 kN (12 kip) HVS load was determined. To compare the measured strains with the computed strains, a similar condition of temperature differential in the concrete slab was considered. The maximum measured strains obtained under the condition of a close-to-zero temperature differential in the concrete slabs were used for this purpose. The selected measured strain data were obtained from the following testing times: 1) Trial 16 at 12:30 pm for SC; and 2) Trial 21 at 8:48 am for ICC-PMF, when the measured temperature differential was nearly zero. The measured maximum strains from the strain gauges in the test slabs compared to the computed strain are shown in Fig. 8, which shows good matching between the measured and computed values.

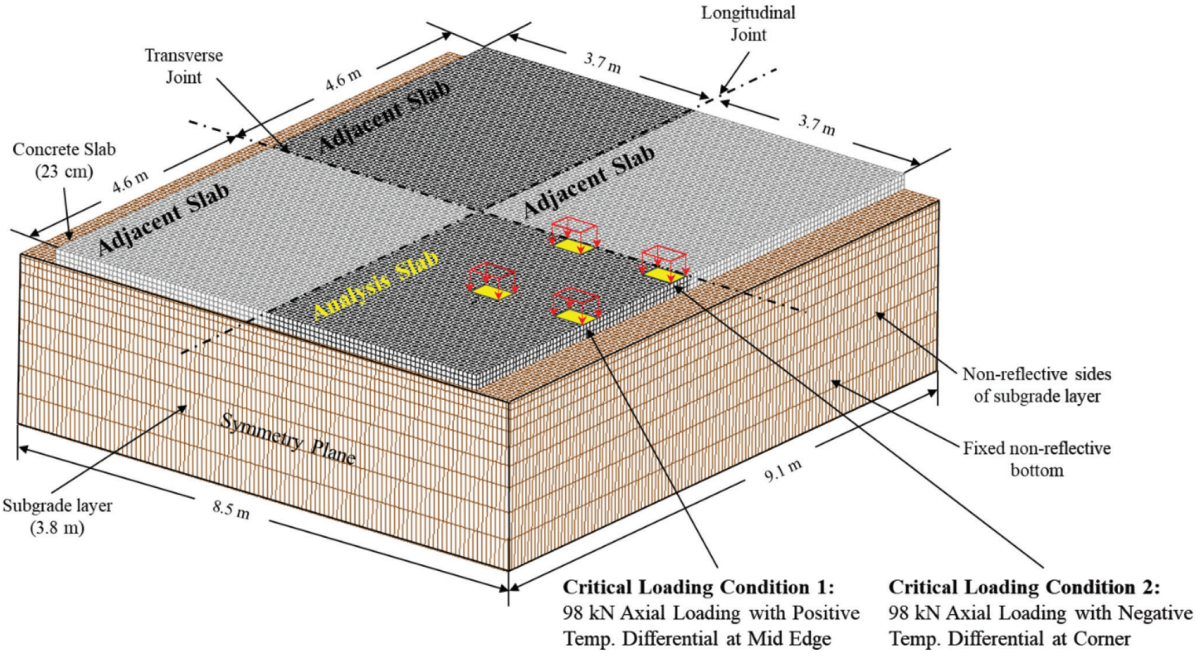

Fig. 6—3-D FE model for four test slabs and location of critical loading conditions with combined environmental and wheel loading.

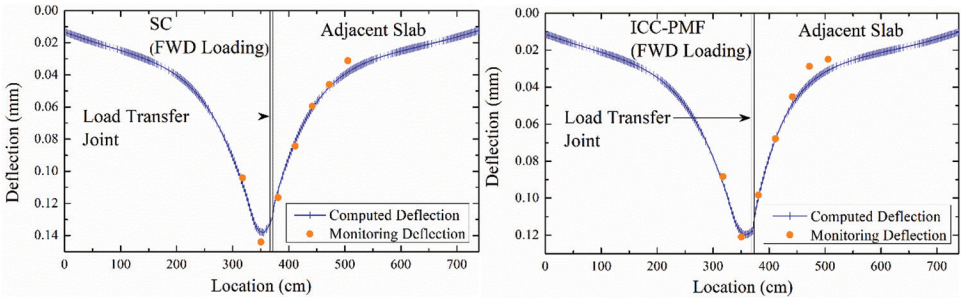

Fig. 7—Determination of spring stiffness across joint using FWD basin: (left) comparison between calculated deflection and recorded deflection by loading on SC mixture; and (right) ICC-PMF.

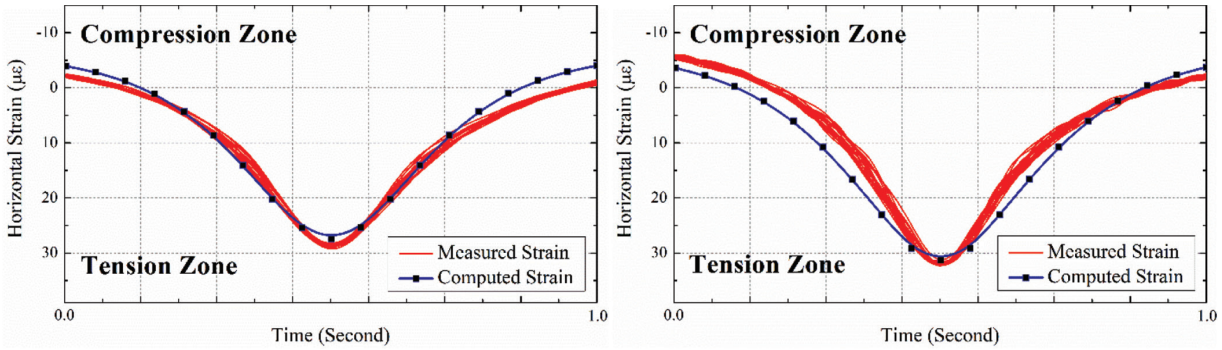

Fig. 8—Comparison between measured strain from sensor under HVS loading 20 times and computed strain of: (left) SC mixture; and (right) ICC-PMF.

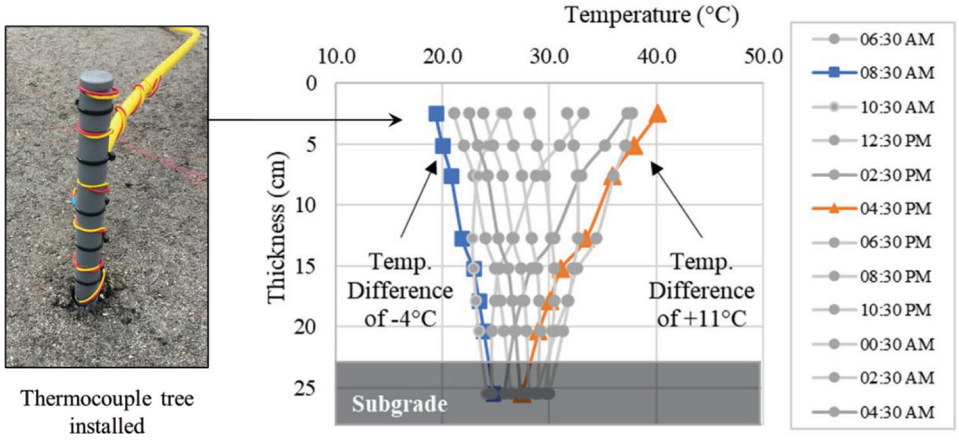

Fig. 9—Recorded temperature differential to validate inputted environmental loading for critical stress analysis.

Table 7—Computed maximum stresses and stress-to-strength ratios for test slabs

Selected concrete mixtures	Temperature differential, °C	MOE, MPa	MOR, kPa	Computed stress, kPa		Stress-to-strength ratio	
				Corner	Mid-edge	Corner	Mid-edge
SC	+11.1	29,647	5688	1896	3495	0.33	**0.61**
	–5.5	29,647	5688	1290	1080	0.23	0.19
ICC-SRA	+11.1	27,923	5792	1695	3102	0.29	**0.54**
	–5.5	27,923	5792	1156	934	0.20	0.16
ICC-PMF	+11.1	25,855	4929	2143	2612	0.43	**0.53**
	–5.5	25,855	4929	1153	1142	0.23	0.23
ICC-OAG 100	+11.1	26,544	5205	1537	2865	0.30	**0.55**
	–5.5	26,544	5205	1076	852	0.21	0.16

Note: Maximum numbers within each concrete mixture are marked in bold.

Assessment of critical stress analysis

A main design requirement for a rigid pavement should be the prevention of fatigue failure. All mechanistic-based designs use linear-elastic stress analysis to predict the stress-to-strength ratio as the indicator of fatigue resistance.[50,51] To compare the fatigue resistance of the test slabs, the validated FE model was used to calculate the maximum tensile stress under a critical load-temperature condition. Table 7 summarizes the results of the critical stress analysis, which show that the maximum stresses and maximum stress-to-strength ratios were obtained when a 98 kN (22 kip) axle load was applied to the mid-edge of the pavement slab with a temperature differential of +11.1°C (52°F). Furthermore, the slab's temperature was recorded for 4 months from the thermocouple trees along the slab depth, as shown in Fig. 9, and this revealed that the designed temperature differential used in the critical stress analysis was acceptable.

The computed stress-to-strength ratios for SC, ICC-SRA, ICC-PMF, and ICC-OAG 100 were 0.61, 0.54, 0.53, and 0.55, respectively, when applied to the critical loading condition proven by Tia et al.[44] and field monitoring. Because fatigue models commonly take advantage of a stress-to-strength ratio to predefine the slab's performance of fatigue cracking,[43] this result indicates that the hybrid ICC

mixtures outperformed the SC mixture in terms of fatigue cracking resistance, as evidenced by the lower stress-to-strength ratios. In line with critical stress analysis to predict fatigue resistance, an accelerated pavement test using HVS was conducted. The test slabs of SC and ICC-PMF, which had low computed stress-to-strength ratios (0.61 and 0.53, respectively), did not show any visible cracks after HVS loading. Figure 10 shows the pictures of the surfaces of all slabs after HVS loading.

LIFE-CYCLE COST ANALYSIS ON USE OF ICC IN PAVEMENT APPLICATIONS

Predicted service life based on AASHTO

This study undertakes a life-cycle cost analysis (LCCA) to examine the application of ICC with OAG, SRA, and PMFs in concrete pavement, compared with SC (as the control condition). The AASHTO design equation for concrete pavement[52] was employed to scrutinize the potential performance of the Class I (pavement) concrete mixtures, as shown in Eq. (3).

$$\log_{10}W_{18} = Z_R \cdot S_o + 7.35\log_{10}(D+1) - 0.06 + \frac{\log_{10}\left(\frac{\Delta PSI}{3}\right)}{1+\left(\frac{1.64\times10^7}{(D+1)^{8.46}}\right)} + (4.22 - 0.32p_t) \times \log_{10}\frac{S_c' \cdot C_d(D^{0.785}-1.132)}{215.63J\left(\frac{D^{0.75}-18.42}{\left(\frac{E_c}{k}\right)^{0.25}}\right)} \quad (3)$$

This design equation originated from the AASHTO Road Test, conducted in Ottawa, IL, in 1993. It establishes a correlation between the number of 80 kN (18 kip) equivalent single-axle loads (ESALs) that a pavement can carry before reaching a predetermined terminal serviceability index as a function of various relevant pavement design parameters. A conventional rigid pavement in Florida, featuring a slab thickness of 23 cm (9 in.), serves as the model for this hypothetical analysis.

The subsequent values were employed for the various design parameters: where W_{18} represents the predicted number of 80 kN (18 kip) ESALs, Z_R is the standard normal deviate, with a value of 0.35; S_0 denotes the combined standard error of the traffic prediction and performance prediction, which is assigned a value of –1.645; D is the pavement slab thickness of 23 cm (9 in.); ΔPSI indicates the disparity between the initial design serviceability index (p_o) and the design terminal serviceability index (p_t), with p_t being 1.9; S_c' denotes the concrete flexural strength; J is the load transfer coefficient used to adjust for load transfer characteristics of a specific design valued at 3.2; C_d is the drainage coefficient and is set at 1; E_c indicates the concrete modulus of elasticity; and k represents the modulus of subgrade reaction, established at 2.76 MPa (400 psi).[14,53] Using an annual average daily traffic (AADT) metric of 48,500 for Archer Road, Gainesville, FL, from the FDOT database[54] (equivalent to an annual W_{18} of 408,800), Table 8 presents the estimated pavement service lives for the concrete mixtures studied. All ICC mixtures are projected to have a longer service life than SC based on the analysis of service life predictions. These outcomes can be attributed to the hybrid ICC mixtures possessing a higher flexural strength and lower MOE than the SC mixture.

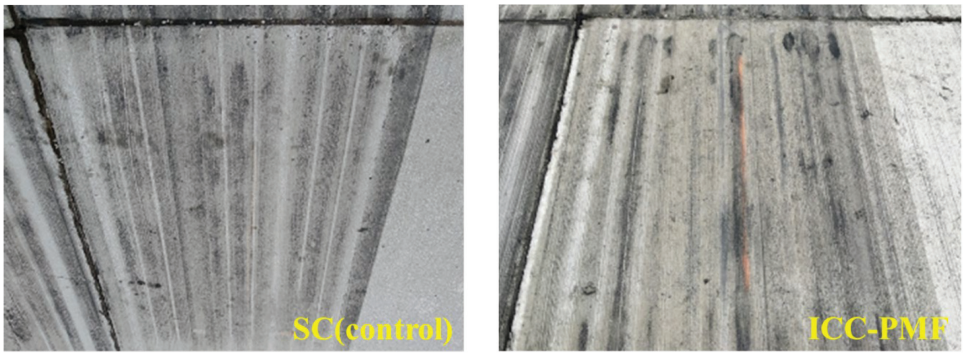

Fig. 10—Test slabs surface after HVS loading: (left) no crack on surface of SC mixture; and (right) no crack on surface of ICC-PMF.

Table 8—Calculated W_{18} using AASHTO design and associated estimated service life

Ten concrete mixtures	S_c', MPa	E, MPa	Total calculated W_{18}	Service life of pavement	
				Year	Mixture/SC
SC (control)	5.08	34,335	7,391,536	18.1	1.00
ICC-SRA	5.47	32,405	9,735,108	23.8	1.31
ICC-PMF	5.37	33,232	9,019,921	22.1	1.22
ICC-OAG 100	5.67	33,508	10,845,391	26.5	1.46

Table 9—Concrete cost for one lane mile of rigid pavement

Ten concrete mixtures	Service life of pavement, years	Cost per yd^3, $	Total concrete cost, $	EAC at 0%, $	EAC at 5%, $
SC (control)	18.1	157.9	277,981	15,358 (4)	23,698 (4)
ICC-SRA	23.8	181.8	320,051	13,448 (3)	23,297 (3)
ICC-PMF	22.1	159.2	280,149	12,677 (2)	21,229 (2)
ICC-OAG 100	26.5	154.8	272,473	10,282 (1)	18,777 (1)

Note: 1 yd^3 = 0.765 m^3; $ is USD.

Life-cycle cost analysis

In this study, only the material costs were incorporated into the LCCA for the rigid pavement. Unit costs for each concrete mixture were computed by aggregating the material expenses for all constituents within each mixture. To illuminate the genuine expenditure related to rigid pavement, the comprehensive material cost for a concrete lane mile, assuming a thickness of 23 cm (9 in.) and a width of 3.65 m (12 ft), was calculated for each concrete mixture, the details of which are elucidated in Table 9. Using the predicted service life of each concrete, as presented in Table 8, in conjunction with the unit cost, the equivalent annual cost (EAC) was computed for each concrete mixture by applying Eq. (4).

$$\text{Equivalent annual cost (EAC)} = \frac{PW \times i}{\frac{[(1+i)^n - 1]}{(1+i)^n}} \quad (4)$$

where i represents the interest rate per year; PW signifies the present worth total cost; and n stands for the years of service life. Table 9 presents the EAC computations using interest rates of 0 and 5%. In scenarios that preclude interest, all hybrid concrete mixtures exhibit a lower EAC than SC. Employing an interest rate of 5%, the same hybrid concrete mixtures demonstrated a reduced EAC relative to SC. Notably, the concrete mixtures yielding the lowest EAC were the concretes incorporating both ICC and OAG (ICC-OAG 100). Their relative EACs were 67% and 79%, compared with SC, when analyzed with interest rates of 0% and 5%, respectively. These findings suggest that the hybrid ICC is a potentially promising concrete design for pavements when considering aspects of extended service life and cost-effectiveness.

CONCLUSIONS AND RECOMMENDATIONS

This paper presents comprehensive results that describe the behavior of internally cured concrete (ICC) mixtures with three possible enhanced techniques incorporating shrinkage-reducing admixture (SRA), polymeric microfibers (PMFs), and optimized aggregate gradation (OAG). To evaluate the ICC mixtures for rigid pavement applications, a laboratory testing program, full-scale field-testing program, critical stress analysis, and life-cycle cost analysis (LCCA) were conducted to evaluate the potential benefits of hybrid ICC mixtures. A summary of the conclusions from the results presented in this paper is as follows:

- All concrete mixtures, with or without incorporating internal curing (IC), exhibited satisfactory plastic, hardened, and durability properties suitable for pavement applications.
- Each ICC mixture incorporating SRA, PMFs, and OAG exhibited favorable results of the increased modulus of rupture (MOR)-modulus of elasticity (MOE) ratio (R/E) when compared with the non-ICC concrete mixture.
- The OAG design method is also effective in ICC mixtures because the concrete strength did not decrease when the cement content was reduced by 10%.
- From the validated finite element (FE) analysis, the ICC-PMF slab had a lower stress-to-MOR ratio than the standard concrete (SC) slab, indicating potentially better performance. This is due to the ICC's enhanced properties of lower MOE, lower coefficient of thermal expansion (CTE), lower density, and increased toughness when compared with ordinary non-ICC concrete (SC).
- Based on the LCCA, the hybrid ICC is a promising concrete design for rigid pavements due to its extended service life and cost-effectiveness.
- From the overall analysis, all hybrid ICC mixtures are shown to be suitable for use in rigid pavements and have better-than-expected performances than SC.

This study conducted a comprehensive research program encompassing laboratory tests, numerical analysis, field evaluation, and LCCA to assess the potential of hybrid ICC mixtures for rigid pavements. Given the limitations within these scopes, the authors recommend the following considerations for future studies:

- This paper assessed the feasibility of hybrid ICC mixtures using SRA, PMFs, and OAG. A deeper investigation into the intricate mechanisms influencing the properties of concrete for rigid pavements would likely provide valuable insights for future research.
- Surface friction is a crucial property for concrete mixtures in rigid pavements, warranting investigation with hybrid ICC mixtures.

AUTHOR BIOS

Sangyoung Han *is an Assistant Professor in the Department of ICT Integrated Ocean Smart City Engineering at Dong-A University, Busan, South Korea. He received his PhD from The University of Texas at Austin, Austin, TX, in 2022. His research interests include the concrete mixture characteristics and analysis of reinforced and prestressed concrete structures.*

Thanachart Subgranon *is a Professional Engineer at Fugro, responsible for deep foundation testing. He specializes in bidirectional testing. He received his PhD in civil engineering at the University of Florida, Gainesville, FL, in 2020. His research interests include concrete pavements and materials, accelerated pavement testing, and instrumentation for pavements and materials research.*

Hung-Wen Chung *is the Field Services Manager for the Gainesville satellite office of ECS Florida, LLC. He received his PhD from the University of*

Florida in 2020. He has over 10 years of experience specializing in concrete and construction materials, with a focus on pavement and structures.

Kukjoo Kim *is a Professional Engineer at the Defense Installations Agency, Ministry of National Defense, South Korea. He received his PhD from the University of Florida in 2017. His research interests include ultra-high-performance concrete and analysis of protective structures against blast loadings.*

Mang Tia *is a Professor of civil engineering at the University of Florida, where he has been a faculty member since 1982. His research interests include concrete pavements and materials, asphalt pavements and materials, accelerated pavement testing, and instrumentation for pavements and materials research.*

ACKNOWLEDGMENTS

This work was supported by the Dong-A University research fund.

REFERENCES

1. Russell, H. G.; Miller, R. A.; Ozyildirim, H. C.; and Tadros, M. K., "Compilation and Evaluation of Results from High-Performance Concrete Bridge Projects, Volume I: Final Report," *Report* No. FHWA HRT-05-056, Federal Highway Administration, McLean, VA, 2006, 180 pp.

2. Castro, J.; Spragg, R.; and Weiss, J., "Water Absorption and Electrical Conductivity for Internally Cured Mortars with a W/C between 0.30 and 0.45," *Journal of Materials in Civil Engineering*, ASCE, V. 24, No. 2, Feb. 2012, pp. 223-231.

3. Shattaf, N. R.; Alshamsi, A. M.; and Swamy, R. N., "Curing/Environment Effect on Pore Structure of Blended Cement Concrete," *Journal of Materials in Civil Engineering*, ASCE, V. 13, No. 5, Oct. 2001, pp. 380-388. doi: 10.1061/(ASCE)0899-1561(2001)13:5(380)

4. Bentz, D. P., "Influence of Curing Conditions on Water Loss and Hydration in Cement Pastes with and without Fly Ash Substitution," NISTIR *Report* No. 6886, National Institute of Standards and Technology, Gaithersburg, MD, 2002, 21 pp.

5. Sant, G.; Lura, P.; and Weiss, J., "Measurement of Volume Change in Cementitious Materials at Early Ages: Review of Testing Protocols and Interpretation of Results," *Transportation Research Record: Journal of the Transportation Research Board*, V. 1979, No. 1, Jan. 2006, pp. 21-29. doi: 10.1177/0361198106197900104

6. RILEM Technical Committee 196-ICC, "Internal Curing of Concrete: State-of-the-Art Report," K. Kovler and O. M. Jensen, eds., RILEM Publications SARL, Bagneux, France, 2007, 141 pp.

7. ACI Committee 231, "Report on Early-Age Cracking: Causes, Measurement, and Mitigation (ACI 231R-10) (Reapproved 2020)," American Concrete Institute, Farmington Hills, MI, 2010, 46 pp.

8. Weiss, J., "Internal Curing for Concrete Pavements," Tech Brief No. FHWA-HIF-16-006, Federal Highway Administration, Washington, DC, 2016, 7 pp.

9. Jensen, O. M., and Hansen, P. F., "Autogenous Deformation and RH-Change in Perspective," *Cement and Concrete Research*, V. 31, No. 12, Dec. 2001, pp. 1859-1865. doi: 10.1016/S0008-8846(01)00501-4

10. Cusson, D., and Hoogeveen, T., "Internal Curing of High-Performance Concrete with Pre-soaked Fine Lightweight Aggregate for Prevention of Autogenous Shrinkage Cracking," *Cement and Concrete Research*, V. 38, No. 6, June 2008, pp. 757-765. doi: 10.1016/j.cemconres.2008.02.001

11. Radlinska, A.; Rajabipour, F.; Bucher, B.; Henkensiefken, R.; Sant, G.; and Weiss, J., "Shrinkage Mitigation Strategies in Cementitious Systems: A Closer Look at Differences in Sealed and Unsealed Behavior," *Transportation Research Record: Journal of the Transportation Research Board*, V. 2070, No. 1, Jan. 2008, pp. 59-67. doi: 10.3141/2070-08

12. Lopez, M.; Kahn, L. F.; and Kurtis, K. E., "Characterization of Elastic and Time-Dependent Deformations in High Performance Lightweight Concrete by Image Analysis," *Cement and Concrete Research*, V. 39, No. 7, July 2009, pp. 610-619. doi: 10.1016/j.cemconres.2009.03.015

13. Kim, H. K.; Jeon, J. H.; and Lee, H. K., "Workability, and Mechanical, Acoustic and Thermal Properties of Lightweight Aggregate Concrete with a High Volume of Entrained Air," *Construction and Building Materials*, V. 29, Apr. 2012, pp. 193-200. doi: 10.1016/j.conbuildmat.2011.08.067

14. Bentz, D. P., and Weiss, W. J., "Internal Curing: A 2010 State-of-the-Art Review," NISTIR *Report* No. 7765, National Institute of Standards and Technology, Gaithersburg, MD, 2011, 94 pp.

15. Byard, B. E.; Schindler, A. K.; Barnes, R. W.; and Rao, A., "Cracking Tendency of Bridge Deck Concrete," *Transportation Research Record: Journal of the Transportation Research Board*, V. 2164, No. 1, Jan. 2010, pp. 122-131. doi: 10.3141/2164-16

16. Jones, W. A., and Weiss, W. J., "Freezing and Thawing Behavior of Internally Cured Concrete," *Advances in Civil Engineering Materials*, V. 4, No. 1, 2015, pp. 144-155. doi: 10.1520/ACEM20140044

17. Wei, Y., and Hansen, W., "Characterization of Moisture Transport and Its Effect on Deformations in Jointed Plain Concrete Pavement," *Transportation Research Record: Journal of the Transportation Research Board*, V. 2240, No. 1, Jan. 2011, pp. 9-15. doi: 10.3141/2240-02

18. Amirkhanian, A. N., and Roesler, J. R., "Unrestrained Curling in Concrete with Fine Lightweight Aggregates," *Journal of Materials in Civil Engineering*, ASCE, V. 29, No. 9, Sept. 2017, p. 04017092. doi: 10.1061/(ASCE)MT.1943-5533.0001941

19. Johnson, A. M.; Smith, B. C.; Johnson, W. H.; and Gibson, L. W., "Evaluating the Effect of Slab Curling on IRI for South Carolina Concrete Pavements," *Report* No. FHWA-SC-10-04, South Carolina Department of Transportation, Columbia, SC, 2010, 30 pp.

20. Beckemeyer, C.; Khazanovich, L.; and Yu, H. T., "Determining Amount of Built-in Curling in Jointed Plain Concrete Pavement: Case Study of Pennsylvania 1-80," *Transportation Research Record: Journal of the Transportation Research Board*, V. 1809, No. 1, Jan. 2002, pp. 85-92. doi: 10.3141/1809-10

21. Lange, D. A., and Shin, H.-C., "Early Age Stresses and Debonding in Bonded Concrete Overlays," *Transportation Research Record: Journal of the Transportation Research Board*, V. 1778, No. 1, Jan. 2001, pp. 174-181.

22. Rao, C., and Darter, M. I., "Evaluation of Internally Cured Concrete for Paving Applications," Applied Research Associates, Inc., Champaign, IL, Sept. 2013, 121 pp.

23. Nmai, C. K.; Tomita, R.; Hondo, F.; and Buffenbarger, J., "Shrinkage-Reducing Admixtures," *Concrete International*, V. 20, No. 4, Apr. 1998, pp. 31-37.

24. Weiss, J., and Berke, N. S., "Admixtures for Reducing Shrinkage and Cracking," *Early Age Cracking in Cementitious Systems: Report of RILEM Technical Committee TC 181-EAS: Early Age Shrinkage Induced Stresses and Cracking in Cementitious Systems*, A. Bentur, ed., RILEM Publications SARL, Bagneux, France, 2002, pp. 323-336.

25. Gettu, R.; Roncero, J.; and Martin, M. A., "Study of the Behavior of Concrete with Shrinkage Reducing Admixtures Subjected to Long-Term Drying," *Concrete: Material Science to Application – A Tribute to Surendra P. Shah*, SP-206, P. Balaguru, A. Naaman, and W. Weiss, eds., American Concrete Institute, Farmington Hills, MI, 2002, pp. 157-166 pp.

26. Bentz, D. P.; Geiker, M. R.; and Hansen, K. K., "Shrinkage-Reducing Admixtures and Early-Age Desiccation in Cement Pastes and Mortars," *Cement and Concrete Research*, V. 31, No. 7, July 2001, pp. 1075-1085. doi: 10.1016/S0008-8846(01)00519-1

27. Weiss, J.; Lura, P.; Rajabipour, F.; and Sant, G., "Performance of Shrinkage-Reducing Admixtures at Different Humidities and at Early Ages," *ACI Materials Journal*, V. 105, No. 5, Sept.-Oct. 2008, pp. 478-486.

28. Lawler, J. S.; Zampini, D.; and Shah, S. P., "Microfiber and Macrofiber Hybrid Fiber-Reinforced Concrete," *Journal of Materials in Civil Engineering*, ASCE, V. 17, No. 5, Oct. 2005, pp. 595-604. doi: 10.1061/(ASCE)0899-1561(2005)17:5(595)

29. Passuello, A.; Moriconi, G.; and Shah, S. P., "Cracking Behavior of Concrete with Shrinkage Reducing Admixtures and PVA Fibers," *Cement and Concrete Composites*, V. 31, No. 10, Nov. 2009, pp. 699-704. doi: 10.1016/j.cemconcomp.2009.08.004

30. Plagué, T.; Desmettre, C.; and Charron, J.-P., "Influence of Fiber Type and Fiber Orientation on Cracking and Permeability of Reinforced Concrete under Tensile Loading," *Cement and Concrete Research*, V. 94, Apr. 2017, pp. 59-70. doi: 10.1016/j.cemconres.2017.01.004

31. Löfgren, I., "Fibre-Reinforced Concrete for Industrial Construction - A Fracture Mechanics Approach to Material Testing and Structural Analysis," PhD thesis, Chalmers University of Technology, Gothenburg, Sweden, 2005, 162 pp.

32. Roesler, J.; Bordelon, A.; Brand, A. S.; and Amirkhanian, A., "Fiber-Reinforced Concrete for Pavement Overlays: Technical Overview," InTrans Project *Report* No. 15-532, National Concrete Pavement Technology Center, Iowa State University, Ames, IA, Apr. 2019, 100 pp.

33. Biddle, D., "Fiber-Reinforced Concrete - Pavements," FORTA Corporation, Grove City, PA, Mar. 2020, 39 pp.

34. Lawler, J. S.; Wilhelm, T.; Zampini, D.; and Shah, S. P., "Fracture Processes of Hybrid Fiber-Reinforced Mortar," *Materials and Structures*, V. 36, No. 3, Apr. 2003, pp. 197-208.

35. Nobili, A.; Lanzoni, L.; and Tarantino, A. M., "Experimental Investigation and Monitoring of a Polypropylene-Based Fiber Reinforced Concrete Road Pavement," *Construction and Building Materials*, V. 47, Oct. 2013, pp. 888-895. doi: 10.1016/j.conbuildmat.2013.05.077

36. Mehta, P. K., and Monteiro, P. J. M., *Concrete: Microstructure, Properties, and Materials*, fourth edition, McGraw-Hill Education, New York, 2013.

37. Lindquist, W.; Darwin, D.; Browning, J.; McLeod, H. A. K.; Yuan, J.; and Reynolds, D., "Implementation of Concrete Aggregate Optimization," *Construction and Building Materials*, V. 74, Jan. 2015, pp. 49-56. doi: 10.1016/j.conbuildmat.2014.10.027

38. Kwan, A. K. H., and Ling, S. K., "Lowering Paste Volume of SCC through Aggregate Proportioning to Reduce Carbon Footprint," *Construction and Building Materials*, V. 93, Sept. 2015, pp. 584-594. doi: 10.1016/j.conbuildmat.2015.06.034

39. Cook, M. D.; Ley, M. T.; and Ghaeezadah, A., "Effects of Aggregate Concepts on the Workability of Slip-Formed Concrete," *Journal of Materials in Civil Engineering*, ASCE, V. 28, No. 10, Oct. 2016, p. 04016097. doi: 10.1061/(ASCE)MT.1943-5533.0001608

40. MDT, "Concrete Aggregate Combined Gradation Example," Montana Department of Transportation, Helena, MT, 2016, 6 pp.

41. FDOT, "Standard Specifications for Road and Bridge Construction: FY 2023-24," Florida Department of Transportation, Tallahassee, FL, 2023, 1299 pp.

42. AASHTO PP 84-17, "Standard Practice for Developing Performance Engineered Concrete Pavement Mixtures," American Association of State Highway and Transportation Officials, Washington, DC, 2017.

43. Smith, K. D., and Roesler, J. R., "Review of Fatigue Models for Concrete Airfield Pavement Design," *Airfield Pavements: Challenges and New Technologies: Proceedings of the 2003 Airfield Pavement Specialty Conference*, Las Vegas, NV, Sept. 2003, pp. 231-258.

44. Tia, M.; Wu, C. L.; Ruth, B. E.; Bloomquist, D.; and Choubane, B., "Field Evaluation of Rigid Pavements for the Development of a Rigid Pavement Design System—Phase IV," University of Florida, Gainesville, FL, 1989.

45. Wells, S. A.; Phillips, B. M.; and Vandenbossche, J. M., "Quantifying Built-in Construction Gradients and Early-Age Slab Deformation Caused by Environmental Loads in a Jointed Plain Concrete Pavement," *International Journal of Pavement Engineering*, V. 7, No. 4, 2006, pp. 275-289. doi: 10.1080/10298430600798929

46. Mehta, P. K., "Durability of Concrete—Fifty Years of Progress?" *Durability of Concrete: Second International Conference, Montreal, Canada 1991*, SP-126, V. M. Malhotra, ed., American Concrete Institute, Farmington Hills, MI, 1991, pp. 1-32.

47. Paul, Á., and Lopez, M., "Assessing Lightweight Aggregate Efficiency for Maximizing Internal Curing Performance," *ACI Materials Journal*, V. 108, No. 4, July-Aug. 2011, pp. 385-393.

48. ACI Committee 544, "Report on Fiber Reinforced Concrete (ACI 544.1R-96) (Reapproved 2009)," American Concrete Institute, Farmington Hills, MI, 1996, 66 pp.

49. Von Quintus, H. L., and Simpson, A. L., "Back-Calculation of Layer Parameters for LTPP Test Sections, Volume II: Layered Elastic Analysis for Flexible and Rigid Pavements," *Report* No. FHWA-RD-01-113, Federal Highway Administration, McLean, VA, 2002, 146 pp.

50. Darter, M.; Khazanovich, L.; Snyder, M.; Rao, S.; and Hallin, J., "Development and Calibration of a Mechanistic Design Procedure for Jointed Plain Concrete Pavements," *Proceedings of the 7th International Conference on Concrete Pavements: The Use of Concrete in Developing Long-Lasting Pavement Solutions for the 21st Century*, Orlando, FL, Sept. 2001, pp. 113-131.

51. Packard, R. G., and Tayabji, S. D., "New PCA Thickness Design Procedure for Concrete Highway and Street Pavements," *Proceedings of the Third International Conference on Concrete Pavement Design and Rehabilitation*, Purdue University, West Lafayette, IN, Apr. 1985, pp. 225-236.

52. AASHTO, "AASHTO Guide for Design of Pavement Structures 1993," American Association of State Highway and Transportation Officials, Washington, DC, 1993, 624 pp.

53. Mindess, S.; Young, J. F.; and Darwin, D., *Concrete*, second edition, Prentice Hall PTR, Hoboken, NJ, 2002, 644 pp.

54. FDOT, "Florida Department of Transportation Traffic Information," Florida Department of Transportation, Tallahassee, FL, https://www.fdot.gov/statistics/trafficdata/default.shtm. (last accessed Apr. 4, 2024)

aci Foundation

Building the Future

We're Building the Future

OUR MISSION

We make strategic investments in ideas, research, and people to create the future of the concrete industry.

Through its councils and programs, the ACI Foundation helps to keep the concrete industry at the forefront of advances in material composition, design, and construction.

OUR FOCUS

- Identifying technologies and innovations which provide needed solutions for the concrete industry
- Seeking concrete research projects that further the knowledge and sustainability of concrete materials, construction, and structures
- Supporting our future concrete innovators and leaders by administering fellowships and scholarships
- Helping honorably discharged veterans with our Veterans Rebate for ACI Certification program

www.acifoundation.org

ACI MATERIALS JOURNAL TECHNICAL PAPER

Title No. 121-M26

Assessment of Approaches for Determining Time-Zero of Concrete

by Liang Li

*Time-zero is of considerable significance for determining both deformational and mechanical properties of high-performance concrete from very early ages. In this paper, four methods for determining the time-zero are investigated comparably, including stress evolution measurement, autogenous strain method, ultrasonic testing, and temperature rate method. A critical review of the theoretical basis behind each method is presented, with emphasis on the applicability and limitations of each method. Based on a case study, the practical capabilities of all four methods for determining the time-zero of high-performance concrete with a water-binder ratio (*w/b*) of 0.25 are experimentally assessed. It is found that the ultrasonic testing and temperature rate methods are better suited due to their simplicity and availability compared to the other two methods. Besides, the temperature of cement-based composites at very early ages can affect the determined values of time-zero, which needs further research.*

Keywords: autogenous strain; early ages; high-performance concrete; setting times; temperature rate; time-zero; ultrasonic pulse velocity (UPV).

INTRODUCTION

Research background

The time-zero, defined as the time point when concrete materials form a stable solid skeleton to sustain tensile and compressive stresses (Huang and Ye 2017; Li et al. 2020a; Sant et al. 2009), plays a critical role in the study of the mechanical and deformational properties of early-age concrete. Additionally, the time-zero of concrete is also important for assessing and scheduling construction operations, such as finishing, saw-cutting, and curing. However, despite great practical significance, the time-zero of high-performance concrete has been less investigated in the literature, mainly due to the lack of convenient test measures and the complexity of cement hydration at early ages. In previous studies (ASTM C191-08 2008; Miao et al. 2007; Tenório Filho et al. 2019; Huang and Ye 2017; Li et al. 2020a; Lura et al. 2009; Ma et al. 2019; Sant et al. 2009; Sleiman et al. 2010), different experimental approaches for measuring the time-zero of cement pastes or mortars have been proposed, but the practicability of those proposed test methods for determining the time-zero of high-performance concrete has been less evaluated. Moreover, the consistency of the time-zeros measured according to different methods also requires further research.

For simplicity, the initial or final setting time of mortar sieved from concrete measured by penetration resistance has often been regarded as the time-zero (*fib* 2013; JSCE 2007; Kanstad et al. 2003; Kawashima and Shah 2011; Struble and Lei 1995). However, which setting time (initial or final) better reflects the time-zero remains debatable. In the literature (Carette and Staquet 2015; JSCE 2007; Struble and Lei 1995), the final setting time was regarded as the time-zero when the mechanical properties of cement-based composites started to develop, while the initial setting time was indicated as the time-zero in Kong et al. (2015), Trtnik et al. (2008), and Zhutovsky and Kovler (2017). According to the Australian standard AS 1012.18 (1996), the initial and final setting times of concrete are defined as the time points when the sieved mortar from concrete reaches a penetration resistance of 3.5 and 28.0 MPa, respectively. Similar penetration resistance tests are also recommended in ASTM C403/C403M (2008) and the Japanese standard JIS A 1147 (2019).

RESEARCH SIGNIFICANCE

In this paper, four common methods for measuring the time-zero of high-performance concrete are reviewed and examined in-depth: stress evolution measurement, autogenous strain measurement, ultrasonic pulse velocity (UPV) testing, and temperature rate method. By evaluating the four approaches, a fundamental and comprehensive understanding of the reliability and applicability of each approach is expected to be established. On that basis, the practical implications of determining the time-zero for construction operations and the potential impact on the prediction of early-age concrete properties are highlighted. Furthermore, the reliability of using either the initial or final setting time measured by penetration resistance to approximate the time-zero of high-performance concrete is also assessed, based on a case study of determining the time-zero and setting times of a concrete mixture with a water-binder ratio (*w*/*b*) of 0.25. Besides, this paper aims to assess the consistency of the common methods used in practice and has no intention of stressing the accuracy because the definition of time-zero in different methods cannot be the same.

EXPERIMENTAL PROCEDURE

Stress evolution measurement

To determine the time-zero of concrete, one direct approach is to monitor the stress of concrete induced by externally restrained volume changes at early ages (Darquennes et al. 2011; Delsaute et al. 2017; Klausen 2016; Li et al. 2020a).

ACI Materials Journal, V. 121, No. 3, May 2024.

MS No. M-2023-093.R2, doi: 10.14359/51740565, received October 31, 2023, and reviewed under Institute publication policies.

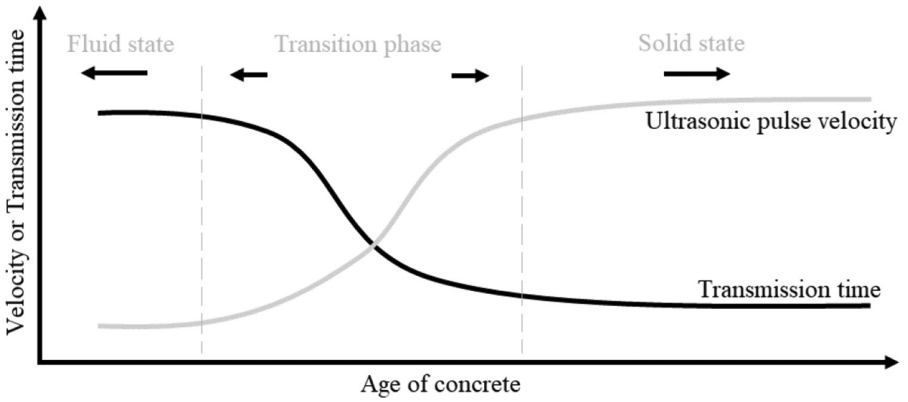

Fig. 1—Schematic diagram of evolutions of transmission time and UPV.

Generally, the volume changes may consist of thermal strain, autogenous strain, and drying shrinkage. While considerable volume changes tend to occur before setting, the concrete is too young to develop compressive or tensile stress. As the solidification of early-age concrete proceeds, the early-age stress induced by restrained volume changes gradually builds up. Accordingly, the time point when concrete starts to develop stresses induced by externally restrained deformation can be considered as the time-zero (Klausen 2016; Li et al. 2020a; Wei and Hansen 2013). However, due to the lack of suitable test facilities for measuring the stress of young concrete, the method for determining the time-zero according to the stress evolution has been less used in practice. In this paper, using the advanced temperature-stress testing machine (TSTM) that has been successfully used to measure a number of early-age properties of concrete (Dabarera et al. 2022; Li et al. 2020a, 2021; Nguyen et al. 2019), the stress evolution method for determining the time-zero of concrete is studied.

Autogenous strain measurement

The time-zero can also be determined by analyzing the development of the autogenous strain of young concrete under a restraint-free condition. Generally, before the time-zero, the autogenous strain of early-age concrete evolves quite rapidly (essentially identical to chemical shrinkage) because the solid skeleton has not formed yet. As the state of concrete transfers from fluid to solid, the bulk modulus evolves, and as a consequence, the rate of the evolution of autogenous strain drops over time (Lura et al. 2003). The remarkable turning point in the rate of autogenous strain can approximately be defined as the time-zero. Compared to the stress evolution measurement, the autogenous strain method seems to be relatively easier, yet the reliable deformation measurement from as early as the final setting time remains challenging. Many researchers reported that corrugated plastic tubes could be used to measure the autogenous strain of cement paste and mortar (Huang and Ye 2017; Jensen and Hansen 1995; Wyrzykowski et al. 2017). However, such proposed corrugated tubes with typical inside diameters ranging from 25 to 30 mm are evidently not suitable for measuring the autogenous strain of concrete. In this paper, the autogenous strain method for determining the time-zero of concrete is evaluated using the TSTM employed in Dabarera et al. (2022), Li et al. (2020a), and Nguyen et al. (2019), and the reliability of the measured data is also examined.

UPV testing

Ultrasonic testing has been extensively used to assess the hardening process of cement-based composites (Karaiskos et al. 2015; Reinhardt et al. 2000; Trtnik et al. 2008) based on the time (t) that it takes an ultrasonic pulse to propagate through a specimen, as given by Eq. (1)

$$t = \frac{L}{V} \tag{1}$$

where L is the length of pulse transmission (mm); and V is the UPV (m/s).

Figure 1 shows a schematic diagram of the evolutions of transmission time and UPV as a function of concrete age. Within a short period after mixing, fresh concrete remains in an approximately fluid state, and the UPV (V) therein is similar to that in water (Trtnik et al. 2008). As cementitious material hydrates and the solidification of concrete proceeds, the UPV begins to increase quickly. For a given pulse transmission length (L), the sharp increase in the velocity results in a corresponding sharp decrease in the transmission time (t). Karaiskos et al. (2015) suggested that the phase corresponding with the rapid decrease in the transmission time (or the sharp increase in the UPV) could be considered the transition period between fluid and solid states of early-age concrete. On that basis, the time of the onset of the drastic decrease in transmission time (or the onset of the drastic increase in UPV) was defined as the time-zero (Sant et al. 2009; Trtnik et al. 2008; Zhutovsky and Kovler 2017). However, such a time-zero may just represent the onset of the formation of the local solid skeleton of early-age concrete (Karaiskos et al. 2015). To determine a more reasonable time-zero corresponding to the formation of an interconnected network that enables a relatively stable propagation of ultrasonic pulse, further research is performed in this paper.

Temperature rate method

To facilitate the description of the theoretical basis of the temperature rate method, first, the hydration heat evolution

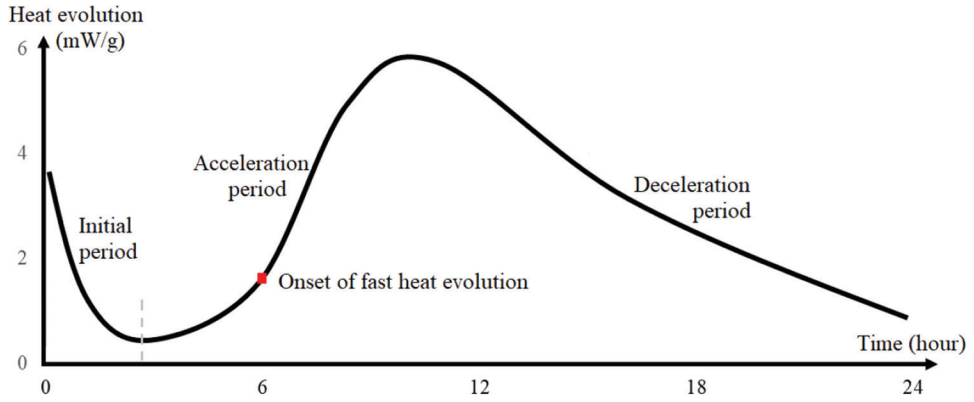

Fig. 2—Schematic diagram of hydration heat evolution of cement.

of cementitious materials should be reviewed (refer to Fig. 2). During the first ~3 hours following mixing, cement hydration is at an initial period in which the evolution of hydration heat reduces over time (Bullard et al. 2011; Scrivener et al. 2019). As a result, the temperature rise of concrete may be quite limited in this short period. At the end of the initial period, the hydration reaction starts to accelerate and enters the main hydration phase, which consists of an acceleration period and a deceleration period (Bullard et al. 2011; Scrivener et al. 2019). During the acceleration period, the onset of the fast evolution of hydration heat indicates that the silicates (mainly C_3S) start to hydrate quickly, leading to a rapid formation of an interconnected solid skeleton of cement paste (Bensted 1987; Carette and Staquet 2015).

According to the theory of heat transfer (Hunger et al. 2009; Rastrup 1954; De Schutter and Taerwe 1995), the temperature change induced by hydration heat in adiabatic conditions can be expressed as

$$\Delta T = \frac{\Delta Q}{mc} \tag{2}$$

where m is the mass (kg); c is the specific heat capacity (J/(kg·°C)); and ΔQ is the production of hydration heat (J) within a time interval Δt.

Accordingly, the rate of change in temperature ($R(t)$) induced by hydration heat can be determined by Eq. (3). In reality, the rate of temperature change is affected by ambient temperature and the thermal boundary conditions of concrete. Even so, as long as the concrete temperature is governed by the heat of hydration, the time point when the rate of temperature rise begins to accelerate is deemed negligibly affected by ambient and boundary conditions (Cusson and Hoogeveen 2007). According to the theory of heat transfer (Hunger et al. 2009; Rastrup 1954; De Schutter and Taerwe 1995), the main factor resulting in the change in $R(t)$ is the acceleration and deceleration of hydration heat evolution, as shown in Fig. 2. Besides, the decrease in the specific heat (c) during the transition phase from fluid to solid state of fresh concrete can also cause the change in $R(t)$. Based on the rate of temperature change of early-age concrete, the onset of the sharp increase in $R(t)$ has been recommended as the time-zero (Cusson and Hoogeveen 2007; Li et al. 2020a). However, due to the lack of substantial studies, further research is needed to verify the reliability of such a method.

$$R(t) = \frac{\Delta T}{\Delta t} \tag{3}$$

Table 1—Composition of concrete mixture

Components	kg/m^3
Cement	560
Fly ash	120
Silica fume	40
Water	180
Fine sand	240
Coarse sand	250
10 mm aggregate	930
High-range water-reducing admixture	3.2

RAW MATERIALS AND TEST SETUPS

Concrete mixture design

As one of the typical high-performance concretes studied and used in Australia (Dabarera et al. 2021, 2022; Li et al. 2020a, 2022; Li 2021), a concrete mixture with a w/b of 0.25 and 28-day compressive strength of approximately 85.0 MPa was used to demonstrate the determination of time-zero and setting time through different approaches (refer to Table 1). The oxide compositions of cementitious materials and the particle size of sands and aggregates are listed in Tables 2 and 3. The slump of the fresh concrete, measured in accordance with the Australian standard AS 1012.3.1 (2014), was 230 ± 10 mm.

Test setups and specimens

The TSTM, which has been successfully used in the author's previous research (Dabarera et al. 2021, 2022; Li et al. 2020a, 2021), was used to determine the time-zero of early-age concrete in this paper, as shown in Fig. 3. In addition, a pulse analyzer conforming to ASTM C597 (2016) was used for ultrasonic testing of early-age concrete. In this work, three concrete specimens were cast, and after casting, all specimens were sealed to minimize drying. Two of the three specimens were prepared for the TSTM system: 1) one specimen (the dog-bone-shaped TSTM specimen [refer

to Fig. 3]), with dimensions of 80 x 80 x 1000 mm, was primarily to monitor the stress evolution induced in early-age concrete as a result of restrained volume changes (Li et al. 2020a); 2) the other specimen (the free deformation specimen, with dimensions of 80 x 80 x 1000 mm [refer to Fig. 3]) aimed to collect deformation of early-age concrete under restraint-free conditions. The third concrete specimen, with dimensions of 75 x 75 x 280 mm, was prepared for ultrasonic testing. Approximately 5 hours after casting, the specimen was demolded for performing UPV tests. According to ASTM C597-16, two transmission lengths of 280 and 75 mm were measured in the analysis of ultrasonic pulse transmission in the concrete specimen (refer to Fig. 4). The frequency of the ultrasonic pulse used was 55 kHz, and the pulse rate was 0.5 seconds.

In addition, three mortar samples sieved from fresh concrete were prepared:

- Two of the three samples (with dimensions of ϕ160 x 160 mm), cast in cylindrical plastic containers, were used to determine the initial and final setting times by penetration resistance. After casting, the two samples were stored and tested in a room with the temperature controlled at 23 ± 1.5°C.
- The third mortar sample, with dimensions of ϕ100 x 120 mm, was for measuring the temperature rise within the sample due to cement hydration. To minimize the influence of the ambient environment, the sample was sealed with plastic film and coated with polyethylene foam. The analog temperature sensors (with a measurement range between 0 and 100°C and an accuracy of ±0.75°C [refer to Fig. 5]) were used for the temperature measurements in this study.

Table 2—Oxide compositions of cement, fly ash, and silica fume (by mass, %)

	Cement	Fly ash	Silica fume
CaO	63.9	3.80	—
SiO_2	19.5	59.4	89.9
Al_2O_3	5.40	20.4	—
SO_3	2.64	0.20	0.84
Fe_2O_3	2.83	10.9	—
MgO	1.40	1.50	—
Na_2O	0.32	0.67	0.11
K_2O	0.42	1.42	0.23
Loss on ignition	3.11	0.70	3.80

EXPERIMENTAL RESULTS AND DISCUSSION

Time-zeros measured by stress evolution and autogenous strain development

The temperature and stress profiles of the TSTM concrete specimen under restrained conditions were recorded from approximately 5.0 hours after mixing, as plotted in Fig. 6. From 5.0 to ~8.3 hours, the measured total stress remained almost zero, which implied that in this period, the concrete was too young to form a solid skeleton and failed to behave like a solid. After 8.3 hours, the evolution of early-age stress induced by the restrained thermal strain and autogenous shrinkage was observed. Accordingly, this time point of 8.3 hours (as marked in the red square in Fig. 6), from which the concrete started to form the capacity for bearing

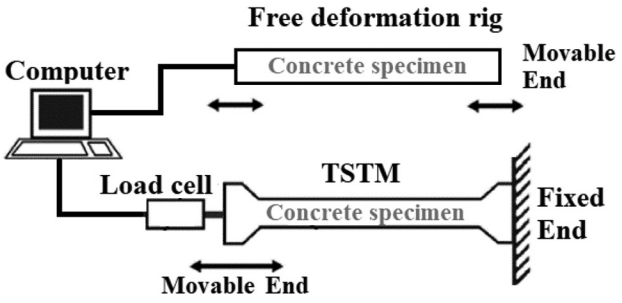

Fig. 3—Diagram of advanced TSTM used.

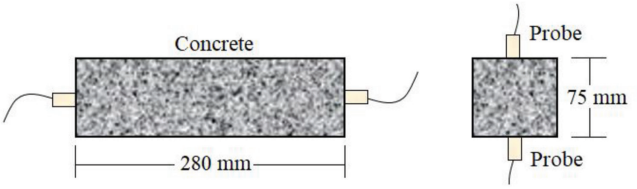

Fig. 4—Transducer probe arrangement for ultrasonic testing.

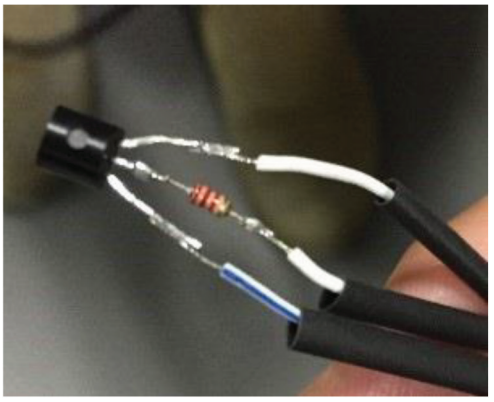

Fig. 5—Analog temperature sensor.

Table 3—Particle-size distribution of aggregates

Sieve size, mm		14.00	9.50	4.75	2.36	1.18	0.60	0.30	0.15	0.075
Passing rate, %	Fine sand	100	100	97.4	83.1	68.7	44.7	16.5	4.5	1.0
	Coarse sand	100	100	99.5	75.5	46.3	26.9	14.1	7.3	3.3
	Aggregate	100	86.8	6.8	2.0	1.7	1.5	1.3	1.1	0.4

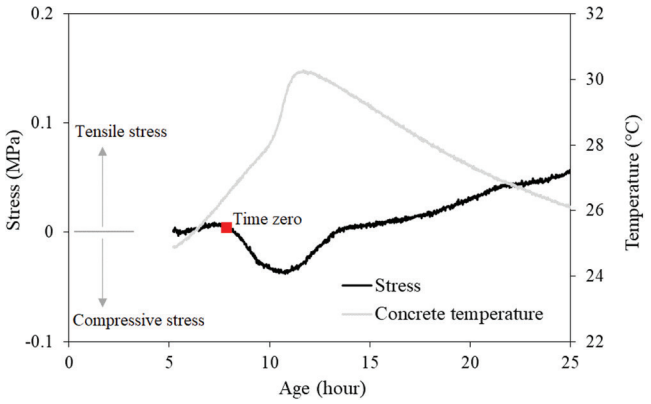

Fig. 6—Time-zero of concrete determined by stress evolution due to restrained deformation.

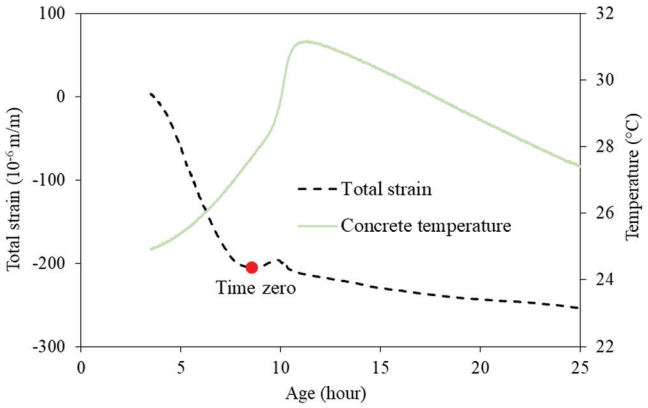

Fig. 7—Time-zero determined by free strain profile of early-age concrete.

measurable stress (Li et al. 2020a; Shen et al. 2018; Wei and Hansen 2013), should be considered as the time-zero. From 8.3 to ~10.5 hours, the measured stress became increasingly compressive (Fig. 6), resulting from the accumulation of the restrained thermal expansion. After that, due to the combined effect of thermal contraction and autogenous shrinkage, the compressive stress reduced and gradually transferred into tensile stress.

Figure 7 presents the development of the measured total strain of the concrete specimen in the free deformation test. The total strain comprises thermal strain and autogenous strain. From 4.0 to ~8.5 hours, even though the temperature of the specimen increased by approximately 2.5°C, negligible thermal expansion (estimated at 10 to 15 × 10^{-6} m/m) took place due to the low coefficient of thermal expansion of concrete (Li et al. 2020b, 2021; Sellevold and Bjøntegaard 2006). Because the autogenous strain (at least ~210 × 10^{-6} m/m) was more than one order of magnitude larger than the thermal expansion during this period, the specimen contracted significantly (refer to Fig. 7). As the solid skeleton of the hydrating concrete formed gradually, the evolution rate of autogenous strain reduced over time. At ~8.5 hours, the evolution rate was nearly zero, indicating that an integral solid skeleton of concrete was established. Therefore, this time point (8.5 hours) could be referred to as the time-zero (Tenório Filho et al. 2019; Li et al. 2020a). After the time-zero, the specimen expanded slightly (refer to Fig. 7), which was a combined effect of thermal expansion induced by rapid temperature rise (~3.6°C) partly counteracted by autogenous strain. At ~10.2 hours, the thermal expansion reached a summit (refer to Fig. 7), which aligned well with the occurrence time of the maximum compressive stress induced by the restrained expansion (refer to Fig. 6).

Time-zero determined by UPV measurement

Following the experimental approach introduced earlier, the transmission time of the ultrasonic pulse in the concrete specimen was determined at different ages for two transmission lengths of 280 and 75 mm, as shown in Fig. 4. The evolutions of the measured transmission time and its rate of change for each transmission length are plotted in Fig. 8(a) and (b), respectively. It can be seen that both the transmission time and its rate of change decreased rapidly at very early ages and started to stabilize at the age of ~8.0 hours. The rate of the change in transmission time stabilized at 8.0 hours, indicating that the solid hydrates of cementitious materials might have formed an interconnected network that enables a relatively stable propagation of ultrasonic pulse (Sant et al. 2009). It is noteworthy that the featured time point determined by the rate of change in transmission time (8.0 hours) appears to be consistent with the time-zero measured by the stress evolution measurement and autogenous strain method (8.3 and 8.5 hours, respectively). Besides, based on the measured transmission time, the UPV of the concrete specimen can be calculated (refer to Fig. 8(c)). According to the rate of the velocity change, the same time-zero point can also be obtained, as marked in Fig. 8(c). Therefore, defining the time point from which the rate of change in the transmission time (or the UPV) became essentially constant as the time-zero seems appropriate. Accordingly, the time-zero of the tested concrete specimen in this study, determined on the basis of ultrasonic testing, was ~8.0 hours.

Time-zero estimated by temperature rate method

The temperature of the mortar sample with dimensions of ϕ100 x 120 mm, measured by the temperature sensor embedded in the core of the sample, is plotted in Fig. 9. During the first ~3.0 hours after mixing, the temperature of the mortar sample remained almost unchanged because the limited heat production by hydration was offset by the heat loss to the ambient. From 3.0 to ~10.0 hours, due to the acceleration of cement hydration, the temperature of the mortar increased significantly (refer to Fig. 9). After peaking at 47.6°C, the sample entered a temperature-decreasing phase in which the loss of heat to the ambient exceeded the production of hydration heat. The rate of the temperature change of the mortar sample calculated by combining the measured temperature and Eq. (3) is plotted in Fig. 9. Based on the rate of temperature change, the time-zero of the mortar sample was determined at ~7.9 hours (refer to Fig. 9).

In addition to the mortar sample, the temperature of the concrete specimen in the free deformation test was also measured (from the age of ~4.0 hours), as shown in Fig. 10. From ~4.0 to 11.5 hours, the temperature of the concrete specimen increased significantly. After peaking at a temperature of 31.6°C, the concrete temperature started to decrease

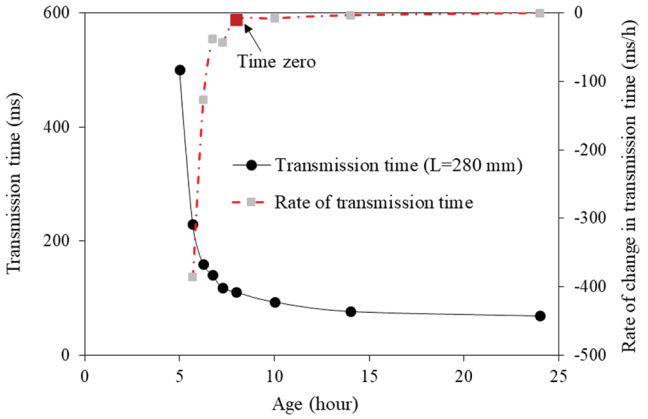

(a) L=280 mm

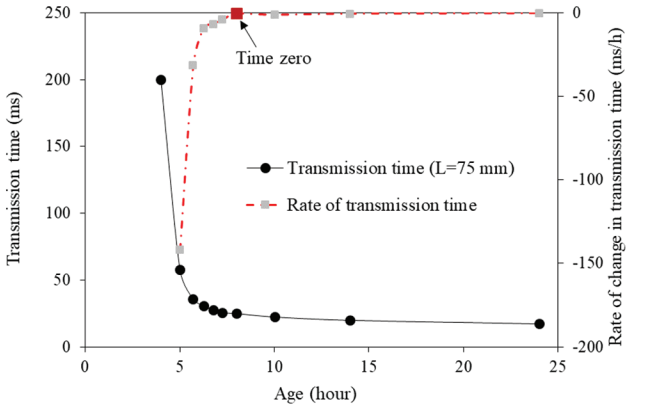

(b) L=75 mm

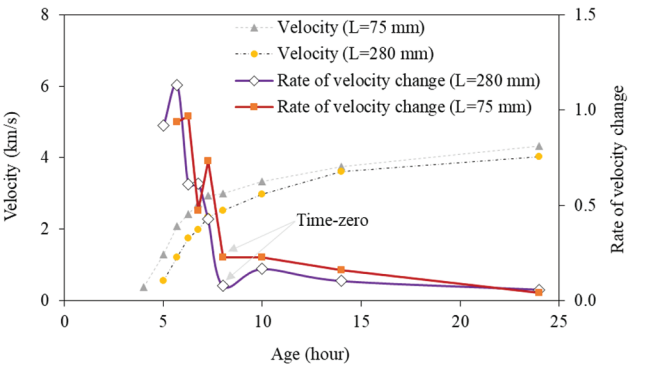

(c) Rate of velocity

Fig. 8—Time-zero measured by rate of transmission time of ultrasonic pulse.

gradually due to the combined effect of reduced rate of hydration and heat loss (as explained earlier). Based on the calculated rate of temperature change of the specimen, the time-zero of concrete was estimated at approximately 8.4 hours (refer to the red marker in Fig. 10). Comparing the time-zeros plotted in Fig. 9 and 11, a notable difference is that although the same temperature rate method was used, the determined time-zero of mortar (~7.9 hours) was slightly earlier than the time-zero of concrete (~8.4 hours).

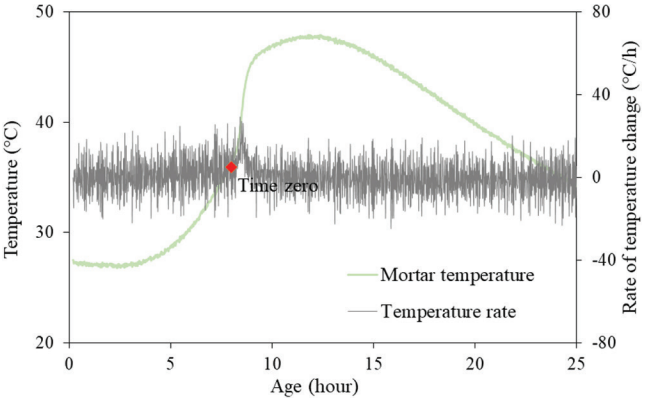

Fig. 9—Time-zero of mortar measured by rate of temperature change.

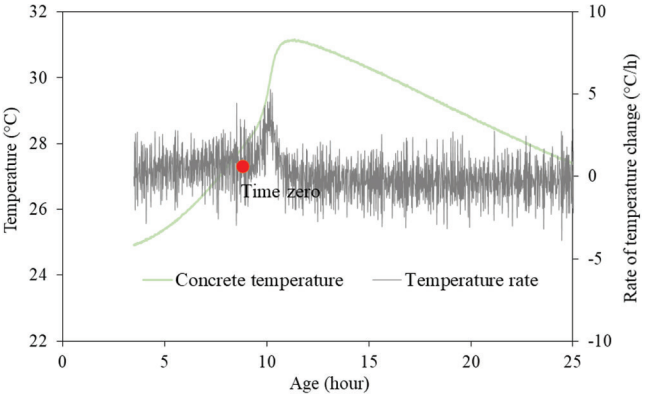

Fig. 10—Time-zero of young concrete measured by rate of temperature change.

Such a difference may result mainly from different temperature profiles of the mortar sample and the concrete specimen (Carette and Staquet 2015; Pinto and Hover 1999): higher temperature rise leads to an accelerated development of solidification, and therefore, earlier occurrence in the time-zero.

Initial and final setting times of concrete

Setting times of mortar sieved from fresh concrete were measured by penetration resistance, in accordance with AS 1012.18-1996. The results are plotted in Fig. 11, in which each data point represents the average value of four penetration resistance measurements. The obtained initial and final setting times are approximated at ~5.0 and 6.9 hours when the penetration resistance of mortar reaches 3.5 and 28.0 MPa, respectively. Compared to the measured time-zeros from other methods, the obtained initial and final setting times (5.0 and 6.9 hours, respectively) are shorter. Consequently, using the initial or final setting time to approximate the time-zero corresponding to the formation of the solid skeleton of concrete seems questionable. Assuming the initial or final setting time as the time-zero can compromise the reliable predictions of early-age concrete properties (for example, strength, Young's modulus, and autogenous shrinkage) and even mislead construction operations (for example, finishing, saw-cutting, and curing). Further discussion can be found in the following section.

COMPARISON OF RESULTS AND PROSPECTIVE RESEARCH

To properly determine the time-zero, defined as the time point when concrete materials form a stable solid skeleton to sustain tensile and compressive stresses (Huang and Ye 2017; Li et al. 2020a; Sant et al. 2009), different methods proposed in the literature are reviewed and examined in this work. Through the previous analysis, the time-zeros and setting times of mortar and concrete obtained using different experimental approaches are summarized in Fig. 12. All measured time-zeros fall within a narrow range between ~7.9 and ~8.5 hours from mixing, indicating a good consistency among the four methods as well as their reliability. However, compared to the complexity of monitoring the strain and stress of early-age concrete, the pulse transit time and temperature can be conveniently measured using readily available test equipment. Although the temperature rate method has been investigated less in the literature, this study implies good applicability of the method for measuring the time-zero of concrete. Besides, the turning point of the change in the rate of the transmission time of the ultrasonic pulse in concrete appears to be a reliable indicator of the time-zero as well. Overall, the temperature rate method and UPV testing both show good reliability and suitability for determining the time-zero of concrete. In addition, it should be underlined that the actual temperature profiles of mortar and concrete samples can affect the determination of the time-zero (Carette and Staquet 2015; Pinto and Hover 1999) due to the temperature dependence of cement hydration reactions. To realistically reflect the time-zero of concrete elements in practice, the temperature rate method appears to be the best option due to its simplicity and availability. Without considering the actual temperature profile of cement-based composites, the estimated time-zero at laboratory conditions may be less accurate. Therefore, further research is needed to shed light on the effect of temperature on the solidification process of cement-based composites.

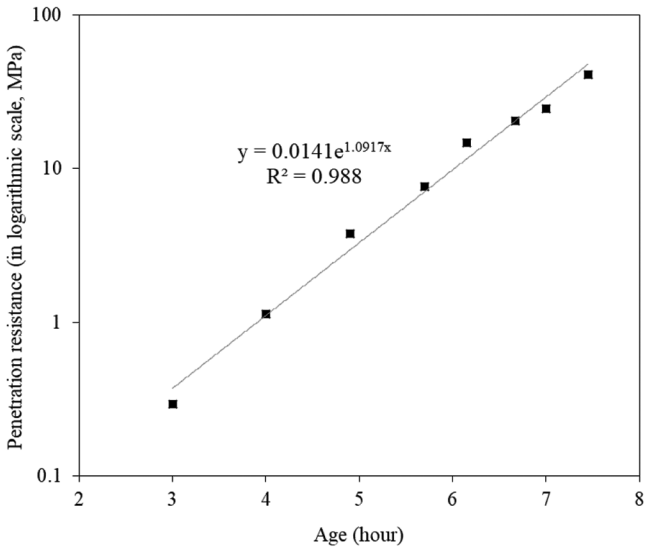

Fig. 11—Penetration resistance of mortar sieved from concrete.

In Fig. 12, it can be observed that the initial and final setting times of mortar measured by penetration resistance both appear earlier than the time-zero determined by other methods. Accordingly, using the initial or final setting time to represent the time-zero seems inappropriate. In particular, the strain tends to be overestimated when referring to the initial or final setting time as the time-zero for the start of counting autogenous strain. Such an overestimation has been reported in the determination of autogenous strain of cement pastes (Huang and Ye 2017; Ma et al. 2019). Besides autogenous strain, using the initial or final setting time to approximate the time-zero may also compromise the predictions of other properties of concrete from very early ages, including tensile/compressive strength and elastic modulus. Besides, the standard experimental procedure of performing penetration resistance tests to measure the initial or final setting time of mortar sieved from concrete may also need further revisions to reflect the influence of temperature on the setting times.

SUMMARY AND CONCLUSIONS

In this paper, four different methods (namely, stress evolution measurement, autogenous strain measurement, ultrasonic pulse velocity [UPV] testing, and temperature rate method) for determining the time-zero of concrete and mortar are reviewed and evaluated based on a case study. Both the theoretical basis and the actual applicability of each method are demonstrated. Besides, the initial and final setting times of concrete measured by penetration resistance are also included and investigated for comparison. Based on the obtained results, the following conclusions can be drawn:

- The applicability and reliability of different methods for determining the time-zero of high-performance

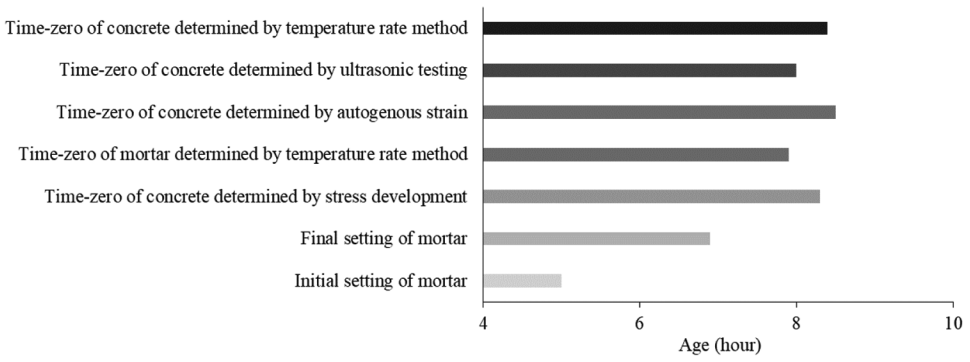

Fig. 12—Measured time-zeros and setting times of concrete and mortar in case study.

concrete are examined. In determining the time-zero of high-performance concrete with a water-binder ratio (w/b) of 0.25, all time-zeros measured by the four different methods vary within a narrow range between ~7.9 and ~8.5 hours after mixing. Such a variation may result from different temperature profiles of the mortar and concrete samples tested. A high temperature can lead to an accelerated development of solidification, therefore contributing to earlier occurrence of the time-zero. To realistically reflect the time-zero of cement-based composites on site and take the temperature effect into account, the temperature rate method appears to be more suitable in practice than the other methods. In particular, when other methods are not accessible, the temperature rate method is strongly recommended due to the simplicity and the availability of temperature measurement.

- The initial and final setting times measured by penetration resistance are both earlier than the determined time-zeros of the high-performance concrete. Accordingly, the simple assumption of using the initial or final setting time to approximate the time-zero corresponding to the formation of the solid skeleton of concrete seems questionable. Using initial or final setting time as time-zero tends to overestimate the magnitude of the autogenous strain of concrete at early ages, compromise the reliable predictions of other early-age properties, and even mislead construction operations. Besides, it should be noted that to consider the temperature influence on setting times, the existing experimental procedure to measure the initial or final setting time by penetration resistance tests should be revised.

AUTHOR BIOS

Liang Li *is currently a Research Fellow in the School of Civil Engineering at The University of Queensland, Brisbane, QLD, Australia, where he received his PhD in civil engineering in 2021. His research interests include cement-based composites and low-carbon-footprint construction materials.*

ACKNOWLEDGMENTS

The financial support from the Research Training Program granted by the Australian Government is gratefully acknowledged. Part of the research also received funding from the Australian Research Council (Grant No. DP220103362 and DP180103160). The author would like to thank V. Dao (The University of Queensland, Brisbane, QLD, Australia) for his valuable discussion. The author declares that he has no known competing financial interests or personal relationships that could have appeared to influence the work reported in this paper.

REFERENCES

AS 1012.3.1:2014, 2014, "Methods of Testing Concrete – Method 3.1: Determination of Properties Related to the Consistency of Concrete – Slump Test," Standards Australia, Sydney, NSW, Australia, 6 pp.

AS 1012.18-1996, 1996, "Methods of Testing Concrete – Method 18: Determination of Setting Time of Fresh Concrete, Mortar and Grout by Penetration Resistance (Reconfirmed 2014)," Standards Australia, Sydney, NSW, Australia, 6 pp.

ASTM C191-08, 2008, "Standard Test Methods for Time of Setting of Hydraulic Cement by Vicat Needle," ASTM International, West Conshohocken, PA, 8 pp.

ASTM C403/C403M-08, 2008, "Standard Test Method for Time of Setting of Concrete Mixtures by Penetration Resistance," ASTM International, West Conshohocken, PA, 7 pp.

ASTM C597-16, 2016, "Standard Test Method for Pulse Velocity Through Concrete," ASTM International, West Conshohocken, PA, 4 pp.

Bensted, J., 1987, "Some Applications of Conduction Calorimetry to Cement Hydration," *Advances in Cement Research*, V. 1, No. 1, Oct., pp. 35-44. doi: 10.1680/adcr.1987.1.1.35

Bullard, J. W.; Jennings, H. M.; Livingston, R. A.; Nonat, A.; Scherer, G. W.; Schweitzer, J. S.; Scrivener, K. L.; and Thomas, J. J., 2011, "Mechanisms of Cement Hydration," *Cement and Concrete Research*, V. 41, No. 12, Dec., pp. 1208-1223. doi: 10.1016/j.cemconres.2010.09.011

Carette, J., and Staquet, S., 2015, "Monitoring the Setting Process of Mortars by Ultrasonic P and S-Wave Transmission Velocity Measurement," *Construction and Building Materials*, V. 94, Sept., pp. 196-208. doi: 10.1016/j.conbuildmat.2015.06.054

Cusson, D., and Hoogeveen, T., 2007, "An Experimental Approach for the Analysis of Early-Age Behaviour of High-Performance Concrete Structures under Restrained Shrinkage," *Cement and Concrete Research*, V. 37, No. 2, Feb., pp. 200-209. doi: 10.1016/j.cemconres.2006.11.005

Dabarera, A.; Li, L.; and Dao, V., 2021, "Experimental Evaluation and Modelling of Early-Age Basic Tensile Creep in High-Performance Concrete," *Materials and Structures*, V. 54, No. 3, June, Article No. 130. doi: 10.1617/s11527-021-01722-w

Dabarera, A.; Li, L.; Lura, P.; and Dao, V., 2022, "Experimental Assessment and Modelling of Effective Tensile Elastic Modulus in High Performance Concrete at Early Age," *Construction and Building Materials*, V. 319, Feb., Article No. 126125. doi: 10.1016/j.conbuildmat.2021.126125

Darquennes, A.; Staquet, S.; Delplancke-Ogletree, M.-P.; and Espion, B., 2011, "Effect of Autogenous Deformation on the Cracking Risk of Slag Cement Concretes," *Cement and Concrete Composites*, V. 33, No. 3, Mar., pp. 368-379. doi: 10.1016/j.cemconcomp.2010.12.003

De Schutter, G., and Taerwe, L., 1995, "Specific Heat and Thermal Diffusivity of Hardening Concrete," *Magazine of Concrete Research*, V. 47, No. 172, Sept., pp. 203-208. doi: 10.1680/macr.1995.47.172.203

Delsaute, B.; Torrenti, J.-M.; and Staquet, S., 2017, "Modeling Basic Creep of Concrete since Setting Time," *Cement and Concrete Composites*, V. 83, Oct., pp. 239-250. doi: 10.1016/j.cemconcomp.2017.07.023

fib, 2013, "*fib* Model Code for Concrete Structures 2010," International Federation for Structural Concrete, Lausanne, Switzerland, 434 pp.

Huang, H., and Ye, G., 2017, "Examining the 'Time-Zero' of Autogenous Shrinkage in High/Ultra-High Performance Cement Pastes," *Cement and Concrete Research*, V. 97, July, pp. 107-114. doi: 10.1016/j.cemconres.2017.03.010

Hunger, M.; Entrop, A. G.; Mandilaras, I.; Brouwers, H. J. H.; and Founti, M., 2009, "The Behavior of Self-Compacting Concrete Containing Micro-Encapsulated Phase Change Materials," *Cement and Concrete Composites*, V. 31, No. 10, Nov., pp. 731-743. doi: 10.1016/j.cemconcomp.2009.08.002

Jensen, O. M., and Hansen, P. F., 1995, "A Dilatometer for Measuring Autogenous Deformation in Hardening Portland Cement Paste," *Materials and Structures*, V. 28, No. 7, Aug., pp. 406-409. doi: 10.1007/BF02473076

JIS A 1147:2019, 2019, "Method of Test for Time of Setting of Concrete Mixtures by Penetration Resistance," Japanese Industrial Standards, Japanese Standards Association, Tokyo, Japan, 11 pp.

JSCE, 2007, "Standard Specifications for Concrete Structures," Japan Society of Civil Engineers, Tokyo, Japan.

Kanstad, T.; Hammer, T. A.; Bjøntegaard, Ø.; and Sellevold, E. J., 2003, "Mechanical Properties of Young Concrete: Part II: Determination of Model Parameters and Test Program Proposals," *Materials and Structures*, V. 36, No. 4, May, pp. 226-230. doi: 10.1007/BF02479615

Karaiskos, G.; Deraemaeker, A.; Aggelis, D. G.; and Van Hemelrijck, D., 2015, "Monitoring of Concrete Structures Using the Ultrasonic Pulse Velocity Method," *Smart Materials and Structures*, V. 24, No. 11, Nov., Article No. 113001. doi: 10.1088/0964-1726/24/11/113001

Kawashima, S., and Shah, S. P., 2011, "Early-Age Autogenous and Drying Shrinkage Behavior of Cellulose Fiber-Reinforced Cementitious Materials," *Cement and Concrete Composites*, V. 33, No. 2, Feb., pp. 201-208. doi: 10.1016/j.cemconcomp.2010.10.018

Klausen, A. B. E., 2016, "Early Age Crack Assessment of Concrete Structures: Experimental Investigation of Decisive Parameters," PhD thesis, Norwegian University of Science and Technology, Trondheim, Norway, 250 pp.

Kong, X.-M.; Zhang, Z.-L.; and Lu, Z.-C., 2015, "Effect of Pre-soaked Superabsorbent Polymer on Shrinkage of High-Strength Concrete," *Materials and Structures*, V. 48, No. 9, Sept., pp. 2741-2758. doi: 10.1617/s11527-014-0351-2

Li, L., 2021, "Deformational and Mechanical Early-Age Properties of High Performance Concrete with and without Superabsorbent Polymers," PhD thesis, The University of Queensland, Brisbane, QLD, Australia, 131 pp.

Li, L.; Dabarera, A.; and Dao, V., 2022, "Evaluation of Zero-Stress Temperature and Cracking Temperature of High Performance Concrete at

Early Ages," *Materials and Structures*, V. 55, No. 7, Sept., Article No. 181. doi: 10.1617/s11527-022-02019-2

Li, L.; Dabarera, A. G. P.; and Dao, V., 2020a, "Time-Zero and Deformational Characteristics of High Performance Concrete with and without Superabsorbent Polymers at Early Ages," *Construction and Building Materials*, V. 264, Dec., Article No. 120262. doi: 10.1016/j.conbuildmat.2020.120262

Li, L.; Dao, V.; and Lura, P., 2021, "Autogenous Deformation and Coefficient of Thermal Expansion of Early-Age Concrete: Initial Outcomes of a Study Using a Newly-Developed Temperature Stress Testing Machine," *Cement and Concrete Composites*, V. 119, May, Article No. 103997. doi: 10.1016/j.cemconcomp.2021.103997

Li, L.; O'Moore, L.; Dux, P.; Lura, P.; and Dao, V., 2020b, "Evolution of Coefficient of Thermal Expansion of Concrete at Early Ages," *ACMSM25: Proceedings of the 25th Australasian Conference on Mechanics of Structures and Materials*, C. M. Wang, J. C. M. Ho, and S. Kitipornchai, eds., Springer, Singapore, pp. 295-304.

Lura, P.; Couch, J.; Jensen, O. M.; and Weiss, J., 2009, "Early-Age Acoustic Emission Measurements in Hydrating Cement Paste: Evidence for Cavitation during Solidification Due to Self-Desiccation," *Cement and Concrete Research*, V. 39, No. 10, Oct., pp. 861-867. doi: 10.1016/j.cemconres.2009.06.015

Lura, P.; Jensen, O. M.; and van Breugel, K., 2003, "Autogenous Shrinkage in High-Performance Cement Paste: An Evaluation of Basic Mechanisms," *Cement and Concrete Research*, V. 33, No. 2, Feb., pp. 223-232. doi: 10.1016/S0008-8846(02)00890-6

Ma, Y.; Yang, X.; Hu, J.; Zhang, Z.; and Wang, H., 2019, "Accurate Determination of the 'Time-Zero' of Autogenous Shrinkage in Alkali-Activated Fly Ash/Slag System," *Composites Part B: Engineering*, V. 177, Nov., Article No. 107367. doi: 10.1016/j.compositesb.2019.107367

Miao, C.-W.; Tian, Q.; Sun, W.; and Liu, J.-P., 2007, "Water Consumption of the Early-Age Paste and the Determination of 'Time-Zero' of Self-Desiccation Shrinkage," *Cement and Concrete Research*, V. 37, No. 11, Nov., pp. 1496-1501. doi: 10.1016/j.cemconres.2007.08.005

Nguyen, D. H.; Nguyen, V. T.; Lura, P.; and Dao, V. T. N., 2019, "Temperature-Stress Testing Machine – A State-of-the-Art Design and Its Unique Applications in Concrete Research," *Cement and Concrete Composites*, V. 102, Sept., pp. 28-38. doi: 10.1016/j.cemconcomp.2019.04.019

Pinto, R. C. A., and Hover, K. C., 1999, "Application of Maturity Approach to Setting Times," *ACI Materials Journal*, V. 96, No. 6, Nov.-Dec., pp. 686-691.

Rastrup, E., 1954, "Heat of Hydration in Concrete," *Magazine of Concrete Research*, V. 6, No. 17, Sept., pp. 79-92. doi: 10.1680/macr.1954.6.17.79

Reinhardt, H. W.; Große, C. U.; and Herb, A. T., 2000, "Ultrasonic Monitoring of Setting and Hardening of Cement Mortar—A New Device," *Materials and Structures*, V. 33, No. 9, Nov., pp. 581-583. doi: 10.1007/BF02480539

Sant, G.; Dehadrai, M.; Bentz, D.; Lura, P.; Ferraris, C. F.; Bullard, J. W.; and Weiss, J., 2009, "Detecting the Fluid-to-Solid Transition in Cement Pastes," *Concrete International*, V. 31, No. 6, June, pp. 53-58.

Scrivener, K.; Ouzia, A.; Juilland, P.; and Kunhi Mohamed, A., 2019, "Advances in Understanding Cement Hydration Mechanisms," *Cement and Concrete Research*, V. 124, Oct., Article No. 105823. doi: 10.1016/j.cemconres.2019.105823

Sellevold, E. J., and Bjøntegaard, Ø., 2006, "Coefficient of Thermal Expansion of Cement Paste and Concrete: Mechanisms of Moisture Interaction," *Materials and Structures*, V. 39, No. 9, Nov., pp. 809-815. doi: 10.1617/s11527-006-9086-z

Shen, D.; Wang, W.; Liu, J.; Zhao, X.; and Jiang, G., 2018, "Influence of Barchip Fiber on Early-Age Cracking Potential of High Performance Concrete under Restrained Condition," *Construction and Building Materials*, V. 187, Oct., pp. 118-130. doi: 10.1016/j.conbuildmat.2018.07.121

Sleiman, H.; Perrot, A.; and Amziane, S., 2010, "A New Look at the Measurement of Cementitious Paste Setting by Vicat Test," *Cement and Concrete Research*, V. 40, No. 5, May, pp. 681-686. doi: 10.1016/j.cemconres.2009.12.001

Struble, L. J., and Lei, W.-G., 1995, "Rheological Changes Associated with Setting of Cement Paste," *Advanced Cement Based Materials*, V. 2, No. 6, Nov., pp. 224-230. doi: 10.1016/1065-7355(95)90041-1

Tenório Filho, J. R.; de Araújo, M. A. P. G.; Snoeck, D.; and De Belie, N., 2019, "Discussing Different Approaches for the Time-Zero as Start for Autogenous Shrinkage in Cement Pastes Containing Superabsorbent Polymers," *Materials*, V. 12, No. 18, Sept., Article No. 2962.

Trtnik, G.; Turk, G.; Kavčič, F.; and Bokan Bosiljkov, V., 2008, "Possibilities of Using the Ultrasonic Wave Transmission Method to Estimate Initial Setting Time of Cement Paste," *Cement and Concrete Research*, V. 38, No. 11, Nov., pp. 1336-1342. doi: 10.1016/j.cemconres.2008.08.003

Wei, Y., and Hansen, W., 2013, "Early-Age Strain–Stress Relationship and Cracking Behavior of Slag Cement Mixtures Subject to Constant Uniaxial Restraint," *Construction and Building Materials*, V. 49, Dec., pp. 635-642. doi: 10.1016/j.conbuildmat.2013.08.061

Wyrzykowski, M.; Hu, Z.; Ghourchian, S.; Scrivener, K.; and Lura, P., 2017, "Corrugated Tube Protocol for Autogenous Shrinkage Measurements: Review and Statistical Assessment," *Materials and Structures*, V. 50, No. 1, Feb., Article No. 57. doi: 10.1617/s11527-016-0933-2

Zhutovsky, S., and Kovler, K., 2017, "Application of Ultrasonic Pulse Velocity for Assessment of Thermal Expansion Coefficient of Concrete at Early Age," *Materials and Structures*, V. 50, No. 1, Feb., Article No. 5. doi: 10.1617/s11527-016-0866-9

CALL FOR ACTION

ACI Invites You To...

Share your expertise

Do you have EXPERTISE in any of these areas?

- BIM
- Chimneys
- Circular Concrete Structures Prestressed by Wrapping with Wire and Strand
- Circular Concrete Structures Prestressed with Circumferential Tendons
- Concrete Properties
- Demolition
- Deterioration of Concrete in Hydraulic Structures
- Electronic Data Exchange
- Insulating Concrete Forms, Design, and Construction
- Nuclear Reactors, Concrete Components
- Pedestal Water Towers
- Pipe, Cast-in-Place
- Strengthening of Concrete Members
- Sustainability

Then become a REVIEWER for the *ACI Structural Journal* or the *ACI Materials Journal*.

Become a Reviewer for the ACI Journals

How to become a Reviewer:

1. Go to: **http://mc.manuscriptcentral.com/aci;**
2. Click on "Create Account" in the upper right-hand corner; and
3. Enter your E-mail/Name, Address, User ID and Password, and Area(s) of Expertise.

Update your Manuscript Central user account information

Did you know that the database for MANUSCRIPT CENTRAL, our manuscript submission program, is separate from the ACI membership database?

How to update your user account:

1. Go to **http://mc.manuscriptcentral.com/aci;**
2. Log in with your current User ID & Password; and
3. Update your E-mail/Name, Address, User ID and Password, and Area(s) of Expertise.

QUESTIONS?

E-mail any questions to Journals.Manuscripts@concrete.org.

American Concrete Institute

Always advancing

ACI MATERIALS JOURNAL TECHNICAL PAPER

Title No. 121-M27

Development and Characterization of Tension-Hardening Quarry Waste-Based Geopolymer Concrete

by Zoi G. Ralli and Stavroula J. Pantazopoulou

In light of the effort for decarbonization of the energy sector, it is believed that common geopolymer binding materials such as fly ash may eventually become scarce and new geological aluminosilicate materials should be explored as alternative binders in geopolymer concrete. A novel, tension-hardening geopolymer concrete (THGC) that incorporates high amounts of semi-reactive quarry wastes (metagabbro) as a precursor, and coarse quarry sand (granite) was developed in this study using geopolymer formulations. The material was optimized based on the particle packing theory and was characterized in terms of mechanical, physical, and durability properties (that is, compressive, tensile, and flexural resistance; Young's modulus; Poisson's ratio; absorption; drying shrinkage; abrasion; coefficient of thermal expansion; and chloride-ion penetration, sulfate, and salt-scaling resistance). The developed THGC, with an air-dry density of 1940 kg/m³ (121 lb/ft³), incorporates short steel fibers at a volume ratio of 2%, and is highly ductile in both uniaxial tension and compression (uniaxial tensile strain capacity of 0.6% at an 80% post-peak residual tensile strength). Using digital image correlation (DIC), multiple crack formation was observed in the strain-hardening phase of the tension response. In compression, the material maintained its integrity beyond the peak load, having attained 1.8% compressive strain at 80% post-peak residual strength, whereas upon further reduction to 50% residual strength, the sustained axial and lateral strains were 2.5% and 3.5%, respectively. The material exhibited low permeability to chloride ions and significant abrasion resistance due to the high contents of metagabbro powder and granite sand. The enhanced properties of the material, combined with the complete elimination of ordinary portland cement from the mixture, hold promise for the development of sustainable and resilient structural materials with low CO_2 emissions, while also enabling the innovative disposal of wastes as active binding components.

Keywords: CO_2 emissions; digital image correlation (DIC); ductility; durability; geopolymer concrete; metagabbro powder; steel fibers; strain-hardening; tension-hardening.

INTRODUCTION

Tension-hardening fiber-reinforced concrete (THFRC) brings great potential as a structural material in modern infrastructure, primarily owing to the opportunities it offers in structural design on account of its increased tensile deformation capacity. THFRC materials that also combine low CO_2 emissions present an ideal combination, considering the pressing need for more resilient, green structures as a way to tackle the climate emergency. Among the few alternative sustainable construction materials that have emerged in recent years, geopolymer technology for synthesizing concrete has received increasingly more interest among researchers and industry. Motivated by the need for safe disposal of various industrial by-products, such as fly ash (FA), ground-granulated blast-furnace slag (GGBFS), and silica fume (SF), and the prospect of simultaneous elimination of ordinary portland cement (OPC) as a great contributor to the globe's CO_2 emissions, geopolymer concretes can be made using a variety of alternative powders, collectively referred to as geopolymer precursors. The latter are mostly industrial by-products and calcined or raw aluminosilicate resources (for example, metakaolin [MK], weathered rocks, and so on).[1,2]

Imparting tension-hardening characteristics to geopolymer concretes (THGC) is a way to combine the objective of considerably reducing the carbon footprint and recycling of industrial wastes instead of harmful disposal, while at the same time harnessing the benefits of high performance with sustainability. However, owing to the wide variability of the mineral and chemical composition of the wastes, the characterization of both mechanical and durability properties to ensure that the performance requirements are met is a prerequisite for the successful implementation of these materials in construction.

Past experimental characterization studies of THGC have focused on the evaluation of compressive and flexural strength, modulus of elasticity, and tensile strength. Hybrid fiber combinations of steel fibers for improved mechanical strength and synthetic fibers (for example, polyvinyl alcohol [PVA] fibers) for enhanced deformation capacity and fire resistance have been considered.[3-6] The curing method has also been a key parameter in the various THGC variants. It is shown that for FA-based THGC, heat curing enhances flexural hardening and promotes multiple cracking.[7,8] In ambient curing, steel fibers were found to be more effective than synthetic fibers in terms of strength increase and at high contents (>3%) also in achieving deformation capacity increase.[3,6] While most of the available studies are done using conventional geopolymer binders, in a recent study a heat-cured liquid crystal display glass and GGBFS-based THGC with polyethylene (PE) fibers was characterized in terms of mechanical properties. By varying the sand-binder ratio (*S*/*B*), the authors found that higher *S*/*B* enhanced the compressive and tensile strength but compromised the strain capacity.[9]

ACI Materials Journal, V. 121, No. 3, May 2024.

MS No. M-2023-096.R3, doi: 10.14359/51740704, received January 10, 2024, and reviewed under Institute publication policies.

Fewer studies report on the durability of THGC. Heat-cured FA/GGBFS-based THGCs have demonstrated excellent abrasion resistance with mass loss of less than 1 g, satisfying freezing-and-thawing resistance and drying shrinkage of less than 400 με.[10,11] The enhanced performance was attributed to heat curing, which might be impractical for large-scale applications. However, higher shrinkage in the 1500 to 5500 με range was attained when PVA fibers were used in an ambient-cured FA/GGBFS THGC.[6] Satisfactory resistance in sulfate and seawater attack has also been reported for a lightweight GGBFS and copper slag-based THGC incorporating PVA.[11] In the same direction, very low chloride-ion penetrability and high resistance to chloride ingress were found in an ultra-high-performance GGBFS/SF THGC containing steel and polypropylene fibers.[12]

It is noted, however, that it is not possible to generalize the results of the available literature, because both mechanical and durability properties are very much affected by the curing method, mineralogy, and chemical composition of the precursors.

Most of the aforementioned studies were performed on THGCs based on typical geopolymer binders, such as FA. However, with the elimination of coal burning for energy production, by-products that are predominantly used as precursors in geopolymers (for example, FA) are expected to gradually become unavailable in the long term, and may not be a sustainable solution for the decarbonization of infrastructure.[1,13] Therefore, there is a need to develop geopolymer concretes using alternative aluminosilicate powders, such as geological raw materials, that are available worldwide.[1,14] In the present study, this objective is addressed by using high amounts of quarry wastes (metagabbro) as precursors; these contain large concentrations of iron and aluminosilicates, are easily accessible in nature, and enable the development of structural concrete materials with significantly reduced CO_2 footprint.

RESEARCH SIGNIFICANCE

A novel geopolymer concrete is developed in this work which combines three attributes that define the significance of the research: a) the mixture is sustainable, containing no OPC; b) iron-rich quarry waste powders are part of the precursor in the role of binder (and are not just used as aggregate), while partially reactive granite sand participates in the geopolymerization; and c) the hardened material is ductile, exhibiting tension-hardening response with satisfactory tensile strength and strain capacity. As the properties of any geopolymer concrete are particularly sensitive to the composition of its ingredients, a complete characterization of the proposed material is undertaken to illustrate the opportunities available in developing new sustainable concrete materials with favorable properties and reduced CO_2 footprint by directly incorporating pertinent rocks as binders without prior incineration.

EXPERIMENTAL INVESTIGATION

This study presents the development and characterization of primary mechanical, physical, and durability properties of a novel THGC that contains a high amount of quarry waste powder (metagabbro), which is used in the synthesis of the material in partial replacement to conventional geopolymer precursors. The quarry waste powder used in this study, also known as traprock dust, is a by-product of different gradations of manufactured sand from a metagabbro geological deposit. This dust is collected using a blower system and is usually used in quarries for rehabilitation efforts, such as creating slopes around excavating areas. The material is also used for agricultural applications. Note that metagabbro has been recently used as a partial replacement to OPC that improved sorptivity, abrasion resistance, and sulfate attack[15]; however, no previous study exists on metagabbro-based geopolymer composites. Developing a metagabbro-based, steel-fiber reinforced, strain-hardening geopolymer material is pursued in the present study. Due to a lack of geopolymer concrete standards, North American standards (such as those from ASTM International) that were originally developed for material characterization of typical fiber-reinforced concrete (FRC) are used, with the ultimate motive to promote technologies that incorporate reactive aggregates as binder constituents in sustainable THGCs with a low CO_2 footprint.

Materials and methods

The experimental investigation was performed using a variety of aluminosilicate source materials: GGBFS, MK, pumice (PM), small amounts of fly ash type F (FA-F), and the quarry waste powder mentioned previously, metagabbro (MG). The latter is a mafic intrusive igneous rock, rich in iron minerals that can be used for ferro-sialate-based geopolymer binders. Granite sand (GS) was used as a partially reactive aggregate due to its enhanced bonding with the binder,[16] while undensified silica fume (USF) was used as a fine filler for optimum packing. The particle size distribution and chemical compositions of the above materials have been determined as listed in Fig. 1 and Table A.1 (of the Appendix*), using dry and liquid laser scattering particle size and X-ray fluorescence (XRF) techniques, respectively. The microstructure of the dry materials is shown on the left side of Fig. 1. Additionally, to determine the reactivity (amorphous content) of the dry aluminosilicate powders, X-ray diffraction (XRD) was performed. All of precursors ranged from semi-amorphous (FA-F and MG) to highly amorphous (GGBFS, MK, USF, and PM). GS was the most crystalline material, with some amorphous content attributed to its weathered surface. The XRD patterns can be found in the Appendix (Fig. A-1). Regarding the alkaline reagent, a commercially available potassium silicate solution (PSS) with a molar ratio of 1.7 and 55% wt. of H_2O was selected. Potassium silicate solutions with a molar ratio of 1.7 (weight ratio of the oxides in the solution $K_2O/SiO_2 = 1.08$) are preferred compared to lower ratios as they are user friendly (lower causticity) while still being reactive.[2] Straight, brass-coated steel fibers (ℓ_f = 13 mm [0.5 in.] long, d_f = 0.2 mm [0.0079 in.] in diameter, with strength f_s = 2750 MPa [398.85 ksi]) were added at a volume fraction V_f of 2%.

*The Appendix is available at **www.concrete.org/publications** in PDF format, appended to the online version of the published paper. It is also available in hard copy from ACI headquarters for a fee equal to the cost of reproduction plus handling at the time of the request.

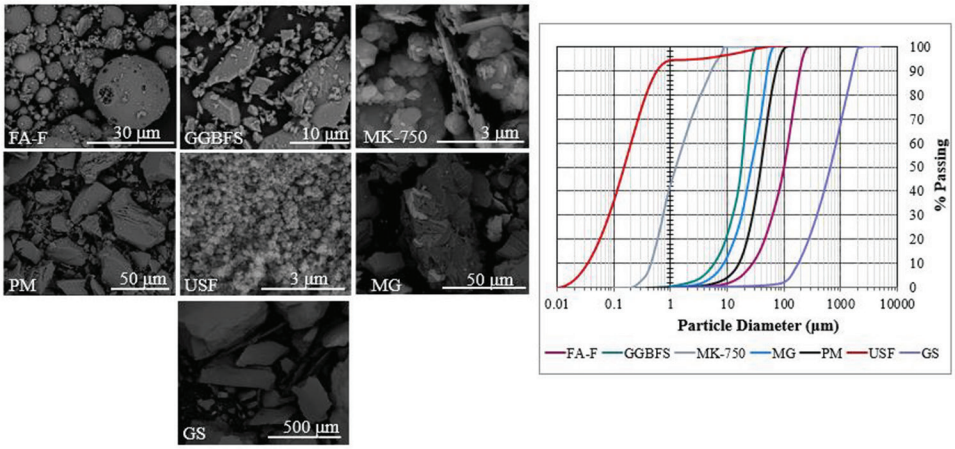

Fig. 1—Scanning electron microscopy (SEM) images of raw materials (left) and their particle size distribution (right).

Previous studies by the authors using FA-F, GGBFS, MK, and USF (but without MG and PM) have illustrated the implications of varying material proportions with respect to compressive strength, flowability, setting time, and stability.[16-18] It has been shown that no significant extension of setting time was achieved, whereas in cases of relatively extended setting time, the compressive strength was compromised. For this reason, in the present study, large parts of FA-F (the major precursor on previous studies) were substituted with the iron-rich quarry waster powders MG and PM, and a rock-based geopolymer concrete was designed using the fundamentals of geopolymer chemistry and particle packing theory.

Geopolymer formulations as described by Davidovits[1] were used to design the matrix. More specifically regarding the binder, the following molar ratios in the microstructure were selected: (K+Ca)/Al = 1 and Si/Al = 3. The first ratio is to prevent free alkalinity, and efflorescence while the second is for the formation of a rigid a three-dimensional (3-D) geopolymer network.[1] When (K+Ca)/Al is less than 1, the aluminosilicate oxides are in excess and might not polycondense; as a result, they remain as white powder inside the hardened geopolymer paste.[1] In addition to that, the high iron content in MG could be exploited to produce a rock-based or ferro-sialate geopolymer concrete. In this case, the trivalent Fe^{3+} substitutes up to 25% of the Al in the 3-D geopolymer network and the targeted ratio in this case is K/Al = 1 and K/Fe = 0.2.[1] For this reason, it was selected to be used as the main precursor. To achieve the aforementioned atomic ratios in the microstructure, 44% wt. of the alkaline solution was assigned to MG, 37% with MK, 6.4% with PM, 5.4% with GGBFS and 2% with FA-F. The rest 5% was left to react with the weathered surface of partially reactive GS. Finally, USF was assumed non-reacting in this system because of its lack of reactive alumina.

After determining the matrix proportions, the modified Andreassen and Andersen Model (REF) was used to produce a high performance geopolymer concrete with optimum packing density and controlled rheology. The modified Andreassen and Andersen (A&A) Curve[19] is based on the continuous Fuller & Thompson curve[20] while taking into consideration the minimum particle size (D_{min}) as any real size distribution of particles must have a finite lower size limit. The model is described in Eq. (1)

$$P(D_i) = \frac{D_i^q - D_{min}^q}{D_{max}^q - D_{min}^q} \; \forall D_i \in [D_{min}, D_{max}] \qquad (1)$$

where P is the fraction that passes the sieve with opening D_i, so it represents the total volume in the mixture with maximum grain size D_i; and D_{max} is the maximum particle size of the mixture. Finally, q is the distribution modulus, a parameter that could be used as an indicator of fresh properties such as workability. The modified A&A curve has been extensively used for self-compacting and UHPC mixtures with a distribution modulus ranging between 0.2 and 0.27.[21-23] In this study, the distribution modulus was set to 0.22. Figure 2 illustrates the modified A&A target curve for q = 0.22 and the mixture curve for both chemically optimized paste (COP) and optimized concrete (OC). As it is demonstrated, the COP does not yield the optimum particle packing and thus manipulation of the mixture is needed through addition of GS and USF. The former balances the curve in the coarse range while the latter covers the range of very fine particles. For the modified A&A target COP curve, D_{max} = 250 µm (0.01 in.) from FA-F, while D_{min} = 0.2 µm (7.87×10^{-6} in.) from MK. The modified A&A target OC curve is determined by taking into consideration the size of the coarsest grain (GS, D_{max} = 1200 µm [0.047 in.]) and the size of the finest grain (USF, D_{min} = 0.01 µm [3.94×10^{-7} in.]). For the optimized concrete mixture, USF is employed at 10% by weight of the mixture, to densify the system. Finally, GS was employed with an S/B of 1.6. The mixture designs with fibers (F) and without fibers, (NF) are presented in Table 1.

Mixing, casting, and curing procedure

Prior to mixing, the alkaline reagent PSS was mixed with half of the water and was stored in the fridge at a temperature of 2°C (35.6°F) for at least 1 day to further delay the setting time when used in the geopolymer concrete mixture.[2] A 25 qt (23.66 L) planetary bench mixer was used. The batching process comprised of mixing of the powdered

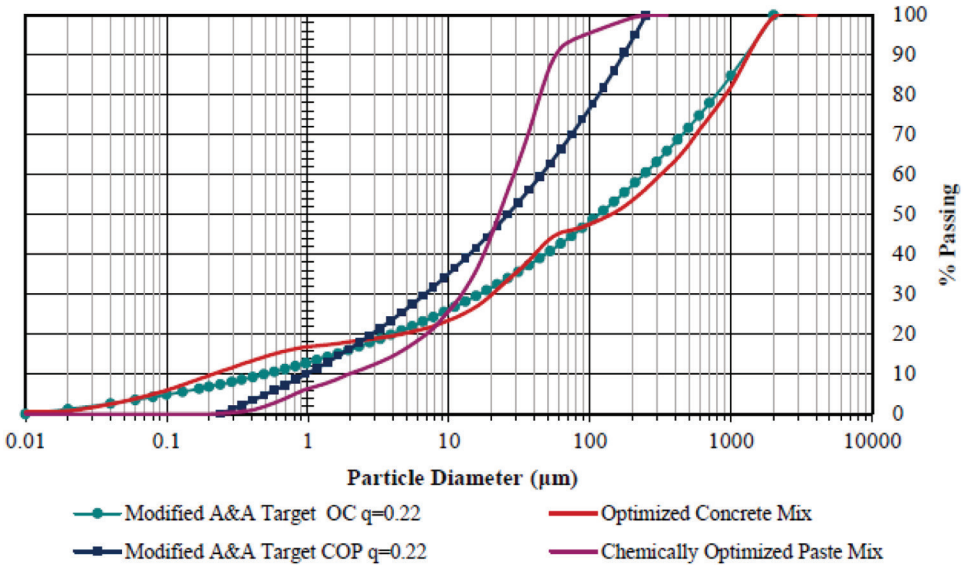

Fig. 2—Particle size distribution for optimized geopolymer paste and concrete related to their ideal (target) modified A&A Curves. (Full-color PDF of this paper can be accessed at www.concrete.org.)

Table 1—Mixture design for fiberless geopolymer matrix (NF) and THGC (F)

Materials	Proportions, kg/m^3	
	NF, kg/m^3	F, kg/m^3
MG	260	255
USF	230	225
GGBFS	180	176
MK	80	78
PM	45	44
FA-F	40	39
PSS	400	392
Water	80	78
GS	980	960
Extra water	22	21
Steel fibers	—	156

Note: 1 kg/m^3 = 6.24 × 10^{-2} lb/ft^3.

precursors and USF for 3 to 4 minutes, followed by the addition of the cold solution of alkaline reagent and water, continued by further mixing at a high speed of 355 rpm for 7 minutes. Subsequently, the sand was added to the system and mixing continued for 3 minutes at an intermediate speed of 185 rpm. After that, the remaining amount of water was added to increase workability and was further mixed at an intermediate speed for 2 minutes. When the mixture became flowable for the batch of THGC, fibers were added, and the mixing continued for 2 more minutes at an intermediate speed of 185 rpm. For characterization of tensile strength, prismatic specimens were cast from one end of the mold for enhanced alignment.[24] Specimens were cured according with the specified provisions in the standards discussed in future sections followed for each of the various physical and durability tests conducted in the study, with the exception of specimens used for characterization of the mechanical properties, which were covered with a wet burlap, wrapped in plastic sheets, and cured until the age of testing.

Testing methods and specimen preparation

Because of the lack of standards for characterization of geopolymer concretes, the testing methods originally developed for conventional FRCs were used in the present study for characterization of the THGC in the fresh and hardened states. These are listed in Table A.2 in the Appendix, along with the essential details of the material characterization campaign (that is, whether a test concerns only the matrix of THGC and the type of specimen tested). Unless otherwise specified in the respective section, results presented are the average and the standard deviation (SD) of three identical specimens.

All the mechanical testing was conducted at 60 days or more because research has shown that the structure of most geopolymers matures slowly and becomes more stable at longer times from casting as compared to conventional concrete.[4] The next section describes the procedures, equipment, and instruments used for mechanical, physical, and durability assessment, whereas the results of the tests are summarized in the following sections.

Flow table test and setting time test—Right after mixing and before casting, the flowability test per ASTM C1856/C1856M[25] and ASTM C1437[26] was conducted to evaluate the fresh properties of the material, namely the static and dynamic flow, respectively (refer to Fig. A-2 of the Appendix). Finally, the initial and final setting times of the geopolymer concrete mixtures were measured according to ASTM C191[27] using Vicat needle measurements. More information can be found in Section A.1 of the Appendix.

Uniaxial compression test—Uniaxial compression test was performed on fiber-reinforced and fiberless 75 x 150 mm (3 x 6 in.) cylinders and 50 mm (2 in.) THGC cubes, according to CSA A23.2-9C[28] on a controls pilot testing machine under force control with a loading rate of 0.25 MPa/s (36.26 psi/s). To obtain the response into the

post-peak range, uniaxial compression tests were performed under displacement control using a closed-loop, servo-hydraulic-controlled testing machine at a loading rate of 0.15 mm/min (0.006 in./min). For the characterization of the constitutive law in compression over the entire strain range, strain gauges, digital image correllation (DIC) virtual extensometers (done using a MATLAB open-source module, Ncorr[29]), and circumferential extensometer (a chain instrument) were used. For more details about the instrumentation, refer to Section A.2 and Fig. A.3 of the Appendix. Reported results are the average of five identical specimens; an additional test was conducted on one specimen to record the response under cyclic compression. The latter was performed in 32 cycles with a duration of 8.25 hours and a loading rate of 0.15 mm/min (0.006 in./min).

Flexural performance test—Prisms with dimensions of 75 x 75 x 280 mm (3 x 3 x 11 in.) were used to determine the flexural performance under four-point loading. Tests were carried out using a stepwise loading rate according with ASTM C1609/C1609M.[30] A schematic of the test setup is shown in the Appendix (Fig. A-4). The distance between the loading rollers and the end supports α (shear span) is equal to the height (h) of the specimen's cross section—that is, 75 mm (3 in.) which is equal to one-third of the total span (L) at testing (third point bending test). Further information about the instrumentation and experimental setup is presented in the Appendix (Section A.2). The nominal flexural strength f_p was calculated using Eq. (2) according to the previous standard, where P_p is the ultimate load and b is the width of the specimen cross section.

$$f_p = \frac{P_p L}{b h^2} \tag{2}$$

Direct tension test—Prisms having dimensions of 25.4 x 50 x 430 mm (1 x 2 x 17 in.) were tested in direct tension by means of a servo-controlled, closed-loop universal testing machine (UTM) at a loading rate of 0.15 mm/min (0.006 in./min).[31,32] The general testing procedure followed that which is used for UHPC (for example, AASHTO T 397-22[33]), but for the thickness which was reduced to fit the available UTM grips. A more detailed description of the testing procedure can be found in the Appendix (Section A.4).

Water content, density, absorption, and volumetric void content test—Cylindrical specimens with dimensions 75 x 150 mm (3 x 6 in.) were tested according to CSA A23.2-11C[34] for determination of water content, density, absorption, and void content. The cylinder molds were filled with a single layer of fresh THGC and were free of releasing agents as per ASTM C1856/C1856M.[25] The mass of the specimens was measured under different conditions: after demolding (I), after controlled air-curing at 23°C (77°F) and 50% relative humidity (G), after oven drying at 110°C (230°F) (A), after immersion in water (B), after boiling at 110°C (230°F) for 5 hours and then surface drying (C), and after suspension in water (D).

Drying shrinkage test—For determination of linear shrinkage, four prisms with dimensions of 25 x 25 x 285 mm (1 x 1 x 11.2 in.) were cast and tested according to CSA A23.2-21C.[35] The prisms were exposed to controlled conditions of 23 ± 2°C (73.4 ± 3.6°F) and a relative humidity of 50%. The change of length of the specimens was recorded using a length comparator at different ages.

Sulfate resistance test—Resistance to sulfate attack was quantified by the length change over time of specimens submerged to sodium sulfate solution with concentration of 50 g/L (3.12 lb/ft^3) according to ASTM C1012/C1012M.[36]

Coefficient of thermal expansion test—75 x 150 mm (3 x 6 in.) cylinders with a gauge length of 100 mm (4 in.) were used for determination of the coefficient of thermal expansion (CTE) at a temperature range between 4.6 and 22.7°C (40.3 and 72.86°F). This temperature range was chosen as an alternative to temperature ranges used in standards that could affect the adhesion of the gauge points.[37] Upon demolding, the cylinders, along with a specimen with an embedded probe thermometer, were placed in a bucket filled with saturated limewater closed with a lid and were maintained for 56 days of curing. More details about the procedure are found in the corresponding section of the Appendix (Section A.6).

Abrasion resistance test—The standard followed for the determination of abrasion resistance is ASTM C944/C944M[38] using sawn cut cylindrical specimens with dimensions 100 x 100 mm (4 x 4 in.). A detailed description of the testing procedure can be found in Section A.7 of the Appendix.

Chloride ion penetration resistance test—The standard CSA A23.2-23C,[39] which refers to an electrical indication of concrete's ability to resist chloride ion penetration, is used. The method is an adaptation of AASHTO T 277,[40] also known as the Rapid Chloride Permeability Test (RCPT). It is noted herein that the method has been criticized as it measures ionic movement and not just chloride ions.[41]

Deicing salt scaling resistance test—To determine the deicing salt scaling resistance of the developed material the CSA A23.2-22C[42] test was performed on a 200 x 240 x 75 mm (8 x 9.5 x 3 in.) slab specimen. This method determines the resistance to scaling of concrete exposed to 50 freezing-and-thawing cycles and deicing chemicals. The temperature interval is –18°C (–0.4°F) for freezing and +22°C (+71.6°F) for thawing, whereas the deicing chemical used in this study is a sodium chloride solution of a 3% concentration. On top of the slab, a ponding area is created for the NaCl solution. The resistance to deicing salt scaling is evaluated both quantitatively through mass loss due to exposure and qualitatively by visual examination. Further details regarding the procedure can be found in Section A.8 of the Appendix.

EXPERIMENTAL RESULTS AND DISCUSSION

Fresh properties: flowability, temperature, and setting time

The measurements of the fresh properties are listed in Table 2. For both the fiberless geopolymer matrix and the THGC, the mixtures were self-consolidating with a slight thixotropic behavior (the material holds its form undisturbed but flows when energy is applied to it—there was a difference between the static spread and the dynamic spread). It

Table 2—Fresh properties of fiberless geopolymer matrix (NF) and THGC (F)

Properties	NF	F
Static spread, mm	126	137
Dynamic spread, mm	184	195
Initial setting time, min	100	92
Final setting time, min	175	163

Note: 1 mm = 39.37 × 10^{-3} in.

is observed that the flowability of the mixture containing fibers was higher than the fiberless geopolymer concrete. This phenomenon has also been reported in the literature[43] but not explained. It is postulated that the low-friction brass coated fibers facilitate sliding of the layers of the material over the underlying layers as the cone mold is retracted and the material spreads laterally under the effect of gravity. Regarding setting time, the high amount of MG prolonged the time of setting as compared to FA-based mixtures developed by the authors.[16] It was observed that the addition of steel fibers increased the workability of the mixture while decreasing the setting time. The workability increase is attributed to the reduction in friction between layers of concrete intercepted by the brass-coated fibers. The reduction of setting time in the F mixture may also be attributed to the fibers. The total number of fibers added in a volume of 2% is approximately 49 × 10^6/m^3 (1.39 × 10^6/ft^3). Given the length and diameter of these inclusions in the fresh material, a total of 400 m^2 (4305.56 ft^2) of surface area would require a significant amount of the available water in the mixture to be wetted (that is, for a monolayer of water molecules to be formed on the fiber surfaces). This water amount is of course available as the fibers do not bind to the liquid potassium silicate chemically. Thus, the water that is used to form the monolayer on the fibers could reduce the setting time of the mixture. Finally, it is worth mentioning that the material remained flowable for approximately 15 minutes after the end of mixing and workable for approximately 30 minutes.

Compressive response, static modulus of elasticity, and Poisson's ratio

The average compressive strength of the unreinforced (plain) geopolymer concrete was 46 MPa (6672 psi). As illustrated in Fig. 3(a), failure is precipitous after the peak, with the cylinders collapsing into fragments beyond the attainment of the peak load. Specimens C1 and C2 developed a Type 3[28] fracture, where columnar vertical cracking goes through both ends and no well-formed cones are visible. These types of failure indicate normal or reduced friction between the loading plates and the specimens. Specimen C3 exhibited a Type 2[28] failure, where only one end has a well-defined cone and vertical cracks fan through caps. Finally compared to previously developed mixtures,[16] the texture of the fractured core was more cohesive, less porosity was observed, and the white dust that had been reported in previous studies at the core of fragmented geopolymer specimens was not visible in this instance, indicating that no reactive material was left unreacted, which in the reference studies had been attributed to excess of aluminosilicate powders compared to the alkaline solution and probably fast setting.[1]

The monotonic stress-axial/lateral strain response of the tested cylinders is shown in Fig. 3(b). Characteristic values of the stress-strain envelope are listed in Table A.3 of the Appendix. Continuous curves correspond to cylinders tested at the age of 63 days, whereas dashed lines correspond to cylinders tested at the age of 196 days. The cyclic uniaxial compressive stress-strain response of the THGC is shown in Fig. 3(c). The compressive strength reached an average ultimate stress value of 47.7 and 51.9 MPa (6918 and 7527 psi) at the ages of 63 and 196 days, respectively. Axial deformation, ε_{co}, at the attainment of compressive strength, was at least 0.003 or more, whereas the axial deformation corresponding to 0.5f_c post-peak was in the range of 0.016 to 0.034. Considering the lateral strains, it is concluded that large axial strain values and the markedly milder descending branch over what was observed in the case of the plain matrix tests were due to the passive confinement provided by the fibers. The prolonged descending branch combined with the high post-peak deformation range indicates the highly ductile nature of the developed geopolymer concrete.

Although ASTM C469/C469M[44] prescribes that the modulus of elasticity should be measured at 40% of the maximum load, it was observed that the THGC lost its linearity earlier than 40%, and thus 30% was used as a reference. The average elastic modulus was 19 GPa (2756 ksi) and the average Poisson's ratio was 0.16. (The detailed results can be found in Table A.3 of the Appendix.) Compared to an OPC-FRC of the same strength, it is evident that the investigated material demonstrates a lower modulus of elasticity and Poisson's ratio. The latter is consistent with the literature.[45] The low modulus might be attributed to the different molecular structure of the material with respect to conventional OPC concrete and the prevalence of K atoms—instead of Ca (more prevalent in OPC concretes) or Na (in geopolymer concretes made with sodium silicate)—thus being responsible for possibly a short range of attraction forces in the molecular structure, and thus a lower stiffness than in cement-based gel structures. The correlation of the modulus of elasticity with the intermolecular interaction energy and the implications of the latter on the macroscopic mechanical properties of concrete have been proven in the literature.[46,47] Furthermore, as discussed in the forthcoming sections of the study, the material was also found to be semi-lightweight with an air-dry density of 1940 kg/m^3 (121.1 lb/ft^3). In the case of lower-density concretes, Eq. (3) may be used for estimation of modulus of elasticity for concretes with mass density between 1500 and 2500 kg/m^3 (93.64 and 156.07 lb/ft^3).[48] Using the obtained compressive strength (f_c') and density (γ_c), the modulus of elasticity using Eq. (4) is 20.3 GPa (2944.26 ksi), which is close to the experimentally obtained value.

$$E_c = \left(3300\sqrt{f_c'} + 6900\right) \cdot \left(\frac{\gamma_c}{2500}\right)^{1.5} \text{(in GPa)} \quad (3)$$

$$E_c = \left(39{,}600\sqrt{f_c'} + 1000\right) \cdot \left(\frac{\gamma_c}{156.07}\right)^{1.5} \text{(in ksi)}$$

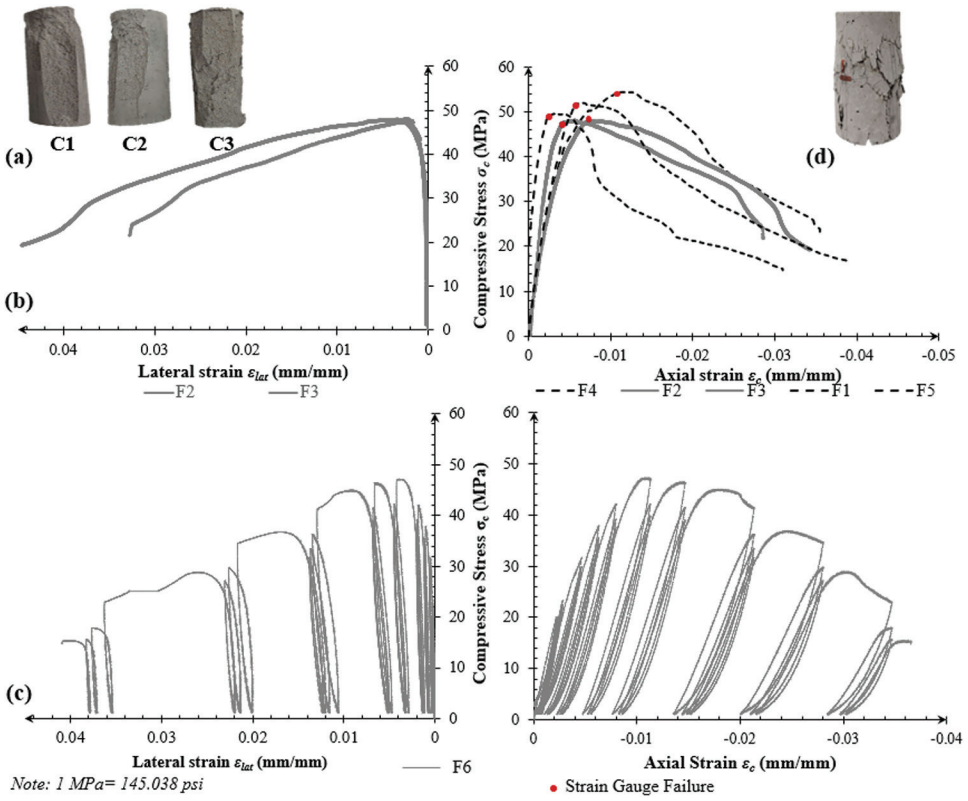

Fig. 3—(a) Fracture pattern of fiberless geopolymer concrete cylinders; (b) stress-axial/lateral strain of THGC under monotonic uniaxial compression; (c) stress-axial/lateral strain of THGC (F6) specimen under cyclic uniaxial compression; and (d) fracture mode of cylindrical THGC specimen.

The fracture pattern of THGC cylinders under uniaxial compression differentiates the material from that of the plain geopolymer concrete matrix. As illustrated in Fig. 3(d), the cylinders held their integrity beyond the peak load even after undergoing high deformations. Vertical cracks parallel to the loading direction indicate the bridging effect of the fibers crossing the cracks. The fracture pattern resembles a failure of Type 3.[28]

From the fiber-reinforced cube specimens, an average compressive strength of 69.0 and 73.2 MPa (10 and 10.6 ksi) was found at 63 and 196 days, respectively. When comparing the results in the average cubic compressive strength to the cylindrical compressive strength at the corresponding age, a strong triaxial state is suggested for the cubic tests. More specifically, the ratio of cubic compressive strength to cylindrical compressive strength at 63 and 196 days of age was 1.41 and 1.45, respectively.

Flexural performance

The resistance curves of the tested specimens are illustrated in Fig. 4(a). The average maximum load was 20.7 kN (4.65 kip), which corresponds to a maximum bending stress of 10.6 MPa (1.5 ksi). The first peak strength (f_1), which corresponds to the familiar modulus of rupture f_r, is marked by the loss of linearity in the ascending branch and can be related to the first cracking strength. It is observed to be 70% of the peak stress proving that the material is indeed strain hardening[30,49] (Fig. 4(b)). Table A.4 in the Appendix summarizes the flexural performance properties of the geopolymer THGC according to ASTM C1609/C1609M. Besides these flexural properties, the drift ratios at various loading stages are also measured to quantify the hardening behavior of the material. Note that the drift β is defined as the ratio of the measured midspan deflection to the distance between the midspan and the support. The average drift at 50% post-peak is 2.36% while at 20% residual strength it is 4.24%. This is an indicator of high ductility.

The failure mode of the specimens was also studied by examining the location and the path of the critical failure crack. In all cases, the localized crack was vertical and propagated perpendicular to the longitudinal axis of the prism, having occurred in the region of the constant moment area or under one of the loading rollers (Fig. 4(c)). Unsymmetrically occurring, flexural cracks are owing to unsymmetrical fiber distribution in case of flow from one end due to the disturbance in flow around the casting point. Average crack width at a residual load of 20% of the peak, was 6.5 mm (0.25 in.), which is half the fiber length (Fig. 4(d)).

Tensile response

The tensile stress σ_t versus the corresponding axial strain of the tested specimens is plotted in Fig. 5(a), with Fig. 5(b) showing a zoom into the ascending branch of the response highlighting the tension hardening behavior. All specimens lost their linearity before reaching the ultimate load, indicating the first apparent cracking at an average strain of 0.00016 which was also observed in the DIC analysis. The average cracking strength was 3.0 MPa (435 psi), whereas the ultimate tensile strength was 7.7 MPa (1.12 ksi), corresponding to a hardening ratio of 2.56. This, along with

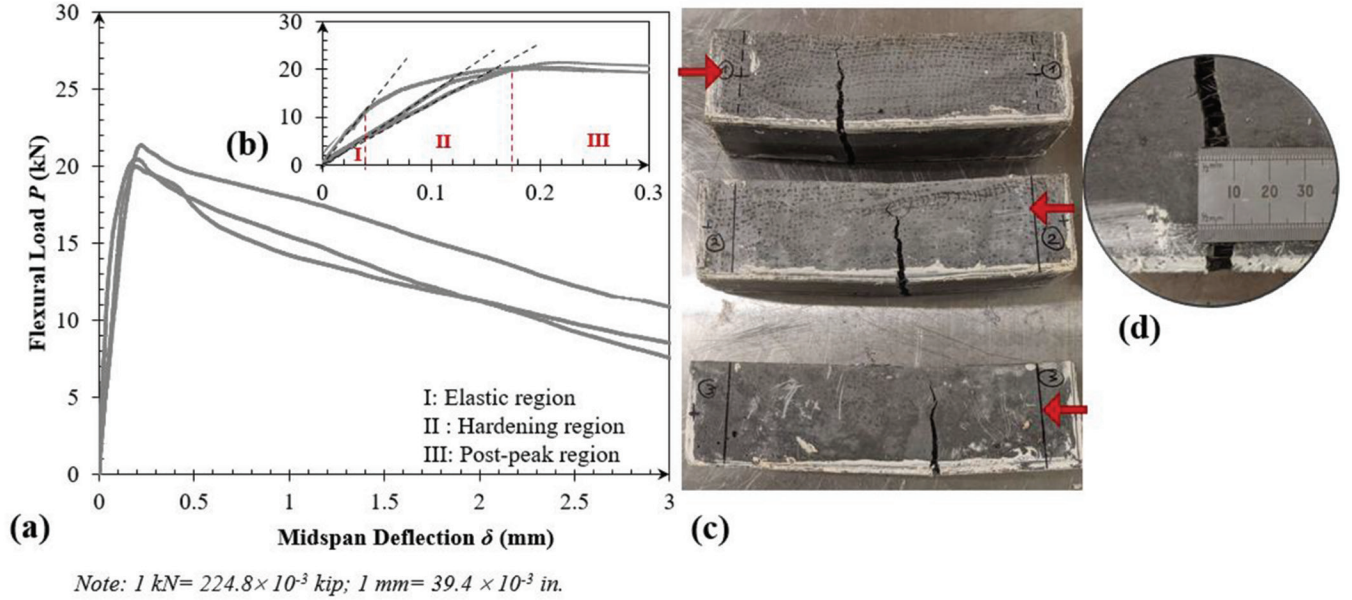

Fig. 4—(a) Resistance curves of tested THGC flexural prisms; (b) zoom in elastic, hardening region, and onset of localization; (c) fractured specimens with red arrows pointing one-way casting direction; and (d) measured crack width.

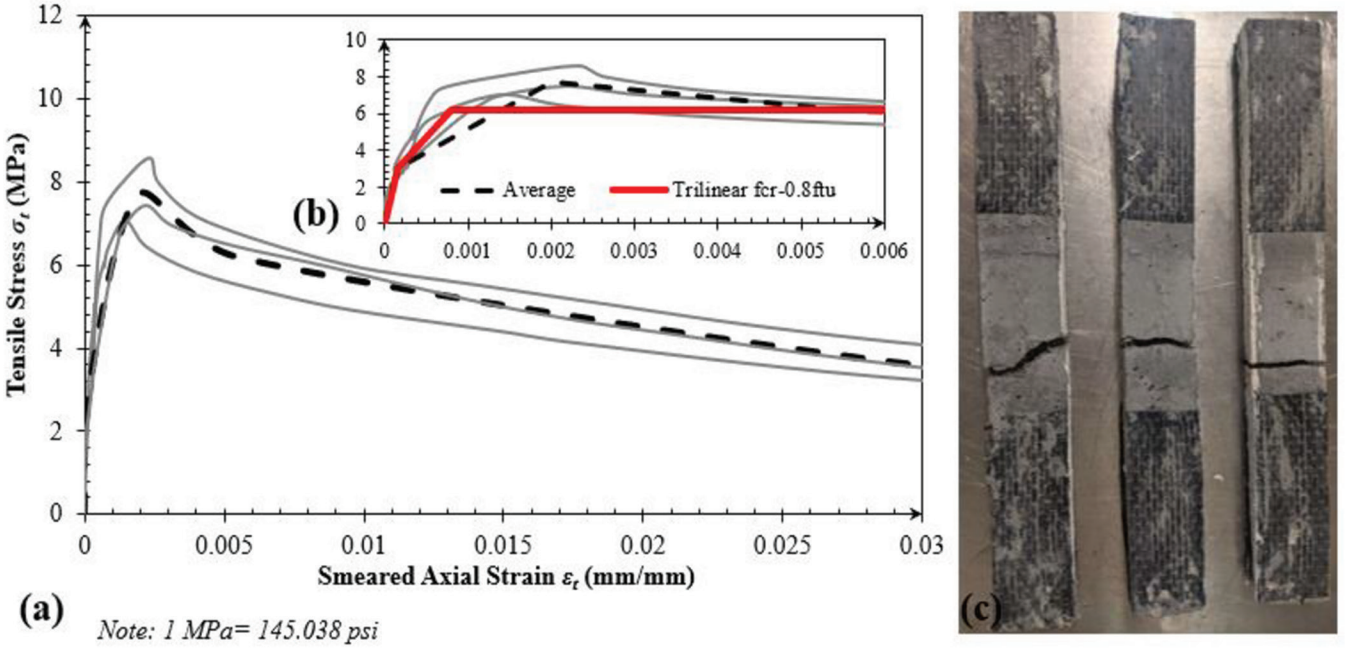

Fig. 5—(a) Tensile law of THGC under uniaxial direct tension; (b) strain-hardening region; and (c) failure planes of THGC direct tension specimens.

a tensile strain capacity of 0.002 corresponding to ultimate strength, satisfy the requirements for classification as THFRC which is established by CSA S6, Annex 8[49] (the results of the individual specimens can be found in Table A.5 of the Appendix). Ductility in the post-peak branch is quantified at a post-peak residual load equal to 80% of the peak value, where the material attains a strain capacity of 0.6% as shown in Fig. 5(b). Regarding the failure mode (Fig. 5(c)), all three specimens developed failure planes inside the gauge length; failure occurred upon localization of the crack which induced eccentricity in the axial stress distribution, eventually leading to residual bending deformation at the end of the test. The latter was inevitable as stress concentrations develop following the initiation of the crack from one side.[50]

To extract the axial strain profiles of the specimens, DIC analysis was performed. (The characteristic points of the load-displacement curve used for DIC analysis are shown in Fig. A.8 of the Appendix.) Five DIC captures are used in Fig. 6 to show the evolution of surface tensile strains at milestone points of the response envelope of each specimen as follows: P_{cr} is the load corresponding to the first cracking tensile strength. P_{max} is the peak load corresponding to the ultimate tensile strength. $P2$ and $P3$ correspond to 0.65 and 0.8 of P_{max} in the ascending branch of the resistance curve,

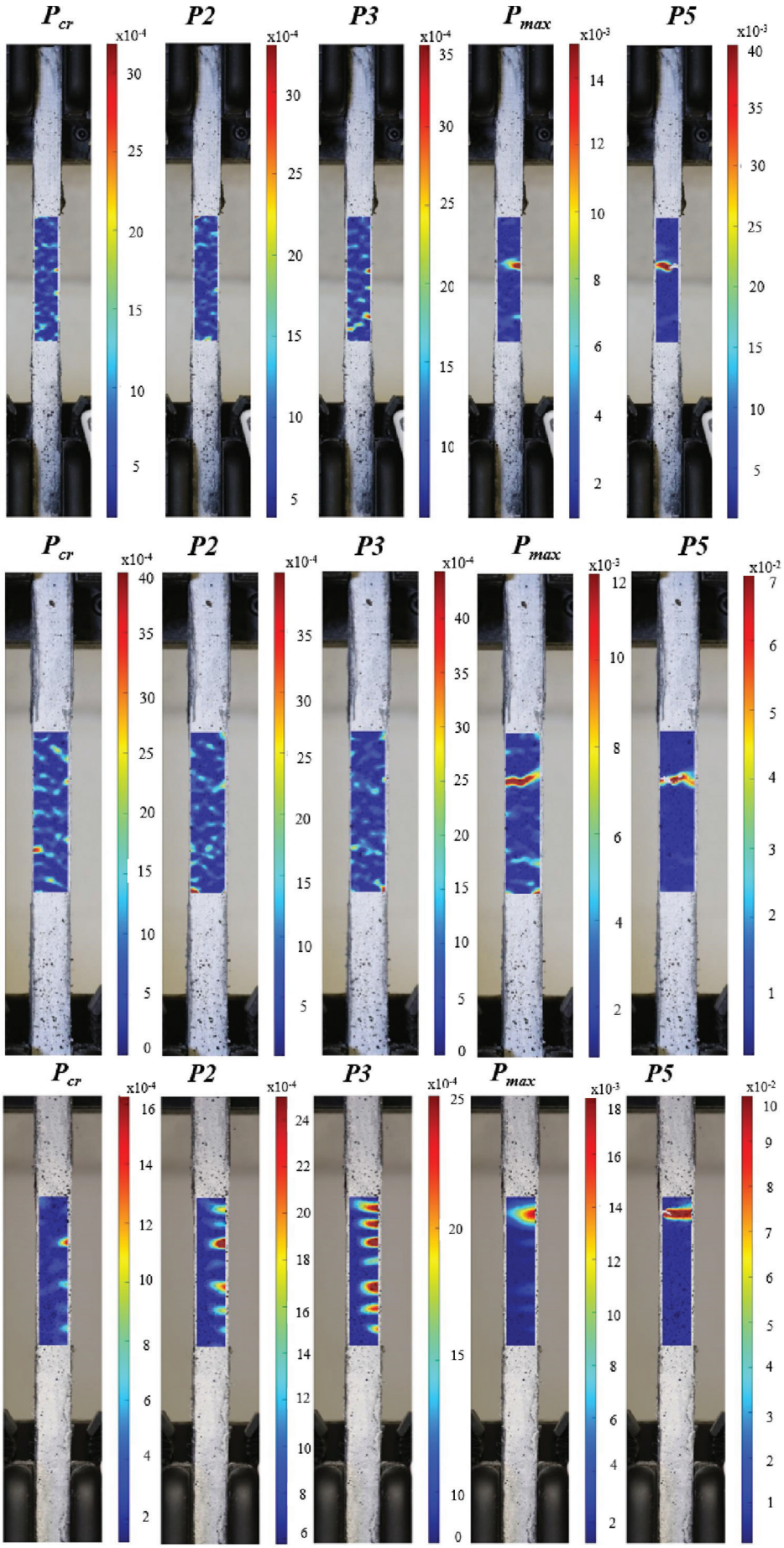

Fig. 6—Tensile strains at characteristic points for samples; No. 1 (top); No. 2 (middle); and No. 3 (bottom).

respectively. Finally, *P*5 represents 80% of the maximum load in the descending branch. At P_{cr} for all specimens, the crack initiation was obvious as a distinct region with orange-red color whereas the rest of the specimens had significantly lower strains as indicated by the blue color in Fig. 6. At *P*2 and *P*3, the tension hardening nature of the material was evident as more microcracks were observed in the gauge length. For P_{max}, which corresponds to the maximum load and thus ultimate strength, localization of cracking is manifested by the contrasting small, localized regions that experience significantly large strains with the rest of the specimen unloading. For specimens No. 2 and 3, additional microcracks were observed, besides the localized crack. However, as it is seen in *P*5, one of these cracks prevailed as the weakest region and kept spreading (localization of damage), while the rest of the cracks were slowly closing.

Water content, density, absorption, and void content

Density absorption and void content were obtained from the measured mass and water content (the detailed results are presented in Table A.7 of the Appendix). The average water content was 12.6%, the absorption after immersion was 8.9%, the absorption after immersion and boiling was 9.3%, the air-dry density was 1940 kg/m^3 (121.1 lb/ft^3), the oven-dry density was 1870 kg/m^3 (116.7 lb/ft^3), density after immersion and boiling was 2050 kg/m^3 (128 lb/ft^3), and the void content was 17.41%. These properties are the averages of three specimens and are consistent with values reported for geopolymer concretes in the literature, because these materials are known for their hydrophilic nature and microporous structure, which results in a lower density compared to OPC concrete.[1]

Drying shrinkage

The change in length over time for the four specimens and their average is illustrated in Fig. 7. At 28 days of drying age, the average shrinkage was –0.22% whereas at 217 days, it was –0.25%. In the case of OPC concrete, the long-term drying shrinkage is expected to be in the range of –0.05%.[35] It is noted that, generally, shrinkage is significantly higher in geopolymer mortars on account of the high capillary pressure generated between wet and dry zones of the micropore network resulting in internal cracking initiation.[4] Another explanation for the high shrinkage could be the use of very fine precursors such as USF and MK, which according to the literature might be associated with higher shrinkage.[51]

Coefficient of thermal expansion

The average CTE of the developed THGC was 10.01 × 10^{-6} mm/mm/°C (5.561 × 10^{-6} in./in./°F)—that is, very close to the CTE of steel and conventional concrete. This value is also considered an indicator of the Si/Al ratio of the geopolymer. For different formulations, it is observed that CTE is proportional to the amount of molecular SiO_2 found inside the geopolymer's 3-D network.[1]

Sulfate resistance

As illustrated in Fig. 7, in the secondary axis, the developed geopolymer concrete showed no expansion; on the contrary, a slight shrinkage strain was observed (–0.024% in 217 days). This is consistent with studies from the literature.[1,52] In the case of OPC concrete, the long-term expansion due to sulfates is expected to be in the range of +0.02%.[1] The high sulfate resistance of geopolymer concrete was attributed to the different mechanisms of geopolymerization. The main product of geopolymerization is not hydrates, which are susceptible to sulfates. Contrary to the case of hydration in OPC, in geopolymer concretes there are generally negligible amounts of calcium hydrates (as in its majority, it is part of the 3-D geopolymer network) that would react with sulfuric compounds to form ettringite and thus cause expansion.[53,54] However, to some extent, due to the presence of calcium, the formation of gypsum and ettringite might occur but not to the same amount and extent as in OPC.[55] In this study, it is evident from the chemical composition of Table 1, that calcium is present in higher amounts in GGBFS.

Abrasion resistance

The average mass loss due to abrasion after two cycles was 0.713 g (1.57 × 10^{-3} lb) over an abraded surface of 7854 mm^2 (12.56 in.^{2}). The specimens demonstrated significantly high abrasion resistance; to assess the values, they were contrasted with those obtained using the same test setup for a proprietary UHPC.[32] The average mass loss was 40% less than that of UHPC. The difference between the final states of the two material samples is shown in Fig. 8(a). Although UHPC demonstrated significantly higher compressive strength and lower porosity, the better abrasion performance of the developed THGC is attributed to MG used as a precursor and the granite aggregates.

Chloride-ion penetration resistance

The tests were conducted for 6 hours, at which point the control software automatically terminated the test. No temperature spikes were observed with a stable temperature between 22 and 25°C (71.6 and 77°F). The average charge passing was 989 Coulombs, which is less than 1000 Coulombs, indicating very low chloride penetration as specified by the standard.[39] The low chloride transport is also linked to the high Si/Al ratio as observed in the literature.[56]

Although the results support the classification of the produced geopolymer in the low penetrability category, there are some concerns about the suitability of this technique for geopolymer concretes. In RCPT, it is assumed that the current flow passes through the sample by pore solution which acts as an electrolyte. For geopolymers, it has been found that the pore solution includes other ions and is highly alkaline.[12] This highlights the following two limitations. First, as the method measures the current passed, which is related to all ions in the pore solution and not just chloride ions, higher values are expected, thus underestimating the resistance of the material to chloride ingress. Meanwhile, RCPT is highly dependent on the conductivity of the material, which is related to the alkali content. For these reasons,

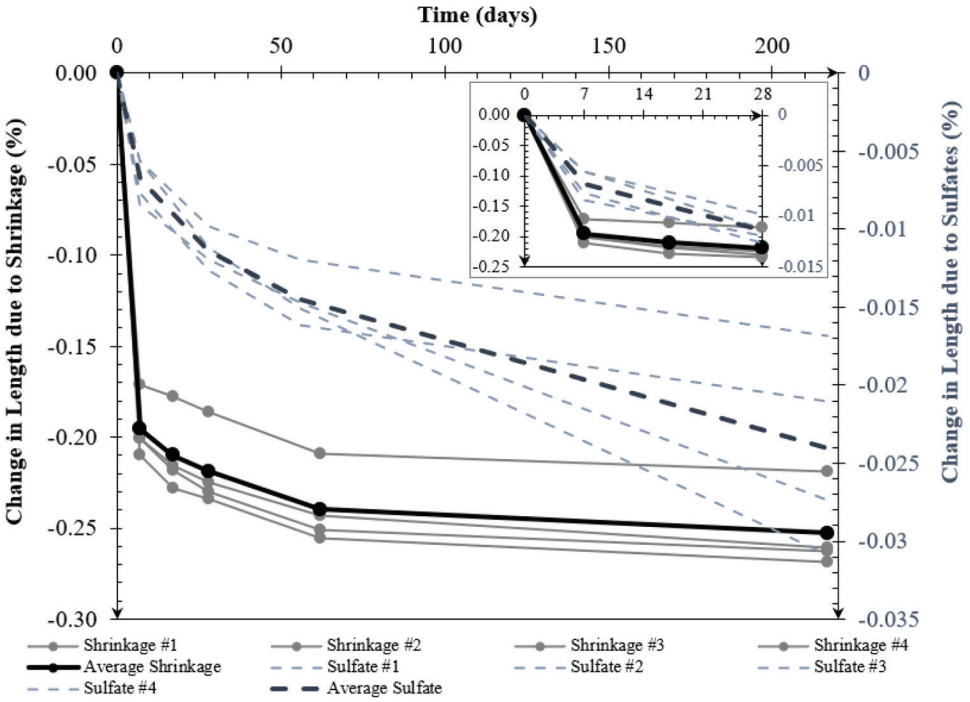

Fig. 7—Change of length due to shrinkage and sulfate exposure: (a) in 217 days; and (b) in first 28 days.

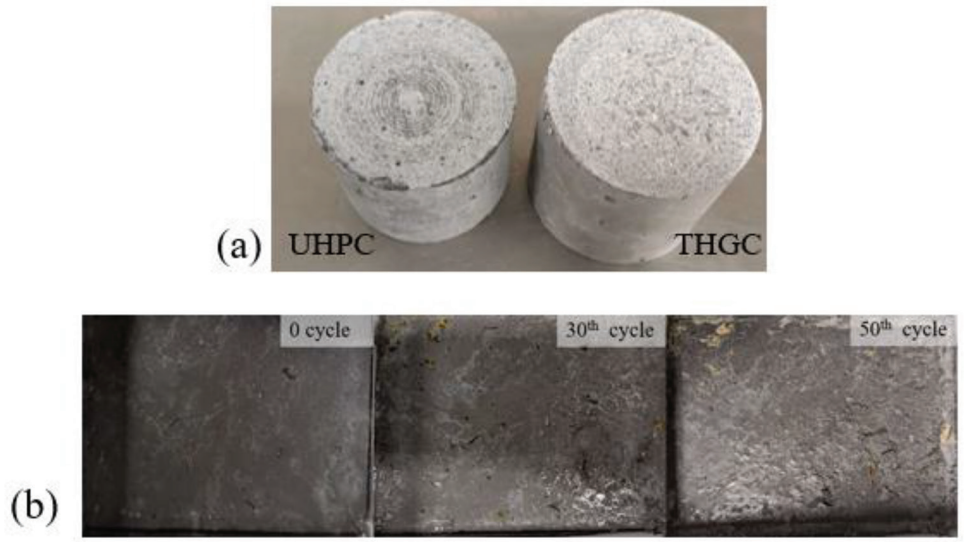

Fig. 8—(a) Abraded cylinders of UHPC and THGC; and (b) visualization of deterioration through deicing salt scaling cycles.

geopolymer concretes tested with RCPT in the literature show a higher flow rate than OPC concretes.[12]

Deicing salt-scaling resistance

Table 3 summarizes the material loss at each freezing-and-thawing cycle related to the surface exposed to the deicing solution. The cumulative material loss after 50 cycles is 0.33 kg/m^2 (0.067 lb/ft^2), less than the 0.8 kg/m^2 (0.164 lb/ft^2) upper limit for 50 cycles, which is set by bridge regulators in cold climates (for example, the Ministry of Transportation of Ontario, Canada[57]), for materials used in bridge construction.[58,59] Regarding the visual ratings as illustrated in Fig. 8(b), there are some popouts at the end of the test period, indicating slight to moderate scaling of the surface mortar, classifying the material in Category 2-A per CSA A23.2-22C.

Sustainability analysis of geopolymer matrix

Finally, a sustainability analysis of the developed geopolymer concrete matrix (without the fibers) is conducted to assess the CO_2 mitigation. The sustainability indexes used are the energy intensity and the CO_2 emissions generated by the production of the materials used in the mixture. Table 4 shows the energy intensity and CO_2 emissions for different components used in the proposed concrete but also usually found in construction materials. It is worth noting here than MG is a local quarry waste not commercialized as FA and slag, and thus its energy intensity and CO_2 emissions for its production are assumed to be zero.

Table 3—Deicing salt-scaling resistance results

Number of cycles	Mass loss, g	Visual rating	Characteristics of scaling surface
5	0.02	0	No significant scaling observed
15	0.21	1	Slight scaling (3 mm depth, maximum, no coarse aggregate visible)
30	3.00	2-A	Slight to moderate scaling of surface mortar (several popouts)
50	5.60	2-A	Slight to moderate scaling of surface mortar (several popouts)
Total loss, g	8.83	—	
Total, kg/m^2	0.33	—	

Note: 1 g = 2.20 × 10^{-3} lb; 1 kg/m^2 = 1.4223 lb/in.^{2}.

Table 4—Energy intensity and CO_2 emissions for materials used in this study and generally in concrete mixture design

Material	Energy intensity, MJ/kg	CO_2 emissions, kg/kg	Reference
Ordinary portland cement	4.7	1.02	Davidovits[1]
Fly ash	0.1	0.009	Hammond and Jones[60]
Silica fume	0.1	0.008	Hammond and Jones[60]
River sand	0.081	0.0048	Hammond and Jones[60]
Granite sand	0.81	0.0459	Bascetin et al.[61]
Slag	1.33	0.07	Hammond and Jones[60]
Metakaolin	2.5	0.37	Hammond and Jones[60]
Potassium silicate solution	2.1	0.28	Davidovits[1]
MG quarry waste powder	0	0	Assumed
Pumice	1.681	0.0022	Lava Mining & Quarrying SA[62]
Water-reducing admixtures	11.47	0.6	Zheng[63]
Water	0.01	0.001	Hammond and Jones[60]

The aforementioned sustainability indicators were used to calculate the total energy intensity and CO_2 emissions of the geopolymer matrix. The results are compared with four different concrete mixtures available in the literature with the same compressive strength (Table 5) and different levels of OPC replacement by weight (0, 50, 60 and 70%). The comparative results are illustrated in Fig. 9. It is observed that the proposed geopolymer matrix leads to a CO_2 emission reduction in the range of 56 to 87% as compared to high-performance concrete (HPC) and FA-based engineered cementitious composites (ECC) (Fig. 9(a)). The highest reduction is observed with reference to an HPC made of 100% OPC, while the lowest reduction (56%) corresponds to an ECC where 70% of the OPC is substituted by FA. The energy intensity reduction is also significant with the highest value to be 70%.

Table 5—Different concrete mixtures used for comparative sustainability analysis

Reference	Mixture design label
Kobayashi et al.[64]	HPC-PC
Yao et al.[65]	ECC1-0.5PC
Yao et al.[65]	ECC2-0.4PC
Eshghi[66]	ECC1-0.3PC
Present study	GPC-NF

CONCLUSIONS

This study was dedicated to the development and full characterization of a novel, cementless, tension-hardening, fiber reinforced geopolymer concrete where the main binder material used is a naturally occurring rock that is rich in aluminosilicates, known as metagabbro. In the study, this material was used in the form of quarry waste powder. The experimental campaign included an investigation of fresh-state, mechanical, physical, and durability properties. Based on the experiments on the two geopolymer mixtures (matrix and with fibers) discussed herein, the following conclusions are made:

1. The material is self-consolidating with satisfactory setting time without the addition of chemical admixtures. This is significant as two main issues of geopolymer concrete often found in the literature are the high viscosity and the fast setting time.

2. High ductility was observed both in tension and compression. In the case of compression, due to the passive confinement provided by the fibers, at 50% post peak, the average axial deformation was 0.028, while the lateral strain was 0.038. In the case of tension, the ultimate apparent tensile strain at peak tensile stress was 0.002. These limits are approximately 10-fold the respective values of normal concrete. The high ductility was also proven through the tension-hardening characteristics both in tension and in flexure. The hardening ratio in tension was more than 2.5

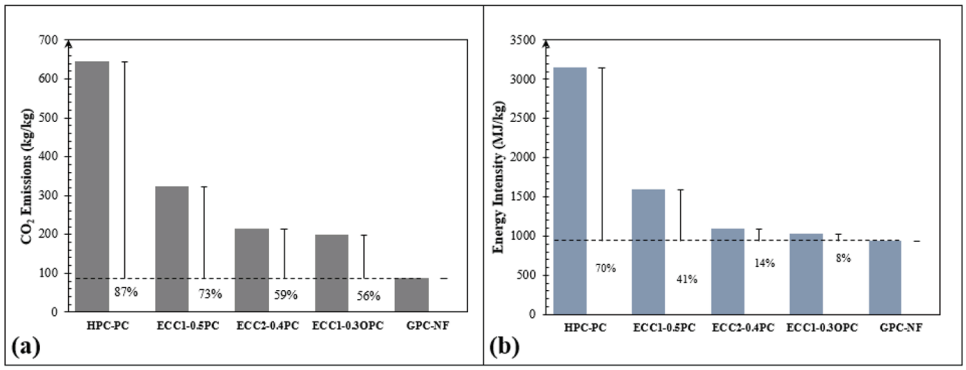

Fig. 9—Material sustainability indicator for 1 metric tonne of different concrete matrixes: (a) CO_2 emissions; and (b) energy intensity.

and multiple cracking was evident through digital image correlation (DIC).

3. The splitting test is not recommended for fiber-reinforced concrete (FRC), as the results are highly dependent on fiber distribution, which may be grossly random in the case of cylinder specimens.

4. Compared to ordinary portland cement (OPC) concretes of the same compressive strength, geopolymer concrete exhibited lower Young's modulus and Poisson's ratio. This is consistent with the literature and might be attributed to its different molecular structure. Another possible explanation is the semi-low air-dry density of the material.

5. The ratio between cylindrical and cubic compressive strength was 0.7, while in OPC concrete, it is approximately 0.8 for medium to high strengths.

6. The developed tension-hardening geopolymer concrete (THGC) is semi-lightweight with an air-dry density of slightly less than 2000 kg/m^3 (125 lb/ft^3).

7. In terms of abrasion and sulfate resistance, the material demonstrated superior properties, better than ultra-high-performance concrete (UHPC). The high resistance in abrasion was attributed to the granite aggregates and the metagabbro quarry by-product, which was used as the precursor. Meanwhile, the exposure to sodium sulfate did not cause any expansion. This can be explained by the negligible amount of calcium hydrates that would cause the ettringite formation and the consequent expansion when exposed to sulfates.

8. In terms of chloride ion resistance, the material is classified in the very low penetrability range. However, the Rapid Chloride Permeability Test (RCPT) might underestimate the resistance to chloride ion penetration in the case of geopolymer concretes. This is because the latter has an alkaline pore solution rich in K^+ ions, and the test measures the movement of all ions and not only the chlorides.

9. The developed THGC shows satisfactory deicing salt scaling resistance with a mass loss under the 0.8 kg/m^2 (0.164 lb/ft^2) limit used in bridge construction.

10. The proposed geopolymer matrix led to a 56 to 87% carbon footprint reduction compared to selected high-performance concrete (HPC) and engineered cementitious composites (ECCs) of comparable strength reported in the literature.

11. Further improvement of the performance of the material is possible by calcining the waste powder, which would increase the amorphous content and therefore the reactivity.

AUTHOR BIOS

Zoi G. Ralli *is a Postdoctoral Fellow in the Department of Civil Engineering at York University, Toronto, ON, Canada, where she received her PhD. She received her MASc in novel materials, a 5-year University Diploma in civil engineering, from Democritus University of Thrace, Xanthi, Greece. She is a member of ACI Committees 239, Ultra High-Performance Concrete; 241, Nanotechnology of Concrete; and 242, Alternative Cements; and ACI Subcommittees 239-C, Structural Design on UHPC, and 239-D, Materials and Methods of Construction with UHPC. Her research interests include resilient and sustainable high-performance concrete (HPC) such as geopolymer concretes and ultra-high-performance concrete (UHPC).*

Stavroula J. Pantazopoulou, *FACI, is a Professor of civil engineering at York University. She received her MSc and PhD degrees from the University of California, Berkeley, Berkeley, CA, and a 5-year University Diploma in civil engineering from the National Technical University of Athens (NTUA), Athens, Greece. She is a member of ACI Committees 341, Performance-Based Seismic Design of Concrete Bridges; 374, Performance-Based Seismic Design of Concrete Buildings; 408, Bond and Development of Steel Reinforcement; and 445, Shear and Torsion. Her research interests include earthquake engineering and seismic assessment, design, and retrofit of structures with novel engineering materials, including engineered cementitious composites (ECCs) and UHPC.*

ACKNOWLEDGMENTS

The authors wish to express their gratitude and sincere appreciation to Woellner, Drain Bros Excavating Ltd, Pumice Hess Stone, and Lorama Group for donating the alkaline reagent solution, granite sand and quarry waste powder, pumice, and metakaolin, respectively. Funding for the work was provided by NSERC-Canada, DG grants.

REFERENCES

1. Davidovits, J., *Geopolymer Chemistry & Applications*, fifth edition, Geopolymer Institute, Saint-Quentin, France, 2020.

2. Ralli, Z. G., and Pantazopoulou, S. J., "State of the Art on Geopolymer Concrete," *International Journal of Structural Integrity*, V. 12, No. 4, 2021, pp. 511-533. doi: 10.1108/IJSI-05-2020-0050

3. Al-Majidi, M. H.; Lampropoulos, A.; and Cundy, A. B., "Tensile Properties of a Novel Fibre Reinforced Geopolymer Composite with Enhanced Strain Hardening Characteristics," *Composite Structures*, V. 168, 2017, pp. 402-427. doi: 10.1016/j.compstruct.2017.01.085

4. Ranjbar, N., and Zhang, M., "Fiber-Reinforced Geopolymer Composites: A Review," *Cement and Concrete Composites*, V. 107, 2020, p. 103498. doi: 10.1016/j.cemconcomp.2019.103498

5. Cheng, Z.; Liu, Z.; Hao, H.; Lu, Y.; and Li, S., "Multi-Scale Effects of Tensile Properties of Lightweight Engineered Geopolymer Composites Reinforced with MWCNTs and Steel-PVA Hybrid Fibers," *Construction and Building Materials*, V. 342, 2022, p. 128090. doi: 10.1016/j.conbuildmat.2022.128090

6. Wang, Y.; Chan, C. L.; Leong, S. H.; and Zhang, M., "Engineering Properties of Strain Hardening Geopolymer Composites with Hybrid Polyvinyl

Alcohol and Recycled Steel Fibres," *Construction and Building Materials*, V. 261, 2020, p. 120585. doi: 10.1016/j.conbuildmat.2020.120585

7. Shaikh, F. U. A., "Deflection Hardening Behaviour of Short Fibre Reinforced Fly Ash Based Geopolymer Composites," *Materials & Design*, V. 50, 2013, pp. 674-682. doi: 10.1016/j.matdes.2013.03.063

8. Nematollahi, B.; Qiu, J.; Yang, E. H.; and Sanjayan, J., "Microscale Investigation of Fiber-Matrix Interface Properties of Strain-Hardening Geopolymer Composite," *Ceramics International*, V. 43, No. 17, 2017, pp. 15616-15625. doi: 10.1016/j.ceramint.2017.08.118

9. Yoo, D.-Y.; Lee, S. K.; You, I.; Oh, T.; Lee, Y.; and Zi, G., "Development of Strain-Hardening Geopolymer Mortar Based on Liquid-Crystal Display (LCD) Glass and Blast Furnace Slag," *Construction and Building Materials*, V. 331, 2022, p. 127334. doi: 10.1016/j.conbuildmat.2022.127334

10. Al-Mashhadani, M. M.; Canpolat, O.; Aygörmez, Y.; Uysal, M.; and Erdem, S., "Mechanical and Microstructural Characterization of Fiber Reinforced Fly Ash Based Geopolymer Composites," *Construction and Building Materials*, V. 167, 2018, pp. 505-513. doi: 10.1016/j.conbuildmat.2018.02.061

11. Yaswanth, K. K.; Revathy, J.; and Gajalakshmi, P., "Influence of Copper Slag on Mechanical, Durability and Microstructural Properties of GGBS and RHA Blended Strain Hardening Geopolymer Composites," *Construction and Building Materials*, V. 342, 2022, p. 128042. doi: 10.1016/j.conbuildmat.2022.128042

12. Mousavinejad, S. H. G., and Sammak, M., "Strength and Chloride Ion Penetration Resistance of Ultra-High-Performance Fiber Reinforced Geopolymer Concrete," *Structures*, V. 32, 2021, pp. 1420-1427. doi: 10.1016/j.istruc.2021.03.112

13. Scrivener, K.; Martirena, F.; Bishnoi, S.; and Maity, S., "Calcined Clay Limestone Cements (LC3)," *Cement and Concrete Research*, V. 114, 2018, pp. 49-56. doi: 10.1016/j.cemconres.2017.08.017

14. Simão, L.; Souza, M. T.; Ribeiro, M. J.; Klegues Montedo, O. R.; Hotza, D.; Novais, R. M.; and Raupp-Pereira, F., "Assessment of the Recycling Potential of Stone Processing Plant Wastes Based on Physicochemical Features and Market Opportunities," *Journal of Cleaner Production*, V. 319, 2021, p. 128678. doi: 10.1016/j.jclepro.2021.128678

15. Rashwan, M. A.; Lasheen, E. S. R.; and Shalaby, B. N., "Incorporation of Metagabbro as Cement Replacement in Cement-Based Materials: A Role of Mafic Minerals on the Physico-Mechanical and Durability Properties," *Construction and Building Materials*, V. 210, 2019, pp. 256-268. doi: 10.1016/j.conbuildmat.2019.03.191

16. Ralli, Z. G.; Pantazopoulou, S. J.; and Papangelakis, V. G., "Microstructural Characterization of High-Performance Fiber Reinforced Geopolymer Concrete," *Acta Polytechnica CTU Proceedings*, V. 33, 2022.

17. Ralli, Z. G., and Pantazopoulou, S. J., "Effect of Aggregate Skeleton and Admixtures on Fresh and Hardened Properties of High-Strength Geopolymer Mortars," *SynerCrete 2023: International RILEM Conference on Synergising Expertise towards Sustainability and Robustness of Cement-based Materials and Concrete Structures*, 2023, pp. 415-428.

18. Ralli, Z. G., "Development, Material and Structural Performance of Tension Hardening Fiber Reinforced Geopolymer Concrete (THFRGC)," doctoral dissertation, York University, Toronto, ON, Canada, 2022.

19. Andreasen, A. H. M., and Andersen, J., "Über die Beziehung zwischen Kornabstufung und Zwischenraum in Production aus losen Körnern (mit einigen Experimenten)," *Colloid & Polymer Science*, V. 50, No. 30, 1930, pp. 217-228.

20. Funk, J. E., and Dinger, D. R., *Predictive Process Control of Crowded Particulate Suspensions: Applied to Ceramic Manufacturing*, Springer, 1993.

21. Khayat, K. H., and Mehdipour, I. "Design and Performance of Crack-Free Environmentally Friendly Concrete 'Crack-Free Eco-Crete," Center for Transportation Infrastructure and Safety, Missouri University of Science and Technology, Rolla, MO, 2014.

22. Li, P. P.; Yu, Q. L.; and Brouwers, H. J. H., "Effect of Coarse Basalt Aggregates on the Properties of Ultra-High Performance Concrete (UHPC)," *Construction and Building Materials*, V. 170, 2018, pp. 649-659. doi: 10.1016/j.conbuildmat.2018.03.109

23. Yu, R.; Spiesz, P.; and Brouwers, H. J. H., "Development of an Eco-Friendly Ultra-High Performance Concrete (UHPC) with Efficient Cement and Mineral Admixtures Uses," *Cement and Concrete Composites*, V. 55, 2015, pp. 383-394. doi: 10.1016/j.cemconcomp.2014.09.024

24. Yang, Y.; Massicotte, B.; Genikomsou, A. S.; Pantazopoulou, S. J.; and Palermo, D., "Comparative Investigation on Tensile Behaviour of UHPFRC," *Materials and Structures*, V. 54, No. 4, 2021, p. 147. doi: 10.1617/s11527-021-01747-1

25. ASTM C1856/C1856M-17, "Standard Practice for Fabricating and Testing Specimens of Ultra-High Performance Concrete," ASTM International, West Conshohocken, PA, 2017.

26. ASTM C1437-07, "Standard Test Method for Flow of Hydraulic Cement Mortar," ASTM International, West Conshohocken, PA, 2007.

27. ASTM C191-21, "Standard Test Methods for Time of Setting of Hydraulic Cement by Vicat Needle," ASTM International, West Conshohocken, PA, 2021.

28. CSA A23.2-9C, "Compressive Strength of Cylindrical Concrete Specimens," CSA Group, Toronto, ON, Canada, 2014.

29. Blaber, J.; Adair, B.; and Antoniou, A., "Ncorr: Open-Source 2D Digital Image Correlation Matlab Software," *Experimental Mechanics*, V. 55, No. 6, 2015, pp. 1105-1122. doi: 10.1007/s11340-015-0009-1

30. ASTM C1609/C1609M-19. "Standard Test Method for Flexural Performance of Fiber-Reinforced Concrete (Using Beam With Third-Point Loading)," ASTM International, West Conshohocken, PA, 2019, 9 pp.

31. Yang, Y., "Tensile Behaviour of Ultra-High-Performance Steel Fiber Reinforced Concrete," master's thesis, York University, Toronto, ON, Canada, 2019.

32. Husain, S. A. B., "Characterization of UHPFRC Materials for Bridge Construction: An Opportunity to Offset the Need for Prestressing in Bridge Decks," master's thesis, York University, Toronto, ON, Canada, 2021.

33. AASHTO T 397, "Standard Method of Test for Uniaxial Tensile Response of Ultra-High Performance Concrete," American Association of State Highway Transportation Officials, Washington, DC, 2022.

34. CSA A23.2-11C, "Test Methods and Standard Practices for Concrete," CSA Group, Toronto, ON, Canada, 2014, pp. 573-576.

35. CSA A23.2-21C, "Test Method for Length Change of Hardened Concrete," CSA Group, Toronto, ON, Canada, 2014, pp. 629-635.

36. ASTM C1012/C1012M-18, "Standard Test Method for Length Change of Hydraulic-Cement Mortars Exposed to a Sulfate Solution," ASTM International, West Conshohocken, PA, 2018.

37. Ralli, Z.; Husain, S.; Pantazopoulou, S.; Booya, E.; and Loh, P., "Evaluation of CSA Prequalification Procedures of UHPC Materials for Bridge Construction," *Third International Interactive Symposium on Ultra-High Performance Concrete*, Iowa State University Digital Press, Ames, IA, 2023.

38. ASTM C944/C944M-19. "Standard Test Method for Abrasion Resistance of Concrete or Mortar Surfaces by the Rotating-Cutter Method," ASTM International, West Conshohocken, PA, 2019, 5 pp.

39. CSA A23.2-23C, "Electrical Indication of Concrete's Ability to Resist Chloride Ion Penetration," CSA Group, Toronto, ON, Canada, 2014, pp. 644-657.

40. AASHTO T 277, "Standard Method of Test for Electrical Indication of Concrete's Ability to Resist Chloride Ion Penetration," American Association of State Highway and Transportation Officials, Washington, DC, 2022, pp. 1-15.

41. Stanish, K. D.; Hooton, R. D.; and Thomas, M. D. A., "Testing the Chloride Penetration Resistance of Concrete: A Literature Review," University of Toronto, Toronto, ON, Canada, 1997.

42. CSA A23.2-22C, "Scaling Resistance of Concrete Surfaces Exposed to Deicing Chemicals Using Mass Loss," CSA Group, Toronto, ON, Canada, 2014, pp. 636-643.

43. Wang, W.; Shen, A.; Lyu, Z.; He, Z.; and Nguyen, K. T. Q., "Fresh and Rheological Characteristics of Fiber Reinforced Concrete-A Review," *Construction and Building Materials*, V. 296, 2021, p. 123734. doi: 10.1016/j.conbuildmat.2021.123734

44. ASTM C469/C469M-22, "Standard Test Method for Static Modulus of Elasticity and Poisson's Ratio of Concrete in Compression," ASTM International, West Conshohocken, PA, 2022, 6 pp.

45. ACI Committee 242, "Alkali-Activated Cements—Report (ACI PRC-242-22)," American Concrete Institute, Farmington Hills, MI, 2022, 20 pp.

46. Young, J. F.; Mindess, S.; Gray, R. J.; and Bentur, A., *The Science and Technology of Civil Engineering Materials*, first edition, Pearson Hall, 1997, 334 pp.

47. Archontas, N. D., and Pantazopoulou, S. J. "Microstructural Behavior and Mechanics of Nano-Modified Cementitious Materials," *Advances in Concrete Construction*, V. 3, No. 1, 2015, pp. 15-37.

48. Neville, A. M., *Properties of Concrete*, fifth edition, Trans-Atlantic Publications, Inc., 2012.

49. CSA S6, "Annex 8.1 of CSA-S6: Canadian Highway Bridge Design Code (CHBDC)-Fiber Reinforced Concrete," CSA Group, Toronto, ON, Canada, 2018.

50. Ralli, Z., and Pantazopoulou, S., "Correlation Between Tensile Strength and Modulus of Rupture for Ultra High-Performance Concrete (UHPFRC)," *Proceedings of 2019 National Accelerated Bridge Construction Conference Including Automation, Service Life and UHPC*, Miami, FL, 2019.

51. Yang, L.; Shi, C.; and Wu, Z., "Mitigation Techniques for Autogenous Shrinkage of Ultra-High-Performance Concrete—A Review,"

Composites, Part B: Engineering, V. 178, 2019, p. 107456. doi: 10.1016/j.compositesb.2019.107456

52. Rangan, B. V., "Engineering Properties of Geopolymer Concrete," *Geopolymers: Structures, Processing, Properties and Industrial Applications*, Elsevier Ltd., 2009, pp. 211-226.

53. Wallah, S. E., and Rangan, B. V., "Low-Calcium Fly Ash-Based Geopolymer Concrete: Long-Term Properties," Curtin University of Technology, Perth, Australia, 2006.

54. Rangan, B. V.; Hardjito, D.; Wallah, S. E.; and Sumajouw, D. M. J., "Studies on Fly Ash-Based Geopolymer Concrete," *Geopolymer 2005 Proceedings*, 2005. pp. 133-137.

55. Song, X.-J.; Munn, R.; Marosszeky, M.; and Brungs, M., "Investigation of Cracking Developed in Sulphuric Acid Resistant Concretes," CIA 22nd Biennial Conference, Melbourne, Australia, 2005.

56. Osio-Norgaard, J.; Gevaudan, J. P.; and Srubar, W. V. III, "A Review of Chloride Transport in Alkali-Activated Cement Paste, Mortar, and Concrete," *Construction and Building Materials*, V. 186, 2018, pp. 191-206. doi: 10.1016/j.conbuildmat.2018.07.119

57. LS-412, "Test Method for Scaling Resistance of Concrete Surfaces Exposed to Deicing Chemicals," Ontario Ministry of Transportation, Toronto, ON, Canada.

58. Bouzoubaâ, N.; Bilodeau, A.; Fournier, B.; Hooton, R. D.; Gagné, R.; and Jolin, M., "Deicing Salt Scaling Resistance of Concrete Incorporating Supplementary Cementing Materials: Laboratory and Field Test Data," *Canadian Journal of Civil Engineering*, V. 35, No. 11, 2008, pp. 1261-1275. doi: 10.1139/L08-067

59. Hooton, D. R., and Vassilev, D., "Deicer Scaling Resistance of Concrete Mixtures Containing Slag Cement, Phase 2: Evaluation of Different Laboratory Scaling Test Methods," National Concrete Pavement Technology Center, Ames, IA, 2012.

60. Hammond, G. P., and Jones, C. I., "Embodied Energy and Carbon in Construction Materials," *Proceedings of the Institution of Civil Engineers - Energy*, V. 161, No. 2, 2008, pp. 87-98.

61. Bascetin, A.; Adiguzel, D.; and Tuylu, S., "The Investigation of Co2 Emissions for Different Rock Units in the Production of Aggregate," *Environmental Earth Sciences*, V. 76, No. 7, 2017, p. 279. doi: 10.1007/s12665-017-6602-0

62. Lava Mining & Quarrying SA, "Pumice Stone-Environmental Product Declaration," The International EPD® System, 2021.

63. Zheng, H., "Concrete for Sustainability," *SCCT Annual Concrete Seminars. Standing Committee on Concrete Technology (SCCT) 27*, 2009.

64. Kobayashi, K.; Iizuka, T.; Kurachi, H.; and Rokugo, K., "Corrosion Protection Performance of High Performance Fiber Reinforced Cement Composites as a Repair Material," *Cement and Concrete Composites*, V. 32, No. 6, 2010, pp. 411-420. doi: 10.1016/j.cemconcomp.2010.03.005

65. Yao, Y.; Zhu, Y.; and Yang, Y., "Incorporation Superabsorbent Polymer (SAP) Particles as Controlling Pre-Existing Flaws to Improve the Performance of Engineered Cementitious Composites (ECC)," *Construction and Building Materials*, V. 28, No. 1, 2012, pp. 139-145. doi: 10.1016/j.conbuildmat.2011.08.032

66. Eshghi, N., "Behavior and Analysis of Strain Hardening Fiber Reinforced Cementitious Composites under Shear and Flexure," master's thesis, York University, Toronto, ON, Canada, 2018.

ACI in Your Classroom

Integrate ACI into your classroom!

To support future leaders, ACI has launched several initiatives to engage students in the Institute's activities and programs – select programs that may be of interest to Educators are:

- **Free student membership –** encourage students to sign up
- **Special student discounts on *ACI 318 Building Code Requirements for Structural Concrete*, *ACI 530 Building Code Requirements and Specification for Masonry Structure*, & *Formwork for Concrete* manual.**
- **Access to *Concrete International* –** free to all ACI student members
- **Access to *ACI Structural Journal* and *ACI Materials Journal* –** free to all ACI student members
- **Free sustainability resources –** free copies of Sustainable Concrete Guides provided to universities for use in the classroom
- **Student competitions –** participate in ACI's written and/or team-based competitions
- **Scholarships and fellowships –** students who win awards are provided up to $15,000 and may be offered internships and paid travel to attend ACI's conventions
- **ACI Award for University Student Activities –** receive local and international recognition for your University's participation in concrete-related activities
- **Free access to the *ACI Collection of Concrete Codes, Specifications, and Practices* –** in conjunction with ACI's chapters, students are provided free access to the online ACI Collection
- **ACI online recorded web sessions and continuing education programs –** online learning tools ideal for use as quizzes or in-class study material

https://www.concrete.org/educatorsandresearchers/aciinyourclassroom.aspx

ACI MATERIALS JOURNAL TECHNICAL PAPER

Title No. 121-M28

Contribution of Shrinkage-Reducing Admixture and Lightweight Sand to Moist-Curing Requirement for Fiber-Reinforced Ultra-High-Performance Concrete

by Le Teng, Alfred Addai-Nimoh, and Kamal H. Khayat

This study evaluates the potential to use shrinkage-reducing admixture (SRA) and pre-saturated lightweight sand (LWS) to shorten the external moist-curing requirement of ultra-high-performance concrete (UHPC), which is critical in some applications where continuous moist-curing is challenging. Key characteristics of UHPC prepared with and without SRA and LWS and under 3 days, 7 days, and continuous moist curing were investigated. Results indicate that the combined incorporation of 1% SRA and 17% LWS can shorten the required moist-curing duration because such a mixture under 3 days of moist curing exhibited low total shrinkage of 360 με and compressive strength of 135 MPa (19,580 psi) at 56 days, and flexural strength of 18 MPa (2610 psi) at 28 days. This mixture subjected to 3 days of moist curing had a similar hydration degree and 25% lower capillary porosity in paste compared to the Reference UHPC prepared without any SRA and LWS and under continuous moist curing. The incorporation of 17% LWS promoted cement hydration and silica fume pozzolanic reaction to a degree similar to extending the moist-curing duration from 3 to 28 days and offsetting the impact of SRA on reducing cement hydration. The lower capillary porosity in the paste compensated for the porosity induced by porous LWS to secure an acceptable level of total porosity of UHPC.

Keywords: lightweight sand (LWS); moist-curing duration; shrinkage-reducing admixture (SRA); ultra-high-performance concrete (UHPC).

INTRODUCTION

Ultra-high-performance concrete (UHPC) can be considered an advanced sustainable material because its great mechanical performance and high durability can achieve a long service life.[1-3] The proper curing protocol is a key factor in achieving the great performance of UHPC.[4,5] Steam curing with a relative humidity of 95% and a temperature of 90°C (194°F) is a common method for preparing UHPC based on ACI 239R. It should be mentioned that the risk of expansion damage induced by delayed ettringite formation is low for UHPC subjected to steam curing. This can be mainly attributed to the insufficient water for the formation of secondary ettringite.[6,7] The compressive strength can be greater than 150 MPa (21,755 psi) after 48 hours of curing due to the promotion of cement hydration. Previous studies show that autoclave curing is also appropriate for curing UHPC[4,8]; UHPC subjected to 10 hours of autoclave curing with a pressure of 1.0 MPa (145 psi) and a temperature of 185°C (365°F) exhibited 45% higher compressive strength compared to the UHPC cured under 23°C (73.4°F) and relative humidity of 95% for 28 days.[8] However, it is difficult to provide the steam or autoclave curing in cast-in-place applications, such as thin-bonded overlay rehabilitation, joints to connect prefabricated elements, and piers and other vertical structural elements.[9,10]

The conventional curing strategy used in field casting is to spray the water- or wax-based concrete curing compound onto the UHPC surface, followed by covering the plastic sheet.[9,11] Such external moist curing can reduce the shrinkage and surface dehydration risk. Khayat et al.[12] reported that the thin-bonded UHPC overlay had a high risk of cracking at early age with the use of inappropriate external curing. The importance of external moist curing can be attributed to two reasons. First, the external curing water can penetrate the UHPC elements at an early age. This can promote cement hydration.[13,14] It should be mentioned that fibers cannot effectively bridge cracks when the fiber-matrix bond strength is inadequate. Furthermore, the external curing can delay the decreasing rate of internal relative humidity (IRH), which significantly mitigates the stress caused by the restrained shrinkage.[15] In the laboratory, continuous moist curing is a common curing protocol to secure the high mechanical performance of UHPC at room temperature of 20°C (68°F). Continuous moist curing can result in a 35% enhancement in compressive strength at 28 days compared to air-drying curing.[13] The mechanical properties of UHPC under moist curing can usually be lower than those of UHPC subjected to accelerated curing at early age combined with moist curing at a later age.[4,5,14] Xu et al.[16] reported the that the 1-year compressive strength of UHPC subjected to steam curing at 90°C (194°F) for 48 hours followed by continuous moist curing at 20°C (68°F) was 25% higher than that of UHPC subjected to continuous moist curing at 20°C (68°F). This can be attributed to the dense hydrated cement paste and reduced porosity.[5,16]

The adequate duration of moist curing is also important to achieve low shrinkage of UHPC to secure a low level of internal stress and decrease the risk of cracking when UHPC is subjected to restrained conditions.[17-19] Valipour and Khayat[13] reported that the extension of moist-curing duration from 1 to 7 days decreased the total shrinkage equal to the sum of autogenous and drying shrinkage from 700 to 130 με (80% reduction) for UHPC at 7 days. However, it is not

ACI Materials Journal, V. 121, No. 3, May 2024.

MS No. M-2023-101.R1, doi: 10.14359/51740566, received October 24, 2023, and reviewed under Institute publication policies.

always feasible to maintain long-term moist curing or sealed conditions in field applications, especially for structural rehabilitation, given the negative impact on transportation.

One possible solution to shorten the required moist-curing duration without influencing shrinkage is to use an expansive agent. The expansion caused by the expansive agent is supposed to compensate for the shrinkage of UHPC to keep the low total volumetric variation over time. However, such expansion may not be concurrent with the shrinkage. For instance, Teng et al.[17] proposed that UHPC made with a CaO-based expansive agent exhibited a high expansion during the first 7 days, followed by a rapid shrinkage. Furthermore, the hydration of the expansive agent can consume the water used for cement hydration, which can impair the UHPC's mechanical properties.[13,17]

Using internal curing material can be considered a promising method to reduce the duration of external moist curing. In the case of UHPC, the low water-binder ratio (*w*/*b*) can cause self-desiccation during cement hydration, which can lead to high autogenous shrinkage.[20] The incorporation of internal curing material, such as pre-saturated lightweight sand (LWS), is effective in decreasing autogenous shrinkage to lower the total shrinkage, given that the water released from internal curing material can retard the drop in the IRH.[21-25] The autogenous shrinkage at 7 days was shown to decrease by 20% when 25% of river sand in UHPC was substituted by volume by LWS.[25] However, the incorporation of LWS at a high content cannot eliminate autogenous shrinkage but impairs the mechanical performance. The autogenous shrinkage at 7 days and compressive strength at 28 days decreased from 720 to 435 με and 120 to 70 MPa (17,405 to 10,150 psi) when all the conventional concrete sand was replaced with LWS for UHPC made with 0.17 *w*/*b*.[26] This reduction in mechanical performance is because the porosity of UHPC increased with the use of porous LWS.[25,26]

Shrinkage-reducing admixture (SRA) can be incorporated to decrease the required duration of moist curing in terms of achieving low shrinkage. This can be attributed to the absorption of amphiphilic molecules onto the interface between water and air/solids, which can decrease the surface tension of water in capillary pores.[27-29] As the 2% SRA was added, the autogenous shrinkage of UHPC was shown to decrease by 35%,[30] and the drying shrinkage of UHPC reduced by 40%.[31] However, incorporating SRA can impair the mechanical properties due to the decreased cement hydration.[31,32] For example, the compressive strength of UHPC reduced from 125 to 110 MPa (18,130 to 15,955 psi) as the dosage of SRA increased from 0 to 2%.[31]

The incorporation of a combination of SRA and LWS is more efficient in lowering the UHPC shrinkage without significantly affecting the compressive strength. For example, the addition of 3% SRA combined with 35% LWS significantly reduced the autogenous shrinkage at 7 days and led to a 15 MPa (2175 psi) enhancement in the compressive strength at 28 days.[13] Cheng et al.[33] reported that as the 45% LWS and 0.5% SRA were combined, the autogenous shrinkage and drying shrinkage were reduced by 80% and 60%, respectively, and the decrease in compressive strength was within 10%. Therefore, the authors are concerned that the addition of an appropriate combination of SRA and LWS has the possibility to shorten the external moist-curing duration without greatly affecting the mechanical performance and total shrinkage of UHPC (refers to autogenous and drying shrinkage). This study evaluated the effect of LWS, SRA, and moist-curing duration on shrinkage, compressive strength, and flexural performance of UHPC. Thermogravimetric analysis (TGA) was conducted to monitor the development of cement hydration, and backscatter scanning electron microscopy (BSEM) and mercury intrusion porosimetry (MIP) were carried out to investigate the pore structure of UHPC mixtures. The result of this work aims to provide guidance on using LWS and SRA to accelerate structural rehabilitation without increasing cracking risk at the early age of repaired material, given the restrained shrinkage.

RESEARCH SIGNIFICANCE

Ensuring sufficient moist-curing duration is essential to mitigate shrinkage and enhance the mechanical properties of UHPC, but it can slow down the construction and rehabilitation rate. Previous studies reported that incorporating SRA and LWS can secure low shrinkage and adequate mechanical performance. However, limited studies evaluated the potential of using SRA and LWS to shorten the moist-curing duration. This study investigated the coupled impact of SRA, LWS, and moist-curing duration on the micro and macro performance of UHPC. The results can be of interest to concrete technologists and contractors seeking methods to decrease the required moist-curing duration.

MIXTURE DESIGN AND SPECIMEN PREPARATION

Raw materials and mixture proportions

The Reference mixture was the nonproprietary UHPC with 0.2 *w*/*b* designed by Meng et al.[34] Type III cement was substituted with 5% undensified silica fume as well as 40% Class C fly ash to lower high-range water-reducer (HRWR) demand. The Blaine surface areas of fly ash and cement were 465 and 560 m^2/kg, respectively. A combination of 70% coarse sand and 30% fine sand was incorporated to improve the particle packing.[29] The maximum size and D_{50} of the coarse sand were 4.75 and 0.64 mm, respectively. Such values were 2 and 0.35 mm for the fine sand. The straight steel fibers incorporated to increase the ductility measured 13 mm (0.51 in.) in length and 0.1 mm (0.004 in.) in radius. The fiber content was set at 2% by volume of mixture.

A polycarboxylate-based HRWR containing 40% solid content and a specific gravity of 1.08 was employed to keep the constant mini-slump flow of 190 mm (7.5 in.) at the end of mixing. A viscosity-modifying admixture (VMA) in liquid form was used to secure the high thixotropy and homogeneity of the material[35,36]; its solid content and specific gravity were 60% and 1.04, respectively.

A pre-saturated expanded shale LWS with a water absorption of 18.5% was used to replace part of the sand for internal curing. LWS exhibited an irregular shape with open pores at the surface; its maximum diameter and D_{50} were 4.75 and 2.15 mm (0.19 and 0.09 in.), respectively. The replacement ratios were set at 10%, 17%, and 25%,[25]

Table 1—UHPC mixture proportions

Mixture	Type III cement	Silica fume	Class C fly ash	Fine sand	Concrete sand	LWS*	Steel fiber	SRA	VMA	HRWR†
	kg/m^3 (lb/ft^3)							By mass of binder, %		
Ref	649 (40.5)	41 (2.6)	405 (25.3)	302 (18.9)	688 (42.9)	0	156 (9.7)	0	0.5	0.91
SRA1					688 (42.9)	0		1		0.87
SRA2					688 (42.9)	0		2		0.86
LWS10					590 (36.8)	65 (4.1)		0		0.79
LWS17					516 (32.2)	118 (7.4)		0		0.72
LWS25					444 (27.7)	167 (10.4)		0		0.65
LWS17&SRA1					516 (32.2)	118 (7.4)		1		0.69
LWS17&SRA1.5					516 (32.2)	118 (7.4)		1.5		0.67

*Refers to solid content of HRWR.

†Corresponds to saturated surface-dry condition.

indicating that the total *w*/*b* values were 0.21, 0.22, and 0.23, respectively. The SRA, with a solid content of 30% and a specific gravity of 1.01, was employed as the other shrinkage mitigation strategy. Its dosage varied from 1 to 2% by mass of binder.[26] The LWS content that can lead to the highest compressive strength was chosen to combine with 1 and 1.5% SRA. In total, eight UHPC mixtures were prepared in this study, as listed in Table 1. The notation of the mixture reflects the LWS and SRA contents that were added into the mixture. For instance, the LWS17&SRA1 mixture refers to the mixture containing 17% LWS and 1% SRA.

Specimen preparation

A mixer with 19 L (4.2 gal.) capacity was employed to prepare UHPC at room temperature of 20 ± 2°C (68 ± 3.6°F) in compliance with the following procedures: 1) mixing the dry materials in addition to steel fibers for 2 minutes at 1 rps; 2) incorporating 90% of HRWR as well as water then stirring the materials for 3 minutes at 2 rps; 3) adding the remaining solution of mixing water and HRWR combined with VMA and SRA followed by stirring the materials for 1 minute at 2 rps; and 4) incorporating steel fibers gradually and stirring the entire materials for another 2 minutes at 2 rps.

The samples prepared to measure mechanical properties and shrinkage were cast in one lift, and a slight vibration was employed to consolidate the samples. Plastic sheet and wet burlap were then used to cover the samples immediately after casting. After demolding at 1 day, three protocols were employed to cure the samples: 1) 3 days of moist curing followed by air drying (3MC); 2) 7 days of moist curing followed by air drying (7MC); and 3) continuous moist curing (MC). Lime-saturated water was used during the moist curing, and air-drying curing was achieved using the environmental chamber with a relative humidity of 50 ± 4% and a temperature of 23 ± 2°C (73.4 ± 3.6°F).

TEST METHODS

Shrinkage measurement

A sealed specimen measuring 285 x 75 x 75 mm (11.5 x 3 x 3 in.) was prepared to monitor the autogenous shrinkage of UHPC. A 120 mm (4.8 in.) vibrating 120 Ω strain gauge was embedded at the center of the mold before casting. Multiple layers of aluminum tape combined with one layer of plastic sheet were used to seal the specimens. A data acquisition system was used to measure the shrinkage at a 5-minute interval from the final setting time determined using a Vicat needle to 28 days. The samples were cured in a room with a temperature of 23 ± 1°C (68 ± 1.8°F). The total shrinkage corresponding to the sum of autogenous and drying shrinkage was evaluated using prismatic samples measuring 285 x 75 x 75 mm (11.5 x 3 x 3 in.). The test monitoring began after demolding at 1 day of age. The total shrinkage was measured daily in the first 2 weeks, followed on a weekly basis until 56 days. Three samples were measured for each mixture to assess the reliability of the shrinkage results.

Mechanical performance

The compressive strengths of UHPC at 1, 3, 7, 28, and 56 days were measured using cubic specimens measuring 50 x 50 x 50 mm (2 x 2 x 2 in.) according to ASTM C109/C109M. The prismatic specimens were used to determine the flexural properties of UHPC in compliance with ASTM C1609/C1609M. The total length, span, width, and span of the specimens measured 400, 305, 75, and 75 mm (16, 12, 3, and 3 in.), respectively. A low loading speed of 0.1 mm (0.004 in.) per minute was used. The area under the load-deflection curve was determined to calculate the flexural toughness. Three samples were measured for each mixture to assess the reliability of the experimental results.

TGA and MIP

The hydration degree and pore structure were determined using the samples taken from the center of the UHPC cubic specimens at 28 days. Ethyl alcohol was used to soak samples to avoid the hydration of cementitious materials, followed by drying the samples in a vacuum oven at 60°C (140°F). For the TGA testing, powders with a particle size smaller than 75 µm (2.9 5 × 10^{-6} in.) were obtained by grinding the samples at 28 days, then a sample measuring approximately 15 mg (6.8 × 10^{-6} lb) was heated up to 1000°C (1832°F) in a nitrogen gas atmosphere at a rate of 10°C (18°F) per minute. The MIP test was conducted using a porosimeter. Samples measuring

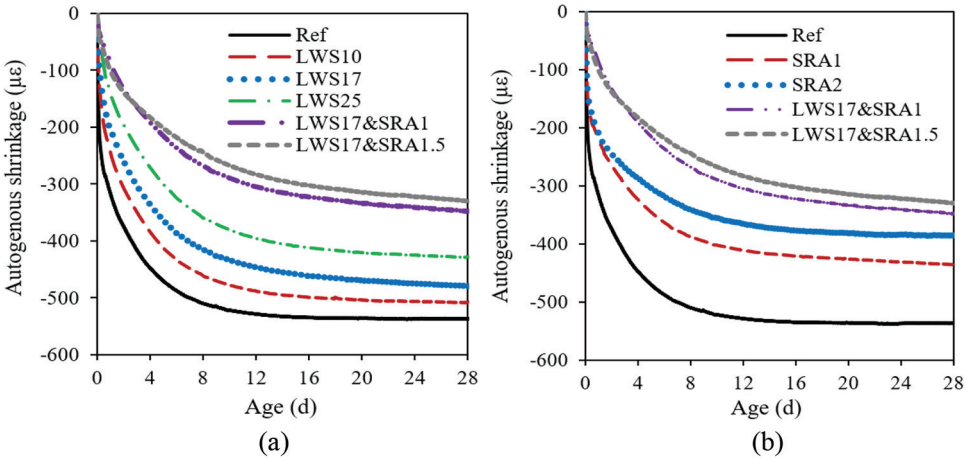

Fig. 1—Variations of autogenous shrinkage of UHPC made with SRA and LWS.

2 to 4 g (0.9×10^{-3} to 1.8×10^{-3} lb) were stored in a glass tube. The surface tension and mercury contact angle were set at 480 mN/m and 130 degrees, respectively. The intrusion volume of mercury was measured when the intrusion pressure gradually increased from 0 to 410 MPa (59,465 psi).

BSEM

Sample preparation for BSEM testing was the same as that of the MIP test. The samples were mounted in epoxy resin, followed by successive polishing to obtain a smooth surface. The polishing procedures were elaborated in previous studies.[37,38] The microscopic morphology was observed using a scanning electron microscope with an accelerating voltage of 20 kV. A gold coating was employed to prepare the sample surface before the test. Three samples were tested for each nonfibrous UHPC mortar mixture. The porosity and proportions of unhydrated binders were determined using nonfibrous UHPC mortar samples. A total of 30 BSEM images was selected randomly from three samples for each mixture. Image-Pro software was used to obtain the gray histogram of selected BSEM images. The pores, unhydrated binder, and hydrated binder can be distinguished by their different gray levels.[39,40] The detailed image process and selection of threshold value for each phase were elaborated in the previous study.[35]

EXPERIMENTAL RESULTS

Autogenous shrinkage

Figure 1 compares the individual and combined impact of SRA and LWS on UHPC autogenous shrinkage. The development of autogenous shrinkage became slower after 7 days. When the content of LWS was enhanced from 0 to 25%, the autogenous shrinkage at 28 days was shown to decrease by 20%, which confirmed that the LWS provided effective internal curing. The reduction in autogenous shrinkage was 30% by incorporating 2% SRA, given the lower surface tension of water in capillary pores.[28,29] The incorporation of the combination of SRA and LWS had a higher efficiency in decreasing the autogenous shrinkage compared with the separate incorporation of SRA and LWS. As shown, the combined addition of 1.5% SRA and 17% LWS resulted in the lowest autogenous shrinkage of 330 με at 28 days. It should be mentioned that the coefficients of variation (COVs) of the results were less than 10%, indicating the results are highly reproducible.

Total shrinkage

Figure 2 presents the impact of LWS, SRA, and the duration of moist curing on the total shrinkage of UHPC, where the COV values of the experimental results were less than 10%. The total shrinkage reflects the sum of autogenous and drying shrinkage after demolding at 1 day. The increasing tendency of total shrinkage became slower after 7 days when the continuous moist curing was employed to cure UHPC mixtures. This agrees with the result of autogenous shrinkage. Furthermore, the total shrinkage exhibited a sharp increase when the specimens were moved from lime-saturated water to the curing chamber.

The moist-curing duration had the greatest effect on reducing total shrinkage, followed by using SRA and LWS. This result is consistent with the findings reported by Valipour and Khayat,[13] where moist curing is more effective in reducing the total shrinkage compared to shrinkage-mitigating materials. An approximately 50% reduction of total shrinkage (520 to 270 με) at 56 days was observed for the Reference UHPC with the extension of the duration of moist curing from 3 to 56 days. Incorporating 2% SRA reduced the total shrinkage at 56 days from 520 to 350 με (33% reduction) for UHPC under 3 days of moist curing. Such reduction was from 520 to 400 με (17% decrease) in mixtures made with 25% LWS. The incorporation of a combination of 1.5% SRA and 17% LWS exhibited the lowest total shrinkage for a given duration of moist curing.

The incorporation of either SRA or LWS can mitigate the duration of moist curing to secure low shrinkage. The 56 days of total shrinkage values were 450 με for the UHPC made with 25% LWS and 360 με for the use of 2% SRA when UHPC was under 3 days of moist curing. Such values were lower than 460 με of the Reference mixture under 7 days of moist curing. The internal curing effect of LWS is more significant for the larger UHPC specimens when continuous moist curing is applied.[20] This demonstrates that the LWS should have a higher potential to shorten the external moist-curing duration in field applications. Furthermore, the

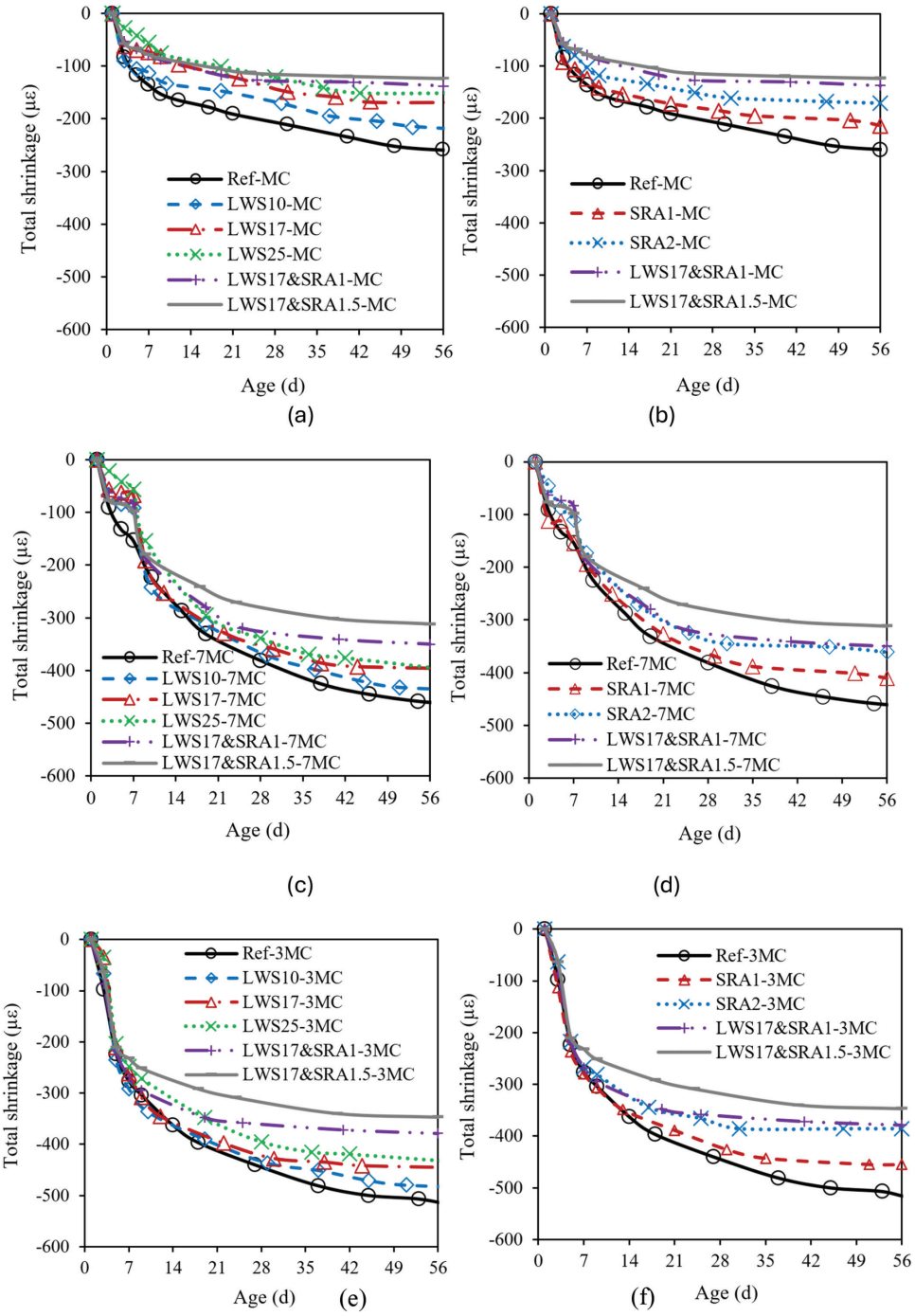

Fig. 2—Impact of LWS, SRA, and moist-curing duration on total shrinkage of UHPC (that is, sum of autogenous and drying shrinkage after demolding at 1 day.)

combined addition of LWS and SRA had a more pronounced effect on shortening the duration of moist curing. For instance, the total shrinkage of the LWS17&SRA1.5 mixture under 3 days of moist curing was 310 με at 56 days; such a value was close to the total shrinkage of the Reference UHPC under continuous moist curing. To sum up, there is great potential to reduce the external moist-curing duration using LWS and SRA in terms of shrinkage. However, this study concentrates on the small laboratory specimens. The effect of LWS and SRA on the shrinkage of large UHPC structural elements needs further study for field application.

Compressive strength

Figure 3 illustrates the impact of SRA, LWS, and moist-curing duration on UHPC compressive strength. The compressive strengths of investigated mixtures containing different shrinkage-mitigating materials and under different curing protocols tested 45 to 60 MPa (6525 to 8700 psi) at 1 day, 85 to 110 MPa (12,325 to 15,955 psi) at 3 days, 100 to 135 MPa (14,505 to 19,580 psi) at 7 days, 115 to 150 MPa (16,680 to 21,755 psi) at 28 days, and 120 to 155 MPa (17,405 to 22,480 psi) at 56 days. In general, UHPC involving 17% LWS had the highest compressive strength given the enhancement in the cement hydration thanks to the

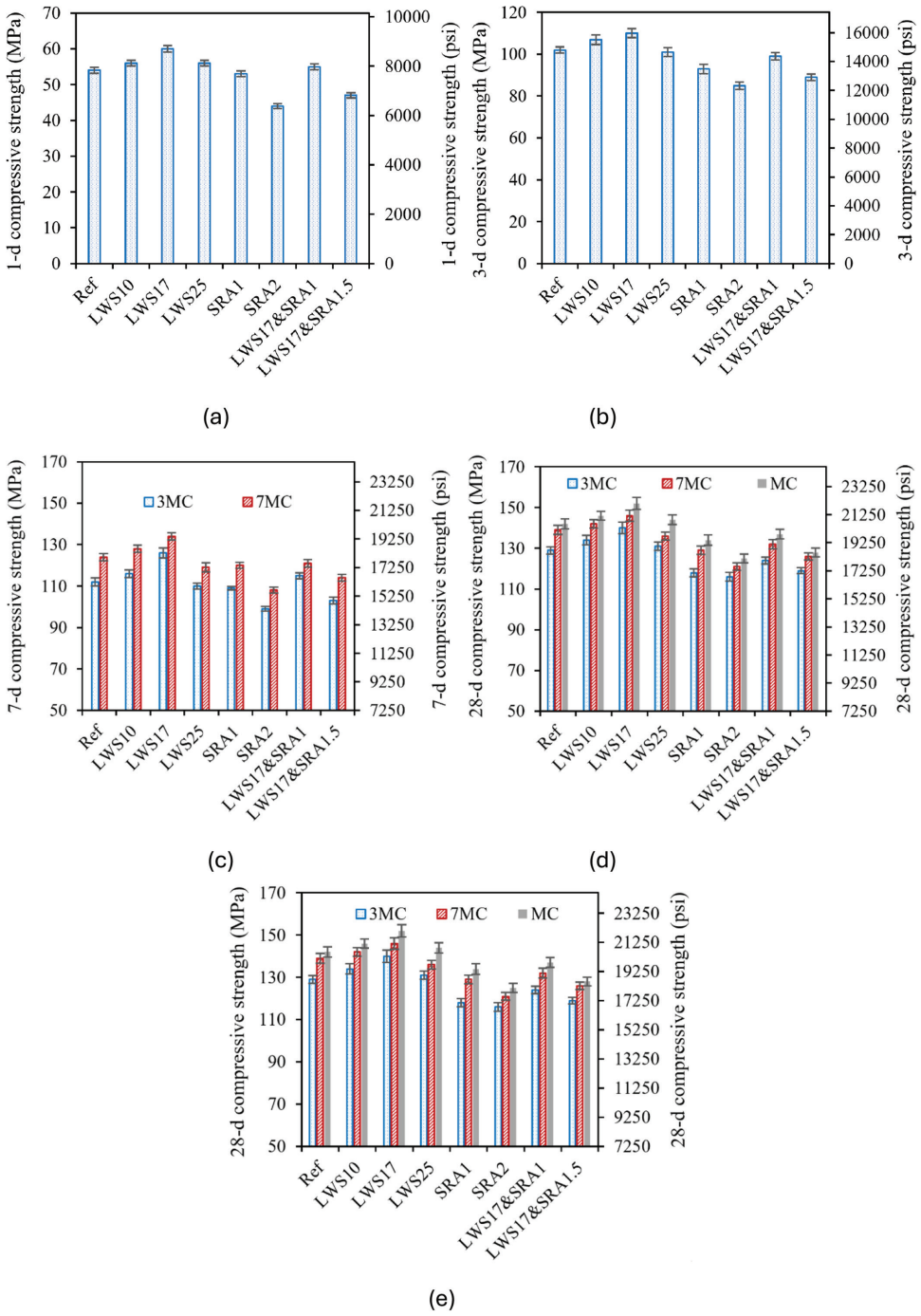

Fig. 3—Impact of LWS, SRA, and moist-curing duration on compressive strength of UHPC at various ages.

internal curing effect.[25,41] However, UHPC made with 25% LWS had 5 to 10% lower compressive strength compared to UHPC containing 17% LWS. One of the possible reasons is the increase of porosity of the UHPC induced by the use of porous LWS at high content.[25,42]

The addition of LWS for internal curing can shorten the moist-curing duration needed to secure high compressive strength. The LWS17 mixture under 3 days of moist curing and the Reference mixture subjected to continuous moist curing had similar compressive strength at 28 days of 140 MPa (20,305 psi). The effect of moist and internal curing on cement hydration was compared earlier in the "TGA" section. The incorporation of SRA considerably impaired UHPC compressive strength. For example, the compressive strength at 28 days was reduced by approximately 15% by incorporating 2% SRA when the 7 days of moist curing was employed. This is because the incorporation of SRA can reduce cement hydration, as elaborated earlier.

Early-age moist curing is essential to enhancing compressive strength. For instance, the extension of the duration of moist curing from 3 to 7 days led to a 5 to 10% enhancement in compressive strength at 56 days for the Reference mixture. However, the enhancement of compressive strength was limited to 2 to 3% only when the moist-curing duration was changed from 7 days to continuous moist curing. This can be due to the fact that the dense microstructure of the hardened

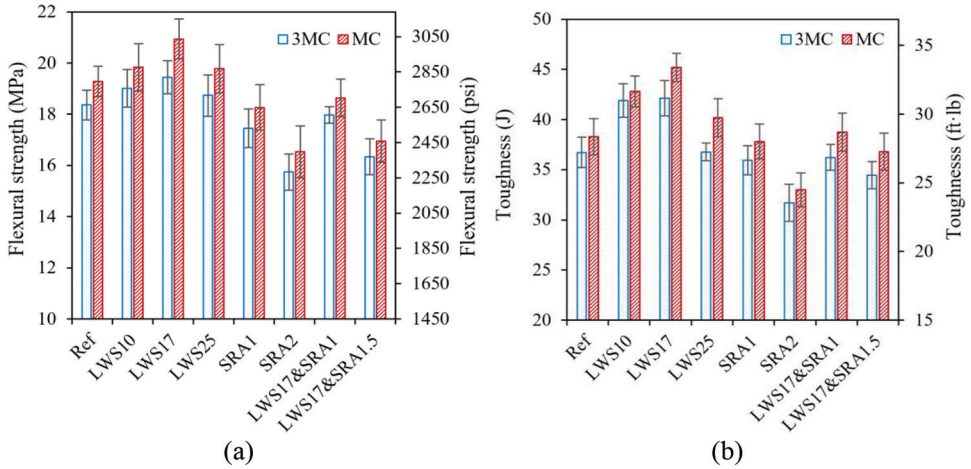

Fig. 4—Influence of LWS, SRA, and moist-curing duration on flexural strength and toughness of UHPC at 28 days.

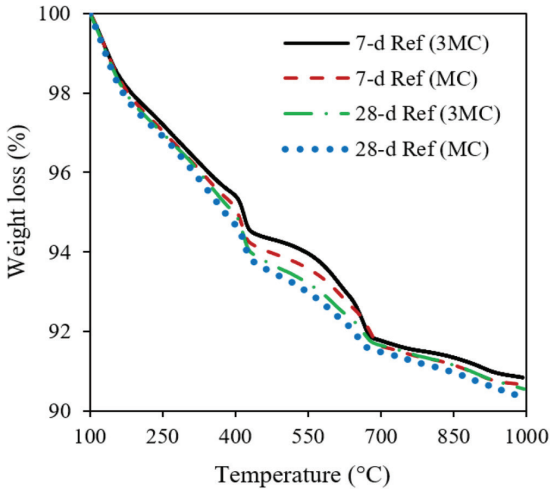

Fig. 5—TGA results of Reference UHPC mixture.

UHPC can decrease the influence of external moist curing on cement hydration.[21] Furthermore, the addition of the combination of 1% SRA and 17% LWS exhibited similar compressive strength compared to the Reference UHPC. In general, it is possible to use LWS and SRA to shorten the external moist-curing duration based on the compressive strength of small UHPC specimens. Given the specimen size effect, it is worth evaluating the influence of LWS and SRA on the mechanical strength of large UHPC elements in future work.

Flexural strength and toughness

Figure 4 shows the influence of LWS, SRA, and the duration of moist curing on flexural properties at 28 days of UHPC. The flexural strength and toughness were from 15 to 21 MPa (2175 to 3045 psi) and 31 to 45 J (23 to 33 ft·lb), respectively. The flexural properties were enhanced by increasing the moist-curing duration and using LWS for internal curing. Furthermore, the use of LWS for internal curing was shown to require a shorter moist-curing duration to achieve high flexural performance compared to UHPC prepared without LWS. For example, the LWS17 mixture subjected to 3 days of moist curing and the Reference UHPC with continuous moist curing had similar flexural strengths. However, the flexural toughness of the former mixture was 8 J (6 ft·lb) higher than that of the latter UHPC. The incorporation of SRA impaired the flexural performance of UHPC. For instance, as the SRA dosage increased from 0 to 2%, a 15% reduction in flexural strength was observed. The LWS17&SRA1 mixture under 3 days of moist curing and the Reference mixtures under continuous curing exhibited a similar flexural strength of 18.5 MPa (2685 psi), which demonstrates that the influence of SRA and decreased moist-curing duration on reducing flexural strength and toughness was compensated by using LWS.

TGA

Figure 5 plots the TGA results of the Reference mixture subjected to various moist-curing durations. The hydration products gradually decomposed with the increase in temperature, and the loss of carbon oxide and chemically bound water can decrease the weight of the sample. The main phase dehydrated at 100 to 400°C (210 to 750°F) was C-S-H, dehydroxylated at 400 to 550°C (550 to 1020°F) was calcium hydroxide (CH), and decarbonated at 550 to 1000°C (1020 to 1830°F) was $CaCO_3$.[43] The CH content and chemically bound water were quantified to determine the hydration degree of UHPC.[44] The CH content can be determined by the ratio of weight loss caused by CH dihydroxylation and $CaCO_3$ decarbonation to the weight of the dried sample before testing.[45-47] The reduction of mass with the increase of temperature from 0 to 550°C (32 to 1020°F) was normalized by the dehydrated sample mass at 550°C (1020°F) to evaluate the content of the chemically bound water.[45] The accurate ranges of the temperature were measured by the derivative thermogravimetric curve.

Figure 6 presents the impact of SRA, LWS, and the duration of moist curing on the UHPC bound water at 7 and 28 days. The enhancement in the bound water content referred to the higher hydration degree of cementitious materials. The content of bound water of UHPC at 28 days was 7 to 13.5% higher than that of the UHPC at 7 days. As the duration of moist curing extended from 3 to 28 days, the content of bound water increased by 3.5 to 11.5%. Furthermore, the addition of 17% LWS led to an enhancement of up to 11% in the bound water content, whereas the bound water decreased by 3 to 9% with the incorporation of 2% SRA. Furthermore, the LWS17 mixture under 3 days of moist curing and the Reference

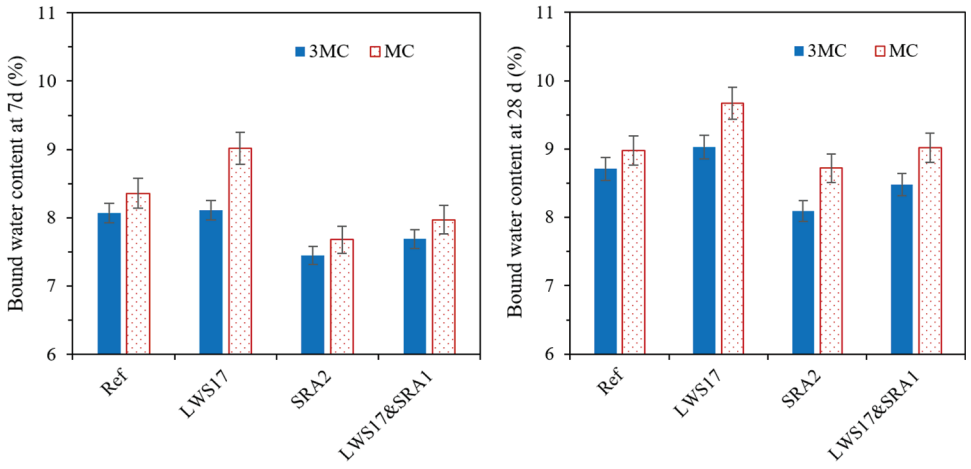

Fig. 6—Impact of SRA, LWS, and moist-curing duration on bound water content of UHPC mixtures at 7 and 28 days.

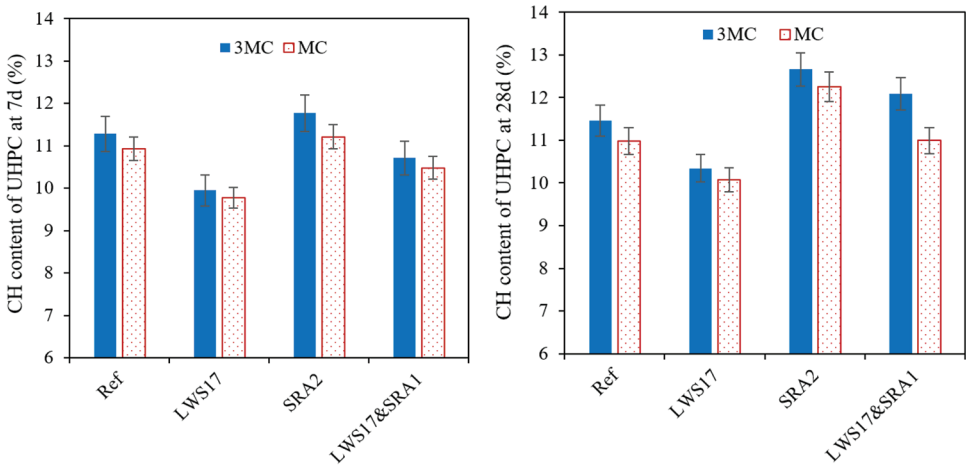

Fig. 7—Impact of SRA, LWS, and moist-curing duration on CH content of UHPC mixtures at 7 and 28 days.

mixture under continuous moist curing exhibited a similar bound water content of 9% at 28 days. This demonstrated that the use of 17% LWS provided a similar curing effect compared to the extension of the duration of external moist curing from 3 to 28 days in terms of the promotion of cement hydration. These results agree with the variation of mechanical performance of UHPC made with the LWS and SRA and subjected to different moist-curing durations.

The variations of CH content with the LWS, SRA, and moist-curing duration of UHPC at 7 and 28 days are shown in Fig. 7. The UHPC mixture subjected to continuous moist curing had 1.5 to 12.5% lower CH content compared to the mixtures under 3 days of moist curing. The incorporation of 17% LWS decreased the CH content by 9 to 13% for UHPC at the same age. Adding LWS for internal curing and extending the duration of moist curing enhanced the cement hydration and pozzolanic reaction of silica fume.[45,48] The CH content increased with the cement hydration but decreased with the silica fume pozzolanic reaction.[45,48] The decrease in CH content indicated that extending the moist-curing duration and incorporating LWS for internal curing were more effective in increasing the silica fume pozzolanic reaction than promoting the hydration of cement. In the case of using SRA, a 4 to 12% increase in CH content was found for UHPC at the same age, given the reduced pozzolanic reaction of silica fume.

Pore structure of UHPC mortar

The impact of SRA, LWS, and the duration of moist curing on the total porosity of UHPC at 28 days is shown in Fig. 8. The total porosity including the pores with sizes from 5 nm to 300 µm (2×10^{-7} to 0.01 in.) ranged between 8.5 and 12.5% for the investigated UHPC mixtures. As the duration of moist curing extended from 3 to 28 days, a 10 to 15% drop in total porosity was observed. The total porosity was enhanced by approximately 11% with the incorporation of 2% SRA, whereas the increasing amplitude was 15 to 20% by incorporating 17% LWS. The incorporation of a combination of 1% SRA and 17% LWS in UHPC subjected to 3 days of moist curing led to the highest porosity of 12.5%.

Table 2 presents the influence of SRA, LWS, and the duration of moist curing on the pore volume distribution, which is divided into gel nanopores (<10 nm [4×10^{-7} in.]), mesopores (10 to 50 nm [4×10^{-7} to 2×10^{-6} in.]), capillary pores (50 to 5000 nm [2×10^{-6} to 2×10^{-4} in.]), and macropores (>5000 nm [2×10^{-4} in.]).[49,50] The longer duration of moist curing resulted in the reduction of all kinds of pores. For example, the extension of the duration of moist curing from 3 to 28 days led to a 35%, 30%, and 35% decrease in

Table 2—Variations of pore size distribution of UHPC mixtures

	Gel nanopores		Mesopores		Capillary pores		Macropores	
	Mean, %	COV, %	Mean, %	COV, %	Mean, %	COV, %	Mean, %	COV, %
Ref-3MC	0.98	5.2	6.29	4.8	2.09	6.4	0.86	5.5
LWS17-3MC	0.95	5.6	5.79	6.5	3.16	5.9	1.98	7.3
SRA1-3MC	1.80	5.7	5.66	5.4	2.88	6.2	1.13	5.9
LWS17&SRA1-3MC	1.72	5.3	5.93	6.1	3.11	5.7	1.77	7.6
Ref-MC	1.41	6.2	5.06	6.3	1.60	5.3	0.82	5.2
LWS17-MC	1.95	4.9	4.77	7.2	2.30	4.8	1.48	7.8
SRA1-MC	1.62	5.5	5.13	5.9	2.06	6.5	0.96	5.7
LWS17&SRA1-MC	1.94	6.4	5.15	4.7	2.97	6.8	1.46	7.6

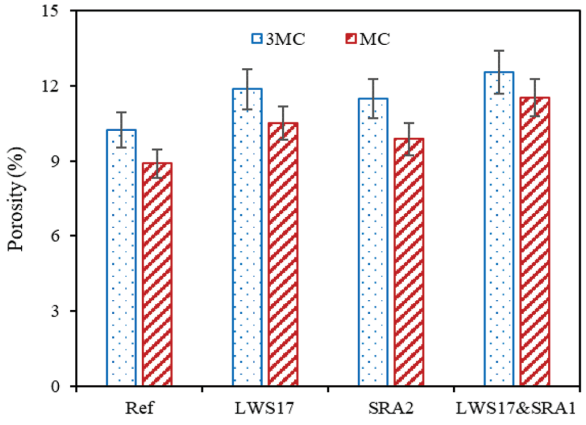

Fig. 8—Impact of SRA, LWS, and moist-curing duration on porosity of UHPC at 28 days.

mesopores, capillary pores, and macropores for the Reference mixture. The addition of 17% LWS for internal curing increased the gel nanopores from 1.41 to 1.95 and reduced the mesopores by 5 to 10%. The gel nanopores refer to the pores in the C-S-H with water held by the hydrogen bond.[49] Therefore, the increase in the gel nanopores indicates that the cement hydration is promoted by the internal curing effect of LWS. Furthermore, the capillary pores and macropores were shown to increase by 40 to 50% and 30 to 50%. This can be attributed to the incorporation of porous LWS, which was the origin of the decreased mechanical performance of UHPC when the high LWS content (that is, 25% in the study) was added (refer to the "Compressive strength" and "Flexural strength and toughness" sections). In the case of SRA, a 25 to 40% increase in the capillary pores was found with the addition of 2% SRA. This is because the addition of SRA can result in lower hydration of cement and silica fume pozzolanic reactivity, as well as increasing the entrained air volume.[32,51] The incorporation of SRA combined with LWS increased the amount of all kinds of pores for UHPC under the same moist-curing duration. For instance, the gel nanopores, mesopores, capillary pores, and macropores of the LWS17&SRA1 mixture subjected to continuous moist curing were approximately 35, 5, 85, and 80% higher than those of the Reference mixture under the continuous moist curing.

BSEM image analysis of UHPC paste

Figure 9 shows the BSEM images of paste LWS17-MC and SRA-3MC samples, which corresponded to the highest and lowest compressive strength, respectively. The unhydrated binders (white and light gray), hydrated binders (dark gray), and pores (black) can be detected. The conventional concrete sand and LWS can also be observed. The images reflected that the LWS17 mixture subjected to continuous moist curing had fewer pores in the paste compared to the SRA2 mixture under 3 days of moist curing.

The influence of SRA, LWS, and the duration of moist curing on porosity and relative content of unhydrated binder of paste of the investigated UHPC at 28 days is presented in Fig. 10. The measured pore diameter varied from 1 to 30 µm (4×10^{-5} to 1.2×10^{-3} in.). The relative content of the unhydrated binder was determined using the ratio of the area of the unhydrated binder to the total area of hydrated and unhydrated binders. The incorporation of 17% LWS led to a 45% and 10% reduction in porosity and relative content of unhydrated binder, respectively, for the mixtures subjected to the 3 days of moist curing. This is because the internal curing effect of LWS enhanced the silica fume pozzolanic reaction and hydration of cement, which reduced the porosity in the paste.[25,41] On the other hand, the porosity of UHPC at 28 days was shown to increase by 10 to 15% with the use of 2% SRA. The relative content of unhydrated binder also increased by 5 to 15%. This demonstrated that the SRA reduced the cement hydration, leading to a higher porosity of UHPC. The change of moist-curing protocol from 3 days of moist curing to continuous moist curing increased the cement hydration degree and decreased the porosity. For example, as the duration of moist curing extended from 3 to 28 days, the LWS17&SRA1 mixture displayed 30% and 10% lower porosity and relative content of unhydrated binder, respectively. In general, the BSEM results were in agreement with the TGA and MIP results.

CONCLUSIONS

This study evaluated the potential of incorporating shrinkage-reducing admixture (SRA) and lightweight sand (LWS) to shorten the required duration of moist curing of ultra-high-performance concrete (UHPC), which can accelerate structural construction and rehabilitation. The SRA dosage varied from 0 to 2% by mass of cementitious

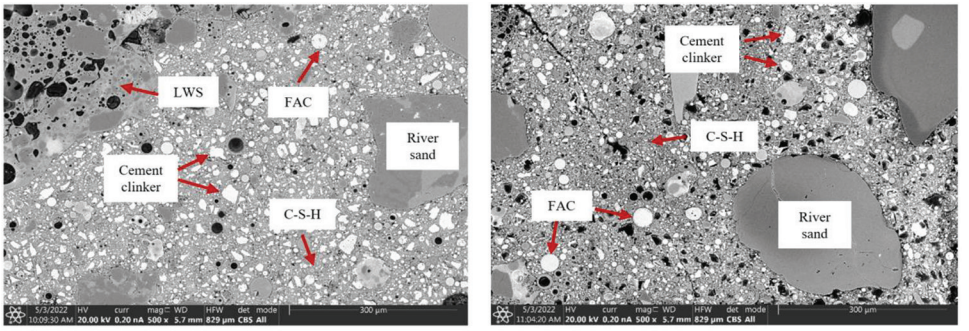

(a) (b)

Fig. 9—Typical BSEM images of: (a) LWS17 mixture subjected to continuous moist curing; and (b) SRA2 mixture under 3 days of moist curing.

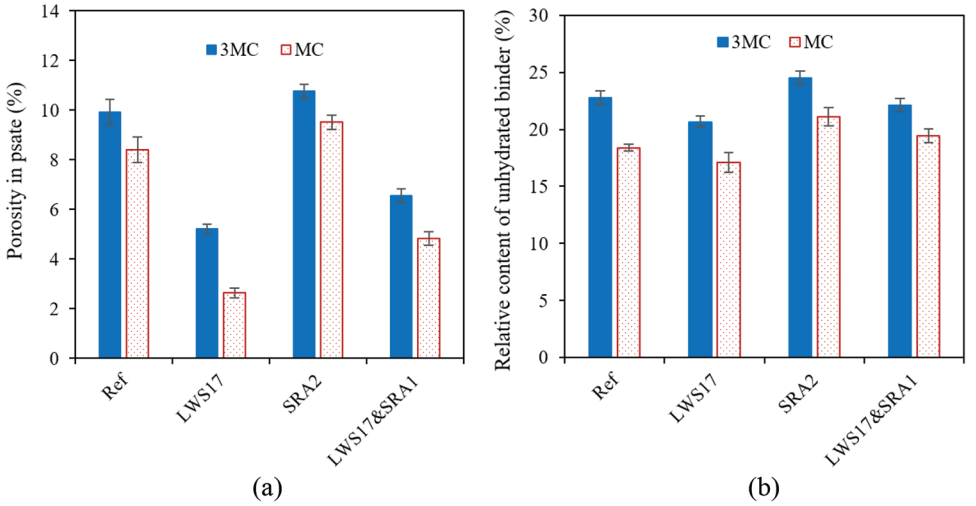

(a) (b)

Fig. 10—Impact of SRA, LWS, and moist-curing duration on total porosity and relative content of unhydrated binder of UHPC paste at 28 days.

materials, and up to 25% of total sand was substituted using the equivalent volume of LWS. The following conclusions can be obtained according to the experimental results:

1. The individual use of SRA or LWS was not effective in decreasing the moist-curing duration. The total shrinkage of the Reference mixture prepared without any SRA and LWS and subjected to continuous moist curing was 40% lower than that of the LWS17 mixture under 3 days of moist curing in spite of the similar compressive strength. Incorporating 2% SRA was shown to impair the compressive strength at 56 days by 10% even when the same moist-curing duration was used.

2. The addition of a combination of LWS and SRA had a greater potential to shorten the moist-curing duration without increasing the autogenous and drying shrinkage and reduce the mechanical properties of UHPC compared to the separate incorporation of SRA or LWS. The mixture containing 1% SRA and 17% LWS and under 3 days of moist curing exhibited total shrinkage at 56 days of 360 με, compressive strength at 56 days of 135 MPa (19,310 psi), and flexural strength at 28 days of 18 MPa (2575 psi) and toughness of 36 J (27 ft·lb). In the case of the Reference mixture subjected to continuous moist curing, these values were 270 με, 145 MPa (20,740 psi), 19 MPa (2720 psi), and 38 J (28 ft·lb).

3. The reduction in cement hydration and silica fume pozzolanic reaction due to the use of SRA and decreased moist-curing duration was compensated by incorporating LWS. A similar CH content of 11.7% and bound water content of 8.8% were observed for the LWS17&SRA1 mixture under 3 days of moist curing and the Reference mixture subjected to continuous moist curing at 28 days.

4. The porosity in the paste of the LWS17&SRA1 mixture under 3 days of moist curing was shown to be 25% less than that of the Reference mixture subjected to continuous moist curing, although the entire porosity of the LWS17&SRA1 mixture was 20% higher than that of the Reference UHPC at a given curing duration. This demonstrates that the internal curing impact of LWS had a greater effect on densifying the microstructure of the cement paste compared to the influence of SRA and decreased moist-curing duration on weakening the microstructure.

DECLARATION OF COMPETING INTEREST

The authors declare that they have no known competing financial interests or personal relationships that could have appeared to influence the work reported in this paper.

AUTHOR BIOS

Le Teng *is a Professor at the School of Materials Science and Engineering at Southeast University, Nanjing, China. He received his PhD from Missouri University of Science and Technology, Rolla, MO. His research interests include enhancing the performance of ultra-high-*

performance concrete (UHPC) through tailoring rheological properties, mitigating shrinkage, and improving the mechanical properties.

Alfred Addai-Nimoh *is a PhD Candidate in the Department of Civil, Architectural, and Environmental Engineering at Missouri University of Science and Technology. His research interests include the rheology of concrete, especially for three-dimensional printing of concrete.*

Kamal H. Khayat, *FACI, is a Professor at Missouri University of Science and Technology and a member of several ACI Committees. His research interests include self-consolidating concrete, the rheology of cement-based materials, fiber-reinforced concrete, high-performance concrete, and repair.*

ACKNOWLEDGMENTS

The authors acknowledge the financial support provided by the Missouri Department of Transportation [Grant Number: TR2021-21]. This research was conducted at the Advanced Construction and Materials Laboratory (ACML) of the Center for Infrastructure Engineering Studies (CIES) at Missouri University of Science and Technology.

REFERENCES

1. Graybeal, B.; Brühwiler, E.; Kim, B.; Toutlemonde, F.; Voo, Y. L.; and Zaghi, M., "International Perspective on UHPC in Bridge Engineering," *Journal of Bridge Engineering*, ASCE, V. 25, No. 11, 2020, pp. 1-16. doi: 10.1061/(ASCE)BE.1943-5592.0001630

2. Du, J.; Meng, W.; Khayat, K. H.; Bao, Y.; Guo, P.; Lyu, Z.; Abu-Obeidah, A.; Nassif, H.; and Wang, H., "New Development of Ultra-High-Performance Concrete (UHPC)," *Composites Part B: Engineering*, V. 224, 2021, p. 109220. doi: 10.1016/j.compositesb.2021.109220

3. Fan, L.; Meng, W.; Teng, L.; and Khayat, K. H., "Effects of Lightweight Sand and Steel Fiber Contents on the Corrosion Performance of Steel Rebar Embedded in UHPC," *Construction and Building Materials*, V. 238, 2020, p. 117709. doi: 10.1016/j.conbuildmat.2019.117709

4. Hamada, H.; Alattar, A.; Tayeh, B.; Yahaya, F.; and Almeshal, I., "Influence of Different Curing Methods on the Compressive Strength of Ultra-High-Performance Concrete: A Comprehensive Review," *Case Studies in Construction Materials*, V. 17, 2022, p. e01390. doi: 10.1016/j.cscm.2022.e01390

5. Shen, P.; Lu, L.; He, Y.; Wang, F.; and Hu, S., "The Effect of Curing Regimes on the Mechanical Properties, Nano-Mechanical Properties and Microstructure of Ultra-High-Performance Concrete," *Cement and Concrete Research*, V. 118, 2019, pp. 1-13. doi: 10.1016/j.cemconres.2019.01.004

6. Heinz, D., and Ludwig, H. M., "Heat Treatment and the Risk of DEF Delayed Ettringite Formation in UHPC," *Proceedings of the International Symposium on Ultra High Performance Concrete*, M. Schmidt, E. Fehling, and C. Geisenhanslüke, eds., Kassel, Germany, 2004, pp. 717-730.

7. Xu, D.; Tang, J.; Hu, X.; Yu, C.; Han, F.; Sun, S.; Deng, W.; and Liu, J., "The Influence of Curing Regimes on Hydration, Microstructure and Compressive Strength of Ultra-High-Performance Concrete: A Review," *Journal of Building Engineering*, V. 76, 2023, p. 107401. doi: 10.1016/j.jobe.2023.107401

8. Chen, T.; Gao, X.; and Ren, M., "Effects of Autoclave Curing and Fly Ash on Mechanical Properties of Ultra-High-Performance Concrete," *Construction and Building Materials*, V. 158, 2018, pp. 864-872. doi: 10.1016/j.conbuildmat.2017.10.074

9. Sritharan, S.; Doiron, G.; Bierwagen, D.; Keierleber, B.; and Abu-Hawash, A., "First Application of UHPC Bridge Deck Overlay in North America," *Transportation Research Record*, V. 26, 2018, pp. 40-47.

10. Teng, L., and Khayat, K. H., "Effect of Overlay Thickness, Fiber Volume, and Shrinkage Mitigation on Flexural Behavior of Thin Bonded Ultra-High-Performance Concrete Overlay Slab," *Cement and Concrete Composites*, V. 134, No. 11, 2022, p. 104752. doi: 10.1016/j.cemconcomp.2022.104752

11. Graybeal, B., and Haber, Z., "Ultra-High Performance Concrete for Bridge Deck Overlays," Report No. FHWA-HRT-17-097, Federal Highway Administration, Washington, DC, 2018.

12. Khayat, K. H.; Teng, L.; and Addai-Nimoh, A., "Performance of Cost-Effective Non-Proprietary UHPC in Thin-Bonded Bridge Overlays," MoDOT Research Report No. cmr 23-011, Missouri Department of Transportation, Jefferson City, MO, 2023.

13. Valipour, M., and Khayat, K. H., "Coupled Effect of Shrinkage-Mitigating Admixtures and Saturated Lightweight Sand on Shrinkage of UHPC for Overlay Applications," *Construction and Building Materials*, V. 184, 2018, pp. 320-329. doi: 10.1016/j.conbuildmat.2018.06.191

14. Kang, H., and Moon, J., "Secondary Curing Effect on the Hydration of Ultra-High-Performance Concrete," *Construction and Building Materials*, V. 298, 2021, p. 123874. doi: 10.1016/j.conbuildmat.2021.123874

15. Liu, Y.; Wei, Y.; Ma, L.; and Wang, L., "Restrained Shrinkage Behavior of Internally-Cured UHPC Using Calcined Bauxite Aggregate in the Ring Test and UHPC-Concrete Composite Slab," *Cement and Concrete Composites*, V. 134, 2022, p. 104805. doi: 10.1016/j.cemconcomp.2022.104805

16. Xu, D.; Tang, J.; Hu, X.; Zhou, Y.; Yu, C.; Han, F.; and Liu, J., "Influence of Silica Fume and Thermal Curing on Long-Term Hydration, Microstructure and Compressive Strength of Ultra-High-Performance Concrete (UHPC)," *Construction and Building Materials*, V. 395, 2023, p. 132370. doi: 10.1016/j.conbuildmat.2023.132370

17. Teng, L.; Valipour, M.; and Khayat, K. H., "Design and Performance of Low Shrinkage UHPC for Thin Bonded Bridge Deck Overlay," *Cement and Concrete Composites*, V. 118, 2021, p. 103953. doi: 10.1016/j.cemconcomp.2021.103953

18. Bao, Y.; Valipour, M.; Meng, W.; Khayat, K. H.; and Chen, G., "Distributed Fiber Optic Sensor-Enhanced Detection and Prediction of Shrinkage-Induced Delamination of Ultra-High-Performance Concrete Overlay," *Smart Materials and Structures*, V. 26, No. 8, 2017, p. 85009. doi: 10.1088/1361-665X/aa71f4

19. Lange, D. A., and Shin, H. C., "Early Age Stresses and Debonding in Bonded Concrete Overlays," *Transportation Research Record: Journal of the Transportation Research Board*, V. 1778, No. 1, 2001, pp. 174-181. doi: 10.3141/1778-21

20. Liu, J.; Farzadnia, N.; Shi, C.; and Ma, X., "Effects of Superabsorbent Polymer on Shrinkage Properties of Ultra-High Strength Concrete Under Drying Condition," *Construction and Building Materials*, V. 215, 2019, pp. 799-811. doi: 10.1016/j.conbuildmat.2019.04.237

21. Liu, J.; Shi, C.; Farzadnia, N.; and Ma, X., "Effects of Pretreated Fine Lightweight Aggregate on Shrinkage and Pore Structure of Ultra-High Strength Concrete," *Construction and Building Materials*, V. 204, 2019, pp. 276-287. doi: 10.1016/j.conbuildmat.2019.01.205

22. Ma, X.; Liu, J.; and Shi, C., "A Review on the Use of LWA as an Internal Curing Agent of High-Performance Cement-Based Materials," *Construction and Building Materials*, V. 218, 2019, pp. 385-393. doi: 10.1016/j.conbuildmat.2019.05.126

23. Snoeck, D.; Jensen, O. M.; and De Belie, N., "The Influence of Superabsorbent Polymers on the Autogenous Shrinkage Properties of Cement Pastes with Supplementary Cementitious Materials," *Cement and Concrete Research*, V. 74, 2015, pp. 59-67. doi: 10.1016/j.cemconres.2015.03.020

24. Shen, D.; Wang, T.; Chen, Y.; Wang, M.; and Jiang, G., "Effect of Internal Curing with Super Absorbent Polymers on the Relative Humidity of Early-Age Concrete," *Construction and Building Materials*, V. 99, 2015, pp. 246-253. doi: 10.1016/j.conbuildmat.2015.08.042

25. Meng, W., and Khayat, K. H., "Effects of Saturated Lightweight Sand Content on Key Characteristics of Ultra-High-Performance Concrete," *Cement and Concrete Research*, V. 101, 2017, pp. 46-54. doi: 10.1016/j.cemconres.2017.08.018

26. Lu, J.; Shen, P.; Ali, H. A.; and Poon, C. S., "Development of High-Performance Lightweight Concrete Using Ultra High Performance Cementitious Composite and Different Lightweight Aggregates," *Cement and Concrete Composites*, V. 124, 2021, p. 104277. doi: 10.1016/j.cemconcomp.2021.104277

27. Rajabipour, F.; Sant, G.; and Weiss, J., "Interactions Between Shrinkage Reducing Admixtures (SRA) and Cement Paste's Pore Solution," *Cement and Concrete Research*, V. 38, No. 5, 2008, pp. 606-615. doi: 10.1016/j.cemconres.2007.12.005

28. Wehbe, Y., and Ghahremaninezhad, A., "Combined Effect of Shrinkage Reducing Admixtures (SRA) and Superabsorbent Polymers (SAP) on the Autogenous Shrinkage, Hydration and Properties of Cementitious Materials," *Construction and Building Materials*, V. 138, 2017, pp. 151-162. doi: 10.1016/j.conbuildmat.2016.12.206

29. Rongbing, B., and Jian, S., "Synthesis and Evaluation of Shrinkage-Reducing Admixture for Cementitious Materials," *Cement and Concrete Research*, V. 35, No. 3, 2005, pp. 445-448. doi: 10.1016/j.cemconres.2004.07.009

30. Yoo, D. Y.; Banthia, N.; and Yoon, Y. S., "Effectiveness of Shrinkage-Reducing Admixture in Reducing Autogenous Shrinkage Stress of Ultra-High-Performance Fiber-Reinforced Concrete," *Cement and Concrete Composites*, V. 64, 2015, pp. 27-36. doi: 10.1016/j.cemconcomp.2015.09.005

31. Liu, J.; Farzadnia, N.; Shi, C.; and Ma, X., "Shrinkage and Strength Development of UHSC Incorporating a Hybrid System of SAP and SRA," *Cement and Concrete Composites*, V. 97, 2019, pp. 175-189. doi: 10.1016/j.cemconcomp.2018.12.029

32. Zhang, W.; Lin, H.; Xue, M.; Wang, S.; Ran, J.; Su, F.; and Zhu, J., "Influence of Shrinkage Reducing Admixtures on the Performance of Cementitious Composites: A Review," *Construction and Building Materials*, V. 325, 2022, p. 126579. doi: 10.1016/j.conbuildmat.2022.126579

33. Cheng, S.; Wu, Z.; Wu, Q.; Chen, X.; and Tu, Y., "Mitigation on the Shrinkage Properties of Ultra-High Strength Concrete via Using Porous

Coral Sand and Shrinkage Reducing Agent," *Journal of Building Engineering*, V. 57, 2022, p. 104861. doi: 10.1016/j.jobe.2022.104861

34. Meng, W.; Valipour, M.; and Khayat, K. H., "Optimization and Performance of Cost-Effective Ultra-High-Performance Concrete," *Materials and Structures*, V. 50, No. 1, 2017, pp. 1-16. doi: 10.1617/s11527-016-0896-3

35. Teng, L.; Huang, H.; Du, J.; and Khayat, K. H., "Prediction of Fiber Orientation and Flexural Performance of UHPC Based on Suspending Mortar Rheology and Casting Method," *Cement and Concrete Composites*, V. 122, 2021, p. 104142. doi: 10.1016/j.cemconcomp.2021.104142

36. Teng, L.; Zhu, J.; Khayat, K. H.; and Liu, J., "Effect of Welan Gum and Nanoclay on Thixotropy of UHPC," *Cement and Concrete Research*, V. 138, 2020, p. 106238. doi: 10.1016/j.cemconres.2020.106238

37. Scrivener, K.; Snellings, R.; and Lothenbach, B., *A Practical Guide to Microstructural Analysis of Cementitious Materials*, CRC Press, Boca Raton, FL, 2016.

38. Huang, H.; Teng, L.; Gao, X.; Khayat, K. H.; Wang, F.; and Liu, Z., "Effect of Carbon Nanotube and Graphite Nanoplatelet on Composition, Structure, and Nano-Mechanical Properties of C-S-H in UHPC," *Cement and Concrete Research*, V. 154, 2022, p. 106713. doi: 10.1016/j.cemconres.2022.106713

39. Pi, Z.; Xiao, H.; Liu, R.; Liu, M.; and Li, H., "Effects of Brass Coating and Nano-SiO_2 Coating on Steel Fiber-Matrix Interfacial Properties of Cement-Based Composite," *Composites Part B: Engineering*, V. 189, 2020, p. 107904. doi: 10.1016/j.compositesb.2020.107904

40. Huang, H.; Teng, L.; Khayat, K. H.; Gao, X.; Wang, F.; and Liu, Z., "For the Improvement of Mechanical and Microstructural Properties of UHPC with Fiber Alignment Using Carbon Nanotube and Graphite Nanoplatelet," *Cement and Concrete Composites*, V. 129, 2022, p. 104462. doi: 10.1016/j.cemconcomp.2022.104462

41. Huang, H.; Teng, L.; Gao, X.; Khayat, K. H.; and Wang, F., "Use of Saturated Lightweight Sand to Improve the Mechanical and Microstructural Properties of UHPC with Fiber Alignment," *Cement and Concrete Composites*, V. 129, 2022, p. 104513. doi: 10.1016/j.cemconcomp.2022.104513

42. Lu, J.; Shen, P.; Ali, H. A.; and Poon, C. S., "Mix Design and Performance of Lightweight Ultra High-Performance Concrete," *Materials and Design*, V. 216, 2022, p. 110553. doi: 10.1016/j.matdes.2022.110553

43. Deboucha, W.; Leklou, N.; Khelidj, A.; and Oudjit, M. N., "Hydration Development of Mineral Additives Blended Cement Using Thermogravimetric Analysis (TGA): Methodology of Calculating the Degree of Hydration," *Construction and Building Materials*, V. 146, 2017, pp. 687-701. doi: 10.1016/j.conbuildmat.2017.04.132

44. Lothenbach, B.; Durdziński, P.; and De Weerdt, K., "Thermogravimetric Analysis," *A Practical Guide to Microstructural Analysis of Cementitious Materials*, first edition, K. Scrivener, R. Snellings, and B. Lothenbach, eds., CRC Press, Boca Raton, FL, 2016, pp. 177-211.

45. Liao, W.; Sun, X.; Kumar, A.; Sun, H.; and Ma, H., "Hydration of Binary Portland Cement Blends Containing Silica Fume: A Decoupling Method to Estimate Degrees of Hydration and Pozzolanic Reaction," *Frontiers in Materials*, V. 6, 2019, p. 78. doi: 10.3389/fmats.2019.00078

46. Adu-Amankwah, S.; Zajac, M.; Stabler, C.; Lothenbach, B.; and Black, L., "Influence of Limestone on the Hydration of Ternary Slag Cements," *Cement and Concrete Research*, V. 100, 2017, pp. 96-109. doi: 10.1016/j.cemconres.2017.05.013

47. Schöler, A.; Lothenbach, B.; Winnefeld, F.; and Zajac, M., "Hydration of Quaternary Portland Cement Blends Containing Blast-Furnace Slag, Siliceous Fly Ash and Limestone Powder," *Cement and Concrete Composites*, V. 55, 2015, pp. 374-382. doi: 10.1016/j.cemconcomp.2014.10.001

48. Wu, Z.; Shi, C.; and Khayat, K. H., "Influence of Silica Fume Content on Microstructure Development and Bond to Steel Fiber in Ultra-High Strength Cement-Based Materials (UHSC)," *Cement and Concrete Composites*, V. 71, 2016, pp. 97-109. doi: 10.1016/j.cemconcomp.2016.05.005

49. Wu, Z.; Khayat, K. H.; and Shi, C., "Effect of Nano-SiO_2 Particles and Curing Time on Development of Fiber-Matrix Bond Properties and Microstructure of Ultra-High Strength Concrete," *Cement and Concrete Research*, V. 95, 2017, pp. 247-256. doi: 10.1016/j.cemconres.2017.02.031

50. Zeng, Q.; Li, K.; Fen-chong, T.; and Dangla, P., "Pore Structure Characterization of Cement Pastes Blended with High-Volume Fly-Ash," *Cement and Concrete Research*, V. 42, No. 1, 2012, pp. 194-204. doi: 10.1016/j.cemconres.2011.09.012

51. Xie, T.; Fang, C.; and Mohamad, Ali, M. S.; andVisintin, P., "Characterizations of Autogenous and Drying Shrinkage of Ultra-High-Performance Concrete (UHPC): An Experimental Study," *Cement and Concrete Composites*, V. 91, 2018, pp. 156-173. doi: 10.1016/j.cemconcomp.2018.05.009

APPENDIX A

Table A1 presents additional information related to the mixture design, including the effective and total *w*/*b*, calculated and measured unit weight, and water absorption used in the mixture design and measured before each batch. Furthermore, Table A2 summarizes the important results, which consist of mini-slump flow, autogenous shrinkage at 28 days, total shrinkage at 56 days, and compressive strength at 28 days.

Table A1—Information related to mixture design

Mixture	*w*/*b*		Measured unit weight, kg/m³	Measured water absorption of LWS, %
	Effective	Total		
Reference	0.2	0.2	2408	17.5 ~ 19.5
SRA1	0.2	0.2	2396	
SRA2	0.2	0.2	2383	
LWS10	0.2	0.21	2363	
LWS17	0.2	0.22	2338	
LWS25	0.2	0.23	2301	
LWS17&SRA1	0.2	0.22	2339	
LWS17&SRA1.5	0.2	0.22	2322	

Note: Effective *w*/*b* refers to mixing water that does not involve water absorbed by LWS; and total water is sum of mixing water and water absorbed by LWS.

Table A2—Typical properties of investigated UHPC mixtures

Mixture	Mini-slump flow, mm	Autogenous shrinkage at 28 days, με	Total shrinkage at 56 days, με			Compressive strength at 28 days, MPa		
			3MC	7MC	MC	3MC	7MC	MC
Reference	172	535	520	460	260	129	139	142
SRA1	177	435	455	410	215	118	129	134
SRA2	175	385	375	350	170	116	121	125
LWS10	176	510	485	440	225	134	142	146
LWS17	173	480	445	400	170	140	146	153
LWS25	175	430	435	395	150	131	136	144
LWS17&SRA1	172	350	380	345	135	124	132	137
LWS17&SRA1.5	170	330	350	310	125	119	126	128

ACI MATERIALS JOURNAL TECHNICAL PAPER

Title No. 121-M29

Curing of Concrete Specimens Containing Metakaolin, Zeolite, and Micro-/Nanobubble Water in Seawater

by P. Mohsenzadeh Tochahi, G. Asadollahfardi, S. F. Saghravani, and N. Mohammadzadeh

In marine structures, concrete requires adequate resistance against chloride-ion penetration. As a result, numerous studies have been conducted to enhance the mechanical properties and durability of concrete by incorporating various pozzolans. This research investigated the curing conditions of samples including zeolite and metakaolin mixed with micro-/nanobubble water in artificial seawater and standard conditions. The results indicated that incorporating zeolite and metakaolin mixed with micro-/nanobubble water, cured in artificial seawater conditions, compared to similar samples that were cured in standard conditions, improved the mechanical properties and durability of concrete samples. The 28-day compressive strength of the concrete samples containing 10% metakaolin mixed with 100% micro-/nanobubble water and 10% zeolite blended with 100% micro-/nanobubble water cured in seawater increased by 25.06% and 20.9%, respectively, compared to the control sample cured in standard conditions. The most significant results were obtained with a compound of 10% metakaolin and 10% zeolite with 100% micro-/nanobubble water cured in seawater (MK10Z10NB100CS), which significantly increased the compressive, tensile, and flexural strengths by 11.13, 14, and 9.1%, respectively, compared with the MK10Z10NB100 sample cured in standard conditions. Furthermore, it considerably decreased the 24-hour water absorption and chloride penetration at 90 days—by 27.70 and 82.89%, respectively—compared with the control sample cured in standard conditions.

Keywords: curing; metakaolin; micro-/nanobubble; seawater; zeolite.

INTRODUCTION

The mechanical properties and good durability of concrete have made it one of the most important construction materials in the world.[1] Still, when exposed to marine environments, it is affected by early corrosion.[2] Many structures made with concrete such as dams, bridges, siphons, and aqueducts have consistent contact with seawater.[3] The mentioned structures in coastal cities are exposed to the salty waters of the oceans and seas. Seawater contains magnesium sulfate, which may attack most of the components of portland cement, and chlorides, which may cause corrosion.[4] On the other hand, because cement mortar is a porous material, liquids or air can pass through small spaces in the cement mortar, which causes pores to form inside, thus affecting the porosity and permeability of the mortar. The presence of these pores in the gel and capillary structure of concrete reduces the durability and mechanical properties of concrete.[5] Pozzolans reduce the permeability and increase the mechanical properties of concrete by modifying its pore structure.[6] Increasing the durability and decreasing the porosity of concrete to resist seawater attack is a necessary tool. Researchers have been working in this regard by using different pozzolans such as silica fume, fly ash, and zeolite in concrete. Recently, in addition to pozzolans, some researchers used micro-/nanobubble water to increase concrete strength and durability. Also, some studies have been working on curing concrete with seawater. Some of the studies are described as follows. Arefi et al.[7] showed that using 100% micro-/nanobubble water instead of tap water resulted in a 19% increase in compressive strength and a 16% increase in tensile strength of concrete samples. Mozaffari Naeeni[8] reviewed micro-/nanobubbles' properties, including pH and dissolved oxygen (DO). Mohsen Zadeh et al.[9] reported that the concurrent use of the pozzolan zeolite and metakaolin to replace part of the consumable cement and micro-/nanobubble water instead of city water considerably increased the durability and mechanical properties of concrete. They indicated that using micro-/nanobubble water in concrete instead of city water increased compressive strength by 14.58%, tensile strength by 18.37%, and flexural strength by 5.92% compared to the control sample. Khoshroo et al.[10] found that using micro-/nanobubble water in concrete mixtures significantly increased the compressive and tensile strengths, reduced the water absorption, and increased the electrical resistivity of concrete samples compared to samples containing tap water. Asadollahfardi et al.[11] found that using 10% metakaolin with 100% micro-/nanobubble water increased compressive strength by 15% and decreased the rapid chloride permeability and 30-minute water absorption by 74.85% and 25.21%, respectively. Yahyaei et al.[12] developed the use of micro-/nanobubble water in self-consolidating concrete (SCC), and the results of experiments demonstrated that using micro-/nanobubble water increased the compressive and tensile strengths and the electrical resistivity of concrete. Kim et al.[13] stated that the hydrogen nanobubbles used in cement mortar, compared to tap water, increased the compressive strength and reduced the pore volume of the samples. Yahyaei et al.[14] investigated the rheology of SCC built with micro-/nanobubbles and high-range water-reducing admixtures (HRWRAs). Half of the samples were made with city water, and the other half with micro-/nanobubble water. This research demonstrated that the concrete sample made with micro-/nanobubble water, compared to the sample made with city water, had

ACI Materials Journal, V. 121, No. 3, May 2024.

MS No. M-2023-191.R1, doi: 10.14359/51740567, received August 18, 2023, and reviewed under Institute publication policies.

reduced static yield stress and plastic viscosity and slightly improved passing ability. Tayebi Jebeli et al.[15] studied the properties of concrete made from waste foundry sand mixed with micro-/nanobubble water. This research illustrated that the samples comprising micro-/nanobubble water significantly increased the compressive strength of concrete.

Lan et al.[16] showed that, by accelerating cement hydration, nanobubble water and nanosilica at low atmospheric pressure improve cement paste's mechanical strength and freezing-and-thawing resistance. Curing plays a substantial role in obtaining high strength and durability properties of concrete, which is achieved through the complete hydration of cement, resulting in the creation of dense microstructures during concrete processing.[17-19] Wegian[2] mixed and cured concrete samples with seawater at the ages of 7 and 14 days. The compressive, tensile, and flexural strengths increased compared to the mixed and cured samples with fresh water. Li et al.[20] found that the compressive strength of the sample consisting of metakaolin, which was mixed with seawater and cured with NaCl solution, increased and prevented the reduction of strength at the age of 56 days. Olutoge and Amusan[21] investigated 140 concrete samples made with and cured in seawater and fresh water and reported that the compressive strength of concrete made and cured in seawater increased at 7, 14, 21, 28, and 90 days.

Microwave heating with low energy consumption and high efficiency is considered a new method for curing concrete samples, and this type of curing can improve concrete curing.[22] Curing the samples quickly with the microwave heating method has increased the initial strength of concrete compared to the traditional steam-curing process.[23] Chen and Gao[24] found that carbonation curing increases compressive strength and improves the microstructure of cement paste. Tian et al.[25] showed that the compressive strength of the samples cured by the autoclave increased significantly within 3 hours compared to other curing methods.

To increase durability and reduce concrete porosity, several researchers have used pozzolans and micro-/nanobubble water in concrete to achieve reliable durability and resist seawater deterioration. To the authors' knowledge, using pozzolans and micro-/nanobubble water and curing in seawater has not been reported.

Therefore, the objective of the present work is to use zeolite, metakaolin, and micro-/nanobubble water concurrently in concrete and cured in seawater to determine the effect on concrete's mechanical and durability properties.

MATERIALS AND METHODS

Materials

Table 1 indicates the physical and chemical properties of tap water, which conforms to WHO 2011,[26] Iranian standard ISIRI 1053,[27] and ASTM C1602/C1602M-06.[28]

The artificial seawater was made according to ASTM D1141-98(2021),[29] and Table 2 indicates the chemical composition of seawater. Also, the pH and water chlorine values according to ASTM D512-12[30] were measured with a multiparameter laboratory device. The pH and chlorine were 8.25 and 1923 ppm for the artificial seawater. To prepare 10 L of artificial seawater, Solution 1 was made from $MgCl_2$ and $CaCl_2$; then, Solution 2 was made from KCl, KBr, NaF, and H_3BO_3 compounds. Finally, to prepare artificial seawater, NaCl and Na_2SO_4 salts were dissolved in 9 L of water, and then 200 mL from Solution 1 and 100 mL from Solution 2 were added to it, and it was diluted to 10 L. In this research, 500 L of artificial seawater was used. The pH of seawater was calculated according to ASTM D1141-98(2021),[29] and 0.1 N NaOH solution was used. The specifications of the aggregate used in concrete production are in accordance with ASTM C33-02.[31] It has a maximum size of 19 mm, and the specific weights of sand and gravel were 2620 and 2680 kg/m^3, respectively.

Table 1—Physical and chemical properties of water

Parameters	Value
pH	8.15
Conductivity, mS/cm	581
Turbidity, NTU	0.41
Temperature, °C	21
Dissolved oxygen, ppm	3.22
Absorption, abs	0.147
Total dissolved solids (TDS), ppm	274
SO_4, mg/L	11-
Cl^{-1}, mg/L	90

Table 2—Chemical composition of seawater, g/L

NaF	H_3BO_3	KBr	KCl	$CaCl_2$	Na_2SO_4	$MgCl_2$	NaCl
0.003	0.027	0.101	0.695	1.16	4.09	5.20	24.53

Table 3—HRWRA properties

Structure and appearance	Polycarboxylate product brown liquid
Specific gravity at 20°C	1.01 ± 0.03 g/cm^3
pH	7 ± 1

Table 3 describes the characteristics of the HRWRA used in the present work. The micro-/nanobubble water was produced based on the cutting method and using a Venturi tube and hydraulic cavitation process at the Shahrood University of Technology. The characteristics of the micro-/nanobubble water are similar to the studies by Mozaffari Naeeni,[8] Arefi et al.,[7] Mohsen Zadeh et al.,[9] and Asadollahfardi et al.[11] Type 1-425 portland cement was used, produced according to ASTM C150/C150M-12.[32] Natural zeolite pozzolan produced according to ASTM C618-05[33] was used. Table 4 shows the chemical specifications of the cement, metakaolin, and zeolite.

Concrete mixture designs

Ten different concrete samples were made according to ASTM C192/C192M-02,[34] and Table 5 indicates the concrete mixture designs. Also, due to the increase in accuracy in the evaluation, the average of three tests was recorded as the final result of all tests. After 24 hours, half of the samples were removed from the molds. The concrete

samples were placed in a saturated limewater container according to ASTM C192/C192M-02,[34] with a temperature of 20 to 25°C until the required age. The other half of the samples were cured in artificial seawater made according to ASTM D1141-98(2021).[29]

Table 6 indicates the various mechanical and durability tests that were performed.

RESULTS AND DISCUSSION

Compressive strength

Figure 1 indicates the compressive strength at 28 and 90 days for different concrete samples. Based on Fig. 1, at 28 days, the micro-/nanobubbles in the NB100 sample resulted in increasing the compressive strength by 13.2% and 3.85%, respectively, compared to the sample cured in standard conditions (C) and the sample cured in seawater conditions (CCS). Also, the increase in compressive strength in the NB100S sample was observed at 21.09 and 11.09% compared to the C and CCS specimens.

Also, the sample consisting of 10% zeolite mixed with 100% micro-/nanobubble water (Z10NB100CS) cured in seawater increased compressive strength by 6.76% compared to the sample containing 10% zeolite mixed with 100% micro-/nanobubble water cured in standard conditions. Also, the sample consisting of 10% metakaolin mixed with 100% micro-/nanobubble water (MK10NB100CS) cured in seawater increased compressive strength by 8.75% compared to the sample consisting of 10% metakaolin mixed with 100% micro-/nanobubble water cured in standard conditions. The compressive strength sample containing 10% zeolite and 10% metakaolin mixed with 100% micro-/nanobubble water (MK10Z10NB100CS) cured in seawater increased by 30.86% compared to the control sample cured in standard conditions.

At 90 days, the compressive strength of all samples cured in seawater increased, except for the control sample cured in seawater (CCS). The reason may be the chloride attack on the control sample cured in seawater. Similarly, the compressive strength of the MK10Z10NB100CS concrete sample increased by 12.31% and 29%, respectively, as compared to the control sample and the sample containing 10% zeolite and 10% metakaolin mixed with 100% micro-/nanobubble water cured in standard conditions. Furthermore, in the samples MK10NB100CS and Z10NB100CS, the compressive strength increased by 22.77% and 18.24%, respectively, compared with the control sample cured in standard conditions. The reason may be the improvement of the hydration process by micro-/nanobubbles and the modification of the microstructure of concrete sample cavities, the effect of filling by pozzolans.

Table 4—Chemical composition of cement, metakaolin, and zeolite, %

Chemical composition	Cement	Metakaolin	Zeolite
SiO_2	22.3	74.2	68.79
CaO	62.36	3.32	3.52
Fe_2O_3	3.64	0.85	0.56
Al_2O_3	17.6	17.6	11.55
K_2O	0.34	0.34	1.33
Na_2O	0.0	0. 0	0.65
MgO	0.25	0.25	0.75
SO_3	0.43	0.43	0.008

Tensile strength

Figure 2 compares the tensile strength of samples cured in seawater at 28 days with standard curing conditions. The tensile strength of the sample containing 10% zeolite plus 100% micro-/nanobubble water cured in seawater (Z10NB100CS) increased by 11% compared to the Z10NB100 sample cured in standard conditions. Also, the tensile strength of the sample containing 10% metakaolin

Table 5—Mixture design of 10 types of concrete mixture

Mixture ID	Fine-grained, kg/m^3	Gravel, kg/m^3	Pea gravel, kg/m^3	Zeolite, kg/m^3	Metakaolin, kg/m^3	Micro-/nano bubbles, kg/m^3	Water, kg/m^3	Cement, kg/m^3	*w*/*c*	HRWRA, %
C	456	557	812	0	0	0	171	380	0.45	0.1
CCS	456	557	812	0	0	0	171	380	0.45	0.1
NB100	456	557	812	0	0	171	0	380	0.45	1.1
NB100CS	456	557	812	0	0	171	0	380	0.45	1.1
Z10NB100	456	557	812	38	0	171	0	342	0.45	1.5
Z10NB100CS	456	557	812	38	0	171	0	342	0.45	1.5
MK10NB100	456	557	812	0	38	171	0	342	0.45	1.4
MK10NB100CS	456	557	812	0	38	171	0	342	0.45	1.4
MK10Z10NB100	456	557	812	38	38	171	0	304	0.45	1.6
MK10Z10NB100CS	456	557	812	38	38	171	0	304	0.45	1.6

Note: C is control sample; CCS is control sample cured in seawater; NB100 is concrete sample using 100% micro-/nanobubble water; NB100CS is concrete sample using 100% micro-/nanobubble water cured in seawater; Z10NB100 is concrete sample using 10% zeolite and 100% micro-/nanobubble water; Z10NB100CS is concrete sample using 10% zeolite and 100% micro-/nanobubble water cured in seawater; MK10NB100 is concrete sample using 10% metakaolin and 100% micro-/nanobubble water; MK10NB100CS is concrete sample using 10% metakaolin and 100% micro-/nanobubble water cured in seawater; MK10Z10NB100 is concrete sample using 10% zeolite, 10% metakaolin, and 100% micro-/nanobubble water; MK10Z10NB100CS is concrete sample using 10% zeolite, 10% metakaolin, and 100% micro-/nanobubble water cured in seawater; *w*/*c* is water-cement ratio.

with 100% micro-/nanobubble water (MK10NB100) and the sample including 10% metakaolin and 10% zeolite mixed with 100% micro-/nanobubble water (Z10NB100) cured in seawater conditions increased by 12.5% and 14%, respectively, compared to the MK10Z10NB100 and MK10Z10NB100 samples, which were cured in standard conditions. The tensile strength of the sample containing 100% micro-/nanobubble water (NB100CS) cured in seawater increased by 12.85% compared to the sample NB100 cured in standard conditions.

Based on Fig. 2, at 90 days of age compared to 28 days, the tensile strength of all concrete samples cured in seawater increased, except the control sample cured in seawater (CCS). In addition, the samples consisting of 10% zeolite blended with 100% micro-/nanobubble water (Z10NB100CS) cured in seawater conditions increased by 9% compared to the Z10NB100 sample cured in standard conditions. Also, the samples containing 10% metakaolin in a mixture of 100% micro-/nanobubble water (MK10NB100CS) cured in seawater conditions increased by 3.05% compared to MK10NB100. In addition, the highest tensile strength belongs to a sample including 10% metakaolin and 10% zeolite mixed with 100% micro-/nanobubble water (MK10Z10NB100CS) cured in seawater, as compared to the control sample cured in standard conditions, which was approximately 30.20%.

Table 6—Method of mechanical and durability testing of concrete sample

Method	Standard
Compressive strength test	BS 1881-116:1983[35]
Tensile strength of Brazilian test method	ASTM C496/C496M-04[36]
Flexural strength test	ASTM C78-02[37]
30-minute and 24-hour water absorption tests	BS 1881-122:1983[38]
Concrete resistivity	FM 5-578[39]
Rapid chloride permeability test (RCPT)	ASTM C1202-07[40]

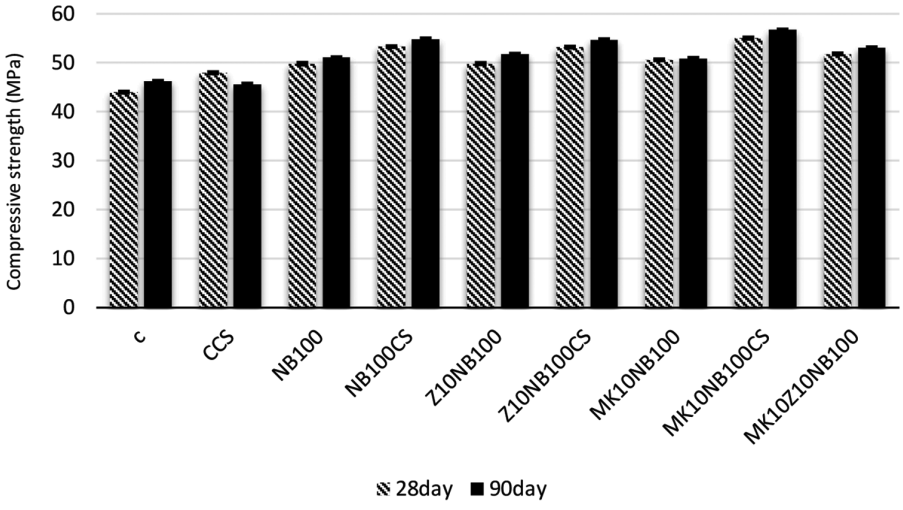

Fig. 1—Results of compressive strength of different concrete samples.

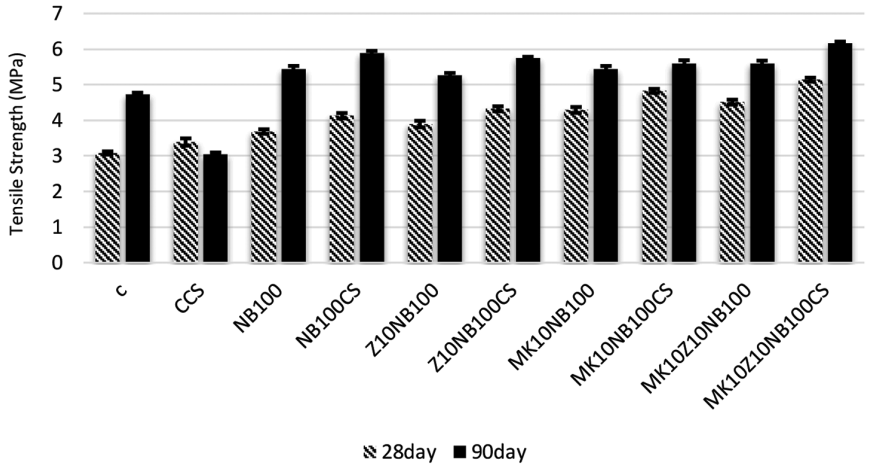

Fig. 2—Results of tensile strength of different concrete samples.

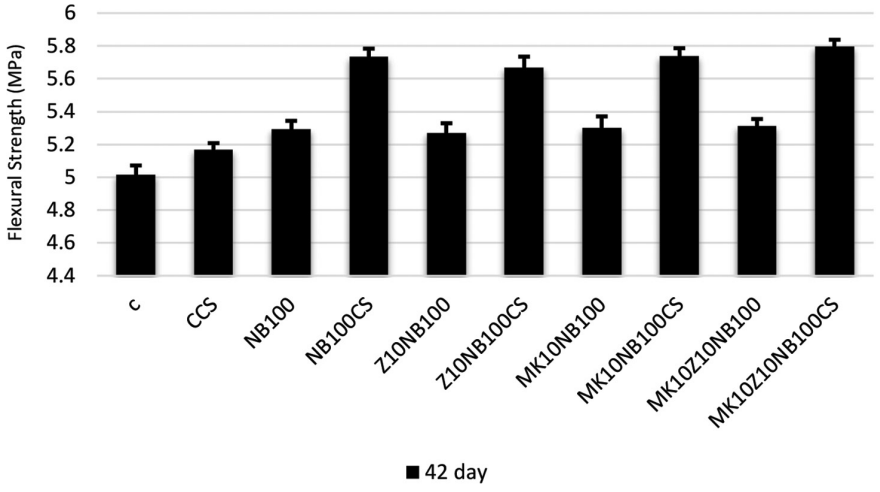

Fig. 3—Results of flexural strength of different concrete samples.

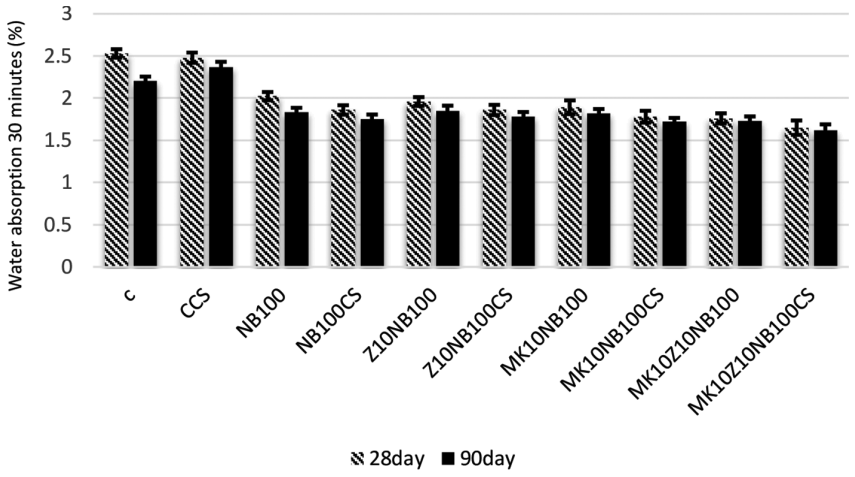

Fig. 4—Results of 30-minute water absorption of different concrete samples.

Flexural strength

Figure 3 shows the flexural strength of various concrete mixture designs. According to Fig. 3, the flexural strength of the sample consisting of 10% zeolite and 100% micro-/nanobubble water after 42 days of water curing in seawater conditions (Z10NB100CS) increased by 9.72% compared to the CCS sample. The increased flexural strength of the sample comprising 10% metakaolin and 100% micro-/nanobubble water (MK10NB100CS) cured in seawater was 11.02% compared to the CCS specimen. Also, the flexural strength of the sample containing 100% micro-/nanobubble water (NB100CS) cured in seawater rose by 9.1% compared to NB100. Furthermore, the sample including 10% metakaolin and 10% zeolite mixed with 100% micro-/nanobubble water (MK10Z10NB100CS) cured in seawater increased by 15.55% compared to the control sample cured in standard conditions.

Water absorption

Figure 4 demonstrates the 30-minute water absorption for various concrete mixture designs. According to Fig. 4, at 28 days, the 30-minute water absorption of the sample that includes 10% metakaolin plus 100% micro-/nanobubble water (MK10NB100CS) cured in seawater decreased by 28.22% and 29.64% compared to the CCS and C samples, respectively. In addition, the 30-minute water absorption of the MK10Z10NB100CS sample decreased by 33%, 34.78%, and 6.25% in comparison with the control sample cured in seawater (CCS), the control sample cured in standard conditions (C), and the sample comprising 10% metakaolin plus 10% zeolite and 100% micro-/nanobubble water (MK10Z10NB100) cured in standard conditions, respectively.

Figure 5 demonstrates the 24-hour water absorption for various concrete mixture designs at 28 and 90 days. According to Fig. 5, at 28 days, the 24-hour water absorption of the sample consisting of 10% zeolite mixed with 100% of the micro-/nanobubble water (Z10NB100CS) cured in seawater decreased by 20.93 and 9.33% in comparison with the control sample cured in seawater (CSS) and the sample with 10% zeolite and 100% micro-/nanobubble water cured in standard conditions (Z10NB100), respectively. Similarly, the most significant decrease of 24-hour water absorption is observed in the MK10Z10NB100CS concrete sample, which decreased by 26.07% and 30.25% in comparison with

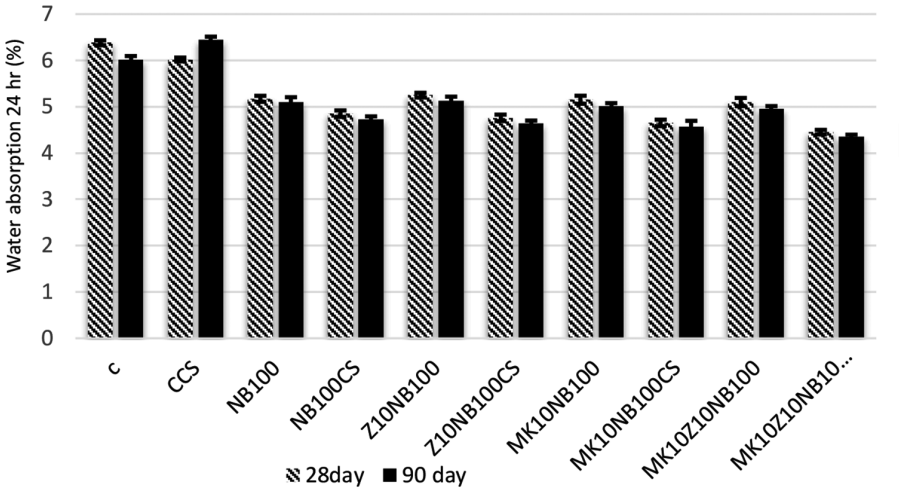

Fig. 5—Results of 24-hour water absorption of different concrete samples.

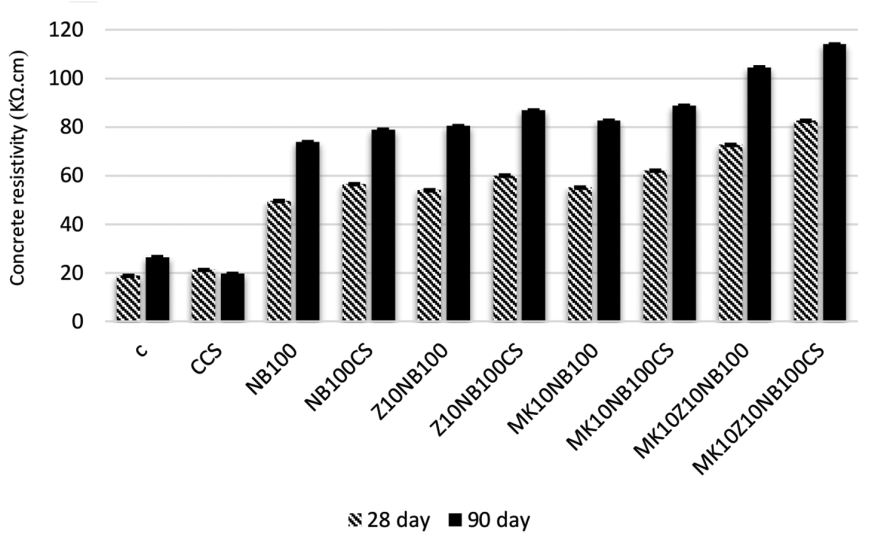

Fig. 6—Results of electrical resistivity of different concrete samples.

the control sample cured in seawater (CCS) and the control sample cured in standard conditions (C), respectively. Finally, the reduction of the water absorption was 19.43 and 6.18%, respectively, in the sample that includes 100% of the micro-/nanobubbles cured in seawater (NB100CS), in comparison with the control sample cured in seawater (CSS) and the NB100 sample.

As described in Fig. 4 and 5, it is observed that the simultaneous use of metakaolin and zeolite in mixing with micro-/nanobubble water in concrete cured in standard and seawater conditions reduced the water absorption of concrete at 28 and 90 days. Still, the 24-hour water absorption of the CCS sample increased at 90 days.

Electrical resistivity

Figure 6 demonstrates the electrical resistivity of various concrete blends. Based on Fig. 6, at 90 days, the lowest and the highest electrical resistivity belong to the control sample cured in seawater (CCS) and the combined sample that includes 10% zeolite with 10% metakaolin combined with 100% micro-/nanobubble water cured in seawater (Z10MK10NB100CS), which were 19.5 and 113.90 kΩ·cm, respectively. Also, the sample that includes 10% metakaolin plus 100% micro-/nanobubble water (MK10NB100CS), the sample that includes 10% zeolite plus 100% micro-/nanobubble water (Z10NB100CS), and the sample with 100% micro-/nanobubble water (NB100CS) cured in seawater had concrete resistivity of 3.31, 3.20, and 3.01 times higher than the control sample (C) cured in standard conditions after 28 days.

Based on Fig. 6, the electrical resistivity of the concrete samples with 10% zeolite plus 100% micro-/nanobubble water (Z10NB100CS) and 10% metakaolin plus 100% micro-/nanobubble water (MK10NB100CS) cured in seawater at 90 days increased by 44.62% and 43.14%, in comparison with the 28-day samples, and the electrical resistivity of both mentioned samples was 4.44 and 4.54 times higher than the concrete resistivity of the control sample (CCS) cured in seawater, respectively. Unlike the control sample cured in seawater, the electrical resistivity of all samples, including pozzolans and micro-/nanobubble water, is significantly increased. This may be due to the concurrent

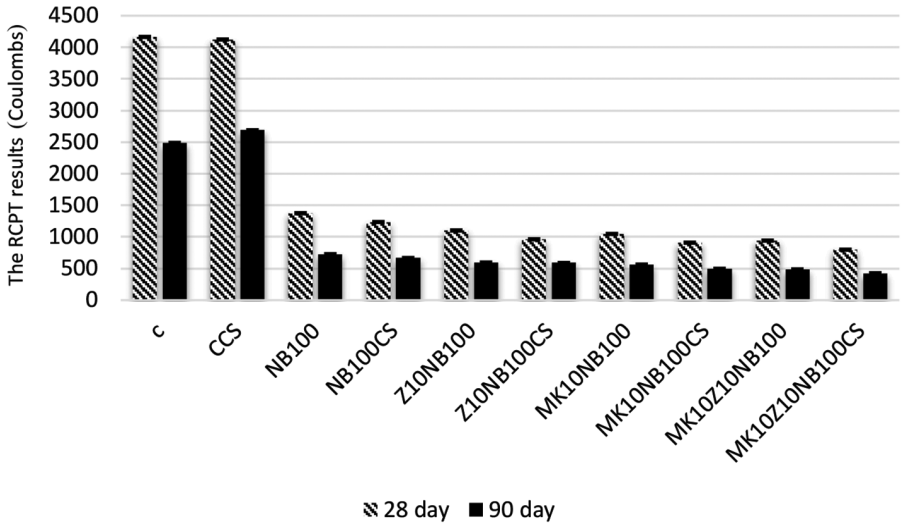

Fig. 7—Results of RCPT for different types of concrete samples.

action of the pozzolans and the micro-/nanobubbles due to the reduction in the porosity, which leads to a decrease in the volume of permeable ions.

Rapid chloride permeability test (RCPT) results

Figure 7 demonstrates the rapid chloride permeability test (RCPT) for several concrete mixture designs at 28 and 90 days. According to AASHTO T 277-07 (2007),[41] the chloride-ion penetrability of control sample C and the Z10MK10NB100CS sample are moderate and very low, respectively.

At 28 days, the RCPT results for the concrete sample that includes 10% zeolite plus 100% micro-/nanobubble water (Z10NB100CS) and the sample that includes 10% metakaolin plus 100% micro-/nanobubble water (MK10NB100CS) cured in seawater were 76.35% and 80.05% lower than the control sample cured in standard conditions. The most significant decrease in the RCPT was relevant to the concrete sample consisting of 10% metakaolin plus 10% zeolite mixed with 100% micro-/nanobubble water (MK10Z10NB100CS) cured in seawater at 28 days, which indicates a reduction of 80.82 and 15.19% compared to the control sample (C) and the sample containing 10% zeolite plus 10% metakaolin mixed with 100% micro-/nanobubble water (MK10Z10NB100) cured in standard conditions. After 90 days, the composite sample that includes 100% micro-/nanobubble water (NB100CS) cured in seawater decreased the RCPT results by 73.22% and 8.43% compared to the control sample and the sample that includes 100% micro-/nanobubble water cured in standard conditions, respectively. In the sample incorporating 10% metakaolin plus 100% micro-/nanobubble water and the sample including 10% zeolite plus 100% micro-/nanobubble water cured in seawater, the RCPT results fell by 81.55% and 78.13% compared with the control sample cured in seawater, respectively. This may reduce the volume of permeable ions due to the performance of pozzolans and micro-/nanobubbles in seawater curing conditions.

Joshi and Chan[42] reported that chlorides penetrate concrete with different mechanisms, and the entry of chloride ions into concrete depends primarily on the pore structure of concrete. Also, seawater reduces the pores and modifies the pore size of the concrete surface due to the different hydration temperatures between seawater and tap water. On the other hand, seawater can decrease pore sizes, such as lesser and larger capillary pores.[43] Therefore, curing concrete in seawater chloride conditions reduces surface cracks in concrete, and the results of this research can confirm this issue.

Also, Arefi et al.[7] showed that substituting 100% micro-/nanobubbles for tap water in the control sample increased compressive and tensile concrete strength by 19% and 16%, respectively. Therefore, this result complies with the results obtained from this research. However, they cured concrete only in tap water. In this study, concrete samples were also cured in seawater. Siddique and Klaus's[44] research demonstrated that the concrete sample containing metakaolin had decreased chloride permeability and increased compressive and tensile strength. Shekarchi et al.[45] showed that the sample containing 15% metakaolin decreased water absorption by 25% and increased the concrete resistivity and compressive strength. The results from the scanning electron microscope (SEM) in the research from Mohsen Zadeh et al.[9] and Asadollahfardi et al.[11] (magnification of 20 and 100 μm) showed that micro-/nanobubble water combined with the pozzolans zeolite and metakaolin improved the mechanical and durability properties of concrete, which is consistent with the findings achieved in this research.

The chemical processes that lead to concrete corrosion are due to the entry of chloride ions, which lead to the formation of fertile salt with the formula $3CaO{\cdot}Al_2O_3{\cdot}CaCl_2{\cdot}10H_2O$,[46,47] as well as several calcium aluminate hydrates (C-A-H), such as monosulfate, that are converted into Friedel's salt.[48] According to the results of this research, in the control sample cured in seawater at 28 days, the durability and mechanical properties increased with the making of Friedel's salt. However, at 90 days, the Friedel's salt disintegrated, and the durability and mechanical properties of the sample decreased. In the samples that included metakaolin, zeolite, and micro-/nanobubble water, the pozzolans and

micro-/nanobubble water with chloride and calcium ions in concrete may improve the process of Friedel's salt formation. Also, micro-/nanobubble water improved the mechanical properties and reduced the permeability of concrete. At 90 days, the mechanical properties and durability of the samples may increase owing to the performance of micro-/nanobubble water and pozzolans in absorbing and inhibiting chloride. To the authors' knowledge, a similar study using nanobubble concrete cured in seawater has not been researched.

CONCLUSIONS

This research studies the mechanical properties and durability of concrete samples consisting of the natural pozzolans metakaolin and zeolite mixed with micro-/nanobubble water cured in seawater and standard conditions.

1. At 28 days, the compressive strength of the control sample cured in seawater increased by 9% compared to the control sample cured under standard conditions. At 90 days, the compressive strength of the control sample cured in seawater was 5% lower than at 28 days, possibly due to chloride attack on concrete samples cured in seawater.

2. At 28 days, the sample consisting of 100% of the micro-/nanobubble water cured in seawater grew substantially in compressive strength, tensile strength, flexural strength, and electrical resistivity (by 6.97%, 12.82%, 11%, and 14%, respectively) compared to the sample including 100% of the micro-/nanobubble water cured in standard conditions. It decreased the 30-minute water absorption and the rapid chloride permeability test (RCPT) by 8.10% and 10.21%, respectively.

3. At 90 days, the compressive and tensile strengths of the concrete sample containing 10% metakaolin and using 100% micro-/nanobubble water (MK10NB100CS) cured in seawater rose considerably (by 11.60% and 3.05%, respectively) compared to the sample containing 10% metakaolin mixed with 100% micro-/nanobubble water cured in standard conditions. It also decreased the 24-hour water absorption and the RCPT by 8.69% and 11.58%, respectively.

4. At 90 days, the compressive strength, tensile strength, and electrical resistivity of the sample containing 10% zeolite in a blend of 100% micro-/nanobubble water cured in seawater grew dramatically (by 5.66%, 9%, and 8%, respectively) compared to the sample including 10% zeolite mixed with 100% of the micro-/nanobubble water cured in standard conditions.

5. At 90 days, the compressive strength, tensile strength, and concrete resistivity of the sample comprising 10% zeolite blended with 100% of the micro-/nanobubble water (Z10NB100CS) cured in seawater were 18.24%, 21.42%, and 3.28 times higher, respectively, than the control sample cured in standard conditions. It also decreased the 30-minute water absorption and the RCPT by 19.09% and 76.35%, respectively.

6. The greatest improvement in the durability and mechanical properties of concrete was in the sample including 10% metakaolin plus 10% zeolite mixed with 100% micro-/nanobubble water (MK10Z10NB100CS) cured in seawater, which increased the compressive and tensile strengths by 29% and 30.20% at 90 days, as compared to the control sample cured in standard conditions. It also increased flexural strength by 15.55% at 45 days, but it decreased the 24-hour water absorption of concrete and the RCPT by 27.70% and 82.89%, respectively.

AUTHOR BIOS

Pouria Mohsenzadeh Tochahi *works in the Department of Civil Engineering at Shahrood University of Technology, Shahrood, Semnan, Iran.*

Gholamreza Asadollahfardi *works in the Department of Civil Engineering at Kharazmi University, Tehran, Iran.*

Seyed Fazlullah Saghravani *works in the Department of Civil Engineering at Shahrood University of Technology.*

Niloofar Mohammadzadeh *works in the Department of Civil Engineering in the School of Engineering at the University of Birmingham, Birmingham, UK.*

REFERENCES

1. Najimi, M.; Sobhani, J.; Ahmadi, B.; and Shekarchi, M., "An Experimental Study on Durability Properties of Concrete Containing Zeolite as a Highly Reactive Natural Pozzolan," *Construction and Building Materials*, V. 35, Oct. 2012, pp. 1023-1033. doi: 10.1016/j.conbuildmat.2012.04.038

2. Wegian, F. M., "Effect of Seawater for Mixing and Curing on Structural Concrete," *The IES Journal Part A: Civil & Structural Engineering*, V. 3, No. 4, 2010, pp. 235-243. doi: 10.1080/19373260.2010.521048

3. Ogunjiofor, E. I., "Possibility of Usage of Seawater for Mixing and Curing of Concrete in Salty Water Localities," *Journal of Engineering Research and Reports*, V. 19, No. 3, 2020, pp. 19-27. doi: 10.9734/jerr/2020/v19i317234

4. Abdel-Magid, T. I.; Osman, O. M.; Ibrahim, O. H.; Mohammed, R. T.; Hassan, S. O.; and Bakkab, A. A.-H., "Influence of Seawater in Strengths of Concrete Mix Design When Used in Mixing and Curing," *Key Engineering Materials*, V. 711, 2016, pp. 382-389. doi: 10.4028/www.scientific.net/KEM.711.382

5. Kumar, R., and Bhattacharjee, B., "Porosity, Pore Size Distribution and In Situ Strength of Concrete," *Cement and Concrete Research*, V. 33, No. 1, Jan. 2003, pp. 155-164. doi: 10.1016/S0008-8846(02)00942-0

6. Valipour, M.; Pargar, F.; Shekarchi, M.; and Khani, S., "Comparing a Natural Pozzolan, Zeolite, to Metakaolin and Silica Fume in Terms of Their Effect on the Durability Characteristics of Concrete: A Laboratory Study," *Construction and Building Materials*, V. 41, Apr. 2013, pp. 879-888. doi: 10.1016/j.conbuildmat.2012.11.054

7. Arefi, A.; Saghravani, S. F.; and Mozaffari Naeeni, R., "Mechanical Behavior of Concrete, Made with Micro-Nano Air Bubbles," *Civil Engineering Infrastructures Journal*, V. 49, No. 1, June 2016, pp. 139-147. doi: 10.7508/ceij.2016.01.010

8. Mozaffari Naeeni, R., "Investigation on the Hydrodynamics Standard Flow Pattern Using Air Micro-Nanobubbles," MSc thesis, Shahrood University of Technology, Shahrood, Semnan, Iran, 2014, 91 pp. (in Persian)

9. Mohsen Zadeh, P.; Saghravani, S. F.; and Asadollahfardi, G., "Mechanical and Durability Properties of Concrete Containing Zeolite Mixed with Meta-Kaolin and Micro-Nano Bubbles of Water," *Structural Concrete*, V. 20, No. 2, Apr. 2019, pp. 786-797. doi: 10.1002/suco.201800030

10. Khoshroo, M.; Shirzadi Javid, A. A.; and Katebi, A., "Effects of Micro-Nano Bubble Water and Binary Mineral Admixtures on the Mechanical and Durability Properties of Concrete," *Construction and Building Materials*, V. 164, Mar. 2018, pp. 371-385. doi: 10.1016/j.conbuildmat.2017.12.225

11. Asadollahfardi, G.; MohsenZadeh, P.; Saghravani, S. F.; and Mohamadzadeh, N., "The Effects of Using Metakaolin and Micro-Nanobubble Water on Concrete Properties," *Journal of Building Engineering*, V. 25, Sept. 2019, Article No. 100781. doi: 10.1016/j.jobe.2019.100781

12. Yahyaei, B.; Asadollahfardi, G.; and Salehi, A. M., "Study of Using Micro-Nano Bubble to Improve Workability and Durability of Self-Compact Concrete," *Structural Concrete*, V. 23, No. 1, Feb. 2022, pp. 579-592. doi: 10.1002/suco.202000208

13. Kim, W.-K.; Kim, Y.-H.; Hong, G.; Kim, J.-M.; Han, J.-G.; and Lee, J.-Y., "Effect of Hydrogen Nanobubbles on the Mechanical Strength and Watertightness of Cement Mixtures," *Materials*, V. 14, No. 8, Apr. 2021, Article No. 1823. doi: 10.3390/ma14081823

14. Yahyaei, B.; Asadollahfardi, G.; Salehi, A. M.; and Esmaeili, N., "Study of Shear-Thickening and Shear-Thinning Behavior in Rheology of

Self-Compacting Concrete with Micro-Nano Bubble," *Structural Concrete*, V. 23, No. 3, June 2022, pp. 1920-1932. doi: 10.1002/suco.202100704

15. Tayebi Jebeli, M.; Asadollahfardi, G.; and Abbasi Khalil, A., "Novel Application of Micro-Nanobubble Water for Recycling Waste Foundry Sand: Toward Green Concrete," *Journal of Construction Engineering and Management*, ASCE, V. 148, No. 9, Sept. 2022, p. 04022096. doi: 10.1061/(ASCE)CO.1943-7862.0002325

16. Lan, X.-L.; Zhu, H.-S.; Zeng, X.-H.; Long, G.-C.; and Xie, Y.-J., "How Nano-Bubble Water and Nano-Silica Affect the Air-Voids Characteristics and Freeze-Thaw Resistance of Air-Entrained Cementitious Materials at Low Atmospheric Pressure?" *Journal of Building Engineering*, V. 69, June 2023, Article No. 106179. doi: 10.1016/j.jobe.2023.106179

17. Hiremath, P. N., and Yaragal, S. C., "Effect of Different Curing Regimes and Durations on Early Strength Development of Reactive Powder Concrete," *Construction and Building Materials*, V. 154, Nov. 2017, pp. 72-87. doi: 10.1016/j.conbuildmat.2017.07.181

18. Richard, P., and Cheyrezy, M., "Composition of Reactive Powder Concretes," *Cement and Concrete Research*, V. 25, No. 7, Oct. 1995, pp. 1501-1511. doi: 10.1016/0008-8846(95)00144-2

19. Tai, Y.-S.; Pan, H.-H.; and Kung, Y.-N., "Mechanical Properties of Steel Fiber Reinforced Reactive Powder Concrete Following Exposure to High Temperature Reaching 800°C," *Nuclear Engineering and Design*, V. 241, No. 7, July 2011, pp. 2416-2424. doi: 10.1016/j.nucengdes.2011.04.008

20. Li, Q.; Geng, H.; Huang, Y.; and Shui, Z., "Chloride Resistance of Concrete with Metakaolin Addition and Seawater Mixing: A Comparative Study," *Construction and Building Materials*, V. 101, Part 1, Dec. 2015, pp. 184-192. doi: 10.1016/j.conbuildmat.2015.10.076

21. Olutoge, F. A., and Amusan, G. M., "The Effect of Sea Water on Compressive Strength of Concrete," *International Journal of Engineering and Science Invention*, V. 3, No. 7, July 2014, pp. 23-31.

22. Wei, W.; Shao, Z.; Qiao, R.; Chen, W.; Zhou, H.; and Yuan, Y., "Recent Development of Microwave Applications for Concrete Treatment," *Construction and Building Materials*, V. 269, Feb. 2021, Article No. 121224. doi: 10.1016/j.conbuildmat.2020.121224

23. Makul, N., "Utilization of Microwave-Accelerated Heating and Dewatering in Low-Pressure Conditions to Accelerated-Cure Type-I Cement Paste for Early-Age Compressive Strength Development," *Journal of Building Engineering*, V. 26, Nov. 2019, Article No. 100920. doi: 10.1016/j.jobe.2019.100920

24. Chen, T., and Gao, X., "Effect of Carbonation Curing Regime on Strength and Microstructure of Portland Cement Paste," *Journal of CO_2 Utilization*, Dec. 2019, pp. 74-86. doi: 10.1016/j.jcou.2019.05.034

25. Tian, W.; Liu, Y.; and Wang, W., "Multi-Structural Evolution of Conductive Reactive Powder Concrete Manufactured by Enhanced Ohmic Heating Curing," *Cement and Concrete Composites*, V. 123, Oct. 2021, Article No. 104199. doi: 10.1016/j.cemconcomp.2021.104199

26. WHO, "Guidelines for Drinking-Water Quality," fourth edition, World Health Organization, Geneva, Switzerland, 2011, 564 pp.

27. ISIRI 1053, "Specifications for Drinking Water: Physical and Chemical Characteristics," Institute of Standards and Industrial Research of Iran, Tehran, Iran, 2011.

28. ASTM C1602/C1602M-06, "Standard Specification for Mixing Water Used in the Production of Hydraulic Cement Concrete," ASTM International, West Conshohocken, PA, 2006, 4 pp.

29. ASTM D1141-98(2021), "Standard Practice for Preparation of Substitute Ocean Water," ASTM International, West Conshohocken, PA, 1998, 3 pp.

30. ASTM D512-12, "Standard Test Methods for Chloride Ion in Water (Withdrawn 2021)," ASTM International, West Conshohocken, PA, 2012, 9 pp.

31. ASTM C33-02, "Standard Specification for Concrete Aggregates," ASTM International, West Conshohocken, PA, 2002, 11 pp.

32. ASTM C150/C150M-12, "Standard Specification for Portland Cement," ASTM International, West Conshohocken, PA, 2012, 9 pp.

33. ASTM C618-05, "Standard Specification for Coal Fly Ash and Raw or Calcined Natural Pozzolan for Use in Concrete," ASTM International, West Conshohocken, PA, 2005, 3 pp.

34. ASTM C192/C192M-02, "Standard Practice for Making and Curing Concrete Test Specimens in the Laboratory," ASTM International, West Conshohocken, PA, 2002, 8 pp.

35. BS 1881-116:1983, "Testing Concrete – Part 116: Method for Determination of Compressive Strength of Concrete Cubes (Withdrawn 2004)," British Standards Institution, London, UK, 1983.

36. ASTM C496/C496M-04, "Standard Test Method for Splitting Tensile Strength of Cylindrical Concrete Specimens," ASTM International, West Conshohocken, PA, 2004, 5 pp.

37. ASTM C78-02, "Standard Test Method for Flexural Strength of Concrete (Using Simple Beam with Third-Point Loading)," ASTM International, West Conshohocken, PA, 2002, 3 pp.

38. BS 1881-122:1983, "Testing Concrete – Part 122: Method for Determination of Water Absorption (Withdrawn 2011)," British Standards Institution, London, UK, 1983, 8 pp.

39. FDOT, "Florida Method of Test for Concrete Resistivity as an Electrical Indicator of Its Permeability," Designation: FM 5-578, Florida Department of Transportation, Tallahassee, FL, 2004.

40. ASTM C1202-07, "Standard Test Method for Electrical Indication of Concrete's Ability to Resist Chloride Ion Penetration," ASTM International, West Conshohocken, PA, 2007, 6 pp.

41. AASHTO T 277-07, "Standard Method of Test for Electrical Indication of Concrete's Ability to Resist Chloride Ion Penetration," American Association of State Highway and Transportation Officials, Washington, DC, 2007, 12 pp.

42. Joshi, P., and Chan, C., "Rapid Chloride Permeability Testing," *Concrete Construction*, Dec. 2002, 5 pp.

43. Ebead, U.; Lau, D.; Lollini, F.; Nanni, A.; Suraneni, P.; and Yu, T., "A Review of Recent Advances in the Science and Technology of Seawater-Mixed Concrete," *Cement and Concrete Research*, V. 152, Feb. 2022, Article No. 106666. doi: 10.1016/j.cemconres.2021.106666

44. Siddique, R., and Klaus, J., "Influence of Metakaolin on the Properties of Mortar and Concrete: A Review," *Applied Clay Science*, V. 43, No. 3-4, Mar. 2009, pp. 392-400. doi: 10.1016/j.clay.2008.11.007

45. Shekarchi, M.; Bonakdar, A.; Bakhshi, M.; Mirdamadi, A.; and Mobasher, B., "Transport Properties in Metakaolin Blended Concrete," *Construction and Building Materials*, V. 24, No. 11, Nov. 2010, pp. 2217-2223. doi: 10.1016/j.conbuildmat.2010.04.035

46. Dyer, T., *Concrete Durability*, CRC Press, Boca Raton, FL, 2014, 447 pp.

47. Bai, J.; Wild, S.; and Sabir, B. B., "Sorptivity and Strength of Air-Cured and Water-Cured PC–PFA–MK Concrete and the Influence of Binder Composition on Carbonation Depth," *Cement and Concrete Research*, V. 32, No. 11, Nov. 2002, pp. 1813-1821. doi: 10.1016/S0008-8846(02)00872-4

48. Zibara, H., "Binding of External Chlorides by Cement Pastes," PhD thesis, University of Toronto, Toronto, ON, Canada, 2001, 342 pp.

ARE YOU A RESEARCHER?

SIGN UP FOR ORCID TODAY!

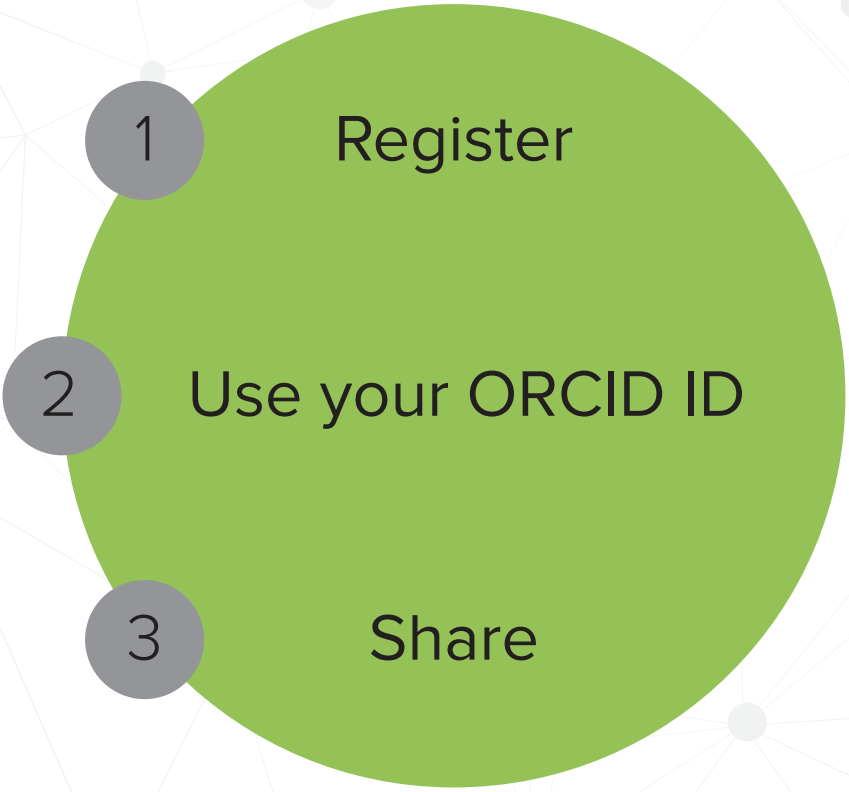

ORCID provides a digital identifier that distinguishes you from every other researcher and, through integration in key research workflows such as manuscript and grant submission, supports automated linkages between you and your professional activities, ensuring that your work is recognized.

ORCID services are FREE and it's as easy as **1-2-3**.

WWW.ORCID.ORG

ACI MATERIALS JOURNAL TECHNICAL PAPER

Title No. 121-M30

Three-Stage Testing Protocol to Recreate Thermomechanical Properties of Mass Concrete

by A. S. Carey, G. B. Sisung, I. L. Howard, B. Songer, D. A. Scott, and J. Shannon

Determining the in-place properties of mass concrete placements is elusive, and currently there are minimal to no test methods available that are both predictive and a direct measurement of mechanical properties. This paper presents a three-stage testing framework that uses common laboratory equipment and laboratory-scale specimens to quantify thermal and mechanical properties of mass high-strength concrete placements. To evaluate this framework, four mass placements of varying sizes and insulations were cast, and temperature histories were measured at several locations within each placement, where maximum temperatures of 107 to 119°C (225 to 246°F) were recorded. The laboratory curing protocols were then developed using this mass placement temperature data and the three-stage testing framework to cure laboratory specimens to represent each mass placement. Laboratory curing protocols developed for center and intermediate regions of the mass placements reasonably replicated thermal histories of the mass placements, while the first stage of the three-stage framework reasonably replicated temperatures near the edge of the mass placements. Additionally, there were statistically significant relationships detected between calibration variables used to develop laboratory curing protocols and measured compressive strength. Overall, the proposed three-stage testing framework is a measurable step toward creating a predictive laboratory curing protocol by accounting for the mixture characteristics of thermomechanical properties of high-strength concretes.

Keywords: high-strength concrete (HSC); insulated curing block; mass placements; programmable environmental chamber.

INTRODUCTION AND BACKGROUND

There have been several attempts to quantify the in-place properties of mass concrete placements using nondestructive test methods presented by ACI Committee 228,[1-5] as well as numerical techniques to quantify complex chemical reactions to predict time-temperature profiles and subsequent mechanical properties.[6] Several methodologies have been developed and studied over time to better understand thermomechanical properties of mass placements, such as cast-in-place cylinders (ASTM C873/C873M-15), the maturity method (ASTM C1074-19), temperature-matched curing (BS 1881-130), and numerical analysis techniques. These methods generally aim to predict the relationship between time-temperature history and mechanical properties in a nondestructive manner. Carey et al.[7] provided an in-depth review of each of these methodologies with respect to quantifying temperature development and mechanical properties in mass placements. A comparison of these methods found that none were both predictive and a direct measure of mechanical properties in the presence of anticipated thermal conditions.

The authors have been developing a testing framework over a multi-year period that is intended to fill this gap. Initial efforts aimed to evaluate the feasibility of using common laboratory equipment to cure 10.2 x 20.3 cm (4 x 8 in.) cylindrical specimens in a similar time-temperature history to modest and mass placements. For modest placements, laboratory curing protocols using a programmable bath and insulating block were successful for placements with a minimum least dimension of 0.15 m (0.5 ft), which were large enough to overcome the influence of environmental conditions by generating a substantial amount of heat.[8] For an insulated mass placement with a diameter of 1.8 m (6 ft) and height of 1.3 m (4 ft), an average internal peak temperature of 94°C (201°F) was produced, and laboratory specimens cured using a programmable bath and insulating block were able to reasonably replicate the time-temperature profile while also reaching a peak temperature of 92°C (198°F).[9] Based on these initial findings, efforts have focused on developing a three-stage testing protocol where thermal histories of mass placements could be recreated using common laboratory equipment to cure laboratory specimens, where the effects of mixture constituents on thermal properties are considered during the development of the laboratory curing protocol (Fig. 1).

RESEARCH SIGNIFICANCE

Determining the in-place properties of mass placements is elusive, and currently there are minimal to no test methods available that are both predictive and a direct measurement of mechanical properties in the presence of anticipated thermal conditions. The authors have developed a testing framework that has the potential to fill this gap in available testing methods. This paper serves as a proof of concept for a three-stage curing procedure initially presented in Carey et al.[7] that is a measurable step toward making the proposed laboratory testing protocols predictive by accounting for individual mixture characteristics of the thermomechanical properties of high-strength concretes (HSCs).

USE OF HIGH-STRENGTH CONCRETE IN MASS PLACEMENTS

In recent years, the use of HSC in larger to mass placements has increased as the need to improve mechanical

ACI Materials Journal, V. 121, No. 3, May 2024.
MS No. M-2023-276.R1, doi: 10.14359/51740705, received May 7, 2023, and reviewed under Institute publication policies.

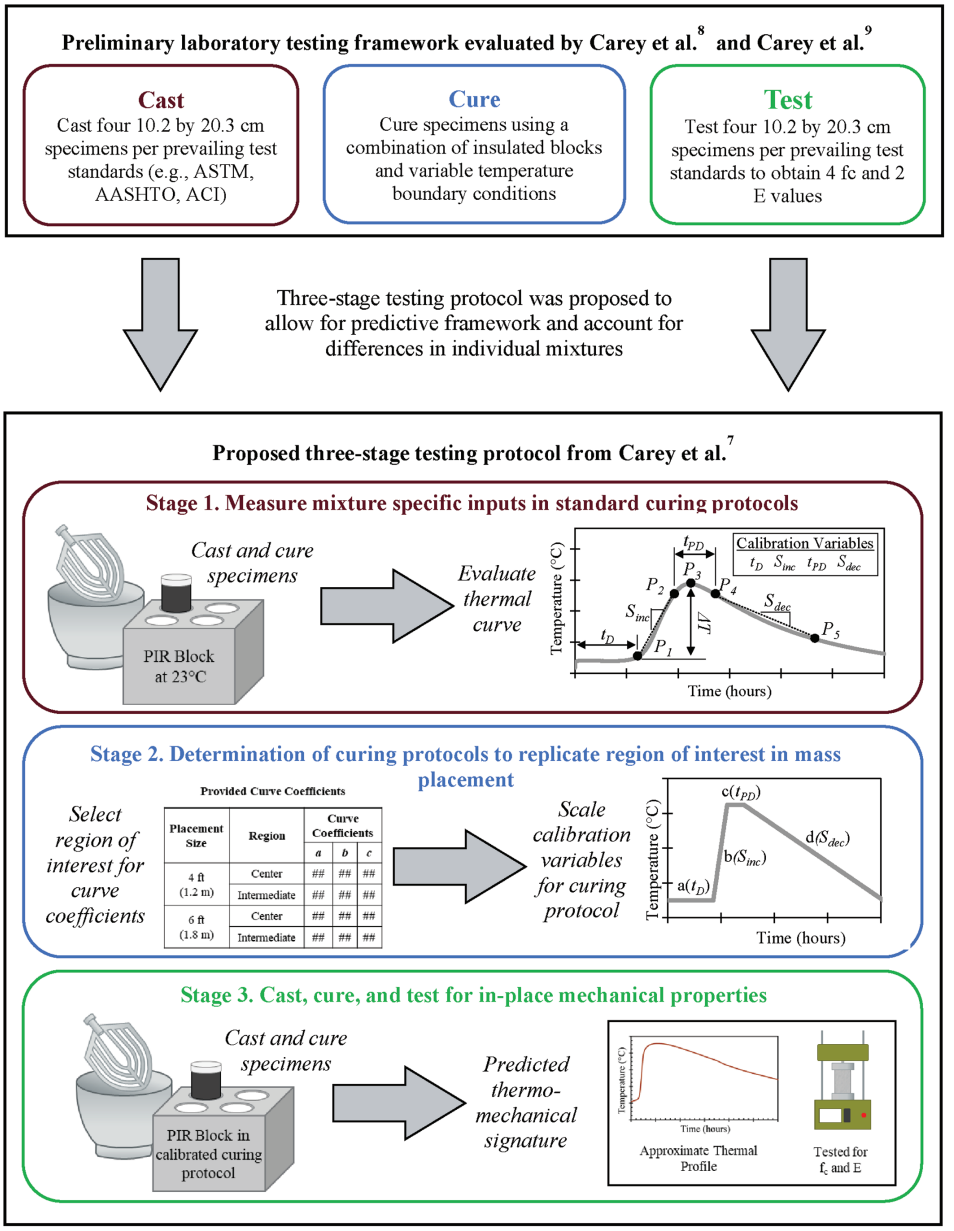

Fig. 1—Summary of preliminary testing framework and proposed three-stage testing protocol. (Note: °F = (9/5)(°C) + 32.)

properties (for example, compressive and tensile strength and durability) has grown. A recent survey of state Departments of Transportation (DOTs) found that, as of 2019, four states routinely use ultra-high-performance concrete (UHPC) in full-scale structural applications, while 15 commonly use UHPC in joints and connections.[10] Scenarios where one may consider using UHPC or HSC in a mass placement include protective structures, retrofitting critical infrastructure elements, and construction in areas where high durability is a first-order consideration (for example, coastal construction). As the development of nonproprietary UHPC mixtures that are usually more economical than proprietary mixtures continues to progress, it is anticipated that more DOTs will begin to use UHPC in their day-to-day construction activities.

When using HSCs with increased cementitious materials contents, internal temperatures often far exceed those of traditional ready mixed concrete (RMC) placements. Table 1 summarizes reported peak temperatures of HSC mass placements.[9,11-15] HSC mass placements evaluated in Table 1 reported a typical maximum temperature of 90°C (194°F), which is similar to the recommended curing temperatures in ASTM C1856/C1856M-17 for mixtures with metallic fibers.[16] Table 1 also reports external temperatures of large, thin slabs and modestly sized columns ranging from 54 to 64°C (129 to 147°F). Though these temperatures were noticeably lower than other Table 1 HSC mass placements where internal temperatures were reported, these external temperatures were comparable to internal temperatures of RMC mass placements.[17,18] While most mass HSC placements exceeded the maximum internal temperature of 70°C (158°F) as defined by ACI PRC-207.1-21,[19] the threat of delayed ettringite formation (DEF) is minimal as the water-cementitious materials ratio (*w/cm*) is typically below 0.20 and the system has low permeability due to its tight microstructure.[20,21] In other words, for mass placements

Table 1—Summary of HSC placements reported in literature

Reference	Placement size	Insulation?	Total cementitious materials, kg/m^3	Reported T_{max}, °C
Kodur et al.[11]	1 m cube	Yes	480.6 I/II + 211.5 SF + 96.1 FA + 173 LSP = 961.2	90
Kodur et al.[11]	1 m cube	No	480.6 I/II + 211.5 SF + 96.1 FA + 173 LSP = 961.2	86
Kodur et al.[11]	1 m cube	No	480.6 I/II + 297.6 SF + 173 LSP = 961.2	96
Sbia et al.[12]	1 m cube	Yes	480.6 I/II + 211.5 SF + 96.1 slag + 173 LSP = 961.2	90
Li et al.[13]	6 x 10 x 2.5 m bridge element	Yes	700 I/II + 100 SF + 200 LSP = 1000	90
Carey et al.[9]	1.8 x 1.3 m column	Yes	732 CH + 126 SF + 82 FA = 940	99
Soliman et al.[14]	4.9 x 1.5 x 0.075 m arch slab	No	549 I/II + 204 SF + 403 GP = 1156	54
Aghdasi et al.[15]	0.7 x 0.7 x 1.1 m column	No	1 part I/II + 0.1 part FA + 0.25 part SF + 0.25 part GP	64

Note: I/II is ASTM C150 Type I/II cement; SF is silica fume; FA is fly ash; LSP is limestone powder; GP is glass powder; CH is Class H cement; all reported T_{max} were measured at center of placement, except for Carey et al.,[9] measured at an intermediate location, and Aghdasi et al.,[15] measured at the surface. 1 m = 3.28 ft; 1 kg/m^3 = 1.69 lb/yd^3; °F = (9/5)(°C) + 32.

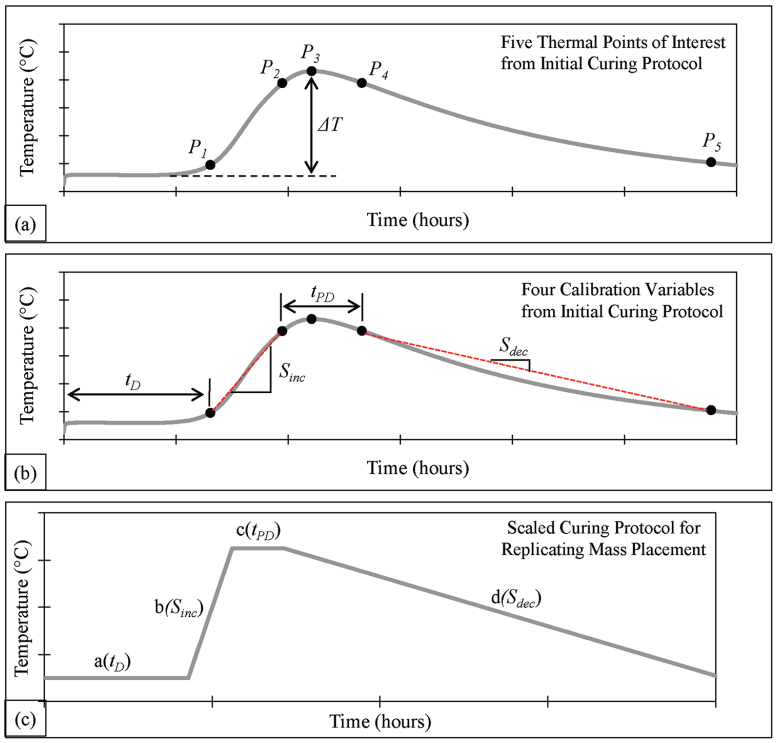

Fig. 2—Development of boundary conditions using proposed three-stage protocol. (Note: °F = (9/5)(°C) + 32.)

where HSC mixtures are used, the deleterious effects of DEF are a secondary concern.

EXPERIMENTAL PROGRAM

Description of three-stage testing protocol

As outlined in Fig. 1, the proposed three-stage testing protocol uses an initial curing regime that measures mixture-specific variables (Stage 1), scales these variables using constants derived from available mass placement data (Stage 2), and then cures specimens using a regime intended to simulate the temperature history of a mass placement (Stage 3). The Stage 1 initial curing protocol uses an insulated curing block to cure hydrating concrete specimens in a variable temperature (VT) bath (or equivalent) programmed to remain at 23°C (73°F). After 3 days of curing, where the temperature surrounding the block remains at 23°C (73°F), the resulting thermal curve is evaluated to determine five thermal points of interest (TPOIs) (Fig. 2(a)). First, maximum temperature (T_{max}) is calculated and reported as P_3. The difference between P_3 and the initial test temperature is then reported as ΔT. P_1 can then be calculated as the point where the temperature begins increasing by more than 5% of ΔT over a 30-minute period, while P_2 is the point where the temperature no longer increases by 5% of ΔT over a 30-minute period. P_4 and P_5 are then reported as the times after peak temperature (P_3) that correspond to temperature values of P_2 and P_1, respectively. Using these five TPOIs, calibration variables are then calculated and are visually defined in Fig. 2(b). Dormant period length (t_D) is calculated as the total time from the start of thermal curing to P_1. Peak temperature dormant period (t_{PD}) is calculated as the time between P_2 and P_4. Rate of temperature increase (S_{inc}) is calculated as the linear slope between P_1 and P_2, while rate of temperature decrease (S_{dec}) is calculated as the linear slope between P_4 and P_5.

Table 2—High-strength mixture batching quantities

Constituent	Specific gravity	Laboratory quantity	Field quantity
Type I/II cement, kg/m^3 (lb/yd^3)	3.15	854 (1440)	854 (1440)
Silica fume, kg/m^3 (lb/yd^3)	2.25	163 (275)	163 (275)
Metakaolin, kg/m^3 (lb/yd^3)	2.60	22 (37)	22 (37)
Manufactured sand, kg/m^3 (lb/yd^3)	2.74	581 (979)	587 (990)
Natural sand, kg/m^3 (lb/yd^3)	2.63	561 (946)	564 (950)
HRWRA, mL/kg (oz./lb)	1.08	23.0 (0.35)	23.0 (0.35)
Retarder, mL/kg (oz./lb)	1.08	1.3 (0.02)	1.3 (0.02)
Defoamer, % weight of water	1.08	0.14	0.08
Water, kg/m^3 (lb/yd^3)	1.00	179 (301)	170 (287)
w/cm	—	0.16	0.16

Note: Laboratory mixtures used oven-dry aggregate, while field mixtures accounted for water during batching process; HRWRA and retarder dosage rates are reported as volume per weight of cementitious materials.

Stage 2 of the Fig. 1 testing protocol scales calibration variables by a set of constants to produce a thermal curing protocol that can be programmed into an environmental chamber to cure laboratory-scale specimens using a time-temperature history that is similar to a mass concrete placement (Fig. 2(c)). Currently, these scaling constants are not fully defined by the authors and will require additional data sets to fully develop. It is ultimately envisioned for scaling constants representative of given mass placement scenarios to be provided to users of the three-stage testing protocol so the framework can be predictive. However, because this paper serves as a proof of concept for the three-stage testing protocol, scaling constants were calculated by dividing calibration variables from each thermocouple (TC) in each mass placement by the calibration variables of the Stage 1 time-temperature profile. Because scaling coefficients were calculated using mass placement data, generated laboratory protocols used in Stage 3 of the Fig. 1 testing protocol should produce time-temperature profiles in laboratory specimens that closely follow those of the mass placements. If the generated laboratory protocols do not yield similar time-temperature profiles, then the proposed framework is not feasible.

Materials

Experiments were conducted on an HSC developed by the U.S. Army Corps of Engineers (Table 2). An ASTM C150 Type I/II cement with a Blaine fineness of 450 m^2/kg (2197 ft^2/lb) was used. Silica fume had a bulk density ranging from 500 to 700 kg/m^3 (843 to 1180 lb/yd^3) and a SiO_2 content of at least 85%. Metakaolin conforming to ASTM C618 had a bulk density of 400 kg/m^3 (674 lb/yd^3) with SiO_2 contents ranging from 51 to 53% and Al_2O_3 ranging from 42 to 44%. Two sands were used: a manufactured granite sand with a water absorption of 1.0% and fineness modulus of 2.69, and a natural sand with a water absorption of 0.5% and a fineness modulus of 2.32. The gradation of each sand is shown in Fig. 3. Coarse aggregates are typically not used in HSC and UHPC mixtures. For laboratory mixtures, aggregates

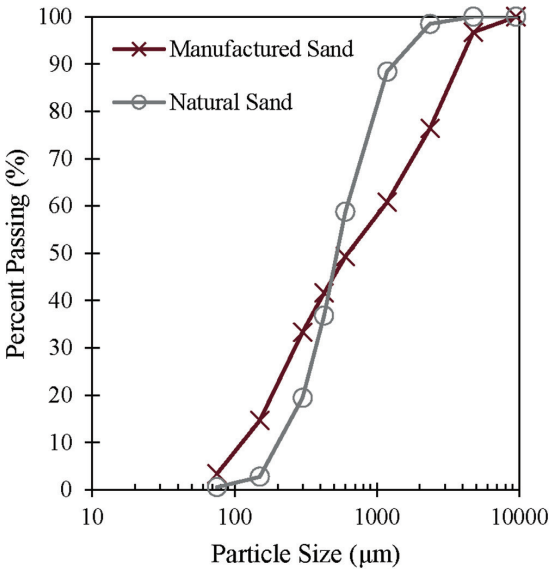

Fig. 3—Gradation of manufactured and natural sand. (Note: 1 μm = 3.93 × 10^{-5} in.)

were air-dried for several weeks and reached uniform moisture contents of 0.5% for manufactured sand and <0.1% for natural sand. For field mixtures, aggregate moisture contents were taken during batching to reach the desired *w/cm*. Three admixtures were used: a high-range water-reducing admixture (HRWRA), a defoamer, and a set retarder.

Mass placement preparation and curing environment

Four mass placements were cast at a facility in south Mississippi in June 2018. Four metal culverts with a wall thickness of 6.4 mm (0.25 in.) and a 12.7 mm (0.50 in.) piece of metal attached to the bottom served as formwork (Fig. 4(a)). Two placements were 1.22 m (4 ft) in diameter and height, while the other placements were 1.83 m (6 ft) in diameter and height. Ten TCs were placed in each culvert at known locations to measure temperature (Fig. 4(b)). TCs were attached to a metal frame that was secured at the center of the placement prior to casting. One placement of each size was fully wrapped in an insulating blanket immediately after casting for the duration of hydration. All placements were cured in an open-ended hangar (that is, they were covered from rain and direct sunlight but not temperature-controlled). TCs were placed next to each placement to record ambient temperature profiles. When the TCs were compared to local weather records, the open-ended hangar did minimize large ambient temperature changes due to daily temperature fluctuations, as typical daily temperature fluctuation was 8.8°C (15.8°F), while the temperature fluctuation inside the facility was 4.3°C (7.7°F).

Laboratory-scale specimen preparation and curing environment

Laboratory mixing occurred at Mississippi State University (MSU) using a benchtop mixer with a paddle attachment to induce shear mixing. Cement, silica fume, metakaolin, manufactured sand, and natural sand were mixed for 1 minute to create a homogenous mixture. 80% of the water

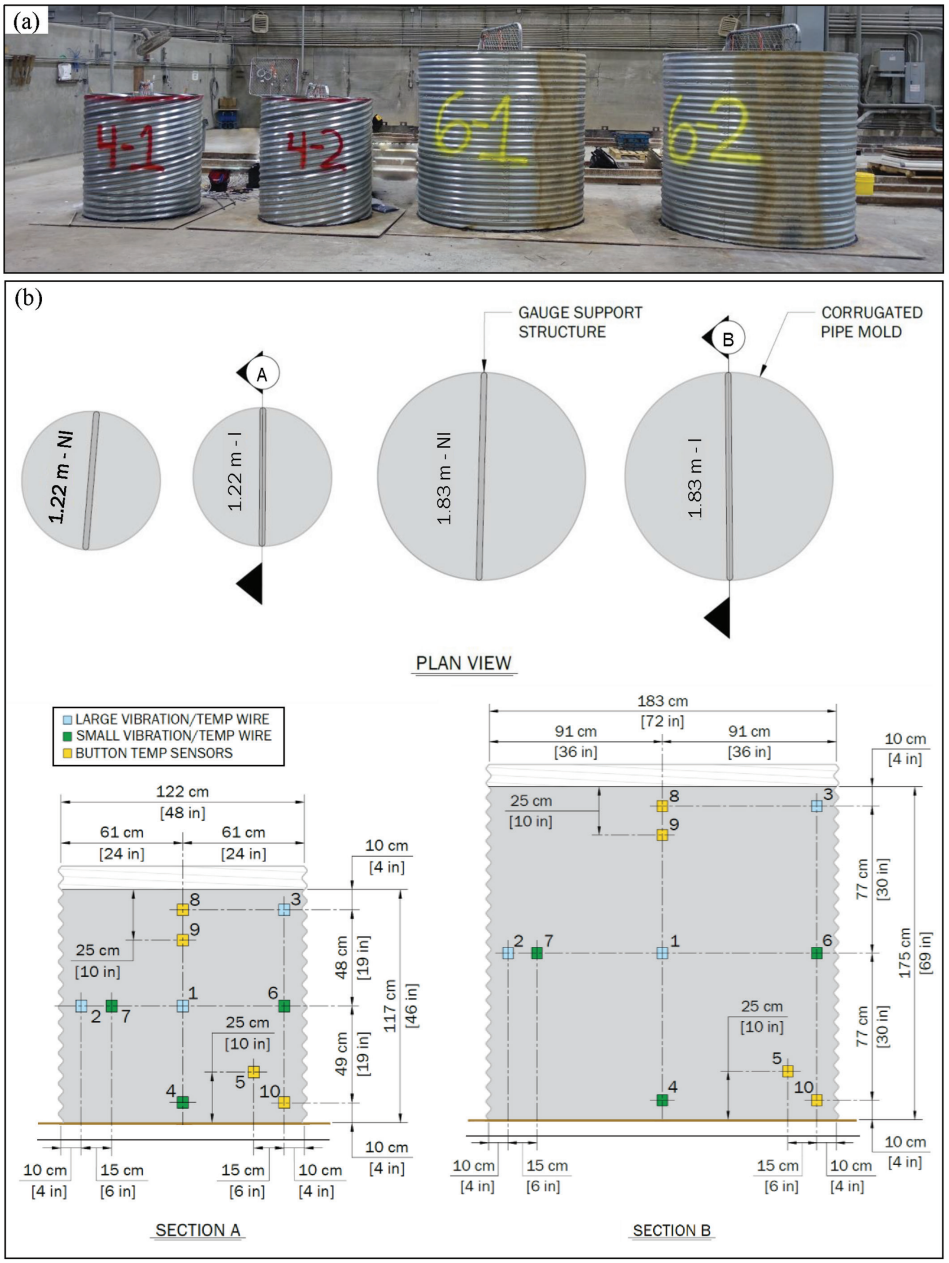

Fig. 4—(a) Mass placements formwork at testing location; and (b) schematic of thermocouple locations. (Note: 1 m = 3.28 ft.)

was added to premixed materials and mixed at a low speed for 1 minute. After 1 minute, the remaining 20% of water, HRWRA, defoamer, and set retarder were added and mixed at an increased mixing speed until a fluid state was achieved. Two 10.2 x 20.3 cm (4 x 8 in.) plastic cylinder molds were filled in two equal lifts and externally vibrated between lifts to remove air voids. After the first lift, a TC was placed in the middle of one of the two specimens. Two mixtures were mixed simultaneously to produce four 10.2 x 20.3 cm (4 x 8 in.) specimens. Once mixed and molded, groups of four specimens were placed in a designated curing environment.

Nineteen curing protocols with varying combinations of insulating block and programmed boundary conditions were used (Table 3). All curing protocols used a VT curing bath that was programmed to alter the air temperature surrounding an insulated curing block (Fig. 5). The VT curing bath consisted of an off-the-shelf concrete curing box that was modified to include a high-temperature water pump, and a programmable temperature controller. This VT curing bath could be replaced with fully commercially available equipment in the future, but it was used herein for continuity with past work (that is, Allard et al.[22] and Carey et al.[8,9]) where previous iterations of the framework have been evaluated. Curing blocks made of polyisocyanurate (PIR; *R*-value = 1.06 m^2·K/W) and aluminum honeycomb (AH; *R*-value = 0.01 m^2·K/W) were used to insulate concrete specimens and were previously used in Carey et al.[9] (Fig. 5).

Of the 15 boundary conditions used in this study, three were recommended in previous studies and are repeated herein for continuity and to evaluate their viability with a different mixture. Carey et al.[8] recommended two protocols for modest placements with least dimensions of 0.15 to 0.50 m (0.5 to 1.6 ft), while Carey et al.[9] recommended a protocol for intermediate regions of an insulated 1.83 m (6 ft)

Table 3—Summary of laboratory curing protocols

Curing protocol	Insulator	Programmed boundary condition				Curing protocol objective
		t_D, hours	S_{inc}, °C/h	t_{PD}, hours	S_{dec}, °C/h	
1	AH	6.0	3.0	4.0	–1.0	Recommended in Carey et al.[8]
2	PIR	—	—	—	—	Recommended in Carey et al.[8]
3	PIR	6.0	11.2	4.0	–0.45	Recommended in Carey et al.[9]
4	PIR	12.5	13.9	25.5	–0.87	Replicate 1.2 m non-insulated placement; R1
5	PIR	13.1	12.3	12.4	–0.77	Replicate 1.2 m non-insulated placement; R2
6	PIR	14.4	8.9	7.3	–0.57	Replicate 1.2 m non-insulated placement; R3
7	AH	14.4	8.9	7.3	–0.57	Replicate 1.2 m non-insulated placement; R3
8	PIR	10.4	14.7	27.4	–0.56	Replicate 1.2 m insulated placement; R1
9	PIR	10.9	13.6	15.6	–0.51	Replicate 1.2 m insulated placement; R2
10	PIR	12.0	10.4	29.3	–0.40	Replicate 1.2 m insulated placement; R3
11	AH	12.0	10.4	29.3	–0.40	Replicate 1.2 m insulated placement; R3
12	PIR	9.8	17.0	50.3	–0.54	Replicate 1.8 m non-insulated placement; R1
13	PIR	9.8	13.8	11.5	–0.48	Replicate 1.8 m non-insulated placement; R2
14	PIR	11.0	6.7	4.0	–0.32	Replicate 1.8 m non-insulated placement; R3
15	AH	11.0	6.7	4.0	–0.32	Replicate 1.8 m non-insulated placement; R3
16	PIR	11.8	15.9	64.5	–0.40	Replicate 1.8 m insulated placement; R1
17	PIR	12.2	13.8	33.7	–0.36	Replicate 1.8 m insulated placement; R2
18	PIR	13.0	6.3	4.5	–0.21	Replicate 1.8 m insulated placement; R3
19	AH	13.0	6.3	4.5	–0.21	Replicate 1.8 m insulated placement; R3

Note: t_D is length of dormant period; S_{inc} is rate of temperature increase; t_{PD} is length of peak temperature; S_{dec} is rate of temperature decrease; boundary condition variables visually defined in Fig. 5; all laboratory experiments were conducted in variable temperature bath; °F = (9/5)(°C) + 32; 1 m = 3.28 ft.

diameter mass placement. The remaining 12 boundary conditions were developed using the three-stage testing protocol and mass placement time-temperature data presented in this paper. Boundary conditions developed in previous efforts were focused on replicating a specific time-temperature profile and were programmed to directly replicate placement temperature profiles. The 12 boundary conditions developed in this paper are the first research activity in evolving toward a predictive testing framework that can generate curing protocols that replicate mass placement temperatures.

Mechanical testing methods

Prior to testing, specimens were ground to obtain plain ends. Compressive strength (f_c) tests for concrete specimens were conducted following ASTM C39/C39M, where specimens were loaded at a rate of 0.24 MPa/s (35 psi/s) until failure. Elastic modulus (E) tests used a linear variable displacement transducer (LVDT) to measure vertical displacement per ASTM C469. An average of two f_c values from identically cured concrete specimens were used to find 40% of the maximum load. E tests were then conducted on the two remaining specimens, which were then tested for f_c, for a total of four f_c and two E per set of four concrete specimens.

RESULTS AND DISCUSSION

Analysis of mass placement time-temperature histories

Time-temperature histories were recorded for each mass placement and are shown in Fig. 6. Temperature trends were expected as increasing placement size and the inclusion of insulation yielded higher peak temperatures. Figure 6 temperatures were all noticeably higher than the peak temperatures reported in Table 1. TPOIs and calibration variables were calculated for each recorded time-temperature history in each mass placement (Table 4). Using Table 4 data and trends in Fig. 5, similar temperature profiles were grouped together to create three temperature regions within each mass placement. Region 1 (R1) was the hottest temperatures (typically at the center of each mass placement), Region 2 (R2) was intermediate temperatures, and Region 3 (R3) was typically temperatures at the edge of each mass placement. Regions were checked using two-tailed t-tests assuming unequal variance at a 0.05 significance level to ensure key variables in each region were different from one another. In other words, R2 was statistically compared to R1 and R3 for each placement. As seen in Fig. 7, there were only three cases where, statistically, there was no difference between variables in two temperature regions: 1) S_{dec} between R1 and R2 in the 1.22 m (4 ft) insulated placement; 2) S_{inc} between R2 and R3 in the 1.83 m (6 ft) non-insulated placement; and 3) S_{dec} between R2 and R3 in the 1.83 m (6 ft) non-insulated placement. In these cases,

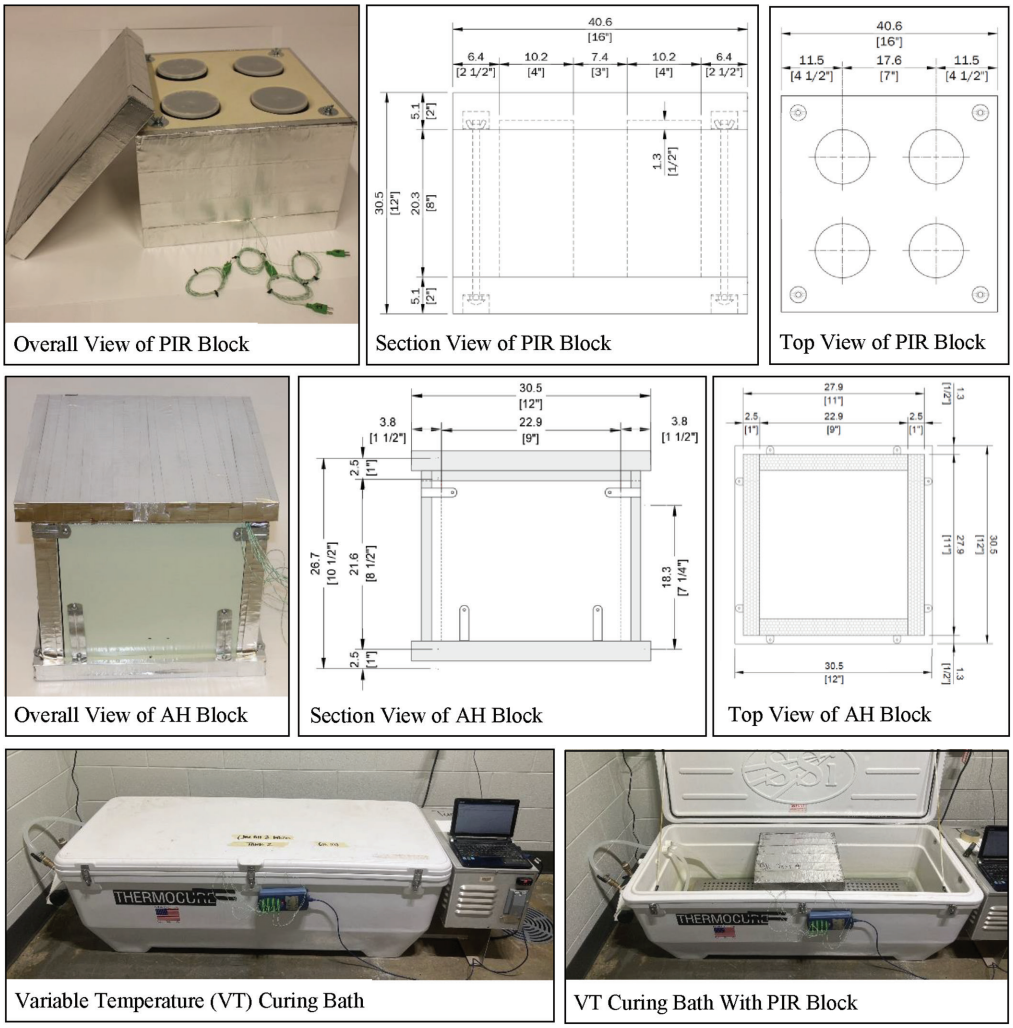

Fig. 5—Insulators and environmental chambers used in study. (Note: Dimensions of curing blocks given in cm [in.].)

visual evaluations of the time-temperature histories justified temperature region grouping.

Analysis of variance (ANOVA) was used to assess overall trends of these mass placements (that is, considering all TCs in each placement regardless of region) at a 0.05 significance level. T_{max} and S_{inc} values (that is, variables defining the time-temperature curve up to peak temperature) were not statistically different between any of the placements reporting *p*-values of 0.39 and 0.37, respectively. However, S_{dec} values of each placement were statistically different from one another with a *p*-value less than 0.01. Additionally, the 1.83 m (6 ft) insulated placement was compared to a placement of the same size and insulation reported in Carey et al.,[9] where a different mixture was used. T_{max} and S_{inc} values were meaningfully different between the placement presented herein (101.1°C and 13.2°C/h [214°F and 23.8°F/h]) and the Carey et al.[9] placement (94.1°C and 3.4°C/h [201.4°F and 6.1°F/h]). However, when evaluating S_{dec}, the two placements were nearly identical (–0.35°C/h [–0.63°F/h] for the placement herein and –0.34°C/h [–0.61°F/h] for the Carey et al.[9] placement). This indicates that mixture characteristics influence initial time-temperature characteristics such as T_{max} and S_{inc}, while the size and insulation of mass placements drive time-temperature histories after peak temperatures have occurred (that is, S_{dec}).

Evaluating feasibility of three-stage testing framework

Figure 8 and Table 5 summarize all data from laboratory-scale specimens that were cured following Table 3 curing protocols. Generally speaking, curing protocols for most center and intermediate regions (that is, R1 and R2) yielded time-temperature profiles that closely resembled mass placements, while the edge region profiles (that is, R3) greatly overestimated mass placement temperatures. R1 protocols produced reasonable time-temperature profiles for 1.22 m (4 ft) placements; however, for the 1.83 m (6 ft) placements, protocols were not successfully implemented due to equipment limitations and extreme temperature ranges. In the 1.83 m (6 ft) non-insulated placement, programmed temperatures exceeded the operating temperature of the VT bath, causing equipment failure, while the combination of VT bath and insulating block could not reach the target temperature for the 1.83 m (6 ft) insulated placement. Further improvements to the proposed three-stage testing protocols are envisioned where equipment with increased

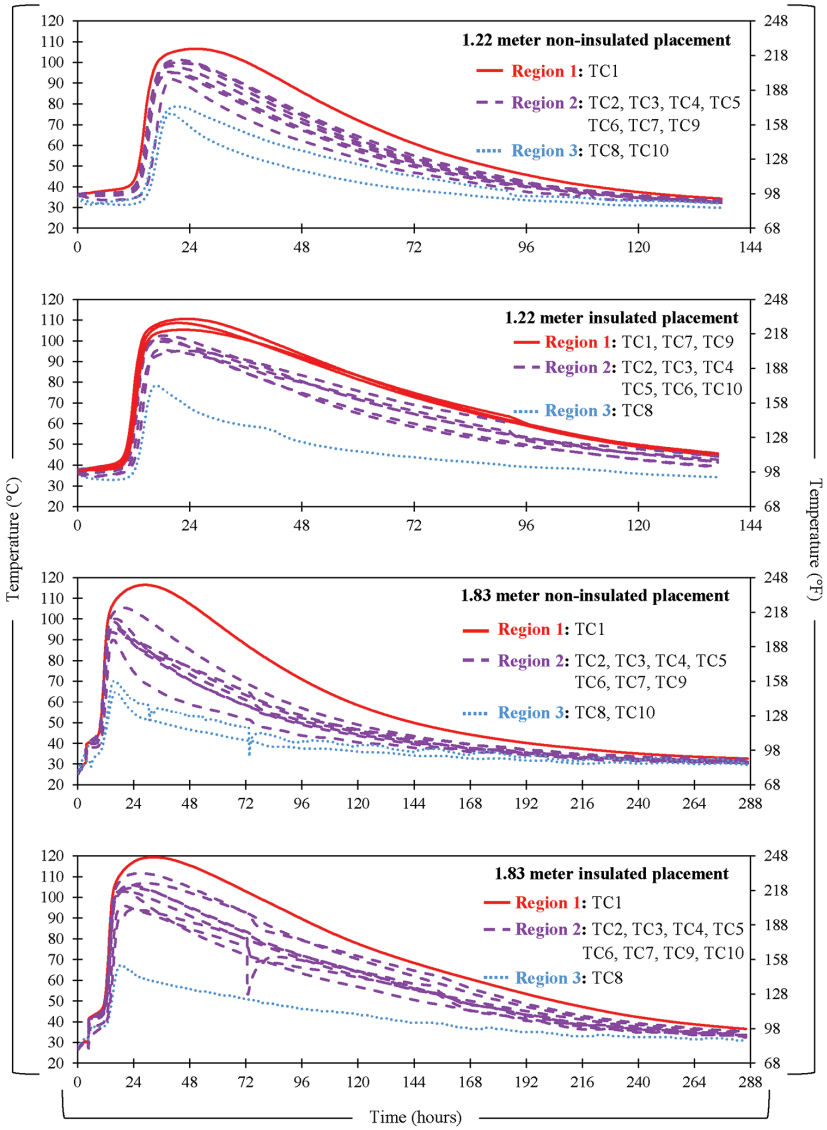

Fig. 6—Recorded time-temperature histories of each mass placement. (Note: 1 m = 3.28 ft.)

operating temperatures is used (for example, programmable ovens in place of a programmable cooler).

R2 protocols produced temperatures that were visually similar to each mass placement. ANOVA testing at a significance level of 0.05 was conducted to compare R2 laboratory curing protocols to mass placements. S_{inc} of the laboratory protocols was significantly different than all four mass placements (p-value <0.01 in all cases), even though programmed S_{inc} rates were the same as each mass placement. This indicates that heat generated by laboratory specimens during hydration increases S_{inc} values to be higher than programmed. T_{max} was significantly different for the 1.22 m (4 ft) insulated placement (p-value of 0.01) and the 1.83 m (6 ft) non-insulated placement (p-value of 0.02), but statistically the same in the 1.22 m (4 ft) non-insulated placement (p-value of 0.13) and 1.83 m (6 ft) insulated placement (p-value of 0.38). The differences in T_{max} for some placements were likely influenced by the meaningfully higher S_{inc} values of laboratory specimens. There was no statistical difference between S_{dec} of laboratory protocols and mass placements (p-values of 0.31, 0.26, 0.08, and 0.47). Although there are some statistical differences in thermal variables between mass placements and laboratory curing protocols, visually, the laboratory protocols reasonably represented mass placement time-temperature profiles. This is considerable evidence of the validity of the three-stage curing protocol concept to recreate mass placement temperature profiles of laboratory specimens.

In addition to the three-stage laboratory protocols developed and evaluated herein, previously recommended curing protocols were also evaluated for continuity with previous efforts. Carey et al.[9] recommended a laboratory protocol to replicate temperatures within an intermediate region of a 1.83 m (6 ft) insulated mass placement. This recommended protocol was developed using one mixture and does not account for changes in mixture constituents. ANOVA testing showed that although T_{max} were statistically the same between the mass placement and laboratory specimens (p-value of 0.14), S_{inc} and S_{dec} were statistically different (p-value <0.01 in both cases). Unlike the recommended protocol from Carey et al.[9] that was developed

Table 4—Calibration variables and scaling constants of mass placements and initial PIR test

Thermal data set	TC	Calibration variables				Scaling constants			
		t_D	S_{inc}	t_{PD}	S_{dec}	a	b	c	d
PIR	—	20.1	9.8	1.4	–1.3	—	—	—	—
1.22 m non-insulated mass placement	1	12.5	13.9	25.5	–0.87	0.62	1.42	18.09	0.69
	2	13.3	12.3	8.8	–0.76	0.66	1.26	6.21	0.60
	3	14.0	11.6	5.0	–0.71	0.70	1.19	3.55	0.57
	4	13.0	11.8	12.3	–0.74	0.65	1.20	8.69	0.59
	5	12.8	12.2	15.3	–0.81	0.63	1.24	10.82	0.65
	6	13.0	12.5	12.0	–0.78	0.65	1.28	8.51	0.62
	7	12.8	12.4	16.3	–0.80	0.63	1.27	11.52	0.64
	8	14.8	9.3	3.3	–0.59	0.73	0.95	2.30	0.47
	9	13.0	13.0	17.3	–0.79	0.65	1.32	12.23	0.63
	10	14.0	8.6	11.3	–0.55	0.70	0.88	7.98	0.43
1.22 m insulated mass placement	1	10.3	15.2	27.0	–0.60	0.51	1.56	19.15	0.48
	2	10.8	14.6	15.8	–0.53	0.53	1.49	11.17	0.42
	3	11.5	13.4	12.5	–0.45	0.57	1.37	8.87	0.36
	4	10.3	13.4	13.3	–0.55	0.51	1.36	9.40	0.44
	5	10.5	13.0	11.8	–0.55	0.52	1.33	8.33	0.44
	6	11.0	14.6	14.3	–0.50	0.55	1.49	10.11	0.40
	7	10.3	14.3	26.0	–0.55	0.51	1.46	18.44	0.44
	8	12.0	10.4	3.0	–0.40	0.60	1.07	2.13	0.32
	9	10.8	14.6	29.3	–0.53	0.53	1.49	20.74	0.42
	10	11.3	12.5	26.3	–0.45	0.56	1.27	18.62	0.36
1.83 m non-insulated mass placement	1	9.8	17.0	50.3	–0.54	0.48	1.73	35.64	0.43
	2	10.0	13.9	8.5	–0.48	0.50	1.42	6.03	0.38
	3	10.3	11.9	3.5	–0.47	0.51	1.22	2.48	0.38
	4	9.3	12.9	14.3	–0.45	0.46	1.32	10.11	0.36
	5	9.5	14.5	10.5	–0.56	0.47	1.48	7.45	0.45
	6	10.0	14.3	8.0	–0.47	0.50	1.46	5.67	0.38
	7	9.8	15.5	25.0	–0.52	0.48	1.58	17.73	0.41
	8	11.3	5.6	4.3	–0.39	0.56	0.57	3.01	0.31
	9	9.8	13.4	10.5	–0.41	0.48	1.37	7.45	0.33
	10	10.8	7.7	3.8	–0.25	0.53	0.79	2.66	0.20
1.83 m insulated mass placement	1	11.8	15.9	64.5	–0.40	0.58	1.63	45.74	0.31
	2	12.0	14.4	32.0	–0.39	0.60	1.47	22.70	0.31
	3	12.8	12.8	21.5	–0.32	0.63	1.30	15.25	0.26
	4	11.8	14.4	22.5	–0.35	0.58	1.47	15.95	0.28
	5	11.8	13.5	16.0	–0.38	0.58	1.38	11.35	0.30
	6	12.3	14.5	31.8	–0.39	0.61	1.48	22.52	0.31
	7	11.8	14.9	47.5	–0.40	0.58	1.52	33.69	0.31
	8	13.0	6.3	4.5	–0.21	0.65	0.64	3.19	0.17
	9	12.0	13.9	56.5	–0.36	0.60	1.42	40.07	0.29
	10	13.3	11.8	41.5	–0.32	0.66	1.20	29.43	0.26

Note: t_D reported in hours; S_{inc} reported in °C/h, t_{PD} reported in hours; S_{dec} reported in °C/h; a, b, c, and d are scaling factors; 1 m = 3.28 ft; °F = (9/5)(°C) + 32.

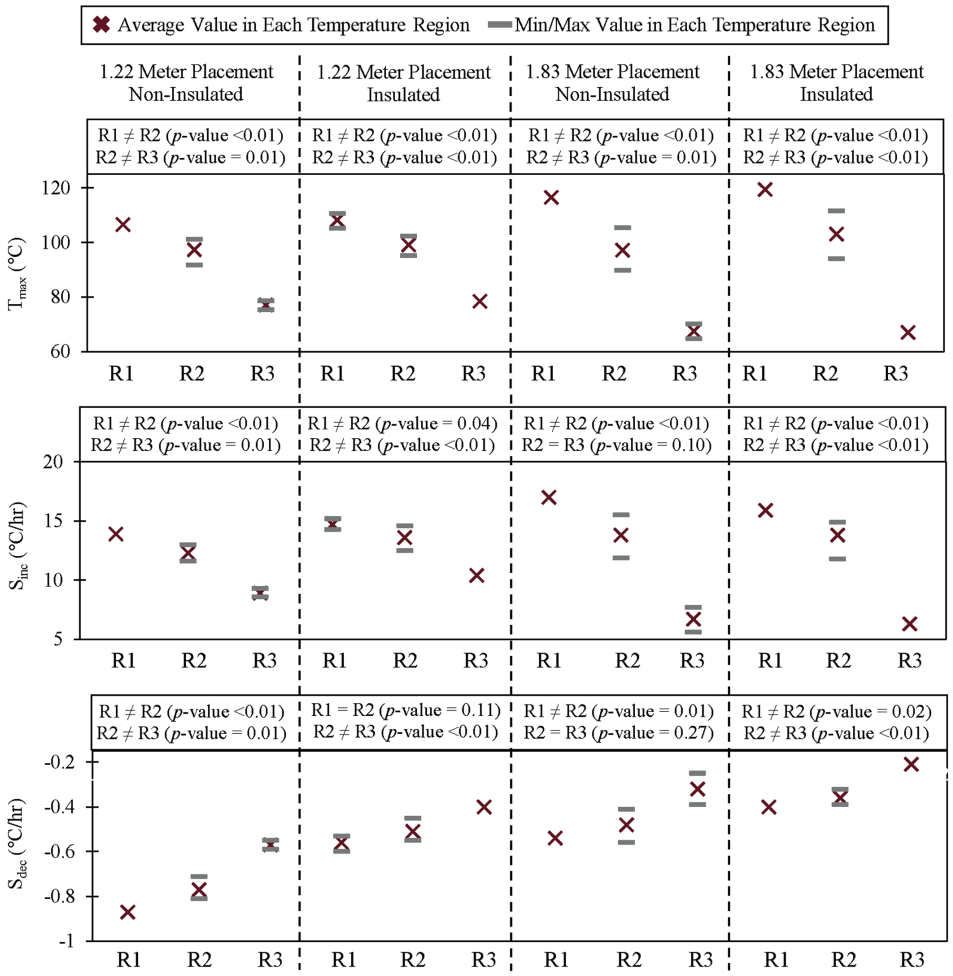

Fig. 7—Summary of t*-tests comparing maximum temperature (*T_{max}*),* S_{inc}*, and* S_{dec} *for R1 to R2 and R2 to R3 for each mass placement. (Note: °F = (9/5)(°C) + 32; 1 m = 3.28 ft.)*

based on one mixture, the three-stage method has the ability to account for different mixtures by adjusting key metrics.

Temperature profiles from R3 of each mass placement (that is, near the surface, where external temperatures can meaningfully influence time-temperature histories) were not accurately replicated. For all four placements, S_{inc}, T_{max}, and S_{dec} were statistically different than the laboratory protocol. The combination of insulation (PIR in the case of Fig. 7) as well as a programmed boundary condition produced temperatures that were much higher than measured mass placement temperatures. R3 three-stage protocols were also conducted using the AH curing block, which had a significantly lower insulating *R*-value than PIR. Even with the decreased insulating value, AH blocks produced time-temperature profiles that were meaningfully different than mass placement temperatures (Fig. 9). S_{inc} and T_{max} of PIR and AH blocks used with R3 curing protocols were similar, while S_{dec} was noticeably different. Although the three-stage protocol did not replicate time-temperature profiles of concrete near the edge of a mass placement, where external temperatures meaningfully influence temperatures, Stage 1 only shows interest in replicating R3 profiles, as discussed in the following paragraph.

Previous efforts reported by Carey et al.[8] evaluated and recommended two curing protocols for modestly sized UHPC placements with least dimensions between 0.15 and 0.50 m (0.5 and 1.6 ft). Laboratory specimens were cured with these recommended protocols and compared to R3 temperature profiles (Fig. 9). For 1.22 m (4 ft) placements, the PIR protocol (3 days in 23°C [73°F] ambient temperatures) reasonably replicated S_{inc} and T_{max} but did not replicate S_{dec} adequately. Although this PIR protocol overpredicted T_{max} of both 1.83 m (6 ft) placements, this laboratory protocol produced closer estimates of R3 mass placement temperatures. When evaluating the AH block protocol, T_{max} was overpredicted in all cases by 10 to 25°C (18 to 45°F). The PIR protocol is promising as this is currently being used as Stage 1 of the three-stage curing protocol, so R3 temperatures could potentially be approximated using Stage 1 of the proposed framework.

Mechanical properties evaluation

Sets of four specimens were tested after undergoing each of the 19 curing protocols. There is no core data from these mass placements to benchmark against; however, ranges of anticipated mechanical properties of the mass placements can be estimated using laboratory data. Although mechanical properties data from curing protocol 12 are reported in Table 5, they are not included in analysis of mechanical properties as the curing protocol failed.

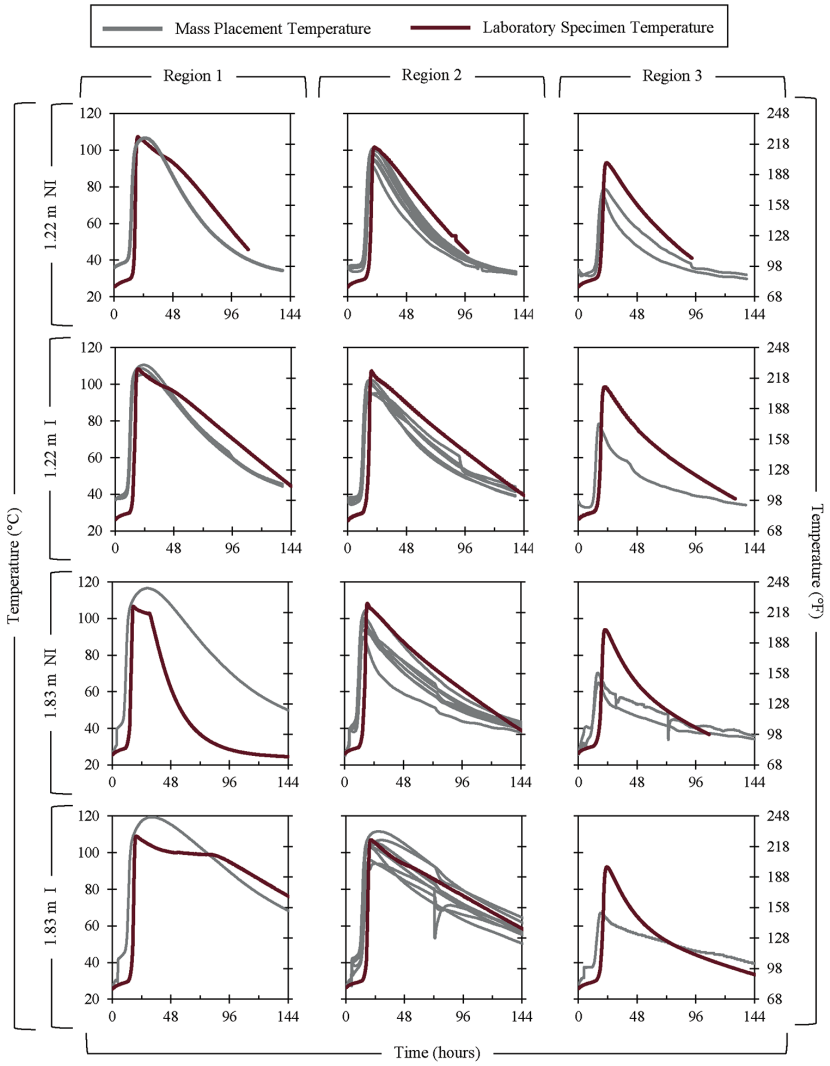

Fig. 8—Time-temperature profiles of mass placements compared to time-temperature profiles of laboratory-cured specimens. (Note: NI is non-insulated; I is insulated; 1 m = 3.28 ft.)

The f_c of laboratory specimens had noticeable variability, with almost 90% of curing protocols producing coefficient of variation (COV) values greater than 10%. ANOVA tests at a 0.05 significance level showed there was no statistical difference in mechanical properties from curing protocols that are intended to represent temperature regions in the non-insulated and insulated 1.22 m (4 ft) placements as well as the non-insulated 1.83 m (6 ft) placement (p-values of 0.72, 0.07, and 0.06, respectively). Although not significantly different, the insulated 1.22 m (4 ft) placement and non-insulated 1.83 m (6 ft) placement were very close to the 0.05 significance threshold. For the insulated 1.83 m (6 ft) placements, mechanical properties from each temperature region were statistically different (p-value = 0.01). Overall, these findings are encouraging as there was statistical significance identified between temperature curing protocols of mass placements and f_c. Future work is needed to compare core strengths of mass placements to strengths of laboratory specimens cured following the Fig. 1 three-stage framework.

Compressive strengths of mass placement curing protocols were also compared to traditional curing protocols. Specimens cured for 28 days in a 23°C (73°F) fog room produced an average f_c of 68 MPa (9860 psi), and 58% of specimens cured to replicate a mass placement were within ±10 MPa (1450 psi) of the 28-day f_c. Mass placement cured specimens were also benchmarked to specimens cured to what is believed by some to be near ultimate strength by curing at 23°C (73°F) for 7 days, followed by 7 days submerged in a 90°C (194°F) water bath. Ultimate strength specimens yielded an average f_c of 94 MPa (13,634 psi), which was meaningfully higher than all reported three-stage protocol cured specimen f_c, except for curing protocol 16 (1.83 m [6 ft] insulated placement; R1). This indicates that thermal treatment (similar to what is described in ASTM C1856/C1856M-17[16]) is likely not representative of strengths within some mass placements.

Linear regression analysis was conducted to determine the statistical relationships of calibration variables (for example, t_D, S_{inc}, t_{PD}, and S_{dec}) and f_c, similar to the analysis in Carey et al.[23] Each variable was compared to f_c, and statistically significant relationships were quantified for t_D (p-value <0.01) and t_{PD} (p-value of 0.05); however, there was not a statistical relationship for S_{inc} (p-value of 0.34) and S_{dec} (p-value of 0.26) (Table 6). This indicates that for the concrete

Table 5—Thermal and mechanical results of laboratory specimens

Curing protocol	Thermal variables			f_c			E		
	T_{max}, °C	S_{inc}, °C/h	S_{dec}, °C/h	n	Avg., MPa	COV, %	n	Avg., MPa	COV, %
1	89.5	12.7	–1.27	4	67	15.8	2	35,878	0.1
2	79.6	9.79	–1.26	4	75	11.8	2	38,380	0.7
3	108.7	17.8	–0.52	4	72	19.2	2	41,378	1.2
4	107.3	26.6	–0.76	4	64	29.8	2	43,010	13.6
5	101.7	19.0	–0.80	4	74	8.7	2	34,610	3.1
6	93.1	14.7	–0.77	4	74	13.0	2	36,136	4.9
7	87.2	14.7	–0.80	4	70	6.3	2	41,752	2.9
8	108.5	20.7	–0.55	4	49	22.6	2	27,374	14.6
9	107.3	22.2	–0.55	4	68	24.3	2	37,514	5.8
10	98.6	16.9	–0.59	4	73	15.8	2	37,928	6.9
11	100.8	18.5	–0.72	4	50	8.9	2	49,585	32.2
12*	—	—	—	3	36	9.2	1	41,172	—
13	108.2	20.0	–0.56	4	45	36.4	2	33,071	20.4
14	93.9	14.8	–0.76	4	67	15.7	2	37,270	1.2
15	85.6	13.4	–0.81	4	59	17.4	2	33,663	28.7
16	109.1	24.8	–0.31	4	95	8.5	2	35,941	3.9
17	107.0	23.3	–0.38	4	64	8.1	2	33,900	4.0
18	92.2	13.9	–0.59	4	80	20.1	2	37,760	17.2
19	85.9	14.0	–0.58	4	72	22.1	2	32,994	8.0

*Curing protocol 12 failed due to equipment limitations. Detailed thermal data are not available; mechanical properties shown as reference but are not included in analysis.

Note: T_{max} is maximum recorded internal specimen temperature; S_{inc} is rate of temperature increase recorded from specimen; S_{dec} is rate of temperature decrease recorded from specimen; f_c is unconfined compressive strength; E is elastic modulus; n is number of replicates; Avg. is average; 1 MPa = 145 psi; °F = (9/5)(°C) + 32.

evaluated herein, the programmed dormant periods statistically influenced f_c, while the programmed slopes (increase and decrease) had no statistical influence on f_c. More analysis is needed on a wide range of mixtures to fully quantify the influence of calibration variables on mechanical properties; however, this analysis shows that the recommended three-stage curing protocol does statistically influence mechanical properties, further highlighting its potential to characterize thermomechanical properties of modest to mass placements where HSCs are used.

The elastic modulus (E) was less variable than f_c, with only 33% of E values having a COV higher than 10%. ANOVA tests at a 0.05 significance level showed there were no statistical differences between E values from temperature regions for each placement (p-values of 0.18, 0.06, 0.47, and 0.68, respectively). Additionally, there were no statistically significant relationships between calibration variables and elastic modulus (Table 6). These findings align with previous research by the authors where, so long as naturally occurring hydration reactions occur (that is, delaying curing protocols until concrete has naturally begun hydration reactions), the elastic modulus is not significantly influenced by changes in curing temperature.[22]

CONCLUSIONS AND RECOMMENDATIONS

This paper focused on vetting a three-stage testing protocol that aims to cure laboratory specimens with a protocol that replicates temperature histories of a mass placement. From this work, the following conclusions can be drawn:

1. Recorded mass placement peak temperatures ranged from 107 to 119°C (225 to 246°F), which were higher than Table 1 reported temperatures and exceeded limits of equipment used by the authors.

2. The three-stage protocol was successful at replicating temperature profiles in regions where exterior temperatures do not play a meaningful role in the time-temperature history. Stage 1 curing procedures were shown to reasonably replicate temperature profiles near the edge.

3. There was a statistically significant relationship between calibration variables (that is, t_D and t_{PD}) used to develop three-stage curing protocols and compressive strength.

Based on these conclusions, the following recommendations with respect to the three-stage curing protocol evaluated herein are provided:

1. More robust and standardized equipment is needed to successfully recreate curing protocols at the extreme temperatures (that is, >115°C [239°F]) recorded in mass placements.

2. Although the upper temperature boundaries of the testing protocol are reasonably understood, more research is needed to quantify the potential of the three-step curing protocol for concretes that do not generate as much heat during hydration.

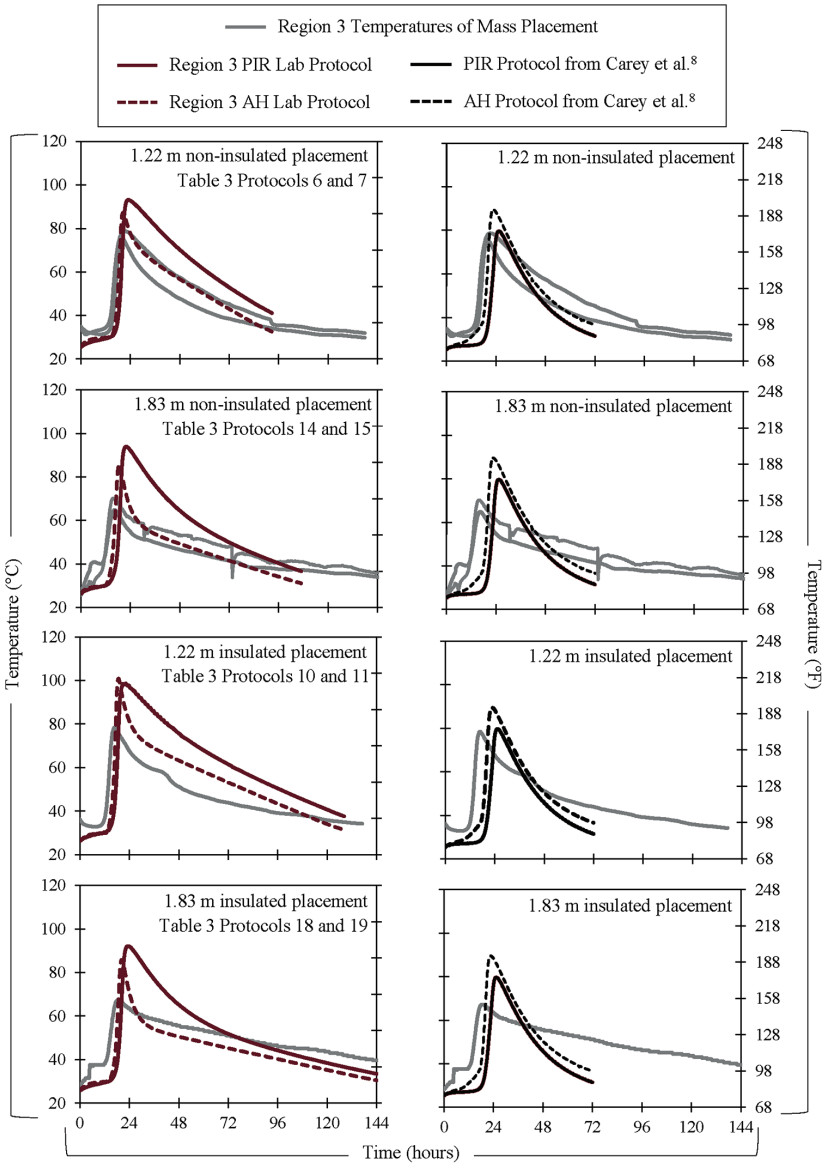

Fig. 9—Comparison of insulating block material and previously published curing protocols from Carey et al.[8] to R3 time-temperature profiles recorded herein. (Note: 1 m = 3.28 ft.)

Table 6—Relationships between calibration variables and mechanical properties

Variable 1	Variable 2	Equation	*p*-value on equation slope	Conclusions
f_c	t_D	$f_c = 6.04(t_D) - 0.34$	<0.01	Statistically significant
	S_{inc}	$f_c = -0.81(S_{inc}) + 78.0$	0.33	Not statistically significant
	t_{PD}	$f_c = 0.30(t_{PD}) + 62.0$	0.05	Statistically significant
	S_{dec}	$f_c = 15.9(S_{dec}) + 76.3$	0.26	Not statistically significant
E	t_D	$E = 1169(t_D) + 21{,}938$	0.14	Not statistically significant
	S_{inc}	$E = -350(S_{inc}) + 40{,}016$	0.28	Not statistically significant
	t_{PD}	$E = -18(t_{PD}) + 36{,}257$	0.76	Not statistically significant
	S_{dec}	$E = -3057(S_{dec}) + 34{,}351$	0.58	Not statistically significant

Note: t_D is length of dormant period in hours; S_{inc} is rate of temperature increase in °C/h; t_{PD} is length of peak temperature in hours; S_{dec} is rate of temperature decrease in °C/h; f_c is unconfined compressive strength in MPa; E is elastic modulus in MPa; p-value ≤ 0.05 indicates statistically significant relationship.

3. Test mass placements that can be cored to measure the in-place compressive strength (f_c) of the placement to compare to the laboratory testing framework.

4. Mass placements with a wide range of constituents should be evaluated within the framework to ensure its validity for multiple mixtures.

AUTHOR BIOS

Ashley S. Carey *is a former Research Engineer II at the Center for Advanced Vehicular Systems in Starkville, MS. She received her bachelor's, master's, and doctorate degrees from Mississippi State University (MSU), Starkville, MS, in 2017, 2019, and 2021, respectively. Her research interests include construction materials, with an emphasis on high-strength concretes and cement-stabilized materials.*

ACI member **Grayson B. Sisung** *is a Graduate Research Assistant at MSU, where she received her bachelor's and master's degrees in 2020 and 2023, respectively. Her research interests include high-strength concretes.*

ACI member **Isaac L. Howard** *is the Director of the Richard A. Rula School of Civil and Environmental Engineering at MSU. He received his bachelor's, master's, and doctorate degrees between 2001 and 2006 from Arkansas State University, Jonesboro, AR; West Virginia University, Morgantown, WV; and the University of Arkansas, Fayetteville, AR, respectively. His research interests include construction materials for infrastructure.*

ACI member **Brad Songer** *is a Research Civil Engineer at the U.S. Army Corps of Engineers Engineer Research and Development Center (ERDC) in Vicksburg, MS. He received his bachelor's degree from Jackson State University, Jackson, MS, in 2019. His research interests include mass concrete and high-strength concretes.*

ACI member **Dylan A. Scott** *is a Research Mechanical Engineer at ERDC. He received his bachelor's degree from the University of Mississippi, Oxford, MS, in 2012, and his master's degree from MSU in 2017. His research interests include high-performance, fiber-reinforced, and alternative-binder concretes.*

ACI member **Jay Shannon** *is the Chief of the Concrete and Materials Branch at ERDC. He received his bachelor's, master's, and doctorate degrees from MSU in 2011, 2012, and 2015, respectively. His research interests include cement and concrete chemistry and sustainability.*

ACKNOWLEDGMENTS

The work described herein was supported by the U.S. Army Engineer Research and Development Center (ERDC) and the Military Engineering Research and Development Area under Contract No. W912HZ-21C0022 (PE 0603119A; Project B03; "Military Engineering Tech Demonstrations"; Task 06). R. Moser was a key technical advisor and program manager. Any opinions, findings, and conclusions or recommendations expressed in this material are those of the authors and do not necessarily reflect the views of the U.S. Government. Permission was granted by the Director, Geotechnical and Structures Laboratory, to publish this information.

REFERENCES

1. ACI Committee 228, "Report on Methods for Estimating In-Place Concrete Strength (ACI 228.1R-19)," American Concrete Institute, Farmington Hills, MI, 2019, 48 pp.

2. ASTM C805/C805M-18, "Standard Test Method for Rebound Number of Hardened Concrete," ASTM International, West Conshohocken, PA, 2018, 4 pp.

3. ASTM C597-16, "Standard Test Method for Pulse Velocity Through Concrete," ASTM International, West Conshohocken, PA, 2016, 4 pp.

4. ASTM C873/C873M-15, "Standard Test Method for Compressive Strength of Concrete Cylinders Cast in Place in Cylindrical Molds," ASTM International, West Conshohocken, PA, 2015, 4 pp.

5. ASTM C1074-19, "Standard Practice for Estimating Concrete Strength by the Maturity Method," ASTM International, West Conshohocken, PA, 2019, 10 pp.

6. Riding, K.; Schindler, A.; Pesek, P.; Drimalas, T.; and Folliard, K., "ConcreteWorks V3 Training/User Manual (P1): ConcreteWorks Software (P2)," Report No. 0-6332-P1 and P2, Texas Department of Transportation, Austin, TX, 2017, 130 pp.

7. Carey, A. S.; Roberson, M. M.; Howard, I. L.; and Shannon, J., "Toward a Method to Predict Thermo-Mechanical Properties of High-Strength Concrete Placements," *Journal of Testing and Evaluation*, V. 52, No. 1, 2024, pp. 689-706. doi: 10.1520/JTE20220554

8. Carey, A. S.; Howard, I. L.; and Shannon, J., "Variable Temperature Insulated Block Curing on Laboratory Scale Specimens to Simulate Thermal Profiles of Modestly Sized Ultra-High Performance Concrete Placements," *Cement and Concrete Composites*, V. 133, 2022, Article No. 104707. doi: 10.1016/j.cemconcomp.2022.104707

9. Carey, A. S.; Howard, I. L.; Shannon, J.; Scott, D. A.; and Songer, B., "Laboratory Curing Protocols to Replicate Thermomechanical Behavior of High-Strength Concrete in Mass Placements," *Journal of Materials in Civil Engineering*, ASCE, V. 34, No. 8, 2022, p. 04022189. doi: 10.1061/(ASCE)MT.1943-5533.0004345

10. Riding, K. A.; Ferraro, C. C.; Hamilton, H. R.; Voss, M. S.; and Alrashidi, R. S., "Requirements for Use of Field-Cast, Proprietary Ultra-High-Performance Concrete in Florida Structural Applications," FDOT Contract No. BDV31-977-94, Florida Department of Transportation, Tallahassee, FL, 2019, 210 pp.

11. Kodur, V. K. R.; Bhatt, P. P.; Soroushian, P.; and Arablouei, A., "Temperature and Stress Development in Ultra-High Performance Concrete during Curing," *Construction and Building Materials*, V. 122, 2016, pp. 63-71. doi: 10.1016/j.conbuildmat.2016.06.052

12. Sbia, L. A.; Peyvandi, A.; Harsini, I.; Lu, J.; Ul Abideen, S.; Weerasiri, R. R.; Balachandra, A. M.; and Soroushian, P., "Study on Field Thermal Curing of Ultra-High-Performance Concrete Employing Heat of Hydration," *ACI Materials Journal*, V. 114, No. 5, Sept.-Oct. 2017, pp. 733-743. doi: 10.14359/51689677

13. Li, S.; Cheng, S.; Mo, L.; and Deng, M., "Effects of Steel Slag Powder and Expansive Agent on the Properties of Ultra-High Performance Concrete (UHPC): Based on a Case Study," *Materials*, V. 13, No. 3, 2020, Article No. 683. doi: 10.3390/ma13030683

14. Soliman, N. A.; Omran, A. F.; and Tagnit-Hamou, A., "Laboratory Characterization and Field Application of Novel Ultra-High-Performance Glass Concrete," *ACI Materials Journal*, V. 113, No. 3, May-June 2016, pp. 307-316. doi: 10.14359/51688827

15. Aghdasi, P.; Heid, A. E.; and Chao, S.-H., "Developing Ultra-High-Performance Fiber-Reinforced Concrete for Large-Scale Structural Applications," *ACI Materials Journal*, V. 113, No. 5, Sept.-Oct. 2016, pp. 559-570. doi: 10.14359/51689103

16. ASTM C1856/C1856M-17, "Standard Practice for Fabricating and Testing Specimens of Ultra-High Performance Concrete," ASTM International, West Conshohocken, PA, 2017, 4 pp.

17. Riding, K. A.; Poole, J. L.; Schindler, A. K.; Juenger, M. C. G.; and Folliard, K. J., "Evaluation of Temperature Prediction Methods for Mass Concrete Members," *ACI Materials Journal*, V. 103, No. 5, Sept.-Oct. 2006, pp. 357-365.

18. Gross, E. D.; Eiland, A. D.; Schindler, A. K.; and Barnes, R. W., "Temperature Control Requirements for the Construction of Mass Concrete Members," Report No. 930-860R, Highway Research Center, Auburn, AL, 2017, 248 pp.

19. ACI Committee 207, "Mass Concrete—Guide (ACI PRC-207.1-21)," American Concrete Institute, Farmington Hills, MI, 2021, 34 pp.

20. Binard, J. P., "UHPC: A Game-Changing Material for PCI Bridge Producers," *PCI Journal*, V. 62, No. 2, 2017, pp. 34-46. doi: 10.15554/pcij62.2-01

21. Heinz, D., and Ludwig, H.-M., "Heat Treatment and Risk of DEF Delayed Ettringite Formation in UHPC," *Ultra High Performance Concrete (UHPC): Proceedings of the International Symposium*, M. Schmidt, E. Fehling, and C. Geisenhanslüke, eds., Kassel, Germany, 2004, pp. 717-730.

22. Allard, T. E.; Carey, A. S.; Howard, I. L.; and Shannon, J., "Time-Temperature Implications of Curing on Mechanical Properties of Ultra-High-Performance Concrete," *ACI Materials Journal*, V. 119, No. 5, Sept. 2022, pp. 251-260. doi: 10.14359/51735978

23. Carey, A. S.; Howard, I. L.; and Shannon, J., "Effects of Silica Fume Purity on Behavior of Ultra-High Performance Concrete," *Advances in Civil Engineering Materials*, V. 11, No. 1, 2022, pp. 354-371. doi: 10.1520/ACEM20220017

ACI MATERIALS JOURNAL

The American Concrete Institute (ACI) is a leading authority and resource worldwide for the development and distribution of consensus-based standards and technical resources, educational programs, and certifications for individuals and organizations involved in concrete design, construction, and materials, who share a commitment to pursuing the best use of concrete.

Individuals interested in the activities of ACI are encouraged to explore the ACI website for membership opportunities, committee activities, and a wide variety of concrete resources. As a volunteer member-driven organization, ACI invites partnerships and welcomes all concrete professionals who wish to be part of a respected, connected, social group that provides an opportunity for professional growth, networking, and enjoyment.

American Concrete Institute